DOKUZ EYLÜL UNIVERSITY
GRADUATE SCHOOL OF NATURAL AND APPLIED SCIENCES

DYNAMIC CHARACTERIZATION OF A WIND TURBINE UNDER DIFFERENT OPERATIONAL AND ENVIRONMENTAL CONDITIONS

by
Onur ÖZTÜRKOĞLU

April, 2023
İZMİR

DYNAMIC CHARACTERIZATION OF A WIND TURBINE UNDER DIFFERENT OPERATIONAL AND ENVIRONMENTAL CONDITIONS

A Thesis Submitted to the
Graduate School of Natural and Applied Sciences of Dokuz Eylül University
In Partial Fulfillment of the Requirements for the Degree of Doctor of Philosophy in Civil Engineering, Structural Engineering Program

by
Onur ÖZTÜRKOĞLU

April, 2023
İZMİR

Ph.D. THESIS EXAMINATION RESULT FORM

We have read the thesis entitled **"DYNAMIC CHARACTERIZATION OF A WIND TURBINE UNDER DIFFERENT OPERATIONAL AND ENVIRONMENTAL CONDITIONS"** completed by **Onur ÖZTÜRKOĞLU** under supervision of **PROF.DR. ÖZGÜR ÖZÇELİK** and we certify that in our opinion it is fully adequate, in scope and quality, as a thesis for the degree of Doctor of Philosophy.

…….....

Prof. Dr. Özgür ÖZÇELİK

Supervisor

…….....	..……..
Prof. Dr. Serap KAHRAMAN	Prof. Dr. Alpaslan TURGUT
Thesis Committee Member	Thesis Committee Member
…….....	..……..
Prof. Dr. Ninel ALVER	Assoc. Prof. Dr. Gürsoy TURAN
Examining Committee Member	Examining Committee Member

Prof. Dr. Okan FISTIKOĞLU

Director

Graduate School of Natural and Applied Sciences

ACKNOWLEDGEMENTS

The research for this dissertation was performed under the supervision of Prof. Dr. Özgür ÖZÇELİK. I would like to express my most sincere gratitude to him. He has been a rigorous and insightful teacher for me and a reliable guide in the research.

I am grateful to my thesis monitoring committee members, who contributed to enriching the thesis with their valuable comments, Prof. Dr. Serap KAHRAMAN and Prof. Dr. Alpaslan TURGUT.

Specifically, I address my gratitude to Prof. Dr. Joel P. CONTE for his hospitality and support during my stay at University of California, San Diego as an international scholar.

I would like to thank the 2214-A Program of the Scientific and Technological Research Council of Turkey (TUBITAK) for providing financial support during my Ph.D. studies in California, USA.

I greatly acknowledge the financial support provided by 1001-Scientific and Technological Research Projects Support Program of The Scientific and Technological Council of Turkey (TUBITAK) under the grant number 120M218. I would also like to thank Assoc. Prof. Dr. Serkan GÜNEL for his participation within the scope of the project, which makes this thesis an interdisciplinary study.

I wish to express my special thanks to my dear friends and colleagues MSc. Yaşar TANER, Asst. Prof. Dr. Umut YÜCEL, Asst. Prof. Dr. Erkan DURMAZGEZER, and MSc. Veysel YURTSEVEN for valuable contributions to this thesis and their support.

Finally, I would like to express my greatest thanks to my family Naziye ÖZTÜRKOĞLU, Mustafa ÖZTÜRKOĞLU and Yasemin GÖRGÜLÜ for their endless love, support, and guidance for all my life.

Onur ÖZTÜRKOĞLU

DYNAMIC CHARACTERIZATION OF A WIND TURBINE UNDER DIFFERENT OPERATIONAL AND ENVIRONMENTAL CONDITIONS

ABSTRACT

In the last decades, there has been an increasing demand for building taller/bigger and more advanced wind turbines in renewable energy investments. To ensure that the turbine continuously generates energy, and stays perfectly operational during its lifespan, there is an increasing need for dynamic characterization of the wind turbines under different operational and environmental conditions. In this thesis, a data acquisition system distributed throughout the tower height is designed. Acceleration, temperature and relative humidity from data acquisition system's own sensors and rotor speed, wind speed, temperature, pitch angle, nacelle direction, and wind direction from SCADA system of the turbine is recorded synchronously. An Autonomous and Continuous System Identification (ACSI) system using the p-LSCF method is developed to process long-term data. The modal parameters of the wind turbine estimated by processing a total of 13277 data files recorded in a seven months period is matched with operational and environmental conditions. A detailed finite element model of the turbine is created. The initial analytical model is calibrated according to the experimentally identified modal parameters using the sensitivity-based finite element model updating. Multi-hazard transient analyses are performed, and the effect of the wind loads on the dynamic behavior of the wind turbine is interpreted. Histograms of the eight operational and environmental conditions in which the data were recorded are presented and the relationship between operational and environmental conditions are presented. The operating principle of the wind turbine is explained in detail. Correlation of the modal parameters and operational/environmental conditions are presented and interpreted.

Keywords: Automated system identification, wind turbine, operational and environmental conditions, data acquisition, sensitivity-based model updating, field testing

FARKLI OPERASYONEL VE ÇEVRESEL KOŞULLAR ALTINDA BİR RÜZGÂR TÜRBİNİNİN DİNAMİK KARAKTERİZASYONU

ÖZ

Son yıllarda, yenilenebilir enerji yatırımlarında daha yüksek, daha büyük ve daha gelişmiş rüzgâr türbinleri inşa etmeye yönelik artan bir talep bulunmaktadır. Türbinin sürekli olarak enerji üretmesini ve kullanım ömrü boyunca sorunsuz şekilde çalışır durumda kalmasını sağlamak için, rüzgâr türbinlerinin farklı operasyonel ve çevresel koşullar altında dinamik karakterizasyonuna olan ihtiyaç artmaktadır. Bu tez kapsamında, kule yüksekliği boyunca dağıtılmış bir veri toplama sistemi tasarlanmıştır. Veri toplama sisteminin kendi sensörlerinden ivme, sıcaklık ve bağıl nem ve türbinin SCADA sisteminden rotor hızı, rüzgâr hızı, sıcaklık, pitch açısı, nasel yönü ve rüzgâr yönü senkronize olarak kaydedilmiştir. Uzun dönemde toplanan verileri işlemek için p-LSCF yöntemini kullanan otonom ve sürekli sistem tanımlama (ACSI) sistemi geliştirilmiştir. Rüzgâr türbininin yedi aylık dönemde kaydedilen toplam 13277 veri dosyası işlenerek tahmin edilen modal parametreleri operasyonel ve çevresel koşulları ile eşleştirilmiştir. Türbinin ayrıntılı bir sonlu eleman modeli oluşturulmuş ve bu analitik model, duyarlık tabanlı sonlu eleman model güncelleme yöntemi kullanılarak deneysel olarak tanımlanan modal parametrelere göre kalibre edilmiştir. Zaman tanım alanınca çoklu tehlike analizleri yapılmış ve rüzgâr yüklerinin rüzgâr türbininin dinamik davranışı üzerindeki etkisi yorumlanmıştır. Verilerin toplandığı sekiz operasyonel ve çevresel koşulun histogramları sunulmuş ve bu koşullar arasındaki ilişki sunulmuştur. Rüzgâr türbininin çalışma prensibi detaylı olarak anlatılmıştır. Modal parametrelerin ile operasyonel/çevresel koşulların korelasyonu sunulmuş ve yorumlanmıştır.

Anahtar kelimeler: Otonom sistem tanımlama, rüzgâr türbini, operasyonel ve çevresel koşullar, veri toplama, duyarlık tabanlı model güncelleme, saha deneyi

CONTENTS

Page

Ph.D. THESIS EXAMINATION RESULT FORM ii
ACKNOWLEDGEMENTS iii
ABSTRACT iv
ÖZ v
CONTENTS vi
LIST OF FIGURES x
LIST OF TABLES xx
ABBREVIATIONS xxi
LIST OF SYMBOLS xxiii

CHAPTER 1 - INTRODUCTION 1

1.1 Introduction 1
1.2 Literature Review 3
1.3 Objectives and Scope 12
1.4 Organization of the Thesis 14

CHAPTER 2 - SYSTEM IDENTIFICATION 16

2.1 Introduction 16
2.2 Operational Modal Analysis 17
2.2.1 Classification of Operational Modal Analysis Methods 18
2.2.2 Poly-reference Least Square Complex Frequency (p-LSCF) Method 20
2.2.3 Stabilization Diagram 21
2.3 Data Acquisition 23
2.3.1 Frequency Range 23
2.3.2 Dynamic Range 23
2.3.3 Minimum Number of Sensors 24
2.3.4 Sampling Frequency 25
2.3.5 Measurement Duration 25

2.4 Signal Processing 26
2.4.1 Inspection of Data Quality 26
2.4.2 Calibration 27
2.4.3 Detrending 27
2.4.4 Filtering 27
2.4.5 Decimation 29

CHAPTER 3 - FINITE ELEMENT MODEL UPDATING 30

3.1 Introduction 30
3.2 Sensitivity-Based Finite Element Updating 31
3.2.1 Objective Function 32
3.2.2 Model Parameters to be Updated 35
3.2.3 Sensitivity Matrix 37
3.3 Optimization Process 44

CHAPTER 4 - REAL-TIME DATA ACQUISITION ON AN OPERATING WIND TURBINE 47

4.1 Introduction of The Wind Turbine 47
4.1.1 Wind Profile of the Region 49
4.2. Data Acquisition System 52
4.2.1 Hardware 53
4.2.1.1 Sensors 54
4.2.1.2 Chassis and Modules 56
4.2.1.3 Other Devices 58
4.2.2 Laboratory Studies and Synchronized Data Recording 61
4.2.3 Placement of Data Acquisition System on the Wind Turbine 63
4.2.4 Establishment of Network Configuration 65
4.2.5 Software 69
4.2.5.1 Codes Developed to Run at Switchyard 69
4.2.5.1.1 SCADA: Part-A. 72

4.2.5.1.2 SCADA: Part-B. 74
4.2.5.2 Codes Developed to Run in Turbine 77
4.2.5.2.1 Turbine: Part-A. 77
4.2.5.2.2 Turbine: Part-B. 80
4.2.5.2.3 Turbine: Part-C. 85
4.2.5.2.4 Turbine: Part-D. 87
4.2.5.2.5 Turbine: Part-E. 90
4.2.5.3 Codes Developed to Run on Campus 92
4.2.5.3.1 Campus: Part-A. 93
4.2.5.3.2 Campus: Part-B. 95
4.2.5.4 Execution of Codes and Data Flow Chart in Switchyard, Turbine, and Campus 98

CHAPTER 5 - AUTONOMOUS SYSTEM IDENTIFICATION 100

5.1 Operational Modal Analysis using p-LSCF Method 100
5.1.1 Preparation of Data 101
5.1.2 Stabilization Diagram 102
5.1.3 Autonomous Mode Picking 105
5.2 Fully Automated Data Acquisition and System Identification Process 107

CHAPTER 6 - MODEL UPDATING OF THE WIND TURBINE 110

6.1 Finite Element Model of the Wind Turbine 110
6.2 Analytical Modal Analysis 112
6.3 Pairing Analytical and Experimental Modes 113
6.4 Construction of Objective Function and Design Variables 115
6.5 Sensitivity Analysis 117
6.6 Model Updating 118
6.7 Multi-Hazard Analysis with Updated Model 120
6.7.1 Earthquake Record 120
6.7.2 Wind Loads 122

6.7.3 Multi-Hazard Analysis Results 129

CHAPTER 7 - THE EFFECT OF OPERATIONAL AND ENVIRONMENTAL CONDITIONS ON WIND TURBINE DYNAMIC CHARACTERISTICS 131

7.1 Introduction 131
7.2 Relationship Between Operational and Environmental Conditions 136
7.3 The Effect of Operational and Environmental Conditions on Mode Frequency 140
7.4 The Effect of Operational and Environmental Conditions on Mode Damping 153
7.5 The Effect of Operational and Environmental Conditions on Mode Shape .. 168

CHAPTER 8 - CONCLUSIONS AND FUTURE WORKS 181

8.1 Conclusions 181
8.2 Recommendations for Future Research 187

REFERENCES 189

LIST OF FIGURES

Page

Figure 2.1 Definition of Linear Time-Invariant (LTI) system 16

Figure 2.2 A stabilization diagram obtained from LSCF method (Peeters, Van der Auweraer, Guillaume, & Leuridan, 2004) 22

Figure 2.3 A stabilization diagram obtained from p-LSCF method (Peeters, Van der Auweraer, Guillaume, & Leuridan, 2004) 22

Figure 2.4 Frequency response function (Brincker, & Ventura, 2015) (a) high-pass filter, (b) low-pass filter, and (c) band-pass filter 29

Figure 3.1 The sensitivity-based FEMU process 31

Figure 3.2 Optimization problem types (a) well-conditioned (b) ill-conditioned and (c) underdetermined (Yucel, 2020) 45

Figure 4.1 (a) The monitored wind turbine and (b) a general view of the wind power plant (Dost Enerji, 2023) 48

Figure 4.2 Tower geometry (right is top) 48

Figure 4.3 Wind direction distribution for four years period 50

Figure 4.4 Wind rose prepared for the region 51

Figure 4.5 Distribution of wind speed classes 51

Figure 4.6 Sensor layout along the tower 52

Figure 4.7 (a) Uniaxial accelerometer, and (b) triaxial accelerometer 55

Figure 4.8 Temperature and relative humidity sensors 56

Figure 4.9 (a) NI 9239 voltage input module and (b) NI 9203 current input module 57

Figure 4.10 NI cDAQ-9185 chassis 59

Figure 4.11 Other components of the data acquisition system: (a) industrial power supply, (b) industrial box PC, (c) workstation, (d) uninterruptible power supply, (e) ethernet switch, (f) splitter, (g) network attached storage, and (g) P2P antenna 60

Figure 4.12 Two panels installed in the laboratory (Personal archive, 2022) 61

Figure 4.13 Accelerometers placed on the shaking table (Personal archive, 2022) 62

Figure 4.14 (a) Voltage data from the accelerometer connected to the chassis at Level-1 (b) Voltage data from the accelerometer connected to the Level-5 chassis, and (c) the difference of voltage data from tow accelerometers 62

Figure 4.15 Illustration of data acquisition system on the wind turbine..... 64

Figure 4.16 (a) Main panel, network attached storage, and uninterruptible power supply at foundation level (0-meter) (b) cabling through the tower, (c) panels at level 2, 3, 4, and 5, (d) placement of the accelerometers on tower with strong magnets, and (e) placement of the temperature and relative humidity sensors (Personal archive, 2022)..... 65

Figure 4.17 Stations and data flow chart of the data acquisition system..... 66

Figure 4.18 Network configuration of data acquisition system..... 66

Figure 4.19 Internet access of industrial computer in turbine with P2P antennas installed in turbine and switchyard..... 68

Figure 4.20 Processing stages of SCADA data in the industrial computer installed in the switchyard..... 70

Figure 4.21 Receiving the desired data from the NI OPC Server by connecting to the SCADA server as a client..... 71

Figure 4.22 Assigning required SCADA data as "Shared Variables" under the project file..... 72

Figure 4.23 SCADA: Part-A; Processing of SCADA data..... 73

Figure 4.24 TCP Listen..... 75

Figure 4.25 STM Write Meta Data 75
Figure 4.26 TM Read Message 75
Figure 4.27 STM Write Message 76
Figure 4.28 SCADA: Part-B; Transferring SCADA data to the turbine 76
Figure 4.29 NI-DAQmx Create Channel 77
Figure 4.30 NI-DAQmx Timing 78
Figure 4.31 NI-DAQmx Start Task 78
Figure 4.32 Turbine: Part-A; Starting a task by selecting channels with NI-DAQmx functions 79
Figure 4.33 NI-DAQmx Read 80
Figure 4.34 Digital FIR Filter 80
Figure 4.35 Detrend function 81
Figure 4.36 Decimate 1D Array function 81
Figure 4.37 Turbine: Part-B; Reading with NI-DAQmx functions and processing collected data 81
Figure 4.38 Digital FIR Filter features 82
Figure 4.39 Time-acceleration plot of raw and filtered data 82
Figure 4.40 PSD graph of raw and filtered data 82
Figure 4.41 Time-acceleration plot of raw and detrended data 83
Figure 4.42 PSD graph of detrended data 84
Figure 4.43 TCP Open Connection 85
Figure 4.44 STM Read Message 85
Figure 4.45 STM Read Meta Data 86
Figure 4.46 Turbine: Part-C; Processing of SCADA data transferred from the switchyard to the turbine 86
Figure 4.47 Get Date/Time String 88

Figure 4.48 Build Path 88
Figure 4.49 TDMS Open 88
Figure 4.50 TDMS Write 88
Figure 4.51 TDMS Close 89
Figure 4.52 Strip Path function 89
Figure 4.53 Turbine: Part-D; filing and saving sensor and SCADA data in .tdms format 89
Figure 4.54 Create Network Stream Writer Endpoint / Create Network Stream Reader Endpoint 91
Figure 4.55 Read Multiple Elements to Stream / Write Multiple Elements to Stream 91
Figure 4.56 Flush Stream 91
Figure 4.57 Destroy Stream Endpoint 91
Figure 4.58 Turbine: Part-E; transferring the sensor and SCADA data collected in the turbine to the campus 92
Figure 4.59 Empty Array 93
Figure 4.60 Obtain Queue 93
Figure 4.61 Enqueue Element 93
Figure 4.62 Release Queue 94
Figure 4.63 Campus: Part-A; Reading SCADA and sensor data sent from the turbine to the campus 94
Figure 4.64 Network Stream Endpoint function 96
Figure 4.65 Open Handle 96
Figure 4.66 Set Recipients 96
Figure 4.67 Set Message 96
Figure 4.68 Send 97
Figure 4.69 Close Handle 97

Figure 4.70 Campus: Part-B; Notification by e-mail in case the data flow to the campus breaks 97

Figure 4.71 Order of Execution of Codes and Data Flow Diagram 99

Figure 5.1 Wind turbine acceleration measurement points and the MACEC model of the turbine..... 102

Figure 5.2 Stabilization diagrams constructed using (a) p-LSCF method, and (b) SSI-DATA method..... 104

Figure 5.3 Procedure for autonomous mode picking..... 106

Figure 5.4 Selected physical modes using autonomous mode picking procedure 106

Figure 6.1 (a) Finite element model for the reinforced concrete foundation and steel tower (b) a simplified model for the rotor and nacelle..... 110

Figure 6.2 Mesh convergence..... 111

Figure 6.3 Finite element meshing of the wind turbine..... 112

Figure 6.4 (a) First (fundamental), and (b) second structural mode shapes 113

Figure 6.5 Paired (a) 1st (fundamental) mode, and (b) 2nd mode shapes 115

Figure 6.6 The sensitivity matrix..... 117

Figure 6.7 Original and corrected data of Imperial Valley Earthquake. a) acceleration, b) velocity, and c) displacement..... 121

Figure 6.8 Lift and drag forces acting on moving rotor blade (Dixon & Hall, 2013) 122

Figure 6.9 Wind profile for 15 m/s wind speed..... 125

Figure 6.10 Defining wind load on analytical model 126

Figure 6.11 Wind loads acting on circular cross-section structures 127

Figure 6.12 Thrust coefficient of surface (CD) 127

Figure 6.13 Tower top displacement histories..... 130

Figure 6.14 Maximum stress (at any point) on the tower histories 130

Figure 7.1 Wind speed histogram 131
Figure 7.2 Temperature histogram..... 132
Figure 7.3 Relative humidity histogram 132
Figure 7.4 Wind direction histogram 133
Figure 7.5 Nacelle direction histogram..... 133
Figure 7.6 Rotor speed histogram 134
Figure 7.7 Pitch angle histogram 135
Figure 7.8 Actual power histogram 135
Figure 7.9 The relationship between wind speed and rotor speed 136
Figure 7.10 The relationship between wind speed and actual power 136
Figure 7.11 The relationship between wind speed and pitch angle 137
Figure 7.12 The relationship between rotor speed and pitch angle 137
Figure 7.13 The relationship between rotor speed and actual power 137
Figure 7.14 The relationship between temperature and relative humidity 139
Figure 7.15 The relationship between wind direction and nacelle direction 139
Figure 7.16 Rotor speed vs frequency (estimated around 0.35 Hz)..... 140
Figure 7.17 Rotor speed vs frequency (estimated around 0.35 Hz) for only active cases only..... 141
Figure 7.18 Wind speed vs frequency (estimated around 0.35 Hz)..... 141
Figure 7.19 Temperature vs frequency (estimated around 0.35 Hz) 141
Figure 7.20 Relative humidity vs frequency (estimated around 0.35 Hz) 142
Figure 7.21 Pitch angle vs frequency (estimated around 0.35 Hz)..... 142
Figure 7.22 Nacelle direction vs frequency (estimated around 0.35 Hz) 142
Figure 7.23 Wind direction vs frequency (estimated around 0.35 Hz)..... 143
Figure 7.24 Rotor speed vs frequency (estimated around 3.00 Hz)..... 144

Figure 7.25 Rotor speed vs frequency (estimated around 3.00 Hz) for active cases only 144
Figure 7.26 Wind speed vs frequency (estimated around 3.00 Hz) 144
Figure 7.27 Temperature vs frequency (estimated around 3.00 Hz) 145
Figure 7.28 Relative humidity vs frequency (estimated around 3.00 Hz) 145
Figure 7.29 Pitch angle vs frequency (estimated around 3.00 Hz) 145
Figure 7.30 Nacelle direction vs frequency (estimated around 3.00 Hz) 146
Figure 7.31 Wind direction vs frequency (estimated around 3.00 Hz) 146
Figure 7.32 Rotor speed vs frequency (estimated around 8.29 Hz) 147
Figure 7.33 Rotor speed vs frequency (estimated around 8.29 Hz) for active cases only 148
Figure 7.34 Wind speed vs frequency (estimated around 8.29 Hz) 148
Figure 7.35 Temperature vs frequency (estimated around 8.29 Hz) 148
Figure 7.36 Relative humidity vs frequency (estimated around 8.29 Hz) 148
Figure 7.37 Pitch angle vs frequency (estimated around 8.29 Hz) 149
Figure 7.38 Nacelle direction vs frequency (estimated around 8.29 Hz) 149
Figure 7.39 Wind direction vs frequency (estimated around 8.29 Hz) 149
Figure 7.40 Rotor speed vs frequency (estimated around 16.00 Hz) 150
Figure 7.41 Rotor speed vs frequency (estimated around 16.00 Hz) for active cases only 151
Figure 7.42 Wind speed vs frequency (estimated around 16.00 Hz) 151
Figure 7.43 Temperature vs frequency (estimated around 16.00 Hz) 151
Figure 7.44 Relative humidity vs frequency (estimated around 16.00 Hz) 152
Figure 7.45 Pitch angle vs frequency (estimated around 16.00 Hz) 152
Figure 7.46 Wind direction vs frequency (estimated around 16.00 Hz) 152
Figure 7.47 Nacelle direction vs frequency (estimated around 16.00 Hz) 153

Figure 7.48 Rotor speed vs damping ratio (around 0.35 Hz frequency)..... 154
Figure 7.49 Rotor speed vs damping ratio (around 0.35 Hz frequency) for active cases only..... 154
Figure 7.50 Wind speed vs damping ratio (around 0.35 Hz frequency)..... 154
Figure 7.51 Wind speed vs damping ratio (around 0.35 Hz frequency) for active cases..... 155
Figure 7.52 Temperature vs damping ratio (around 0.35 Hz frequency) 155
Figure 7.53 Relative humidity vs damping ratio (around 0.35 Hz frequency).... 155
Figure 7.54 Pitch angle vs damping ratio (around 0.35 Hz frequency)..... 156
Figure 7.55 Nacelle direction vs damping ratio (around 0.35 Hz frequency) 156
Figure 7.56 Wind direction vs damping ratio (around 0.35 Hz frequency)..... 156
Figure 7.57 Rotor speed vs damping ratio (around 3.00 Hz frequency)..... 157
Figure 7.58 Rotor speed vs damping ratio (around 3.00 Hz frequency) for active cases only..... 158
Figure 7.59 Wind speed vs damping ratio (around 3.00 Hz frequency)..... 158
Figure 7.60 Temperature vs damping ratio (around 3.00 Hz frequency) 158
Figure 7.61 Relative humidity vs damping ratio (around 3.00 Hz frequency).... 159
Figure 7.62 Pitch angle vs damping ratio (around 3.00 Hz frequency)..... 159
Figure 7.63 Nacelle direction vs damping ratio (around 3.00 Hz frequency) 159
Figure 7.64 Wind direction vs damping ratio (around 3.00 Hz frequency)..... 160
Figure 7.65 Rotor speed vs damping ratio (around 8.29 Hz frequency)..... 161
Figure 7.66 Rotor speed vs damping ratio (around 8.29 Hz frequency) for active cases only..... 161
Figure 7.67 Wind speed vs damping ratio (around 8.29 Hz frequency)..... 161
Figure 7.68 Temperature vs damping ratio (around 8.29 Hz frequency) 162
Figure 7.69 Relative humidity vs damping ratio (around 8.29 Hz frequency).... 162

Figure 7.70 Pitch angle vs damping ratio (around 8.29 Hz frequency)..... 162
Figure 7.71 Nacelle direction vs damping ratio (around 8.29 Hz frequency) 163
Figure 7.72 Wind direction vs damping ratio (around 8.29 Hz frequency)..... 163
Figure 7.73 Rotor speed vs damping ratio (around 16.00 Hz frequency)..... 164
Figure 7.74 Rotor speed vs damping ratio (around 16.00 Hz frequency) for active cases only..... 164
Figure 7.75 Wind speed vs damping ratio (around 16.00 Hz frequency)..... 165
Figure 7.76 Wind speed vs damping ratio (around 16.00 Hz frequency) for active cases only..... 165
Figure 7.77 Temperature vs damping ratio (around 16.00 Hz frequency) 165
Figure 7.78 Relative humidity vs damping ratio (around 16.00 Hz frequency).. 166
Figure 7.79 Relative humidity vs damping ratio (around 16.00 Hz frequency) for active cases only..... 166
Figure 7.80 Pitch angle vs damping ratio (around 16.00 Hz frequency)..... 166
Figure 7.81 Nacelle direction vs damping ratio (around 16.00 Hz frequency) ... 167
Figure 7.82 Wind direction vs damping ratio (around 16.00 Hz frequency)..... 167
Figure 7.83 The principal mode shape estimated around (a) 0.35 Hz frequency, (b) 3.00 Hz frequency, (c) 8.29 Hz frequency, and (d) 16.00 Hz frequency 169
Figure 7.84 Rotor speed vs MAC value (around 0.35 Hz frequency)..... 170
Figure 7.85 Rotor speed vs MAC value (around 0.35 Hz frequency)..... 170
Figure 7.86 Temperature vs MAC value (around 0.35 Hz frequency)..... 170
Figure 7.87 Relative humidity vs MAC value (around 0.35 Hz frequency)..... 171
Figure 7.88 Pitch angle vs MAC value (around 0.35 Hz frequency) 171
Figure 7.89 Nacelle direction vs MAC value (around 0.35 Hz frequency)..... 171
Figure 7.90 Wind direction vs MAC value (around 0.35 Hz frequency) 172
Figure 7.91 Rotor speed vs MAC value (around 3.00 Hz frequency)..... 172

Figure 7.90 Wind speed vs MAC value (around 3.00 Hz frequency) 173
Figure 7.93 Temperature vs MAC value (around 3.00 Hz frequency)..... 173
Figure 7.94 Relative humidity vs MAC value (around 3.00 Hz frequency)..... 173
Figure 7.95 Pitch angle vs MAC value (around 3.00 Hz frequency) 174
Figure 7.96 Nacelle direction vs MAC value (around 3.00 Hz frequency)..... 174
Figure 7.97 Wind direction vs MAC value (around 3.00 Hz frequency) 174
Figure 7.98 Rotor speed vs MAC value (around 8.29 Hz frequency) 175
Figure 7.99 Wind speed vs MAC value (around 8.29 Hz frequency) 175
Figure 7.100 Temperature vs MAC value (around 8.29 Hz frequency)..... 176
Figure 7.101 Relative humidity vs MAC value (around 8.29 Hz frequency) 176
Figure 7.102 Pitch angle vs MAC value (around 8.29 Hz frequency) 176
Figure 7.103 Nacelle direction vs MAC value (around 8.29 Hz frequency)..... 177
Figure 7.104 Wind direction vs MAC value (around 8.29 Hz frequency) 177
Figure 7.105 Rotor speed vs MAC value (around 16.00 Hz frequency)..... 178
Figure 7.106 Wind speed vs MAC value (around 16.00 Hz frequency) 178
Figure 7.107 Temperature vs MAC value (around 16.00 Hz frequency)..... 179
Figure 7.108 Relative humidity vs MAC value (around 16.00 Hz frequency)..... 179
Figure 7.109 Pitch angle vs MAC value (around 16.00 Hz frequency) 179
Figure 7.110 Nacelle direction vs MAC value (around 16.00 Hz frequency)..... 180
Figure 7.111 Wind direction vs MAC value (around 16.00 Hz frequency) 180

LIST OF TABLES

Page

Table 4.1 Properties of the wind turbine 48

Table 4.2 The tower material mechanical properties (S355)..... 49

Table 4.3 Soil properties of power plant area..... 49

Table 4.4 Data acquisition system components..... 54

Table 4.5 Specifications of accelerometers. 55

Table 5.1 Selected physical modes using autonomous mode picking procedure 107

Table 6.1 Mode frequencies. 113

Table 6.2 Environmental and operational conditions while recording data for FEM updating..... 114

Table 6.3 Paired mode frequencies and MAC values 115

Table 6.4 Response residuals of objective function 116

Table 6.5 Parameters to be updated (design variables) 117

Table 6.6 The sensitivity matrix..... 118

Table 6.7 Initial and update parameter values..... 119

Table 6.8 Experimental and analytical mode pairs..... 119

Table 6.9 Imperial Valley earthquake (1940) features..... 120

Table 6.10 Wind turbine blades properties..... 123

Table 6.11 Parameters corresponding to the selected wind speeds and wind loads acting on the rotor..... 124

Table 6.12 Roughness lengths..... 125

Table 6.13 Wind loads acting on turbine tower..... 128

Table 6.14 Wind loads acting on wind turbine..... 129

Table 7.1 Occurrence percentages of reference level..... 169

ABBREVIATIONS

IEA	: International Energy Agency
WWEA	: World Wind Energy Association
AFAD	: Disaster and Emergency Management Authority
MENR	: Ministry of Energy and Natural Sources
OMA	: Operational Modal Analysis
p-LSCF	: poly-reference Least Square Complex Frequency
FDD	: Frequency-Domain Decomposition
BEM	: Blade Element Momentum
GMM-RC	: Gaussian Mixture Model Random Coefficient
SESHMS	: Supervised Event Server Health Monitoring System
SHM	: Structural Health Monitoring
SSI-DATA	: Data-driven Stochastic Subspace Identification
FA	: Fore-Aft
SS	: Side-Side
FBGSs	: Fiber Bragg Grating Sensors
HAWT	: Horizontal-Axis Wind Turbine
NExT	: Natural Excitation Technique
LTI	: Linear Time Invariant
EMA	: Experimental Modal Analysis
SDOF	: Single Degree of Freedom
MDOF	: Multi Degree of Freedom
LSCE	: Least Square Complex Exponential
LSCF	: Least Squares Complex Frequency
NLS	: Nonlinear Least-Squares
FRF	: Frequency Response Function
SVD	: Singular Value Decomposition
RMFD	: Right Matrix-Fraction Description
LSFD	: Least-Squares Frequency-Domain
ASA	: Acoustical Society of America
SD	: Spectral Density
DC	: Direct Current

FIR	: Finite Impulse Response
IIR	: Infinite Impulse Response
MA	: Moving Average
AR	: Auto Regressive
FE	: Finite Element
FEM	: Finite Element Model
FEMU	: Finite Element Model Updating
MAC	: Modal Assurance Criterion
SCADA	: Supervisory Control and Data Acquisition

LIST OF SYMBOLS

t	time
$Y(t)$	output signal
$X(t)$	input signal
$H(t)$	impulse response of the LTI system
D	dynamic range
y_{min}	minimum detectable signal
y_{max}	maximum detectable signal
SN	signal-to-noise ratio
σ_n	RMS value of noise
f_s	sampling frequency
f_v	Nyquist frequency
Δt	sampling time interval
f_{max}	maximum frequency of interest
f_{min}	minimum mode frequency
ζ	damping ratio
$x(n)$	input signal
$y(n)$	filtered signal
$b(k)$	FIR filter constants
$a(k)$	IIR filter constants
p	design variable, parameter to be updated
n	number of the design variables
$z_j(p)$	numerically calculated modal parameters
$\tilde{z}_j$	experimentally identified modal parameters
$r_j(p)$	residuals
l_b	upper bound of design variables
u_b	lower bound of design variables
$r_f(p)$	frequency residuals
$r_s(p)$	mode shape residuals
$\|\bullet\|$	Euclidean norm

m_f	number of frequency residuals
m_s	number of mode shape residuals
θ_ϕ	angle between two modal vectors
ϕ	numerically calculated mode shape
$\overline{\phi}$	experimentally identified mode shape
λ	numerically calculated eigenvalues
$\overline{\lambda}$	experimentally identified eigenvalues
f	mode frequency
ϕ^1	first component of the mode shape vector
ϕ^{ref}	reference component of the mode shape vector
W	weighting matrix
w_j	weighting coefficient
X^e	numerical value of parameter to be updated X for e^{th}
X^e_{ref}	reference value (mostly initial selected value)
K^e_{ref}	initial element stiffness matrix
K^e	updated element stiffness matrix
K	updated global stiffness matrix
K^U	initial global stiffness matrix
n_e	number of updated elements
M	initial global mass matrix
$DS_{5\text{-}95}$	significant duration of an earthquake
I_A	Arias intensity
R_{jb}	Joyner-Boore distance
V_{S30}	shear wave velocity
v_1	reference wind speed
h_1	reference height
v_2	wind speed at any height
h_2	height
z_0	roughness length
F_D	total thrust force on a circular section

ρ	air density
C_D	thrust coefficient of the surface
U_r	wind speed
A_r	area exposed to the wind

CHAPTER 1
INTRODUCTION

1.1 Introduction

Fossil fuels, which have limited reserves in the world, account for 81% of global energy production (International Energy Agency [IEA], 2023). Emissions of greenhouse gases that cause global warming, which is one of the most important problems of our era, are caused by the consumption of these fuels. So, the importance of renewable energy sources such as wind energy is increasing day by day. In recent years, wind energy has become an important renewable energy source and a more attractive alternative to conventional energy generation due to higher capacity utilization factors and shorter return of investments. In the last decade (2011-2021), the installed capacity in wind energy has quadrupled. Furthermore, wind energy capacity, which was 830 GW in 2021, is estimated to reach 3105.9 GW in 2030 with an increase of 374% (World Wind Energy Association [WWEA], 2023). Consequently, in energy investment, there is an increasing demand for building taller/bigger, and more advanced wind turbines even in countries that are considered to be highly seismically active.

In many parts of the world, a large number of wind turbines have been installed in areas where earthquake hazard is high and this trend is still ongoing, especially in countries like Turkey. When looked at in conjunction with, Turkey Seismic Hazard Map (Disaster and Emergency Management Authority [AFAD], 2023) with Annual Average Wind Speed Distribution (Republic of Türkiye Ministry of Energy and Natural Resources [MENR], 2023), it can be seen that the regions with high potential of wind energy have high earthquake hazard levels as well. Therefore, the majority of wind farms built in Turkey are in high earthquake-hazard regions. To ensure that the turbine continuously generates energy, and stays perfectly operational during its lifespan, there is an increasing need to monitor the structural integrity of these large structures and to have a comprehensive understanding of their dynamics from a structural point of view under changing operational and environmental conditions (Hu,

Thöns, Rohrmann, Said, & Rücker, 2015a; Hu, Thöns, Rohrmann, Said, & Rücker, 2015b). One of the main challenges of dynamic characterization of an in-use/operating wind turbine is to deal with its time-variant operational nature of the system, which is a result of a combination of factors such as the presence of rotating components/machinery (blades and turbine nacelle), wind speed, rotor blade rotational speed, pitch angle of blades, orientation of nacelle, wind direction, temperature, and relative humidity.

Field testing of full-scale structures plays a key role in determining the dynamic properties of structures under realistic operational and environmental conditions. Operational Modal Analysis (OMA), also known as only-output modal analysis, is based on measuring only the response (output) of a structure and using the ambient and natural operating vibrations as unmeasured input for system identification. As opposed to input-output methods for modal identification, OMA techniques are used under actual operating conditions and in situations where it is difficult or impractical to externally excite the structure. OMA techniques can be applied to a structure under actual operating conditions to estimate operational natural frequencies and operational aerodynamic damping that are naturally different from the ones obtained under non-operational conditions (Tcherniak, Chauhan, & Hansen, 2010; Tcherniak, & Allen, 2015).

In operational modal analysis, there is a fundamental assumption of the time-invariant nature of the identified/monitored structure. In this case, this fundamental assumption is somewhat violated due to moving/rotating parts and environmental conditions. To solve this problem, a new advanced frequency domain estimation method known as ‘poly-reference Least Square Complex Frequency [p-LSCF] has been proposed (Guillaume, Verboven, Vanlanduit, Auweraer, & Peeters, 2003; Peeters, Auweraer, Guillaume, & Leuridan, 2004; El-Kafafy, Guillaume, & Peeters, 2013). Modal parameter estimates of systems can be found with high accuracy by working on the frequency definition field with this non-iterative method. In this method, stabilization diagrams with frequency, damping, and participation rates are created. Second, mode shapes are obtained. One of the most important features of the

p-LSCF method is to obtain cleaner stabilization diagrams than other modal parameter estimation methods. In this thesis work, which aims to create an autonomous damage detection system without user intervention, it is important to have clean stabilization diagrams so that the peak points of these diagrams can be accurately determined by the system and the physical mode frequencies can be obtained correctly. With this technique, it is possible to extract modal parameters of an in-use structure (in this case, a wind turbine) under normal operating conditions, (i.e., without interrupting the rotation of the turbine). Being able to do this is extremely useful for the case of wind turbine systems since switching it off would result in economic losses. In addition to this, once the system is switched off a different dynamic system emerges where its identified dynamic characteristics would be different from the ones corresponding to operational conditions. Therefore, it is particularly important to characterize a wind turbine under normal operating conditions.

Creating analytical models of structures and performing various analyses using these models is an application that is frequently used in the field of engineering. However, most real structures are too complex to be analytically modeled with precision. Due to the modeling assumptions and the presence of non-structural elements, parameters such as stiffness, mass, and damping need to be updated in light of experimental data (Worden, & Tomlinson, 2019). The Bayesian method, which is one of the probabilistic model updating techniques, is based on the representation of the physical parameters to be updated with probability density functions (Katafygiotis, & Beck, 1998; Beck, & Katafygiotis, 1998). In this method, the priority is considered to be the convergence of mode frequencies due to its close relationship with dynamic behavior (Mottershead, & Friswell, 1993).

1.2 Literature Review

Dynamic characterization of wind turbines has been studied for a while by many researchers. Some of these studies are briefly summarized below.

Butterfield, Scott, & Musial (1992) published one of the first studies on the Blade Element Momentum (BEM) theory. To determine a Horizontal-Axis Wind Turbine (HAWT) performance wind tunnel tests are performed, and the data are compared with BEM theory analyses. The results indicate that BEM theory is an accurate tool to calculate wind forces on wind turbine rotor blades. Yet, for high-yaw angle operations, minor corrections need to be done due to unsteady aerodynamics.

James, Carne, & Lauffer (1993) proposed a novel operational modal analysis method that has been widely used by different researchers in the last three decades. This method is an only-output method that allows modal parameter estimation in the ambient environment. Results from proposed Natural Excitation Technique (NExT) with conventional operational modal analysis methods for a wind turbine parked and operational conditions. Modal parameters are determined as a function of the rotation speed. Further, extracted results using NExT are compared with the analytical aeroelastic theory. With this study, it can be said that wind turbines have played an important role in the development of operational modal analysis methods.

The poly reference Least Squares Complex Frequency (p-LSCF) method, which is non-iterative and makes modal parameter estimation in the frequency domain, is explained in detail and its properties are compared with other methods (Peeters, Van der Auweraer, Guillaume, & Leuridan, 2004). In this method, first, stabilization diagrams containing information on frequency, damping, and participation rates are created. Secondly, mod shapes are obtained. One of the most important features of this method is to obtain more stable stabilization diagrams. Since it is easier to distinguish physical modes in cleaner stabilization diagrams, the method can be easier to automate, especially in higher-order systems. However, a clean stabilization diagram does not mean that some physical modes are not skipped. These modes can be found using previously accepted methods. Generally, for systems with low damping, methods in the time domain are preferred, and for systems with high damping, methods in the frequency domain are preferred. However, the p-LSCF method works well for both cases. The difference of this method from other methods in the frequency domain is that it significantly reduces the parameter estimation time in the wide frequency range

and high model degrees. Methods in the time domain were preferred because they were better in terms of time in analyses with large data sets. However, this method can also be used because it eliminates the time problem.

Shen, Mikkelsen, Sørensen, & Bak (2005) stated that Blade Element Momentum (BEM) theory is an essential method to obtain the performance of rotor blades. The tip loss effect plays a substantial role in the estimate of wind turbine performance. Different tip loss correction methods compared with the results of the experimental tests. A novel tip loss correction model is presented that eliminates the inconsistency of the tip loss correction in the literature.

El-Kafafy, Guillaume, & Peeters (2013) proposed an approach to improve the accuracy of the poly reference Least Square Complex Frequency (p-LSCF) method in particular structural damping estimates at high noise levels. With the two-step procedure, the algorithm maintains a clean stabilization diagram while improving damping estimates. In the first step, to extract the noise from the acceleration data, a parametric maximum likelihood smoothing method is used. Then the p-LSCF method is applied to the smoothed data and the damping values are estimated with considerably high accuracy. The presented approach is tested with experimental and simulated acceleration data sets. It is seen that obtained damping results have better accuracy than the traditional p-LSCF estimator.

Häckell & Rolfes (2013) monitored a wind turbine with 5 MW capacity to extract modal parameters using the triangulation-based method. This method is based on stability diagrams and frequency-damping plane to reduce the number of solutions for system identification. So, it is possible to handle a large number of datasets. Classification of data according to operational and environmental conditions is done with affinity propagation. It is said that any automation of system identification required detailed knowledge of the involved parameter's distributions.

Hu et al. (2015a) focused on a resonance of a 5 MW wind turbine. A total of eight accelerometers are placed on the turbine tower in two perpendicular directions and at

four levels. Acceleration data sets are recorded in the first 2.7 minutes of each hour for two years with 50 Hz. sampling rate. Some operational and environmental conditions (i.e., temperature, wind speed, rotation speed of blades, pitch angle of blades, and absolute angle of nacelle) are associated with the acceleration data. Operational modal analyses are performed in two directions and modal parameters of a wind turbine are estimated. The resonance phenomenon is observed when the first mode frequency matches with harmonic frequency triggered by the rotation of the blades. At around 8 RPM rotor speed, the oscillation amplitude of the tower increases while the damping value decreases. It is stated that a vibration control mechanism is necessary to minimize vibration amplitudes.

Hu et al. (2015b) research the effect of environmental/operational conditions on the dynamic parameters of a wind turbine. Correlation analyses between estimated mode frequencies, damping values, mode shapes and rotation speed of blades, wind speed, pitch angle of blades, and orientation of nacelle are presented. It is stated that nacelle position, the activation of rotor, rotor speed, and wind speed affect the natural frequencies while the mode shapes are influenced by nacelle orientation. In addition, two types of simulated damage on rotor blade and tabular tower are detected using principal component analysis-based methods.

Kilic & Unluturk (2015) presented a data acquisition system called Supervised Event Server Health Monitoring System (SESHMS). With the help of wireless accelerometers, the vibration data is recorded and sent to the server. The system does not rely on the full functionality of each sensor. If one accelerometer fails, the vibration data will reach its destination via another path. It is said that the SESHMS system is a low-cost system and effective in estimating wind turbine future performance.

The study published by Alves et al. (2017) aims to instantly detect the damage in wind turbines. In this context, the authors proposed a damage detection system that can transmit information wirelessly for wind turbines. However, this system is only sensitive to damage in the turbine blades and cannot detect damage in the tower. In this system called Delphos, the decision mechanism is carried out in the network

within the system and only the presence of damage is detected as output. It was also emphasized that the effect of temperature change on natural frequencies is significant, and the effect of environmental factors should not be neglected in future studies.

Avendaño-Valencia & Fassois (2017) studied damage diagnosis in an operating wind turbine considering operational and environmental uncertainty. A Gaussian Mixture Model Random Coefficient (GMM-RC) model-based method is used for structural health monitoring (SHM) of an offshore 5 MW wind turbine. Changes in wind speed, blade rotation, inertial properties as well as wind characteristics lead to non-stationary in vibration signals. Six different structural states are created including a healthy state and five types of damage on the tower, blade, and transmission with four distinct levels. The results of Monte Carlo simulations demonstrate that GMM-RC model-based method consistently shows good performance for the diagnosis of damages at the wind turbine.

Chen, Zhang, Hua, Basu, & Nielsen (2017) presented a wavelet-based linearization method to evaluate the aerodynamic damping of an operating wind turbine. This method is based on the generalized acceleration, velocity, and displacement vector obtained from response measurements. The filtering technique is used to evaluate the quasi-static loads from the measured response of the structure. A time-dependent aerodynamic damping matrix is obtained by wavelet analysis at each time step. The presented method is applied to a 13-degree-of-freedom aeroelastic model of a wind turbine.

Fontecha, Henneke, Kemper, & Feldmann (2017) conducted experiments in a laboratory to develop a model that would better represent the aerodynamic behavior of wind turbines. The purpose of these experiments is to describe the effect of aerodynamic damping and cross-wind vibration in turbines. It is said that the contact length of the gusts formed around the turbine tower has a significant effect on the side-side vibration of the wind turbine. It has been stated that the vibration caused by the wind, which causes the rotation of the rotor blades, is affected by aerodynamic damping.

Neu, Janser, Khatibi, & Orifici (2017) presented a multi-stage clustering approach in operational modal analysis. Unlike the approaches in the literature, it can be applied to complex systems that do not require intervention by any user, can be applied to large systems, require a small number of sensors, and do not have any limitations such as the damping ratio limit for the system under investigation. The data-driven Stochastic Subspace Identification (SSI) method is used in the study to estimate modal parameters. Fiber Bragg Grating Sensors (FBGSs) and piezoelectric sensors are placed on a cantilever composite element representing a wind turbine. The accuracy of the algorithm is tested in the high-damped system and low signal/noise conditions through performing wind tunnel tests. The proposed method detected all physical modes of the structure with only two sensors.

García & Tcherniak (2019) carried out a set of laboratory tests to monitor the structural health of a large turbine blade using only one accelerometer and actuator. In this study, a data-driven vibration structural health monitoring method which is a nonparametric method is used for information extraction. The blade is excited by an electromechanical actuator that introduced an impulse in the blade. The vibration of the blade is measured by a single accelerometer. Different damage types and sizes are considered in the tests. The results demonstrated that only one accelerometer is enough to detect different sizes of damage on the blade. Although, the locations of the accelerometer and actuator affect the estimated damaged locations. So, with a single sensor, the methodology provides rough information about the damage location.

Hofmeister, Bruns, & Rolfes (2019) presented a derivate-free global optimization method for finite element updating to localise structural damages on wind turbine blades. Although metaheuristic approaches are the most widely used for global optimization problems, this work showed that deterministic algorithms are also convenient for engineering problems such as model updating. To validate the approach, a reference finite element model of a wind turbine blade and a fictitious damaged model is created. The model updating scheme employs numerical optimization is applied and compared with the metaheuristic approaches. The introduced method converges quickly on the model updating problem as well as on

test functions. It is said that deterministic optimization methods should be given more attention in engineering optimization problems.

Kim, Kim, & Choe (2019) studied structural health monitoring of blades and towers of floating offshore wind turbines. A wind turbine model is created in a software and numerical accelerometers are placed on the model. Natural frequencies, curvature mode shapes, and displacement mode shapes of the tower and blade are obtained to perform structural health monitoring using an operational modal analysis method. Differences in the obtained modal parameters are used for damage detection. The results show that curvature mode shapes are the most effective modal properties to detect damage of towers and blades. In addition, damage detection performances of curvature mode shapes and displacement mode shapes are verified by the independent finite element method.

Zhou et al. (2019) investigate the dynamic characteristics of a monopile offshore wind turbine. In this study, to record a high-quality vibration signal an artificial excitation is created. With the help of wireless accelerometers deployed on monopile (before the turbine is erected) and tower (after the turbine is erected), acceleration signals are acquired under ambient and artificial excitation and processed by different operational analysis methods. It can be said that the eigensystem realization algorithm method and wake mode identification method can identify modal parameters of the monopile and wind turbine under parked or operating conditions while the stochastic subspace identification method failed to estimate the dynamic characteristic of monopile and wind turbine structure.

Zhao & Lang (2019) stated that environmental conditions affect the structure's behavior and can change accelerometer measurement on the structure. The effect of different environmental conditions needs to be taken into account and extracted while performing SHM. To that end, a model-based SHM method is presented. As a result of this work, the health indicator within the thresholds of the toleration is used to evaluate the existence of damage. A set of data is collected from an operating wind

turbine and processed according to the presented health indicator. The results show the aforementioned method can predict the structural health of the wind turbine.

Chen, Duffour, & Fromme (2020) proposed a two-stage methodology to predict the aerodynamic damping of a horizontal axis wind turbine. Aerodynamic forces induced by wind are obtained using Blade Element Momentum Method. From closed-form expressions for the damping matrix, it is understood that there is a correlation between the aerodynamics and vibration response of the tower. In addition, coupling between side-side and fore-aft motions in a wind turbine can significantly affect the apparent aerodynamic damping.

Meng et al. (2020) tested a 1/100 scaled model of a wind turbine under wind and earthquake effects to investigate a practical method to predict the response of the wind turbine. In the scenario in which the wind and earthquake are applied simultaneously, the overall response of the structure is lower than only the earthquake scenario. With the help of this information, time-consuming fully coupled aeroelastic analysis can be avoided by performing wind and earthquake analysis separately with appropriate aerodynamic damping. The coupling effect between the earthquake and wind increases with the increase of wind speed and decreases with the peak ground acceleration values of the earthquake.

Xi et al. (2020) stated that the total damping of wind turbines consists of four different kinds of damping: structural, aerodynamic, soil, and hydromechanics. Aerodynamic damping is the most variable one of these kinds. To detect aerodynamic damping accurately, a semi-analytical model is presented and applied to two wind turbine models which have 5 MW and 1.5 MW energy production capacity. Blade forces induced by wind are calculated using Blade Element Momentum Method. The findings of the study showed that that the semi-analytical model including the aerodynamic damping has better accuracy than the excluded model for determining the dynamic characteristics of horizontal axis wind turbines.

Cong, Hu, & Li (2022) said that the major sources of errors in modeling an offshore wind turbine with finite elements are structural damping, aerodynamic damping, soil-structure interface damping, and hydrodynamic added mass. To minimize modeling errors, a comprehensive methodology involving complex mode expansion, optimal sensor placement, and cross-mode-based model updating is presented. The methodology is applied to the National Renewable Energy Laboratory 5 MW reference wind turbine. It is seen that the model parameters can be updated utilizing clean modal data while some model parameters cannot be updated when spatially incomplete complete eigenvectors are used.

Khazaee, Derian, & Mouraud (2022) conducted an analytical study to assess damage in the rotor blade by evaluating the tower oscillation. An onshore wind turbine with 5 MW capacity is created using NREL FAST software. Some structural damage is simulated on the blade while tower vibrations are monitored by virtual vibration sensors. A convolutional neural network classifier is developed for classifying tabular tower oscillation. The results showed that damage on rotor blade influences the tower oscillation and blade fault can be easily diagnosed in the side-to-side displacement of the tower.

Pacheco-Chérrez & Probst (2022) used the Frequency-Domain Decomposition (FDD) which is one of the operational modal analysis methods to monitor the structural health of a wind turbine blade. The blade is modeled in two different ways as damaged and undamaged in ANSYS environment and analytical simulations are carried out under wind excitation. Wind loads on the blade are calculated using the Blade Element Momentum (BEM) method. Acceleration data is extracted using virtual sensors on rotor blade used for operational modal analysis. The results indicated that damage on the rotor blades can be detected and located using only stochastic wind excitation.

Hine et al. (2023) deployed a set of wired accelerometers, wireless accelerometers, strain gauges, and an inclinometer on an operational offshore wind turbine. An automated system identification process employing data-driven stochastic subspace

identification (SSI-DATA) is used for estimating the modal parameters of the structure. The fore-aft (FA) and side-side (SS) modes of the wind turbine are estimated with high accuracy. It is said that FA and SS modes can be separated using modal assurance criteria because their frequencies are closely separated from each other.

Pereira et al. (2023) worked on continuous monitoring of an onshore wind turbine. It is stated that manual analysis of long-term data is impractical, and an autonomous data process is extremely necessary for continuous structural health monitoring. A procedure to evaluate dominant modal frequencies and possible resonances is presented and evaluated with the collected data from three different wind turbines by various sensors.

1.3 Objectives and Scope

The thesis research focuses on system identification of an in-service wind turbine under the effect of different operational and environmental conditions. For this purpose, a novel Autonomous and Continuous System Identification (ACSI) system is developed. The system records data through its own accelerometers placed on the different levels of the wind turbine tower and processes the acceleration data via an operational modal analysis method. Modal parameters of the wind turbine stored with the operational (rotor speed, nacelle direction, and pitch angle) and environmental data (temperature, wind speed, wind direction, and relative humidity) for further analyses. Correlations between the modal parameters and operational/environmental conditions are determined.

The main goals of the thesis are to

- design a data acquisition system for the subject wind turbine,
- develop a series of software in charge of fully automated data acquisition and system identification processes,

- calibrate the finite element model of the wind turbine to obtain more realistic representative of the structure, and

- determine the effect of operational and environmental conditions on dynamic characteristics of the wind turbine.

To achieve the objectives stated above, the following works are performed in the scope of the thesis.

A distributed data acquisition system is designed to record acceleration, temperature, and relative humidity data on the wind turbine. After the required tests in the laboratory environment the data acquisition system is placed on the subject wind turbine. Three LabVIEW codes are developed in three stations (the switchyard, the turbine, and the campus) to record data from the turbine, preprocess (filter, decimate, and detrend) the acceleration data, get the operational and environmental data from the Supervisory Control and Data Acquisition (SCADA) system, combine acceleration data with the SCADA data, and transfer all the data to the university campus. A MATLAB code is developed to read data files created by LabVIEW codes, perform system identification using p-LSCF method, and store modal parameters by associating them with the operational and environmental conditions. To understand the dynamic behavior of the wind turbine under wind loads a detailed finite element model of the turbine is created in ANSYS environment. Sensitivity-based finite model updating is performed to create realistic representation of the subject wind turbine. Using the calibrated finite element model, nonlinear transient analyses with and without wind effect are performed and the effect of the wind loads on the dynamic behavior of the wind turbine is determined. The effects of the operational and environmental conditions on the dynamic characteristics of the wind turbine are shown by the graphics and interpreted.

1.4 Organization of the Thesis

The thesis consists of eight chapters and one appendix. Organization of the thesis is presented below.

- In Chapter One, a brief introduction to the wind energy market, the necessity of what has been done within the scope of the thesis work, the literature review, objectives, and scope of the thesis are presented.

- In Chapter Two, system identification is explained. Operational modal analysis and its classification is presented. Least Squares Complex Frequency (LSCF) and Poly-reference Least Squares Complex Frequency (p-LSCF) methods are described in detail and compared with each other. It is emphasized why the p-LSCF method is chosen for system identification within the scope of the thesis. Highlights of data acquisition and signal processing are presented.

- In Chapter Three, the finite element updating concept and sensitivity-based finite element updating are explained. Conducting the objective function and optimization process are presented.

- In Chapter Four, the subject wind turbine is introduced, and the wind profile of the region is analyzed. The hardware and software parts of the real-time data acquisition system specially designed for the subject wind turbine are explained in detail.

- In Chapter Five, a novel Autonomous and Continuous System Identification (ACSI) system, which is fully autonomous from acquiring data from the wind turbine via sensors to the estimation of modal parameters, is presented.

- In Chapter Six, the finite element model of the wind turbine is created, and analytical modal analysis is performed. Finite element model updating is

done in the light of sensitivity analysis. Wind loads on the turbine and the tower are calculated by the developed MATLAB code. Using updated wind turbine model multi-hazard (earthquake and wind) transient analyses are performed with different wind speed levels.

- In Chapter Seven, the operational and environmental conditions in which the data were recorded, and the interrelationships of these conditions are presented. The correlation between operational/environmental conditions and frequencies, damping ratios and mode shapes are shown with the graphics.

- In Chapter Eight, conclusions of the thesis work and recommendations for the future works are summarized.

CHAPTER 2
SYSTEM IDENTIFICATION

2.1 Introduction

Dynamic system behavior of a system is generally described by a Linear Time-Invariant (LTI) system (Figure 2.1). The response of the LTI system can be calculated by Equation 2.1.

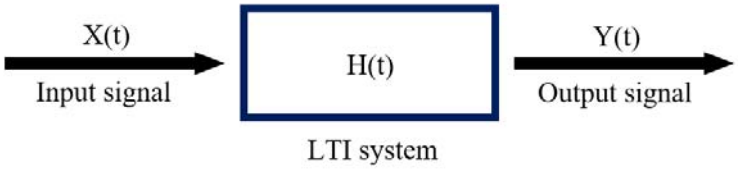


Figure 2.1 Definition of Linear Time-Invariant (LTI) system

$$Y(t) = H(t) \times X(t) \tag{2.1}$$

where H(t) is impulse response of the LTI system, X(t) and Y(t) input and output signals respectively.

An LTI system is governed by constant parameters (does not change with respect to time) reflecting the dynamic characteristics of the physical system. In addition, an LTI system converts an input signal to an output signal with linear mapping. The superposition principle can be applied when working with these systems. The response of an LTI system under different input signals is equal to the sum of the responses under each input signal. For long measurement periods, the LTI system assumption may not be valid due to fatigue damages changing the structural stiffness and damping. Considering that the results converge to reality as the measurement period increases, selecting the optimum length of records is an important issue. Physical systems behave nonlinearly under large loads. In civil engineering structures, response signals are recorded mostly under ambient excitation which is too small to induce nonlinearity of the structures (Rainieri & Fabbrocino, 2014).

The dynamics of a structure can be represented by mass-stiffness-damping or vibration parameters (natural frequencies, mode shapes, and damping ratios). These parameters belong to the structure's free vibration where no excitation exists. The natural free vibration of the structure can be obtained by combining a set of vibration modes having a characteristic mode shape. Each vibration mode is governed by its natural frequency and damping (Rainieri & Fabbrocino, 2014).

In general, system identification is a methodology for constituting a mathematical model by estimating modal parameters (i.e., natural frequencies, damping ratios, and mode shapes) of a dynamic system using experimental data. The modal parameters depend on geometry, material, and boundary condition of the physical system. The experimental verification of the modal parameters is essential for guaranteeing the safety and serviceability of the structures by validation of design models. System identification methods are frequently used for structural health monitoring and quality control for existing structures (Reynders, 2012).

System identification methods can be considered in two parts: Experimental Modal Analysis (EMA) and Operational Modal Analysis (OMA). EMA methods, also known as input-output methods, require measuring both excitation acting on the system and the response of the system. These methods have been applied in various disciplines, such as industrial machinery, automotive engineering, aerospace engineering, and civil engineering. Yet, modal parameter challenges in large and complex structures (i.e., most civil engineering structures) due to the difficulty of measuring the excitations that cause vibration in the structure. On the contrary, OMA methods known as only-output methods, use only the response measurement of the physical system under unknown excitations. This feature allows the applicability of OMA methods to a much wider range (Rainieri & Fabbrocino, 2014).

2.2 Operational Modal Analysis

Civil engineering structures are under immeasurable and noncontrollable loadings such as environmental and operational loads (wind, traffic, microtremors, etc.).

Operational Modal Analysis (OMA) methods are the most common algorithms to identify dynamic characteristics of a civil structure due to the obscurity of excitation and testing techniques do not require an interruption of normal usage of the structure. For example, during a wind turbine test, the operation of the rotor in parallel with energy production does not be interrupted. On the contrary, the operation of the rotor, traffic on a bridge, and human movement in a building help to excite the structure and more accurate estimations of modal parameters. If the structure is under the effect of white noise (the input spectrum is constant) all vibration modes are equally excited, and the response measurements contain all information on the dynamics of the structure. Since the excitations have their spectrum, modal parameters of some modes (generally higher modes) may not be estimated accurately.

Operational Modal Analysis (OMA) rely on following assumptions:

- *Linearity:* The response of the system under a combination of some inputs equals the same combination of responses under each input.
- *Stationary:* Dynamic properties of structure do not change over time. The coefficients of the equation of motion are independent of time.
- *Observability:* A suitable sensor layout is chosen for the test.

When one or more of the above-mentioned assumptions are violated, the results obtained by OMA methods lose their reliability.

Since the input is not measured, the dynamic characteristic of the structure can be interweaved with the characteristic of the excitation. This situation is frequently encountered in the test of structures with rotating parts such as wind turbines, automobiles, planes, etc. In order to overcome this phenomenon and obtain more accurate results, excitation-induced harmonic components in the measurements should be eliminated.

2.2.1 Classification of Operational Modal Analysis Methods

Most OMA methods are derived from EMA (input-output methods) techniques and are based on different stochastic frameworks. Since OMA methods always require

multiple inputs, they cannot be classified according to number of inputs (multiple input – single input). OMA methods can be classified according to four main criteria (Rainieri & Fabbrocino, 2014).

1. *Parametric and nonparametric:* During the system identification, if a method fits a model to data, it is called a parametric method. These methods are more complex and computationally expensive with respect to nonparametric methods. On the other side, nonparametric methods are faster, easy to use, and particularly useful for field testing. A further classification is made for parametric methods such as low-order and high-order methods. Parametric methods usually show better performance than nonparametric ones.

2. *Single Degree of Freedom and Multi Degree of Freedom (SDOF-MDOF):* For a particular structure where only one vibration mode governs natural oscillation, it can be assumed that the structural response is in a particular frequency range. SDOF methods based on this assumption are very fast and simple. MDOF methods should be used for structures with multiple modes in effect or with closely spaced modes.

3. *Local estimates and global estimates:* Mode frequencies and damping ratios are independent of the measurement location. If the vibration data collected from different points are analyzed separately, slightly different damping and frequency values will be obtained. So, the estimation method is local. On the other hand, if the method uses all recorded data at the same time for system identification, it is called global estimating.

4. *Time domain and frequency domain:* This classification is the most common and fundamental for OMA methods. The time domain methods analyze time history response or correlation functions while the frequency domain methods are based on spectral density functions. A response signal can always be converted into time domain or frequency domain. The time domain methods are more suitable than frequency domain counterparts to handle noisy

measurements. Contrary, using the frequency domain methods for higher model order should be the right choice due to the emergence of spurious poles at the high model order in the analyzes made with the methods in the time domain.

In the scope of this thesis work, the poly-reference Least Squares Complex Frequency (p-LSCF) method which is a version of the Least Squares Complex Frequency (LSCF) method is used for the system identification. So, these two frequency-domain methods are briefly explained in the following sections.

2.2.2 Poly-reference Least Square Complex Frequency (p-LSCF) Method

LSCF method is a parametric and frequency-domain modal parameter estimator implementation of the Least Square Complex Exponential (LSCE) estimator (Maia & Silva, 1997; Heylen, Lammens, & Sas, 1998). Due to using frequency-dependent weighting functions, the LSCF method gives more accurate estimates (Pintelon, Guillaume, Rolain, Schoukens, & Van Hamme, 1994; Pintelon & Schoukens, 2001) and most importantly, the estimator provides fast stabilizing while conducting stabilization diagrams (Van Der Auweraer, Guillaume, Verboven, & Vanlanduit, 2001). The theoretical background of the LSCF method can be found in the study of Guillaume, Verboven, Vanlanduit, Van Der Auweraer, & Peeters (2003).

The LSCF model is closely fitted to the measured FRF data. Yet, when converting the model using the Singular Value Decomposition (SVD) the quality of the fitting decreases (Van Der Auweraer, Guillaume, Verboven, & Vanlanduit, 2001). In addition, when determining the stabilization diagram using the LSCF method, only frequencies and damping values (pole information) are used. Thus, closely spaced poles cannot be separated and appear as only one pole in the stabilization diagram. These two disadvantages of the LSCF estimator became the motivation for the development of the p-LSCF method as a poly-reference version of the LSCF method. In this estimator, participation factors are also used when determining the stabilization diagram.

p-LSCF method follows similar procedures to LSCF method to estimate the modal parameters of the physical system:

- Constitution of linear equations for the maximum model order. These equations calculate the polynomial coefficient in a least-square sense.
- Solving eigenvalue problems for increasing model order and determining stabilization diagram.
- Calculation of the mode shapes in a least-square sense (needs user interpretation).

The p-LSCF method requires FRFs to find polynomial coefficients whereas the LSCF method needs impulse responses. This is the main difference between the two methods. In contrast to other frequency-domain OMA methods, in p-LSCF non-physical modes are estimated with negative damping ratios. This feature makes it easier that separating physical modes from non-physical ones (Peeters, Van der Auweraer, Guillaume, & Leuridan, 2004).

Since very clean stabilization diagrams can be obtained in this method, it is suitable to be used in autonomous system identification processes. The theoretical background of the p-LSCF method can be found in the study of Guillaume, Verboven, Vanlanduit, Van Der Auweraer, & Peeters (2003).

2.2.3 Stabilization Diagram

In OMA, the stabilization diagram makes it easy for the user to distinguish physical modes from non-physical modes **(**Heylen, Lammens, & Sas, 1998). A stabilization diagram can be constructed by repeating the analyses of different model orders. The poles are computed from the OMA method's denominator coefficient with (p-LSFC) or without (LSCF) participation factors. Stable poles are marked according to some criteria (i.e., damping values, frequency differences between two adjacent poles, and transfer norms).

Estimates physical poles appear in nearly identical locations by means of frequency while mathematical (virtual) poles tend to jump around. Physically meaningless mathematical poles exist due to the presence of noise mostly (Guillaume, Verboven, Vanlanduit, Van Der Auweraer, & Peeters, 2003). For the same measurement data set, stabilization diagrams obtained from the LSCF method and p-LSCF method are presented.

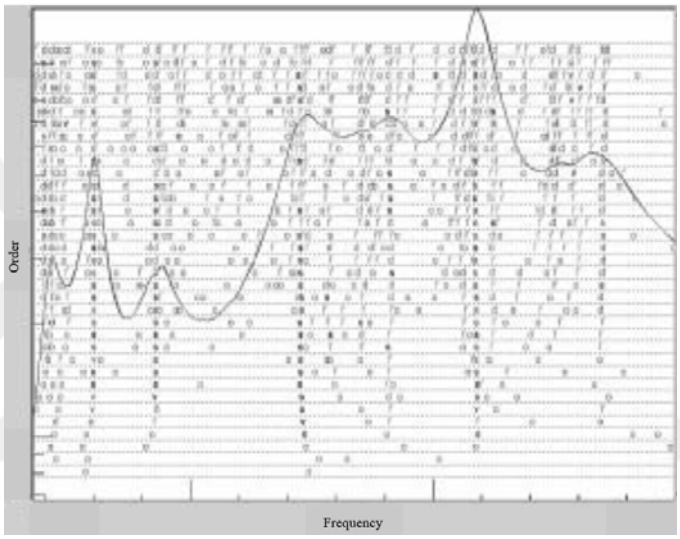


Figure 2.2 A stabilization diagram obtained from LSCF method (Peeters, Van der Auweraer, Guillaume, & Leuridan, 2004)

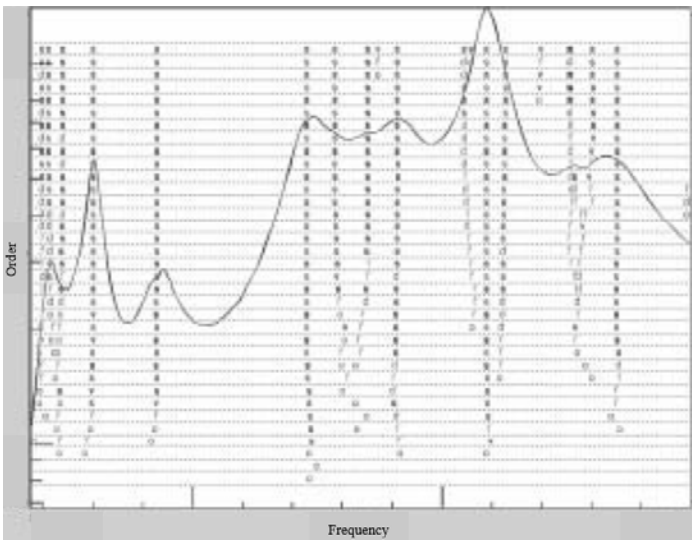


Figure 2.3 A stabilization diagram obtained from p-LSCF method (Peeters, Van der Auweraer, Guillaume, & Leuridan, 2004)

It can be seen from Figures 2.2 and 2.3, the p-LSCF method constructed a very clearer stabilization diagram for the same data set. This feature makes the method useful for autonomous processes.

2.3 Data Acquisition

Measurement of the structure's dynamic response is an important part of OMA. Successful estimation of the modal parameters mostly depends on the quality of the data sets. In the following section, some essential points of data acquisition are briefly explained (Brincker, & Ventura, 2015).

2.3.1 Frequency Range

The frequency range is the maximum and minimum frequencies to be recorded by sensors. Selection of these ranges has a great impact on the measurements and consequently the results. The frequency range should be adjusted to cover the following situations.

- The maximum significant frequency of the physical system
- First natural vibration mode frequency

2.3.2 Dynamic Range

The dynamic range of a data acquisition system can be calculated using Equation (2.62).

$$D = 20\log\left(\frac{y_{\max}}{y_{\min}}\right) \tag{2.2}$$

where y_{max} and y_{min} are the maximum and minimum detectable signals in dB respectively. The minimum detectable signal depends on the followings:

- Electrical noise
- Digital noise

- Low magnitude distortion
- Interference from other measurements

In general, signal-to-noise ratios for a data acquisition system are calculated by Equation (2.63).

$$SN = 20\log\left(\frac{y_{\max}}{\sigma_n}\right) \tag{2.3}$$

where σ_n is the Root Mean Square (RMS) value of the noise. The signal-to-noise ratio should not be less than 5 dB and if it is in the 5-10 dB range the data needs to a correction according to (Acoustical Society of America [ASA], 2001). Using data with a signal-to-noise ratio lower than 40 dB is not recommended.

2.3.3 Minimum Number of Sensors

The more sensors are used in OMA, the better results will be obtained. Yet, using more sensors than necessary also brings some problems like big data and high costs. While defining the minimum number of sensors to be used in a data acquisition system, one should consider the rank of the spectral density (SD) matrix related to the closely spaced modes. For example, if there are two closely spaced modes then the rank of the problem can be considered as two. Another parameter that affects the minimum number of sensors is the number of noise sources. Sensor numbers should be increased with the existence of noise sources.

The locations of the sensors are as important as their numbers. If two sensors are placed too close to each other, then the recording from these two sensors include almost the same information about the dynamics of the structure. So, it can be said that at least five sensors should be used for data recording, and they should be placed separately.

2.3.4 Sampling Frequency

The sampling frequency is the number of data samples recorded per second (unit time). The upper limit of the frequency band can be detected from the measurement called Nyquist frequency (Equation 2.64).

$$f_v = \frac{f_s}{2};\ f_s = \frac{1}{\Delta t} \tag{2.4}$$

where Δt is the sampling time interval, f_s and f_v are sampling and Nyquist frequency respectively. The Nyquist frequency is a consequence of the Fourier transform theory. Any information beyond the Nyquist frequency cannot be detected by any analysis. When choosing the sampling frequency, it should be considered that the Nyquist frequency must be greater than the mode frequencies to be considered.

A good data acquisition system has a built-in antialiasing filter. A typical antialiasing filter affects the measurement between $0.8f_v$-$1.0f_v$ in the frequency domain. So, in practical use, the sampling frequency should be greater than 2.4 times the maximum frequency of interest (f_{max}) (Equation 2.65). Using higher sampling frequency results in a high signal-to-noise ratio which is better for OMA methods.

$$f_s > 2.4 f_{max} \tag{2.5}$$

2.3.5 Measurement Duration

When performing system identification using OMA methods, the length of the time series is an important issue. Since too short time series do not allow enough correlation, it becomes difficult to determine modes, especially at low frequencies. Assuming that the longest correlation time is dependent on the lowest mode frequency, the total duration of measurement must satisfy the condition seen in Equation (2.66).

$$T_{tot} > \frac{10}{\zeta f_{\min}} \tag{2.6}$$

where ζ is the damping ratio of the physical system. Long measurement time gives higher accuracy results. However, it prolongs the system identification process and may increase the cost of the experiment.

2.4 Signal Processing

Once recorded the physical system's response, the measurement contains important information about the dynamics of the structure. Yet, the information is hidden by the chaos created by randomness in the recording. Processing the signal with simple methods ensures that useful information can be detected more clearly. Some signal processing methods are summarized under the following headings (Brincker, & Ventura, 2015).

2.4.1 Inspection of Data Quality

Inspection of acquired data should be done before the test setup is removed from the structure. If any problem is detected, first the problem needs to be solved. After the recording should be acquired from the beginning and the OMA processes should be started. The most common disorders that degrade the quality of data are:

- dropouts: large deviation towards zero,
- spikes: large deviation towards higher values and
- clippings: signal saturation.

The inspection data quality is usually done observationally, but it can also be done by calculating and comparing moving averages.

2.4.2 Calibration

The raw data from the Analog to Digital Converter (ADC) is a series of digital numbers without any unit. So, these numbers should be corrected with a coefficient or FRF for each sensor separately. These calibration values can be mostly found in datasheets prepared by the sensor manufacturer. Although OMA methods deal with only the relative relationship of datasets, the calibration process allows for visual inspection of the data.

2.4.3 Detrending

Detrending is the process of removing Direct Current (DC) offsets of a signal so that it has a constant zero mean. DC components in the signal appear in the low-frequency region. This can obscure low-frequency vibration modes, making them harder to detect.

In general, detrending is done by a high-pass digital FIR filter. For small DC errors, detrending can be done by overlapping data segments and extracting the mean of each window. In this case, to minimize the leakage in Fourier transform, each data segment should be tapered by a window.

2.4.4 Filtering

In most general view, filtering is removing frequencies in some ranges from the signal. In the path of the signal, only the analog filter is the antialiasing filter before the ADC. Once the signal is digitalized, different digital filters may be applied to the measurement. Two main types of digital filters, Finite Impulse Response (FIR) and Infinite Impulse Response (IIR) are shown in Equation (2.67) and Equation (2.68) respectively.

$$y(n) = \sum_{k=0}^{nb-1} b(k)x(n-k) \tag{2.7}$$

$$y(n) = \sum_{k=1}^{na} a(k) y(n-k) \tag{2.8}$$

where x(n) is the input signal, y(n) is the filtered signal, b(k) and a(k) are filter constants for FIR and IIR filters respectively, nb and na are the number of coefficients for FIR and IIR filter respectively.

The FIR filter, also known as Moving Average (MA) filter has a constant delay (frequency-independent) and stable quality. If a sharp filter cut-off is needed, with the FIR filter a lot of number of coefficients must be used. The IIR filter, also known as Auto Regressive (AR) filter can do sharp cut-offs with a limited number of coefficients.

Some filter types usually used for data preparation for OMA methods are:

- high-pass filters: allow passing frequencies higher than the specified corner frequency,
- low-pass filters: allow passing frequencies lower than the specified corner frequency and
- band-pass filters: allow passing frequencies that fall between the specified corner frequencies.

Frequency response functions of different types of filters are presented in Figure 2.4 where f_1 and f_2 are the corner frequencies.

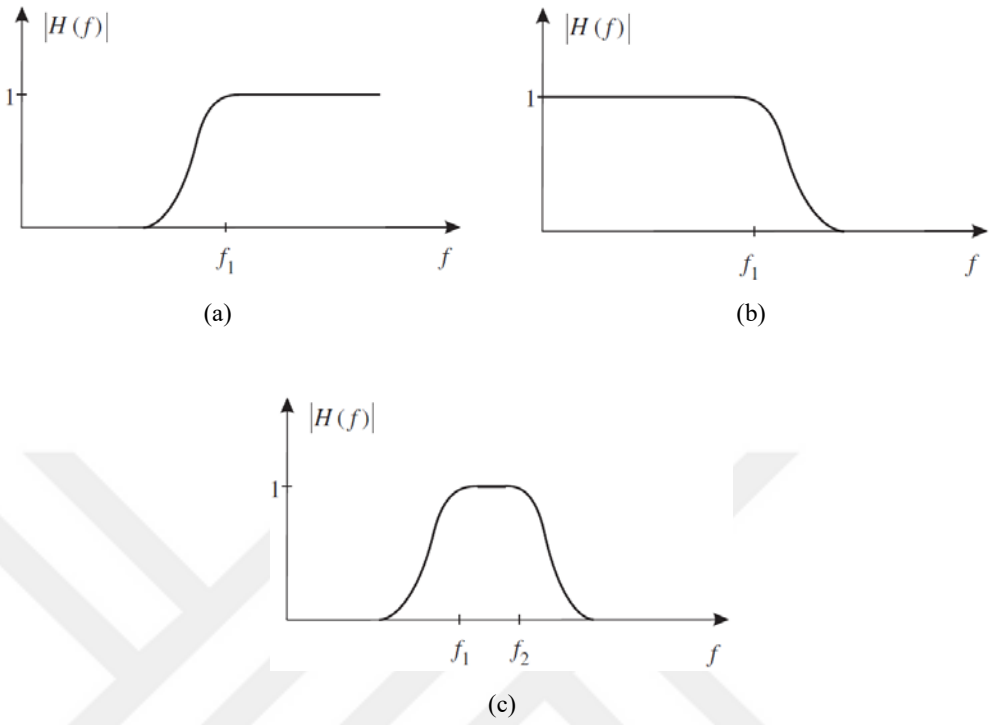


Figure 2.4 Frequency response function (Brincker, & Ventura, 2015) (a) high-pass filter, (b) low-pass filter, and (c) band-pass filter

2.4.5 Decimation

Decimation (down-sampling) means resampling the acquired data at a lower sampling frequency than the first sampling frequency in order to reduce process time or storage space and provide better focus on the frequency bandwidth of interest. To suppress energy between old and new Nyquist frequencies, a digital anti-aliasing filter needs to be used before decimation.

CHAPTER 3
FINITE ELEMENT MODEL UPDATING

3.1 Introduction

Creating numerical models of structures and making various analyzes using these models is commonly preferred in the engineering fields. However, in modeling a real complex structure, parameters such as stiffness, mass and damping need to be updated in the light of experimental data due to the modeling assumptions and the presence of non-structural elements. Finite Element Model Updating (FEMU) is a process of calibration of the initial finite element model of the structure using experimentally identified modal parameters (Worden & Tomlinson, 2019). Although mode frequencies and mode shapes are the most common parameter for FEMU, acceleration time histories, modal curvatures, modal strains, modal strain energies, and modal flexibilities can also be used (Yucel, 2020). Despite measurements errors, the experimental data represent the real structure better than Finite Element (FE) model. So, unknown or uncertain parameters should be adjusted considering test results (Friswell & Mottershead, 1995; Teughels, 2003). The FEMU techniques. FEMU techniques are frequently used for damage detection as well as model calibration (Ozturkoglu, Altunevlek, Olgun, & Ozcelik, 2018; Durmazgezer, Yucel, & Ozcelik, 2019; Yucel, Durmazgezer, Ozcelik, & Misir, 2022).

There are two main categories for FEMU methods: direct (matrix) and indirect (iterative) methods. For direct methods, the updating process is performed in only one step by updating mass and stiffness matrices directly. Using noisy measurements in direct FEMU methods significantly reduces the effectiveness of the method. In the literature there are several direct FEMU methods: optimal matrix, error matrix, eigen structure assignment, and matrix update (Mottershead & Friswell, 1993; Friswell & Mottershead, 1995; Carvalho, Datta, Gupta, & Lagadapati, 2007; Yang & Chen, 2009; Marwala, 2010; Alkayem, Cao, Zhang, Bayat, & Su, 2018). Indirect methods are based on iterative updating (adjusting) of model parameters until the analytical and experimental modal parameters are sufficiently close to each other. Since the physical

model parameters and structure's dynamic characteristics have a nonlinear relationship, the updating process has to be done iteratively.

3.2 Sensitivity-Based Finite Element Updating

The sensitivity-based FEMU is the most common iterative model updating method and it is also an inverse problem. In this method, a finite element model is created to represent the physical structure and analytical modal analysis is performed. In parallel with the recorded data, system identification process is done by performing OMA methods. Vibration modes resulting FEM analysis and OMA are paired. Model parameters are updated to minimize the difference between experimental and analytically obtained modal parameters (objective parameters). The iterative updating process is terminated when it is decided that the difference is low enough. The flowchart of the sensitivity-based FEMU method is presented in Figure 3.1. Model parameters (to be updated) can be selected as one or more of the quantities such as modulus of elasticity, thickness, mass, spring stiffness, shear modulus, boundary conditions, moment of inertia, etc. while objective parameters are mode frequencies, damping ratios, and Modal Assurance Criterion (MAC) values represent consistency of mode shapes.

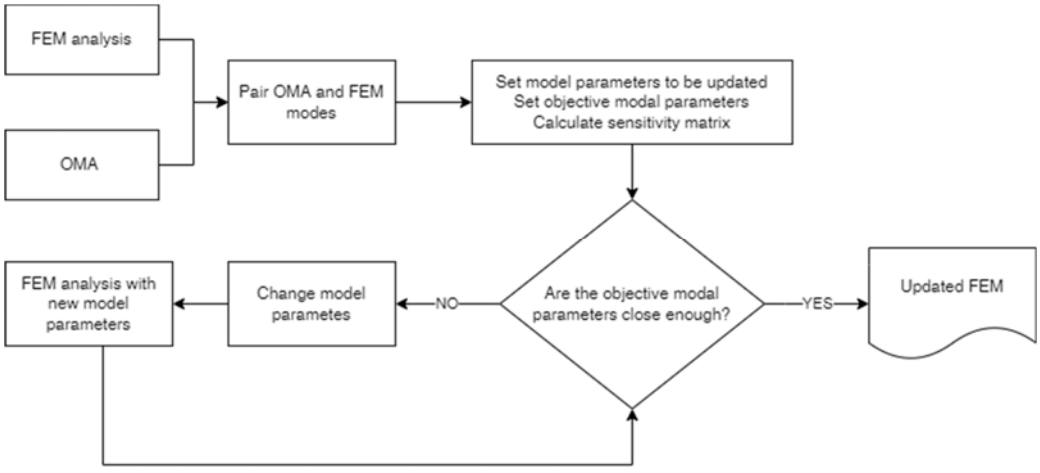


Figure 3.1 The sensitivity-based FEMU process

Model updating processes can be done either in an automated or manual way. The manual method is based on trial-error approach. It takes plenty of time and does not guarantee the best solution (global minimum of the objective function). The automated updating methods are performed by computer-aided software and much faster than the manual way. In general practice, it is recommended that one step manual model updating is done with educated guess before performing multi-step automated updating process (Mottershead & Friswell, 1993; Teughels, 2003).

The sensitivity-based FEMU is explained theoretically in the following sections (Teughels, 2003; Teughels & De Roeck, 2004; Fang, Perera, & De Roeck, 2008; Moaveni, Stavridis, Lombaert, Conte, & Shing, 2013, Yucel, 2020).

3.2.1 Objective Function

Main goal of the sensitivity-based FEMU is to minimize objective function which is representing the difference between experimentally identified and numerically calculated model parameters. The objective function is presented in Equation (3.1).

$$f(p) = \frac{1}{2}\sum_{j=1}^{m}\left[z_j(p) - \tilde{z}_j\right]^2 = \frac{1}{2}\sum_{j=1}^{m}\left[r_j(p)\right]^2; \quad l_b < p < u_b \tag{3.1}$$

where $p \in \mathbb{R}^n$ is design variable, n is the number of design variables, $z_j(p)$ numerically calculated modal parameters, $\tilde{z}_j$ is experimentally identified modal parameters, $r_j(p)$ is residuals, l_b and u_b are upper and lower bounds of design variables respectively. Physically meaningless results can be obtained in an update process that has no change limit for the parameters.

In the scope of this thesis work, model updating is done using mode frequencies and mode shapes as objective parameters, following equations are written in terms of only these properties. The residual vector is presented in Equation (3.2).

$$\min \frac{1}{2}\|r(p)\|^2 = \min \frac{1}{2}\left\| \begin{matrix} r_f(p) \\ r_s(p) \end{matrix} \right\|^2 \tag{3.2}$$

where $r_f(p): \mathbb{R}^n \to \mathbb{R}^{m_f}$ is frequency residuals and $r_s(p): \mathbb{R}^n \to \mathbb{R}^{m_s}$ is mode shape residuals, and $\|\bullet\|$ is Euclidean norm. The component number of residual vector is (Equation 3.3):

$$m = m_f + m_s \tag{3.3}$$

where m_f and m_s are the number of frequency and mode shape residuals respectively. If the number of residuals is higher than the number of design variables (parameters to be updated), Equation (3.2) has a unique solution. Otherwise, there could be an infinite number of solutions. To do high performance model updating, it is desired that having much higher number of residuals than design parameters (n<<m). If this condition is not met for a problem, it is possible to reduce the number of design parameters by grouping them (e.g., selecting only one modulus of elasticity for each element).

MAC is an important tool that shows the similarity of the two modes. It can be selected as one of the objective parameters in the model update, as well as when pairing the experimental and analytical modes in the first place (Allemang, 2003). MAC value of two mode shapes can be calculated using Equation (3.4).

$$MAC(\phi_i, \bar{\phi}_j) = (\cos\theta_\phi)^2 = \frac{\left(\phi_i^T \bar{\phi}_j\right)^2}{\left(\phi_i^T \phi_i^T\right)\left(\bar{\phi}_j^T \bar{\phi}_j\right)} \tag{3.4}$$

where θ_ϕ is the angle between two modal vectors, ϕ and $\bar{\phi}$ are numerical and experimental mode shapes respectively. The MAC value is always between 0 (orthogonal modes) and 1 (overlapping modes). Higher values of MAC indicate good

correlation between the vibration modes. An alternative Equation (3.5) suggested for closely spaced modes.

$$1-MAC(\phi_i,\bar{\phi}_j)+\left|1-\frac{\lambda_i}{\bar{\lambda}_j}\right| \tag{3.5}$$

where λ and $\bar{\lambda}$ are numerical and experimental determined eigenvalues respectively. In Equation (3.5) zero value represents perfect match of modes.

The eigenfrequency residual vector consists of the difference between the analytical and experimental mode frequencies and can be formulated by Equation (3.6).

$$r_f(p)=\frac{\lambda_j(p)-\bar{\lambda}_j}{\bar{\lambda}_j} \quad r_f:\mathbb{R}^n\rightarrow\mathbb{R}^{m_f} \tag{3.6}$$

$$\lambda_j=\left(2\pi f_j\right)^2 \tag{3.7}$$

where f is mode frequency. Since the eigenfrequencies can be estimated very accurately and very sensitive to stiffness of the system, they are irreplaceable objective parameters for FEMU methods.

Since the mode shapes have important information about the structure's dynamics, mode shape residuals are also essential for constructing objective function and can be formulated by Equation (3.8).

$$r_s(p)=\frac{\phi_j^1(p)}{\phi_j^{ref}(p)}-\frac{\tilde{\phi}_j^1}{\tilde{\phi}_j^{ref}} \qquad r_s:\mathbb{R}^n\rightarrow\mathbb{R}^{m_s} \tag{3.8}$$

where ϕ and $\tilde{\phi}$ are numerical and experimental determined modal vectors respectively, ϕ^1 and ϕ^{ref} are first (could be any) and reference component of vector.

While considering mode shape residuals in FEMU, it should be remembered that mode shapes have more estimation uncertainty than mode frequencies.

Considering their importance and estimation quality, residuals of objective function (i.e., frequency residuals and mode shape residuals) could be weighted by a coefficient matrix. So, Equation (3.2) can be reformulated as follows (Equation 3.9).

$$\min \frac{1}{2} r(p)^T W r(p) = \frac{1}{2} \left\| W^{1/2} r(p) \right\|^2 \tag{3.9}$$

where W is the diagonal weighting matrix, $W = diag(..., w_j^2, ...)$. Equation (3.9) becomes Equation (3.10).

$$\frac{1}{2} \left\| W^{1/2} r(p) \right\|^2 = \min \frac{1}{2} \sum_{j=1}^{m} \left(w_j r_j(p) \right)^2 \tag{3.10}$$

where w_j is the weighting coefficient for r_j. In the weighting matrix, only relative values of coefficient are effective in updating process.

3.2.2 Model Parameters to be Updated

In sensitivity-based FEMU, material (e.g., elasticity modulus, shear modulus, mass density, etc.) and geometrical properties (e.g., thickness, moment of inertia, boundary conditions, etc.) are generally used as the parameters to be updated. Because these features are generally uncertain or unknown parameters. Especially in detailed models, as the complexity of the structure increases, the number of parameters that may be erroneous increases. This causes the optimization problem to become ill-conditional which is computationally expensive and does not guarantee the solution. To build a well-conditioned problem, the number of parameters to be updated should be kept relatively low, and these parameters should be the most uncertain or unknown parameters.

Parameters to be updated (design variables) have various units and magnitudes. So, these parameters must be normalized before putting them into the same optimization problem. The normalization of design variables can be done with a dimensionless correction factor (Equation 3.11).

$$a_x^e = -\frac{X^e - X_{ref}^e}{X_{ref}^e} \tag{3.11}$$

where X^e is a numerical value of parameter to be updated X for e^{th} element and X_{ref}^e is the reference value (mostly initial selected value). By definition, the updated parameter is calculated by using Equation (3.12).

$$X^e = X_{ref}^e \left(1 - a_x^e\right) \tag{3.12}$$

A correction factor can be used for only one element or a group of elements having the same value. Although every element in the system matrix can be updated, in civil engineering applications, the parameters affecting the stiffness and the mass density are usually chosen as the parameter to be updated.

If a design parameter and stiffness of the structure related linearly like elasticity modulus, Equation (3.12) becomes Equation (3.13).

$$K^e = K_{ref}^e \left(1 - a^e\right) \quad -\infty \le a^e \le 1 \tag{3.13}$$

where K_{ref}^e and K^e are initial and updated stiffness matrices of element. Negative values of a^e indicate that the element becomes more rigid after the update, while if a is equal to 1, it indicates that stiffness of element is no longer available (physically meaningless for model calibration). After the updating process is done and some element's stiffnesses are updated, the global system stiffness matrix can be calculated using the Equation (3.14).

$$K = K^U + \sum_{e=1}^{n_e} K_{ref}^e \left(1 - a^e\right) \tag{3.14}$$

where K is updated global stiffness matrix, K^U is initial element's stiffness matrix, n_e is the number of updated elements. Similar procedure in Equations (3.13 and 3.14) can be applied to design parameters that have a linear relationship with the mass matrix of the system.

3.2.3 Sensitivity Matrix

The sensitivity matrix represents the change of the residuals with respect to unit change of the design parameters. In sensitivity-based FEMU process, the sensitivity matrix must be calculated in each iteration (Nocedal &Wright, 1999). Equation (3.15) shows the sensitivity matrix also known as the Jacobian matrix.

$$\left[J_p\right]_{mxn} = \begin{bmatrix} \frac{\delta r_1(p)}{\delta p_1} & \frac{\delta r_1(p)}{\delta p_2} & \cdots & \frac{\delta r_1(p)}{\delta p_n} \\ \frac{\delta r_2(p)}{\delta p_1} & \frac{\delta r_2(p)}{\delta p_2} & \cdots & \frac{\delta r_2(p)}{\delta p_n} \\ \cdots & \cdots & \cdots & \cdots \\ \frac{\delta r_m(p)}{\delta p_1} & \frac{\delta r_m(p)}{\delta p_2} & \cdots & \frac{\delta r_m(p)}{\delta p_n} \end{bmatrix}_{mxn} \tag{3.15}$$

where *m* is total number of residuals (eigenfrequency and mode shape residuals), *n* is the number of parameters to be updated *p* (design variables). According to the chain rule sensitivity matrix for each component of system can be calculated by Equation (3.16).

$$\frac{\delta r_j(p)}{\delta p_i} = \sum_{e=1}^{n_e} \frac{\delta r_j}{\delta a^e} \frac{\delta a^e}{\delta p_i} = \sum_{e=1}^{n_e} \frac{\delta r_j}{\delta a^e} N_i\left(x^e\right) \tag{3.16}$$

Eigenfrequency and mode shape residuals Equations (3.17 and 3.18) are determined by taking the derivative of the Equation (3.6 and 3.8) with respect to the correction factors.

$$\frac{\delta r_f}{\delta a^e} = \frac{1}{\bar{\lambda}_j}\frac{\delta \lambda_i}{\delta a^e} \tag{3.17}$$

$$\frac{\delta r_s}{\delta a^e} = \frac{1}{\phi_j^r}\frac{\delta \phi_j^1}{\delta a^e} - \frac{\phi_j^1}{\left(\phi_j^r\right)^2}\frac{\delta \phi_j^r}{\delta a^e} \tag{3.18}$$

where $\frac{\delta \lambda_i}{\delta a^e}$ and $\frac{\delta \phi_j^1}{\delta a^e}$ are sensitivities of eigenfrequencies and mode shapes, respectively.

Since the vibration modes are orthogonal to each other Equation (3.19) can be written and for parallel or same vibration modes Equation (3.20) is valid (Chopra, 2012).

$$\phi_i^T K \phi_j = 0, \quad \phi_i^T M \phi_j = 0 \quad \text{for } i \neq j \tag{3.19}$$

$$\phi_i^T K \phi_i = 1 \quad \phi_i^T M \phi_i = 1 \tag{3.20}$$

where K and M are system stiffness and mass matrices.

For the undamped eigenvalue problem Equation (3.21) can be written.

$$K\phi_j = \lambda_j M \phi_j \tag{3.21}$$

If both sides of the Equation (3.21) are multiplied by ϕ_j^T and considering Equation (3.20) then it becomes Equation (3.22).

$$\phi_j^T \left[K - \lambda_j M \right] \phi_j = 0 \tag{3.22}$$

Equation (3.23) is obtained by derivation Equation (3.22) with respect to a^e.

$$\frac{\delta \phi_j^T}{\delta a^e} \left[K - \lambda_j M \right] \phi_j + \phi_j^T \frac{\delta \left[K - \lambda_j M \right]}{\delta a^e} \phi_j + \phi_j^T \left[K - \lambda_j M \right] \frac{\delta \phi_j}{\delta a^e} = 0 \tag{3.23}$$

Considering K and M matrices are symmetric, $\left[K - \lambda_j M \right] \phi$ and $\phi_j^T \left[K - \lambda_j M \right]$ terms are equal. From Equations (3.21 and 3.23),

$$\phi_j^T \frac{\delta \left[K - \lambda_j M \right]}{\delta a^e} \phi_j = 0 \tag{3.24}$$

$$\phi_j^T \left[\frac{\delta K}{\delta a^e} - \frac{\delta \lambda_j}{\delta a^e} M - \lambda_j \frac{\delta M}{\delta a^e} \right] \phi_j = 0 \tag{3.25}$$

can be written. By the reason of Equation (3.20), Equation (3.25) becomes Equation (3.26).

$$\phi_j^T \frac{\delta K}{\delta a^e} \phi_j - \frac{\delta \lambda_j}{\delta a^e} - \lambda_j \phi_j^T \frac{\delta M}{\delta a^e} \phi_j = 0 \tag{3.26}$$

The sensitivity of eigenvalues is determined by Equation (3.27).

$$\frac{\delta \lambda_j}{\delta a^e} = \phi_j^T \left[\frac{\delta K}{\delta a^e} - \lambda_j \frac{\delta M}{\delta a^e} \right] \tag{3.27}$$

Since the mode shape vector linearly independent Equation (3.28) can be written.

$$\frac{\delta \phi_j}{\delta a^e} = \sum_{q=1}^{d} \alpha_{jq}^e \phi_q \tag{3.28}$$

where d is analytical model order. Equation (3.29) can be obtained by differentiating Equation (3.21).

$$\frac{\delta\left[K-\lambda_j M\right]}{\delta a^e}\phi_j+\left[K-\lambda_j M\right]\frac{\delta\phi_j}{\delta a^e}=0 \tag{3.29}$$

Substituting Equation 3.28 in Equation 3.29 leads to

$$\frac{\delta\left[K-\lambda_j M\right]}{\delta a^e}\phi_j+\left[K-\lambda_j M\right]\sum_{q=1}^{d}a_{jq}^e\phi_q=0 \tag{3.30}$$

Alternatively

$$\sum_{q=1}^{d}a_{jq}^e\left[K-\lambda_j M\right]\phi_q=-\frac{\delta\left[K-\lambda_j M\right]}{\delta a^e}\phi_j \tag{3.31}$$

If both sides of the Equation (3.31) are multiplied by ϕ_s^T where $s \neq j$ Equation (3.32) is obtained.

$$\sum_{q=1}^{d}a_{jq}^e\phi_s^T\left[K-\lambda_j M\right]\phi_q=-\phi_s^T\frac{\delta\left[K-\lambda_j M\right]}{\delta a^e}\phi_j \tag{3.32}$$

From Equation (3.19, 3.20, and 3.21), left side of the Equation 3.32 is equal to 0 except for $s=q$.

$$a_{jq}^e\left[\lambda_q-\lambda_j\right]=-\phi_s^T\frac{\delta\left[K-\lambda_j M\right]}{\delta a^e}\phi_j \quad \text{for} \quad q \neq j \tag{3.33}$$

Equation (3.33) can be written as Equation (3.34).

$$a_{jq}^{e}\left[\lambda_q-\lambda_j\right]=-\phi_q^T\frac{\delta K}{\delta a^e}\phi_j+\frac{\delta\lambda_j}{\delta a^e}\phi_q^T M\phi_j+\lambda_j\phi_q^T\frac{\delta M}{\delta a^e}\phi_j \tag{3.34}$$

From $q\neq j$ and Equation 3.19, Equation 3.34 becomes,

$$a_{jq}^{e}=-\frac{1}{\left[\lambda_q-\lambda_j\right]}\phi_q^T\left[\frac{\delta K}{\delta a^e}-\lambda_j\frac{\delta K}{\delta a^e}\right]\phi_j \quad \text{for} \quad q\neq j \tag{3.35}$$

In the case of $q=j$, the coefficient a_{jq}^{e} must be determined separately. Differentiating Equation (3.20) with respect to a^e, Equation (3.36) is obtained.

$$\frac{\delta\phi_j^T}{\delta a^e}M\phi_j+\phi_j^T\frac{\delta M}{\delta a^e}\phi_j+\phi_j^T M\frac{\delta\phi_j}{\delta a^e}=0 \tag{3.36}$$

Due to M matrix is a symmetric matrix, then Equation 3.36 becomes,

$$2\phi_j^T M\frac{\delta\phi_j}{\delta a^e}=-\phi_j^T\frac{\delta M}{\delta a^e}\phi_j \tag{3.37}$$

From Equations (3.28 and 3.37),

$$2\phi_j^T M\sum_{q=1}^{d}a_{jq}^{e}\phi_q=-\phi_j^T\frac{\delta M}{\delta a^e}\phi_j \tag{3.38}$$

Alternatively

$$2\sum_{q=1}^{d}a_{jq}^{e}\phi_j^T M\phi_q=-\phi_j^T\frac{\delta M}{\delta a^e}\phi_j \tag{3.39}$$

From Equations (3.19, 3.20, and 3.39), Equation (3.40) can be obtained.

$$a_{jj}^{e} = -\frac{1}{2}\phi_j^T \frac{\delta M}{\delta a^e}\phi_j \tag{3.40}$$

From Equations (3.28, 3.35, and 3.40) finally the sensitivity of mode shapes can be obtained using Equation (3.41).

$$\frac{\delta \phi_j}{\delta a^e} = \sum_{q=1:q\neq j}^{d}\left(\frac{\phi_q}{\lambda_j - \lambda_q}\phi_q^T\left[\frac{\delta K}{\delta a^e} - \lambda_j \frac{\delta M}{\delta a^e}\right]\phi_j\right) - \frac{\phi_j}{2}\phi_j^T \frac{\delta M}{\delta a^e}\phi_j \tag{3.41}$$

Using Equation (3.13) Equation 3.42 can be written.

$$\frac{\delta K}{\delta a^e} = -K_{ref}^{e} = \frac{-K^e}{(1-a^e)}; \quad \frac{\delta M}{\delta a^e} = -M_{ref}^{e} = \frac{-M^e}{(1-a^e)} \tag{3.42}$$

From Equations (3.17, 3.18, 3.27, and 3.42), the sensitivity of eigenfrequency residuals can be represented below.

$$\frac{\delta r_j(p)}{\delta p_i} = \sum_{e=1}^{n_w}\left(\frac{1}{\bar{\lambda}_j}\frac{\delta \lambda_j}{\delta a^e}\right)N_i\left(x^e\right) \tag{3.43}$$

$$\frac{\delta \lambda_j}{\delta a^e} = \phi_j^T\left[\frac{-K^e}{(1-a^e)} - \lambda_j \frac{\delta M^e}{\delta(1-a^e)}\right]\phi_j \tag{3.44}$$

If the mass properties are assumed to be exact and subtracted from the parameters to be updated, Equation (3.44) becomes Equation (3.45).

$$\frac{\delta \lambda_j}{\delta a^e} = \phi_j^T\left[\frac{-K^e}{(1-a^e)}\right]\phi_j \tag{3.45}$$

From Equations (3.16, 3.18, 3.41, and 3.42), sensitivity of mode shape residuals can be represented as following equations.

$$\frac{\delta r_j(p)}{\delta p_i} = \sum_{e=1}^{n_w} \left(\frac{1}{\phi_j^r} \frac{\delta \phi_j^1}{\delta a^e} - \frac{\phi_j^1}{\left(\phi_j^r\right)^2} \frac{\delta \phi_j^r}{\delta a^e} \right) N_i\left(x^e\right) \tag{3.46}$$

$$\frac{\delta \phi_j}{\delta a^e} = \sum_{q=1;q\neq j}^{d} \left(\frac{\phi_q}{\lambda_j - \lambda_q} \phi_q^T \left[\frac{-K^e}{(1-a^e)} - \lambda_j \frac{-M^e}{(1-a^e)} \right] \phi_j \right) - \frac{\phi_j}{2} \phi_j^T \frac{M^e}{(1-a^e)} \phi_j \tag{3.47}$$

If only stiffness parameters are selected to be updated, Equation (3.47) becomes Equation (3.48).

$$\frac{\delta \phi_j}{\delta a^e} = \sum_{q=1;q\neq j}^{d} \left(\frac{\phi_q}{\lambda_j - \lambda_q} \phi_q^T \left[\frac{-K^e}{(1-a^e)} \right] \phi_j \right) \tag{3.48}$$

In sensitivity-based FEMU, model order of analytical model (*d*) should be selected as high as possible. In this way, the number of modes to be considered for the sensitivity matrix is greater and the finite element model obtained after the update becomes a better representation of the real structure. Considering that choosing a high number of modes will increase the analysis burden and the contribution of the modes in higher orders is lower, it is necessary to choose the optimum number of models.

Similar to the procedure for weighting residual vector in Equation (3.9), sensitivity (Jacobien) matrix can also be weighted (3.49).

$$W^{1/2} J_p \tag{3.49}$$

where W is the diagonal weighting matrix, $W = diag(..., w_j^2, ...)$. Equation (3.49) becomes Equation (3.50).

$$w_j \left(J_p\right)_j \tag{3.50}$$

The approximate determination of the sensitivity matrix components can be done by using the finite differences method (Equation 3.51).

$$\frac{\delta r_j(p)}{\delta p_i} = \frac{r_j(p+\Delta p) - r_j(p-\Delta p)}{2\Delta p} \tag{3.51}$$

where Δp is small change in parameter to be updated. Since Equation (3.51) requires two extra analyses (next and previous step), the finite difference method is computationally expensive.

3.3 Optimization Process

Finite element model updating is an optimization process. The main goal of this process is to minimize the objective function. In every iteration step, the value of objective function changes. The global minimum point is the point at which this value takes its absolute lowest value. Except for the global minimum point, this value may have the lowest value among the surrounding points, it is called local minimum point. Optimization processes are divided into 3 according to their solution types:

- Well-conditioned: There is only one global minimum point with possible local minimum points. It is the most preferred case. Finding the global minimum point is easy (Figure 3.2(a)).
- Ill-conditioned: There is only one global minimum point which is not clear with possible local minimum points. Finding the global minimum points is relatively hard and computationally expensive (Figure 3.2(b)).
- Underdetermined: There are several global minimum points with possible local minimum points. In this case the algorithm cannot detect which global minimum point is the correspondence of the real structure (Figure 3.2(c)).

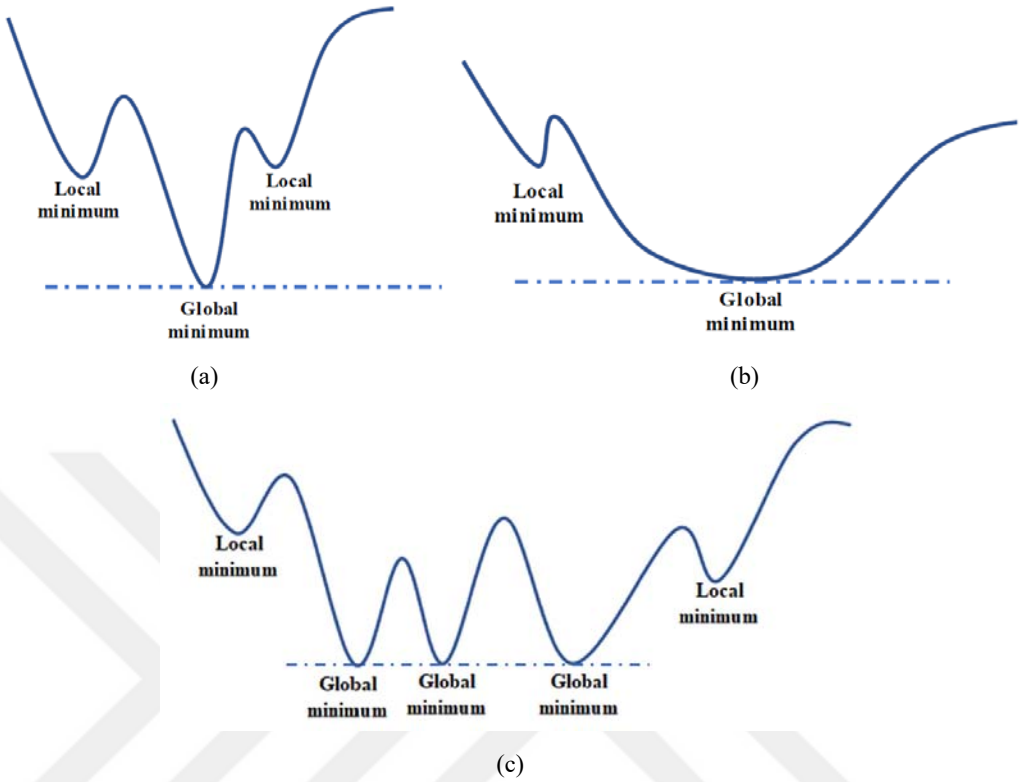


Figure 3.2 Optimization problem types (a) well-conditioned (b) ill-conditioned and (c) underdetermined (Yucel, 2020)

To solve that minimizing problem there are three types of optimization method in the literature.

Local optimization methods start from the initial point and iteratively reach the global minimum, getting better results at each step. Since they use the derivates of objective function, the process converges quickly. But, in some cases, they can be trapped at a local minimum point and cannot reach the absolute minimum. Sequential quadratic programming, augmented Lagrangian, Quasi-Newton, and conjugate gradient are some of the local optimization methods (Nocedal & Wright, 1999; Conn, Gould, & Toint, 2000).

Global optimization methods are not affected by start point of analysis and are more robust than local optimization methods. These methods do not use derivation of the objective function and are based on probability. Simulated annealing, genetic algorithms, and coupled local minimizer are some of the global optimization methods

(Holland, 1975; Kirkpatrick, Gelatt & Vecchi, 1983; Suykens et al., 2001; Suykens, Vandewalle, De Moor, 2001).

Response surface methods fit an approximate surface to the objective function. The surface obtained by using first or second order polynomials. Due to the existence of these polynomials, it can be hard that finding global minimum point for the case with many local minimum points. This problem is overcome by general response surface method which are only convenient for the cases with lower number of parameters to be updated (Alotto, Gaggero, Molimari, & Nervi, 1997; Pahner, 1998).

CHAPTER 4
REAL-TIME DATA ACQUISITION ON AN OPERATING WIND TURBINE

Continuously recording data on an operational wind turbine under different conditions is an essential part of understanding the effects of operational and environmental on the dynamic characteristics of the turbine. In order to record acceleration, temperature, and humidity data from the wind turbine, a data acquisition system is designed. The system not only collects data from its own sensors but also gathers data (rotor speed, nacelle direction, pitch angle, temperature, humidity, wind speed, and wind direction) collected by the turbine Supervisory Control and Data Acquisition (SCADA) system simultaneously.

4.1 Introduction of The Wind Turbine

The subject of this study is a Horizontal Axis Wind Turbine (HAWT) with 2.5 MW capacity (Figure 4.1) operated by a local Turkish company and installed in Urla/Izmir. Due to the regional climatic conditions, wind speed and its direction vary very frequently throughout the year. This mainly causes the turbine's tower, blades, and connection elements to be severely excited. On today's scale, this can be considered a large size wind turbine, which has a hub located at a height of 90 m high above the ground level. It is a pitch regulated wind turbine and has three rotor blades. The nacelle where the generator and its drive train are located is at the top of the steel tower. Some technical characteristics of the wind turbine are given in Table 4.1.



(a) (b)

Figure 4.1 (a) The monitored wind turbine and (b) a general view of the wind power plant (Dost Enerji, 2023)

Table 4.1 Properties of the wind turbine

Property	Value
Rated power	2.5 MW
Rated wind speed	12 m/s
Cut-in wind speed	3 m/s
Cut-out wind speed	25 m/s
Rotor speed	9.6 – 16 RPM
Rotor diameter	90 m
Tower height	78 m
Hub height	90 m
Nacelle mass	91 tons
Rotor mass	55 tons

The tower is a circular steel tower consisting of four segments bolted to a concrete foundation. The diameter and thickness of the tower vary along the height. The diameter decrease is slight in the first three segments, while it is noticeably higher in the top segment Figure 4.2.

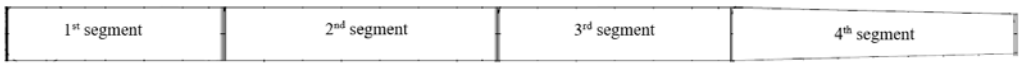


Figure 4.2 Tower geometry (right is top)

The tower is made of S355 structural steel, some parameters of which are shown in Table 4.2.

Table 4.2 The tower material mechanical properties (S355)

Property	Value
Yield Strength	355 MPa
Tensile Strength	510-630 MPa
Elasticity Modulus	210 GPa
Shear Modulus	81 GPa
Density	7850 kg/m^3
Poisson Ratio	0.30

The wind turbine is built on relatively stiff soil. So, the effect of the structure-foundation-soil interaction on the structural behavior is insignificant. Some soil properties are presented in Table 4.3.

Table 4.3 Soil properties of power plant area

Property	Value
Bearing Capacity	3.00 kg/cm^2
Characteristic Periods	T_A=0.15 s, T_B=0.40 s
Coefficient of Soil Reaction	15000 t/m^3
Primer Wave Velocity	399-910 m/s
Seconder Wave Velocity	173-267 m/s

Permission for installation of the data acquisition system, access to the SCADA system, troubleshooting, and long-term structural monitoring have been granted from the operating company (Dost Enerji A.Ş.). The company provided the design papers for the wind turbine, which is forbidden to be released to the public for only research purposes. The monitored wind turbine is 2 km away from the Guzelbahce fault ensuring that the region is in a high seismic zone (Emre et al., 2005).

4.1.1 Wind Profile of the Region

In the earthquake-free state, the oscillation of the wind turbine is largely driven by the wind. Therefore, it will be easier to estimate vibration modes if one of the accelerometers to be placed on the tower is in the direction of the Main Wind Direction

(MWD) of the region. By definition, the accelerometer placed perpendicular to the first one is in the Secondary Wind Direction (SWD).

To determine MWD and SWD four years (January 1st, 2018 – December 31st, 2021) wind data recorded by the SCADA system from 10 wind turbines in the wind farm is examined in detail. A total of 2,102,400 recordings consisting of 10-minute average values, are used. The distribution of the wind direction, and the wind rose obtained according to this distribution, and the distribution of wind speed classes are shown the Figure 4.3, Figure 4.4, and Figure 4.5 respectively. 16 wind directions and 5 wind speed classes are considered.

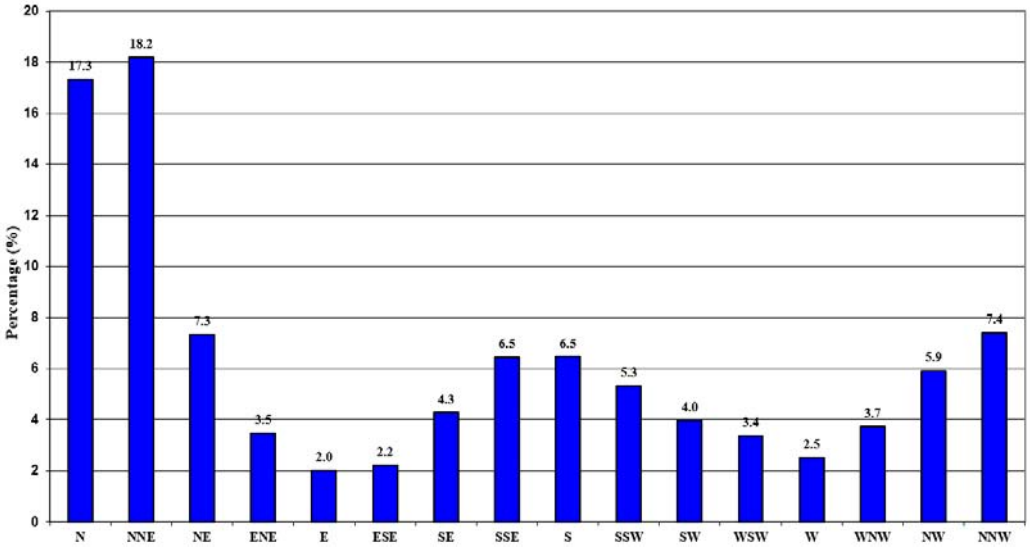


Figure 4.3 Wind direction distribution for four years period

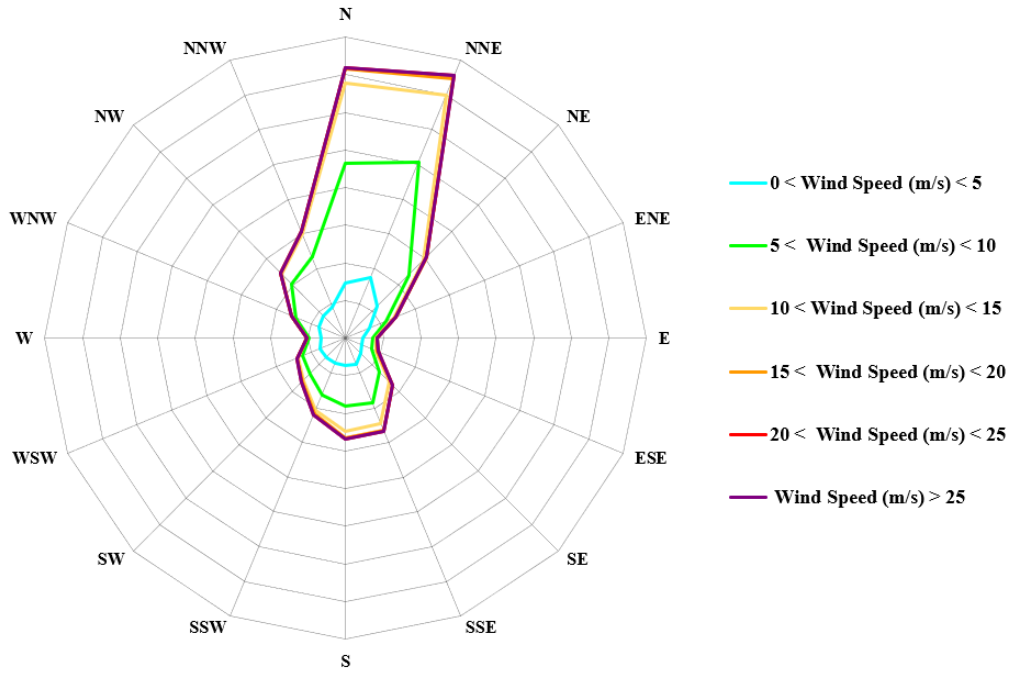


Figure 4.4 Wind rose prepared for the region

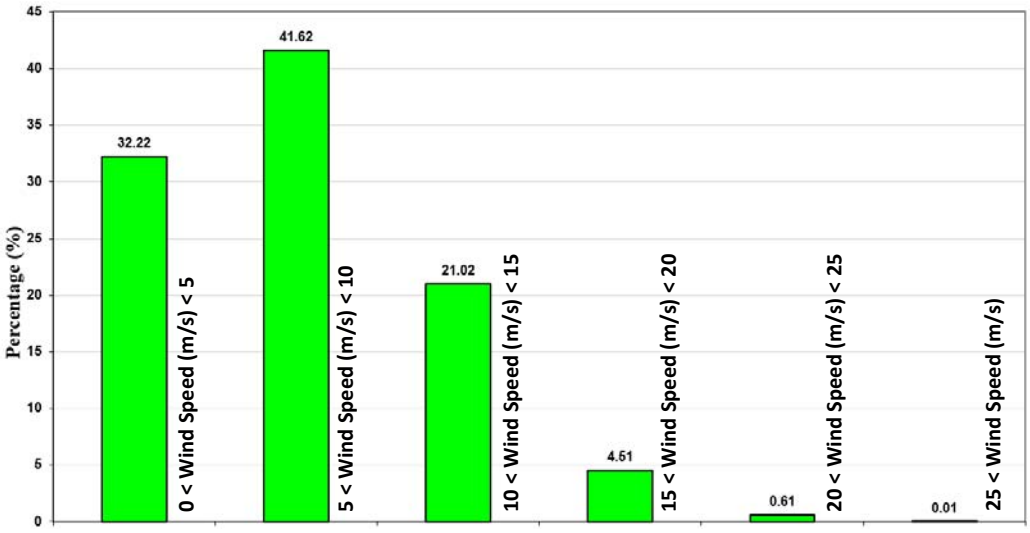


Figure 4.5 Distribution of wind speed classes

In the region, the wind is mainly blowing from the north (N) and north-northwest (NNW) directions. The percentage of these two directions are very close to each other. So, it can be said that the middle of these two directions is the MWD and the direction perpendicular to MWD is called SWD.

4.2. Data Acquisition System

The turbine tower's height is 78 meters, and there are platforms that can be walked on every 20 meters. These levels are named as follows according to their ground clearance; Level 1: 0-meter (foundation), Level 2: 20-meter, Level 3: 40-meter, Level 4: 60-meter, Level 5: 78-meter (top of the tower). Figure 4.6 shows different types of sensors to be placed on the tower and their layouts.

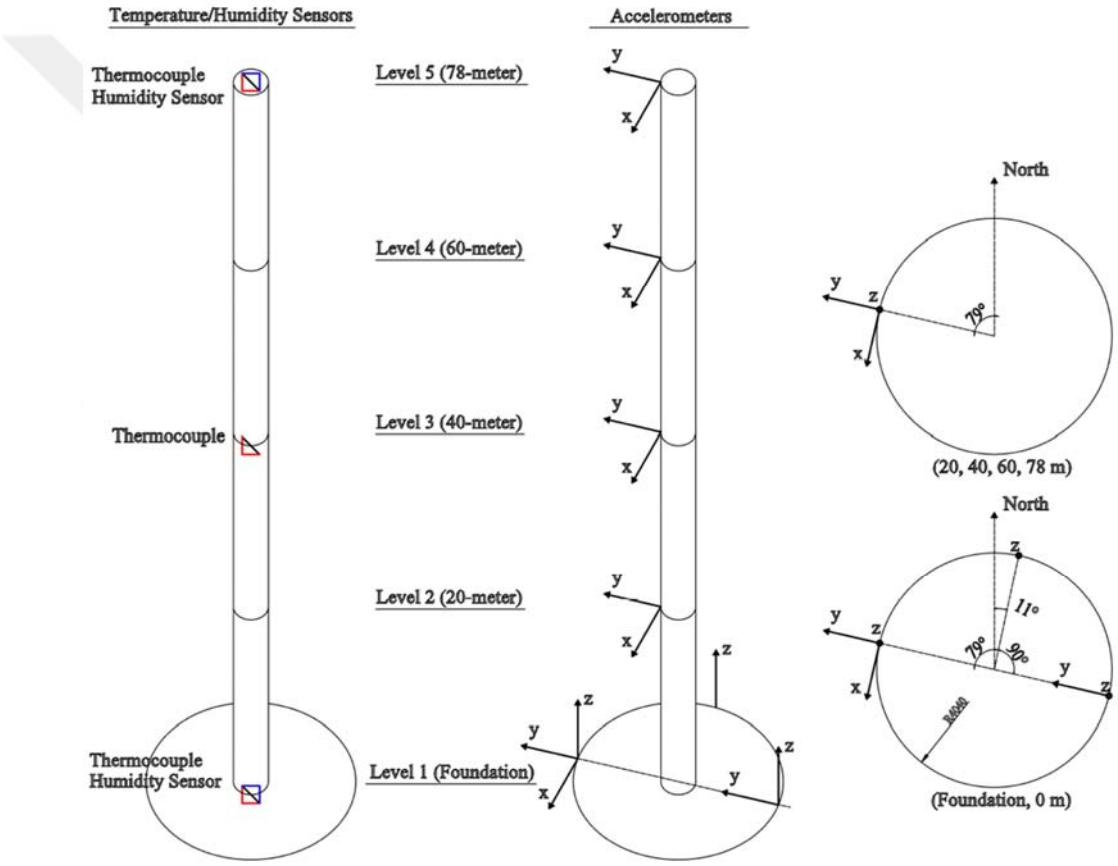


Figure 4.6 Sensor layout along the tower

It can be seen from Figure 4.6 that three uniaxial and one triaxial accelerometers are placed at the foundation level to record horizontal and vertical acceleration. On the other levels (20, 40, 60, and 78 m) along the tower, two uniaxial accelerometers are placed in the perpendicular (X and Y) directions to measure horizontal acceleration. All horizontal accelerometers are placed in MWD (X) and SWD (Y) directions.

Temperature sensors at three levels (0, 40, and 78 m) and relative humidity at two levels (0 and 78 m) are located inside the tower.

4.2.1 Hardware

Data acquisition system components and sensors at each level are listed as follows:

- *Level 1 (0-meter):* One triaxial accelerometer, three uniaxial accelerometers, and one temperature/humidity sensor are on this level. Two NI 9239 modules are connected to a 4-slot cDAQ-9185 chassis to digitize analog sensor data. In addition, the industrial box PC, PoE switch, power supply, UPS, and P2P antenna are on the foundation level.

- *Level 2 (20-meter):* Two uniaxial accelerometers are on this level. A NI 9239 module is connected to a 4-slot cDAQ-9185 chassis to digitize analog sensor data.

- *Level 3 (40-meter):* Two uniaxial accelerometers and one temperature sensor are on this level. A NI 9239 module is connected to a 4-slot cDAQ-9185 chassis to digitize analog sensor data.

- *Level 4 (60-meter):* Two uniaxial accelerometers are on this level. A NI 9239 module is connected to a 4-slot cDAQ-9185 chassis to digitize analog sensor data.

- *Level 5 (80-meter):* Two uniaxial accelerometers and one temperature/humidity sensor are on this level. A NI 9239 and NI 9203 module is connected to a 4-slot cDAQ-9185 chassis to digitize analog sensor data.

All components and their short descriptions are presented in Table 1.

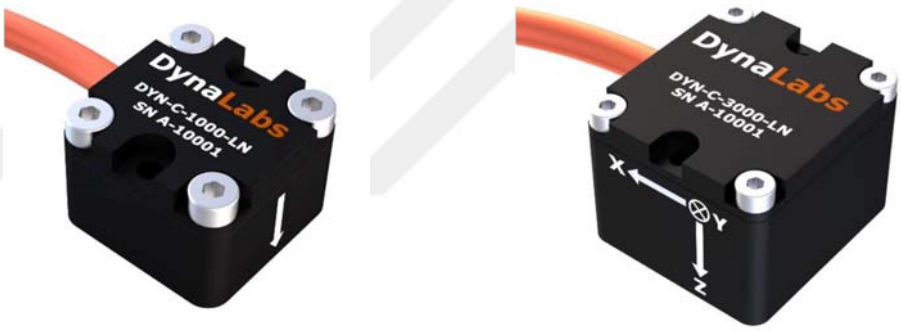
Table 4.4 Data acquisition system components

Device	*Description*
Uniaxial accelerometer	measures acceleration in one-axis
Triaxial accelerometer	measures acceleration in three-axis
Temperature and relative humidity sensor	measures temperature and relative humidity
NI 9239 analog input module	converts a continuous-time and continuous-amplitude analog signal to a discrete-time and discrete-amplitude digital signal
NI cDAQ-9185 chassis	controls the timing, synchronization, and data transfer (max four modules can be attached)
NI PS-16 industrial power supply	provides power for all system in the tower
P2P wireless antenna	transfers data from the switchyard to the turbine tower
Industrial box PC	operates the system and controls data streaming
Workstation	runs analyses
NAS	backs up all collected data
UPS	prevents system shutdown in case of power failure
Industrial ethernet switch	allows devices to communicate with each other
Splitter	separates data and power

4.2.1.1 Sensors

The features of accelerometers, temperature, and relative humidity meters, the essential components of the data collection system to be placed in the turbine tower, are explained below.

Accelerometers: 11 uniaxial accelerometers and 1 triaxial accelerometer (Figure 4.7) are placed on five different levels (0, 20, 40, 60, and 78 m) of the wind turbine to record the acceleration data continuously. These accelerometers have high resolution and low noise characteristics. 8 uniaxial accelerometers are internally mounted in pairs on the tower at qualitative stations, as shown in Figure 4.3 where vibration along two principal directions is measured at each station. These two principal directions are the MWD and SWD. As can be seen from Figure 4.3, one triaxial and three uniaxial accelerometers are mounted on the foundation block to monitor foundation motion (input motion) during future earthquakes. Some specifications of sensors are presented in Table 4.5. All accelerometers provide voltage output.



(a) (b)

Figure 4.7 (a) Uniaxial accelerometer, and (b) triaxial accelerometer

Table 4.5 Specifications of accelerometers.

Acc. Range	(g)	±5
Sensitivity	(mV/g)	540
Frequency Range	(Hz)	700
Noise	(μg/√Hz)	17
Bias Temperature	(mg/°C)	±0.5
Shock Survivability	(g)	2500
Operating Voltage	(V)	5-20

Temperature and Relative Humidity Sensor: Temperature sensors (Figure 4.8) are placed on three different levels (0, 40, and 78 m) and relative humidity sensors are placed on two different levels (0 and 78 m) in order to measure the relative humidity and temperature of the air inside the tower structure. Since the operating company does not approve the sensor placement outside the tower, the outside temperature information is provided over the SCADA system. The sensors can measure between 0% and 100% relative humidity and between -40 ºC and +80 ºC. Two of these sensors provide voltage outputs (0-10 VDC), and the other one provides current outputs (4-20 mA).



Figure 4.8 Temperature and relative humidity sensors

4.2.1.2 Chassis and Modules

Total of seven modules are attached to the five chassis at five different levels to digitize, synchronize and transfer the recorded data. Modules and chassis features are presented below.

NI 9239 Analog (Voltage) Input Module: The NI 9239 (Figure 4.9 (a)) is a 4-channel analog input module for use in data acquisition systems of National Instruments. Each channel provides a ±10 V measuring range at a resolution of 24-bit. The NI 9239 produces maximum of 50 kS/s of data. Six NI 9239 modules are used in the data acquisition system. Accelerometers and two voltage output thermocouples, and RH sensors are connected to these modules.

NI 9203 Analog (Current) Input Module: The NI 9203 (Figure 4.9 (b)) is a module that has eight analog channels and can read analog signals from sensors. The analogue module is used for high-performance control and tracking applications. The input range is ±20 mA and data can be recorded at 16-bit resolution and maximum 200 kS/s sampling rate. One NI 9203 module is used in the data acquisition system, and one current output thermocouple and RH sensors are connected to this module.



(a) (b)

Figure 4.9 (a) NI 9239 voltage input module and (b) NI 9203 current input module

NI cDAQ-9185 Chassis (4 slots): The cDAQ-9185 is a CompactDAQ Ethernet chassis produced by NI. It can be used for especially distributed data acquisition systems. It controls the timing, synchronization, and data transfer between modules and an external server. The chassis provides precise, synchronized timing over the network using Time-Sensitive Networking (TSN). The chassis also has four 32-bit timers. The NI 9239 and NI 9203 modules are connected to cDAQ-9185 in all the levels shown in Figure 4.10.



Figure 4.10 NI cDAQ-9185 chassis

4.2.1.3 Other Devices

NI PS-16 Industrial Power Supply: The PS-16 (Figure 4.11a) can power CompactDAQ systems, different types of sensors, industrial computers, etc. This Industrial Power Supply includes DIN rail mounting and toolless spring-clamp terminals for field connectivity. The PS-16 provide 240 W output power. It can work between -25 °C and +60 °C temperature range. PS-16 supplies the entire data acquisition system in the wind turbine.

Industrial Box PC: Two industrial computers (Figure 4.11b) are used in the health monitoring system. One of the computers is installed on the turbine tower. The other is installed in the switchyard where the SCADA system is located, where data such as nacelle direction, pitch angle, and outside temperature are collected. Before installation in the field, these computers are tested in the laboratory environment, and the necessary software is installed and activated.

Workstation: A workstation (Figure 4.11c) with a high processing capacity that works 24/7 for a long time is installed in a campus environment. The data recorded from the wind turbine and SCADA system is sent to this computer. System identification analyses are performed by using this high-capacity computer.

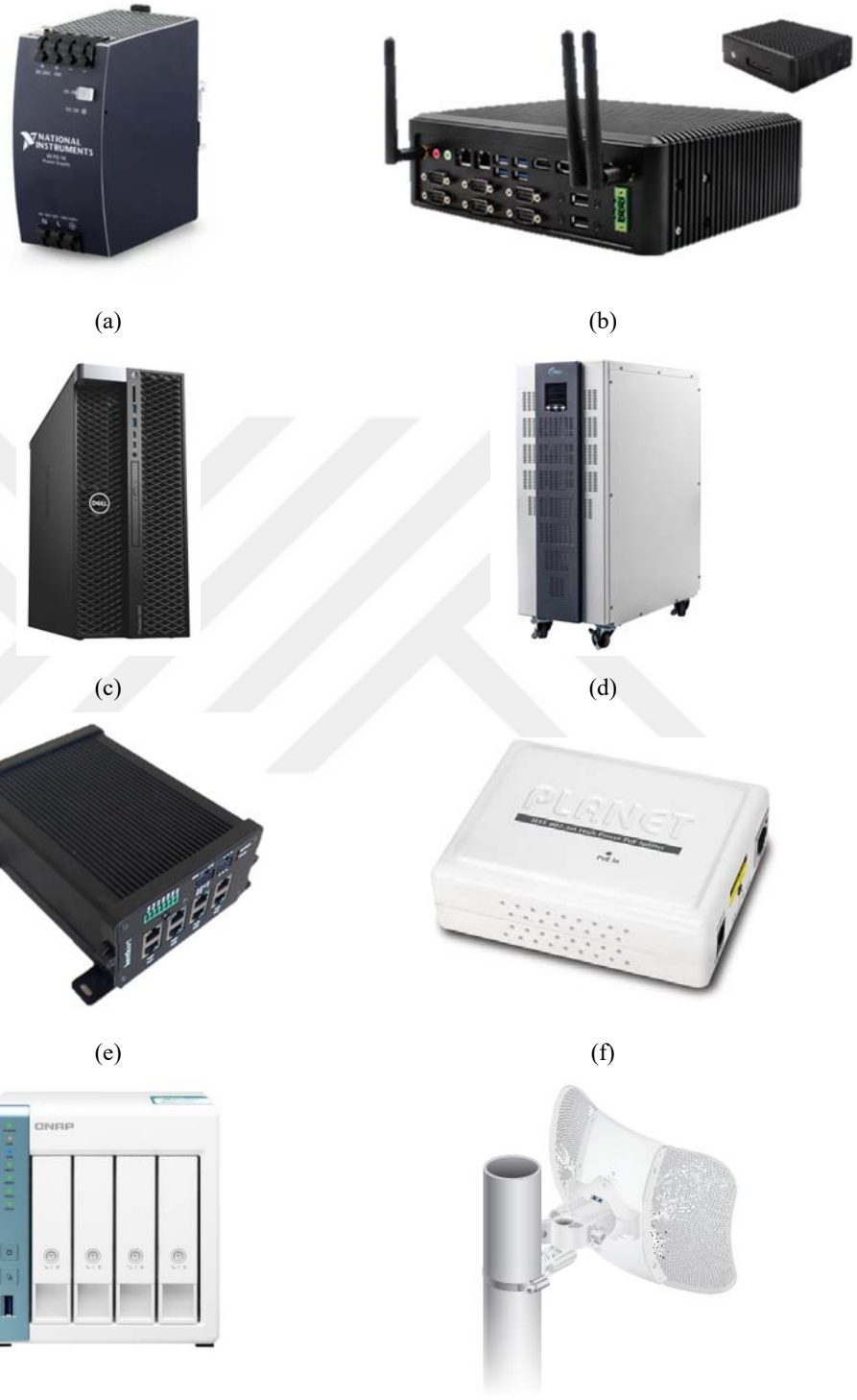
Uninterruptible Power Supply (UPS): Two power supplies (Figure 4.11d) are installed in the turbine tower and the campus so that real-time data flow and processing are not interrupted in case of any power failure.

Industrial Ethernet Switch: The 8-port switch (Figure 4.11e), produced specifically for this project, allows the entire devices in the turbine tower to communicate. At the same time, avoid providing both data and energy through the switch with PoE (ethernet and energy-carrying) cables. It is mounted on the panel for the foundation level (Level-1) of the tower.

Splitter: PoE Ethernet cables provide the data flow between all devices in the system and the power supply. However, since cDAQ chassis do not have a PoE feature, power and data are separated from each other with the help of splitters (Figure 4.11f). With the separated power and data cables, cDAQ chassis are energized, and their participation in the network is ensured. Thus, cables are prevented from being drawn separately for energy and network flow to the cDAQ chassis at each tower level.

Network Attached Storage (NAS): Four-slot NAS device (Figure 4.11g) with four 2 TB hard disks provide ample storage space.

Point to Point (P2P) Wireless Antenna Set: P2P antenna (Figure 4.11h) set provides high-speed data transmission between two remote points in the line of sight. Two antennas are used to transfer the data received from the SCADA system of the turbine in the switchyard to the turbine tower.



(a) (b)

(c) (d)

(e) (f)

(g) (h)

Figure 4.11 Other components of the data acquisition system: (a) industrial power supply, (b) industrial box PC, (c) workstation, (d) uninterruptible power supply, (e) ethernet switch, (f) splitter, (g) network attached storage, and (g) P2P antenna

4.2.2 Laboratory Studies and Synchronized Data Recording

All system elements are checked before installing the data collection system in the field, and possible problems that may occur during installation are minimized. Then, all components of the data collection system are brought together in a laboratory environment, and some tests are done to check the whole data acquisition system. Figure 4.12 shows the components in the two panels installed at the foundation level (0-meter) and 80-meter in the laboratory environment.

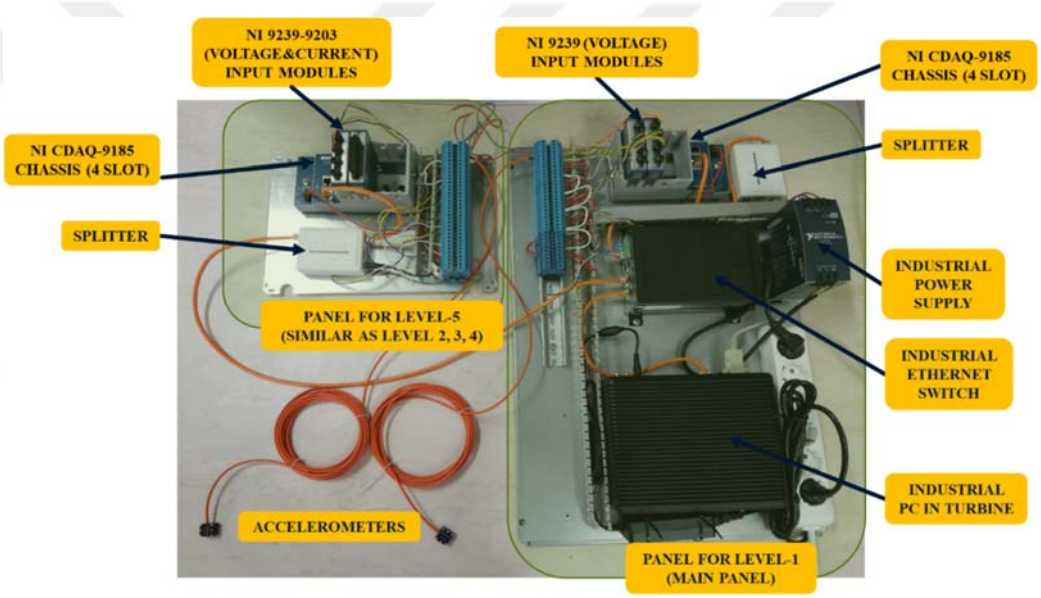


Figure 4.12 Two panels installed in the laboratory (Personal archive, 2022)

Ethernet cards with IEEE 802.1AS protocol on NI cDAQ-9185 chassis have a time-based synchronization feature. Once each chassis at different levels have connected each other via ethernet cables, this feature provides synchronous data recording from all levels. In order to test the synchronous data recording, a test was carried out on the shaking table with the panels prepared in the laboratory. Two accelerometers were connected to the NI 9239 (Voltage) input modules attached to the NI cDAQ-9185 chassis on the panels prepared for Level-1 and Level-5. After accelerometers were fixed to the model structure on the shaking table seen in Figure 4.13, a sinusoidal load was given to the shaking table. Voltage data from two different accelerometers were

converted into g (gravitational acceleration) values, and their graphs were drawn by the code written on the LabVIEW (2020) software (Figure 4.14).

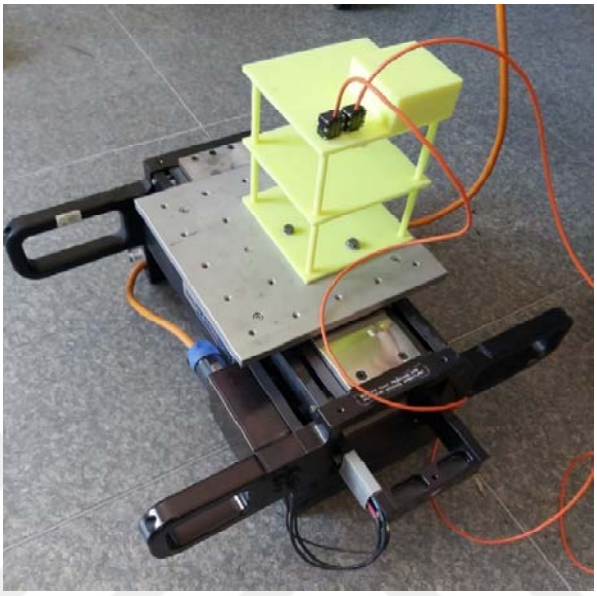


Figure 4.13 Accelerometers placed on the shaking table (Personal archive, 2022)

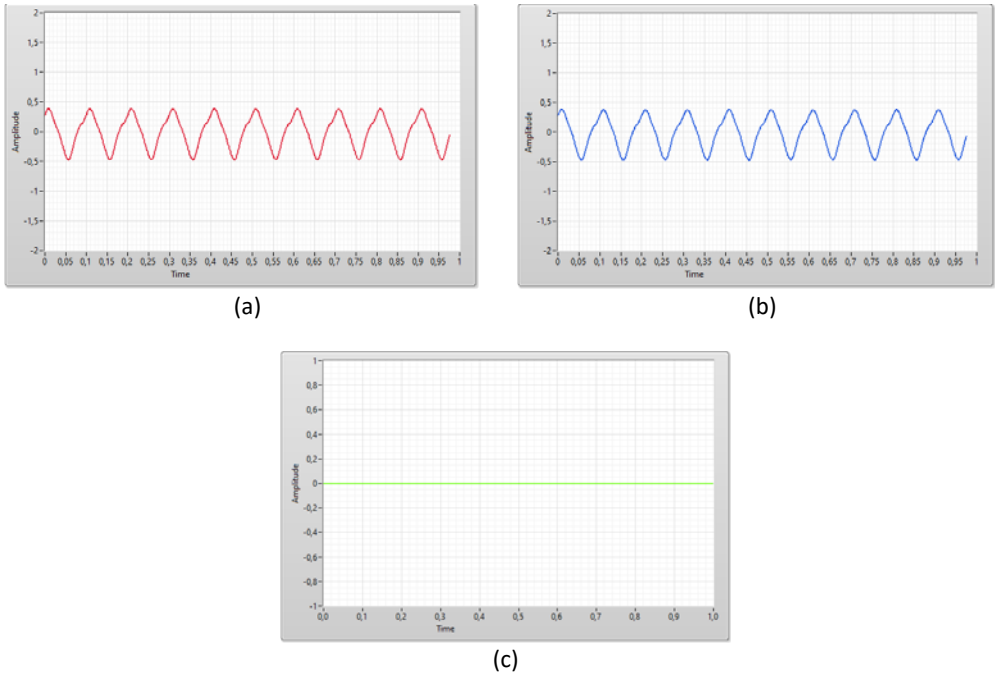


Figure 4.14 (a) Voltage data from the accelerometer connected to the chassis at Level-1 (b) Voltage data from the accelerometer connected to the Level-5 chassis, and (c) the difference of voltage data from tow accelerometers

Accelerometers placed side by side on the structure on the shaking table are expected to give acceleration outputs at the same values. As seen in the graphs in Figure 4.14, the acceleration values read in two different accelerometers are the same in time. In addition, the difference between these two data sets being zero showed that the acceleration data measured from two different chassis were collected synchronously.

4.2.3 Placement of Data Acquisition System on the Wind Turbine

All data acquisition system is placed to the wind turbine according to illustration in Figure 4.15. The installation stages of the data acquisition system components, which are set up and operated in the laboratory environment, are explained step by step below.

The industrial computer, 8-port ethernet switch, power supply, and UPS are placed on the foundation level (Figure 4.16a). The cabling is carried out along the tower from the foundation level (main panel) to all levels as planned in Figure 4.15 to provide power and data flow throughout the tower (Figure 4.16b). Panels with chassis, module, and splitter components are installed on each level (Figure 4.16c). The cable ends are prepared before the sensors are connected to the modules to prevent any contact or connection error. In order to reduce the amount of cabling between the chassis, module, and sensors in the panels and to create a more stable connection, the components is connected via terminal blocks. The placement of the accelerometers in the horizontal and vertical directions is provided by placing them on the strong magnets on the turbine wall (Figure 4.16d). A spirit level is used for proper placement during this process. In addition, the position of the accelerometers relative to each other is measured with a laser meter. The temperature and relative humidity sensors are placed on the Level 1, 3, and 5 (Figure 4.16e).

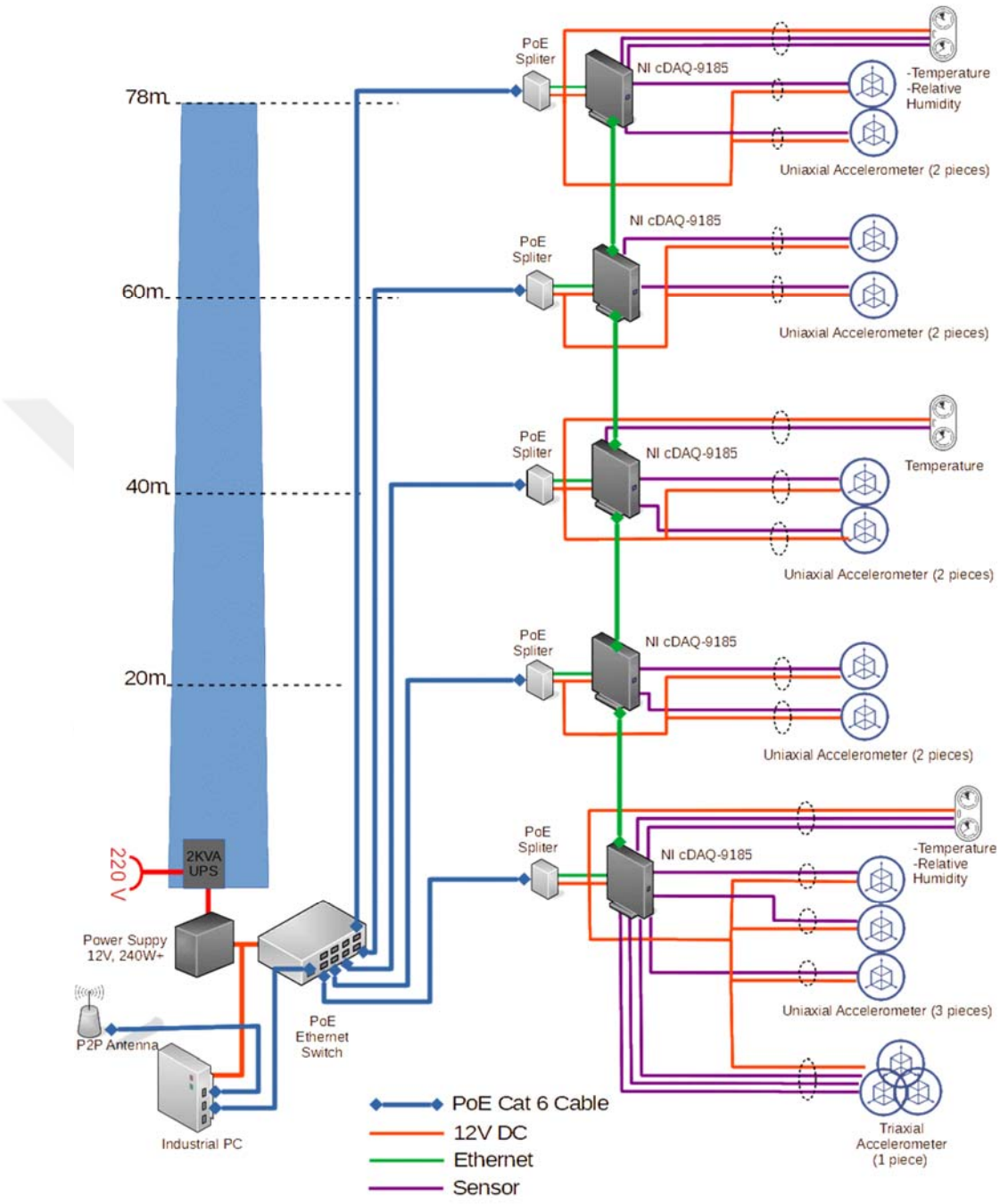


Figure 4.15 Illustration of data acquisition system on the wind turbine

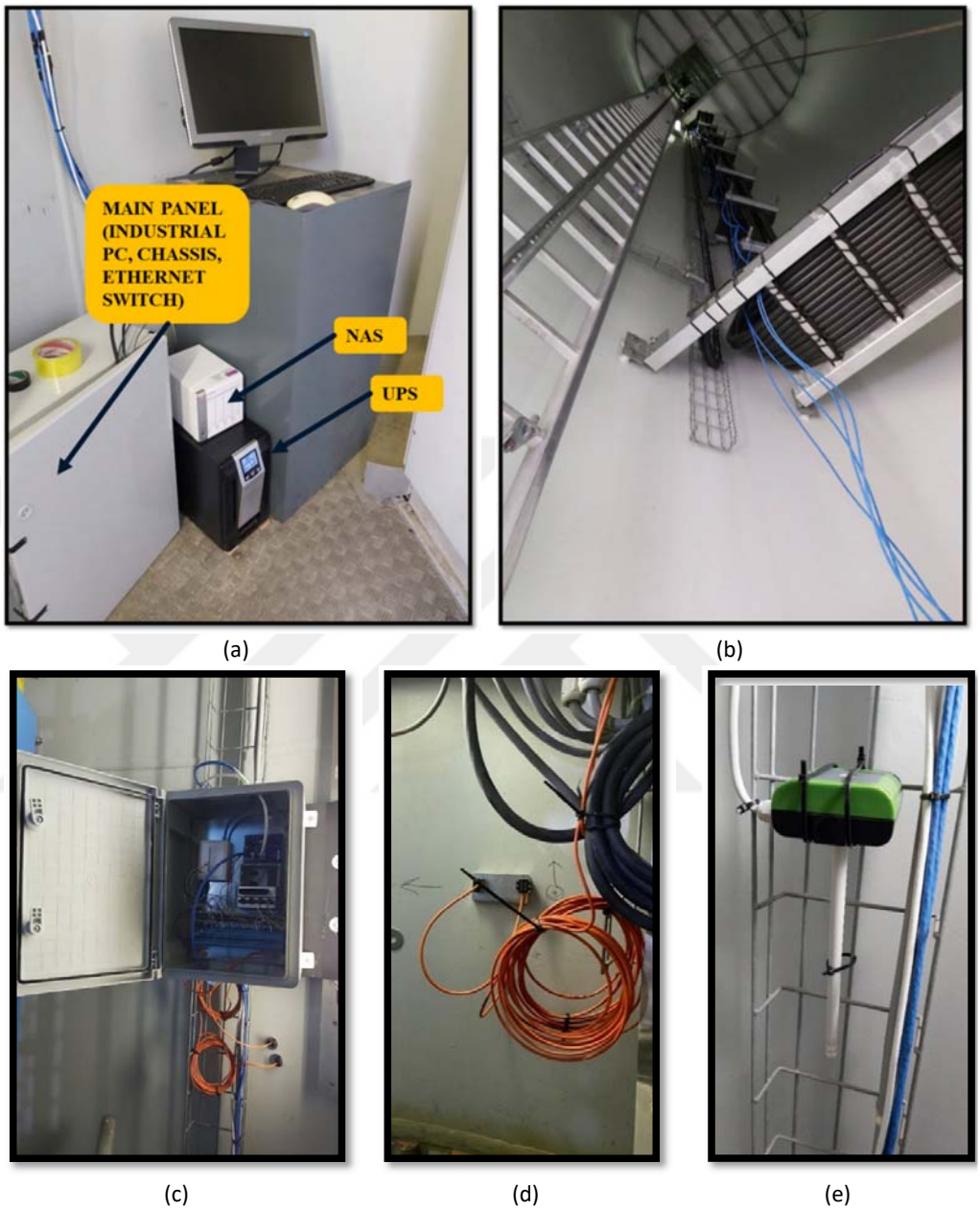


Figure 4.16 (a) Main panel, network attached storage, and uninterruptible power supply at foundation level (0-meter) (b) cabling through the tower, (c) panels at level 2, 3, 4, and 5, (d) placement of the accelerometers on tower with strong magnets, and (e) placement of the temperature and relative humidity sensors (Personal archive, 2022)

4.2.4 Establishment of Network Configuration

One of the main purposes of the thesis is to transfer environmental and operational data collected from SCADA system in switchyard to the wind turbine and transfer all

data (operational, environmental and acceleration data) to the university campus for further analyses. All the data must be synchronized, and their transfer must be in real time. Therefore, the project has three stations: switchyard, turbine, and campus (Figure 4.17).

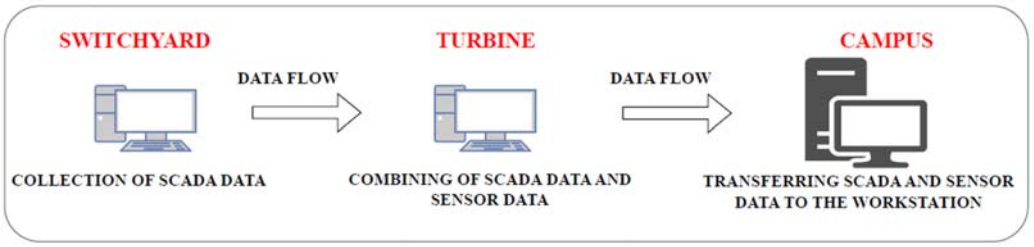


Figure 4.17 Stations and data flow chart of the data acquisition system

The network infrastructure between the switchyard, turbine, and campus is configured after all the components of the data acquisition system are mounted on the wind turbine. Thus, the communication of the whole system within itself is ensured. Network settings are done to ensure that the entire system communicates within itself for all transfer processes to be synchronously and continuously. Figure 4.18 shows the network configuration of data acquisition system.

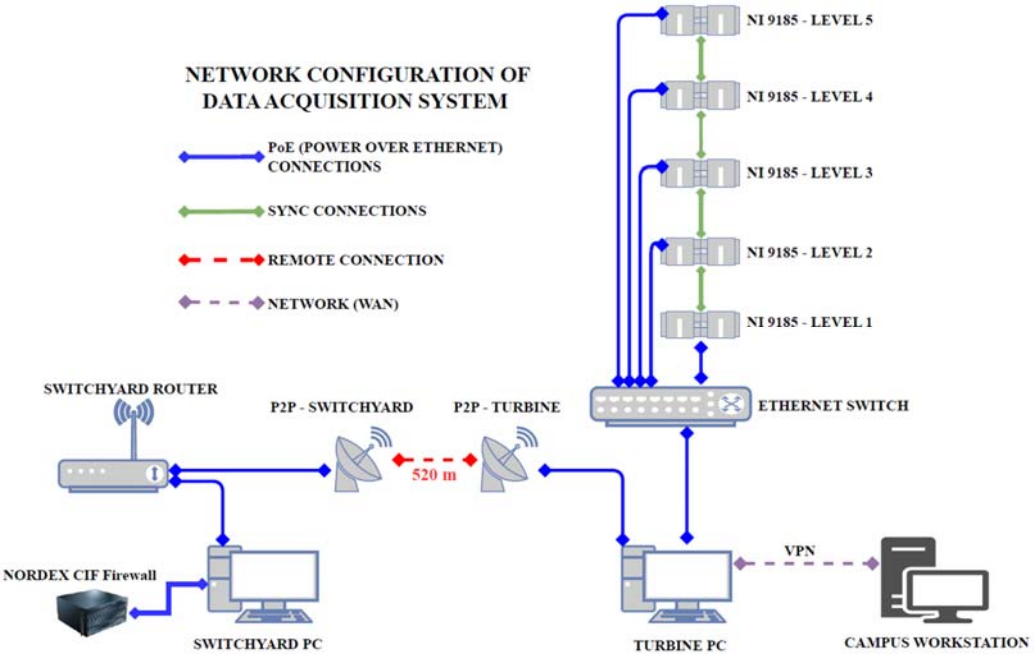


Figure 4.18 Network configuration of data acquisition system

The network diagram shown in Figure 4.18 is explained in detail below.

1) The required network settings are set to obtain the data from the SCADA system installed in the switchyard. The SCADA server is accessed from the industrial box PC in the switchyard. The computer and the firewall are connected with an ethernet cable, and their communication is ensured in order to establish a connection between the computer in the switchyard and the NORDEX CIF Firewall.

2) An ethernet cable is pulled from the operator company's modem in the switchyard to the other port of the computer in the switchyard, and the network settings of the industrial PC are set for internet access.

3) P2P antennas are installed in the switchyard and the turbine. Internet access shared to the computer (and all data acquisition system) in the turbine from the modem belonging to the operator company in the switchyard. Thus, the communication between the turbine and the switchyard are established (Figure 4.19).

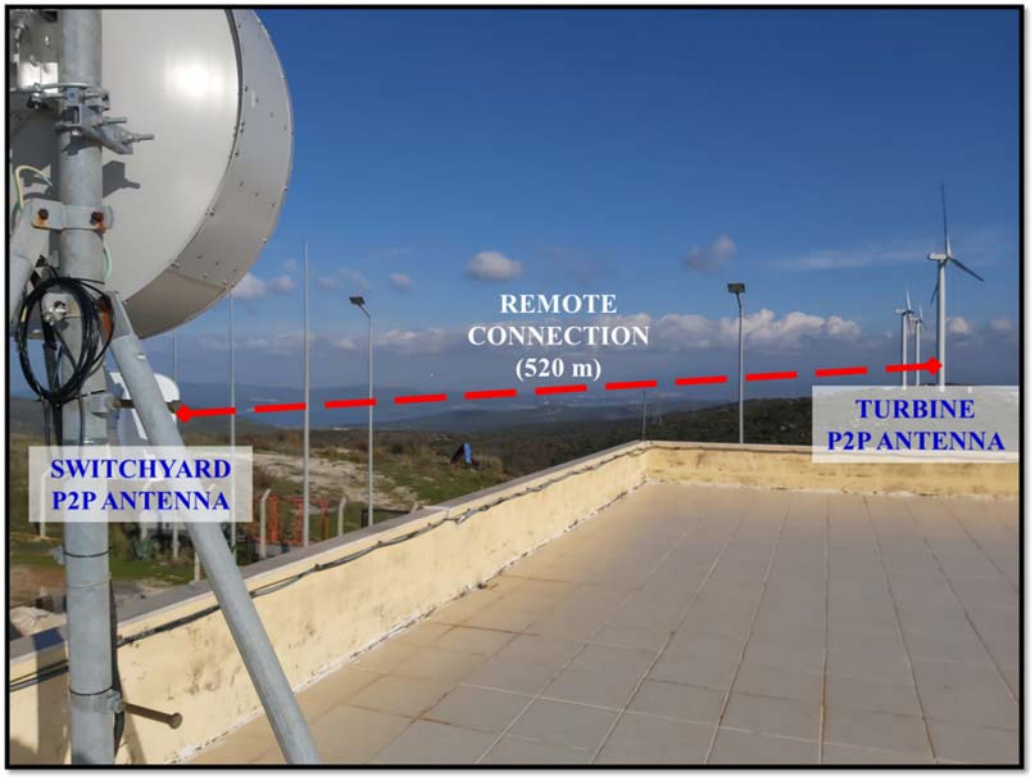


Figure 4.19 Internet access of industrial computer in turbine with P2P antennas installed in turbine and switchyard

4) The computer in the wind turbine and all chassis at each level are connected to the 8-port ethernet switch, and communication with all devices is established.

5) Numerous methods were tried to communicate between the turbine and the campus. Some of these methods consist of trying to create an SSH tunnel between two points and creating an Open VPN virtual connection. However, due to campus firewall permissions, a stable connection could not be achieved with these methods. Therefore, the VPN software used to set a connection between the turbine and the campus. A virtual connection is established between the VPN software installed in the turbine and the computer on the campus. This software assigns virtual IP numbers to the turbine and campus, and communication is ensured. Thus, more stable, and continuous data transfer is observed between the turbine and the campus.

4.2.5 Software

Processes such as processing, transferring, and analysing the data collected within the thesis scope are programmed in the LabVIEW (2020) software. LabVIEW software is an engineering software that provides testing, control, data flow, and development of industrial control systems of data acquisition devices and sensors. The visual programming language (G dataflow) developed by LabVIEW simplifies the integration of hardware and engineering applications such as data acquisition systems. Thus, it provides the most efficient data acquisition from National Instruments (NI) products or other third-party devices. Furthermore, control mechanisms can be developed by analysing the collected data. Data transfers can be provided with signal processing methods, filtering, data packaging, and protocols such as User Datagram Protocol (UDP) and Transmission Control Protocol (TCP). Because of these multifunctional features, LabVIEW software is preferred to code all the processing steps.

It is stated in the previous sections that there are three different stations in the data acquisition system: (1) Switchyard, (2) Turbine, and (3) Campus. The switchyard is the place where the Supervisory Control and Data Acquisition (SCADA) data operational and environmental parameters) is collected. Sensors and all data acquisition devices are in the turbine. Acquired data is processed in the workstation on campus.

The codes and essential functions written to collect and analyse these data continuously and synchronously are explained in detail under the relevant headings (National Instruments, 2023).

4.2.5.1 Codes Developed to Run at Switchyard

Environmental data (e.g., temperature, wind speed, and wind direction) and operational data (rotor speed, nacelle direction, pitch angle, and actual power) can be viewed instantaneously on the SCADA server in the switchyard. The data flowing to

the SCADA server must be transferred to the LabVIEW software. The first thing to do for this process is to install a server on the industrial computer placed in the switchyard and to enable instant monitoring of SCADA data on this server. Then, by creating an interface between the server installed on the computer and the LabVIEW software, the data can be displayed and processed in LabVIEW simultaneously. These process steps are explained according to Figure 4.20.

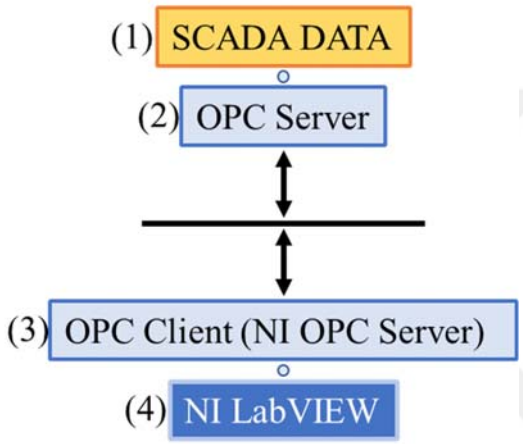


Figure 4.20 Processing stages of SCADA data in the industrial computer installed in the switchyard

1) The Open Platform Communications (OPC) standard is used in reading and transferring SCADA data. The OPC standard defines the interface between client-server and server-server, including real-time data, monitoring events, accessing historical data, and other applications. All SCADA data are monitored instantly on the OPC server established by the operating company in the switchyard. A physical connection is provided with an ethernet cable between the industrial computer installed in the switchyard to access the OPC server and the SCADA server.

2) A third-party software is used to access the OPC server where SCADA data is collected. Thus, this software provided instant access to SCADA data on the industrial computer.

3) The SCADA data must be instantly transferred from the server to the LabVIEW environment. NI OPC Servers module is used for this process. With this module, the

OPC server is connected as a client. Thus, the desired data can be monitored instantly on NI OPC Servers with its name and address (Figure 4.21).

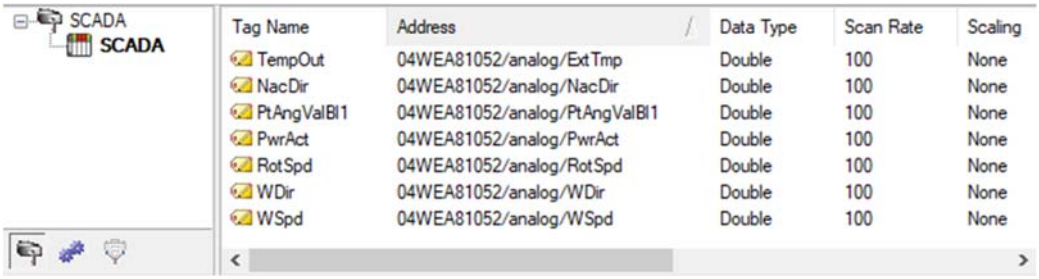


Figure 4.21 Receiving the desired data from the NI OPC Server by connecting to the SCADA server as a client

4) LabVIEW software can use any required data from NI OPC Servers as a variable. For example, WDir (Wind Direction) in Figure 4.21 can be processed after being defined as a variable in LabVIEW software. Outdoor temperature (TempOut), nacelle direction (NacDir), pitch angle (PtAngValBl1), actual power (PwrAct), rotor speed (RotSpd), wind direction (WDir), and wind speed (WSpd) are defined as a variable in the project (Figure 4.22). The definition of these variables in LabVIEW software is Shared Variable. With these functions, meaning shared variables, it is possible to treat data as variables within any loop, between loops in a single diagram, or between projects across the network.

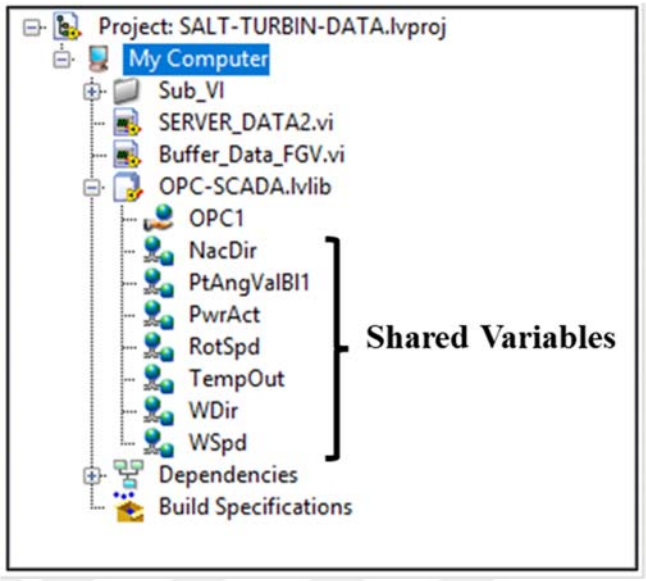


Figure 4.22 Assigning required SCADA data as "Shared Variables" under the project file

SCADA, which includes the operations carried out in the switchyard: Part-A and Part-B are explained in detail as two different sections.

4.2.5.1.1 SCADA: Part-A. In Part-A; After assigning the variables to be used in the project file as Shared Variable connected to NI OPC Servers, coding steps include viewing these data, making them ready for processing, and transfer (Figure 4.23).

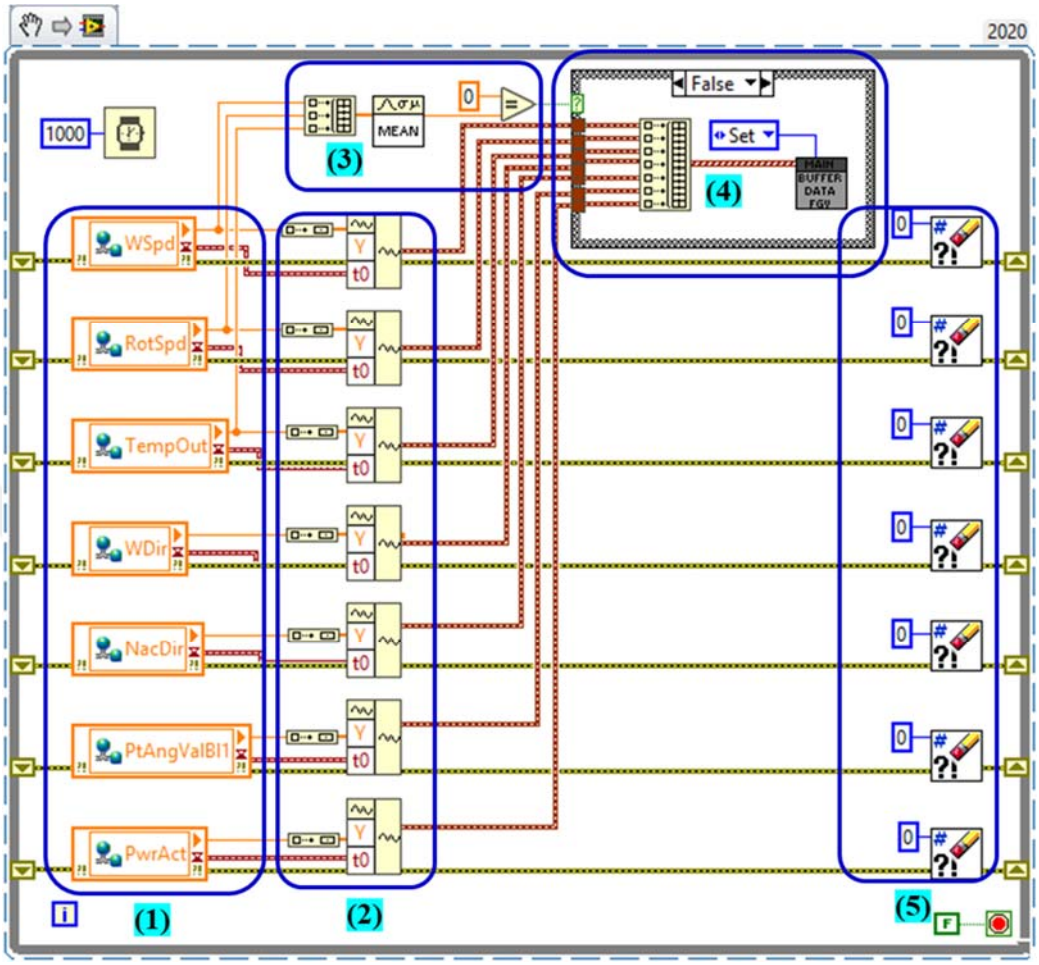


Figure 4.23 SCADA: Part-A; Processing of SCADA data

Part A (1,2,3,4, and 5) is explained in detail below.

Part-A (1): The variables created to be read from the SCADA system under the project file are shown in Figure 4.23. These variables, become functional for any operation when dragged and dropped onto the block diagram where the code is written. This way, seven variables are ready for process in the while loop. The while loop loops every 1000 ms, and these variables in the while loop have three outputs: data in double float data type in orange (wind speed, wind direction, etc.), red in the timestamp of data, and green in error codes that may occur while reading variables.

Part-A (2): The data should be converted to waveform type with three output cables coming out of the variables. This process is done with the Build Waveform function.

Since the data to be converted to the waveform data type must be a string, the data coming from Part-A (1) with the orange cable one by one is converted into a string. The Build Array function is used for this process, and the data in the array format from this function are connected to the relevant part (Y) of the Build Waveform function. Reading timestamps are connected with the red cable, and error messages are connected with the green cable.

Part-A (3): Data flow from NI OPC Servers is checked at this stage. For this purpose, if the mean of the numerical data from the variables is equal to zero, the data flow is stopped, if it is different from zero, the data flow continues by creating the logic, and the operations are continued for the situation where the data flow continues.

Part-A (4): If the data flow continues, all waveform type variables created in Part-A (2) are processed within the for loop to be transferred to the turbine. With the Build Array function in this loop, waveform data from seven different red cables are converted into an index and transferred to another while (SCADA: Part-B) loop for transfer.

Part-A (5): With the Clear Error function seen at this stage, the error messages from the green cables are cleared, and the code is enabled to run without stopping.

4.2.5.1.2 SCADA: Part-B. It includes the coding steps written for the transfer of SCADA data to the industrial computer in the turbine. The transfer mechanism is created with the Transmission Control Protocol (TCP). With the Simple TCP Messaging (STM) functions with TCP infrastructure, a network connection is established between the turbine and the switchyard, and the transfer of SCADA data is ensured. Some essential functions used in coding in SCADA: Part-B is described below.

- *TCP Listen:* Creates a listener and waits for an obtained TCP network connection on the specified port (Figure 24).

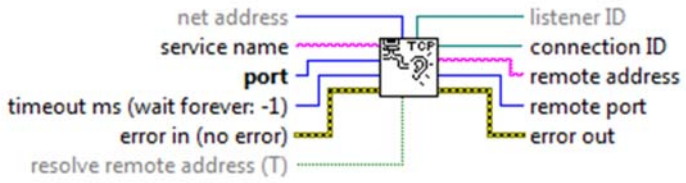


Figure 4.24 TCP Listen

- *STM Write Meta Data:* Used to send metadata information to a remote host. For the message to be interpreted correctly, the metadata must be consistent on both the receiving and sending sides (Figure 4.25).

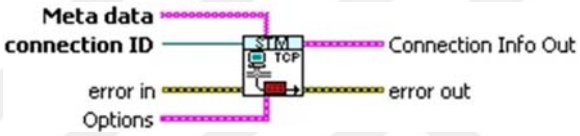


Figure 4.25 STM Write Meta Data

- *STM Read Message:* This function receives any data from a remote host. Also, it reads and unpacks the metadata directory (Figure 4.26).

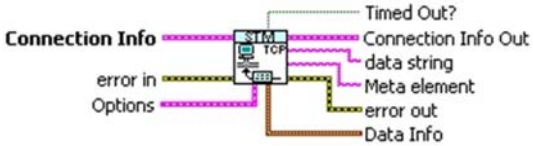


Figure 4.26 TM Read Message

- *STM Write Message:* This function sends any data to a remote host and creates a package based on data, data name, and metadata information. When this function is called, it gets the index of the variable specified by "Name" in the metadata array. It then assembles the message packet via TCP/IP to the remote host using the connection ID (Figure 4.27).

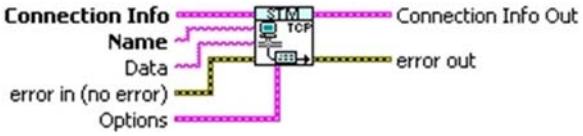


Figure 4.27 STM Write Message

The processes for transferring SCADA data to the turbine are explained according to the numbering in Figure 28.

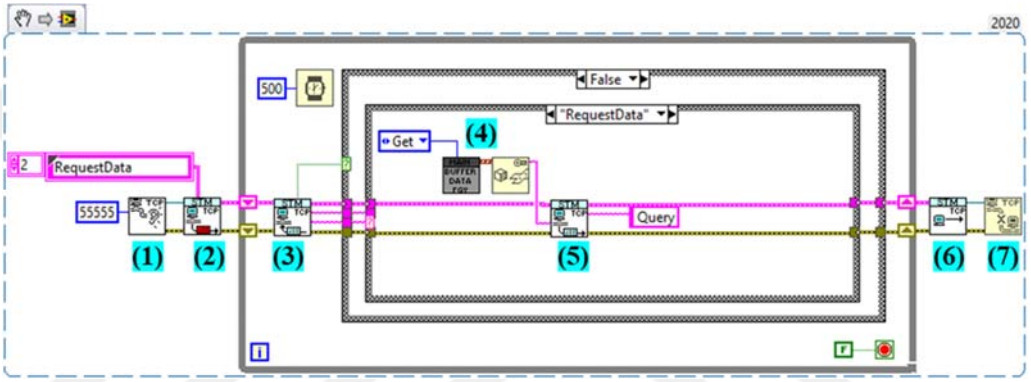


Figure 4.28 SCADA: Part-B; Transferring SCADA data to the turbine

Part-B (1): TCP Listen to function determines which port to establish a TCP connection.

Part-B (2): Metadata groups are determined with the STM Write Meta Data function.

Part-B (3): Metadata names are read and processed in the relevant case with the STM Read Meta Data function. The timeout period of this function is connected to the case structure with a light green cable. As seen in the Figure 4.28, if this function has not timed out (False), if the receiver on the turbine side requests data, it redirects to the "RequestData" case structure.

Part-B (4): Since the data must be in text format in data transfer with STM, the data prepared in Part-A (4) and sent to this loop is converted into text format with the Flatten to String function.

Part-B (5): SCADA data in text format ready for transfer in the "RequestData" case structure is connected to the STM Write Message function with a pink cable and sent to the metadata group (Query) on the receiving side.

Part-B (6-7): If transfer processes are to be terminated, connection reference is taken with STM Get Connection and TCP Close functions, and the TCP connection is closed securely.

4.2.5.2 Codes Developed to Run in Turbine

The coding, which includes the operations performed in the turbine, is explained in detail in five different sections. These sections are named Turbine: Part-A, B, C, D, and E.

*4.2.5.2.1 Turbine: Part-A. i*ncludes selecting channels for the synchronous acquisition of data from sensors connected to NI modules in the tower, selecting sampling rates and number of samples, adjusting timing settings, and starting the task. Some essential functions used in Turbine: Part-A coding are explained in the order below.

- *NI-DAQmx Create Channel:* Creates a channel and adds the created channel to the task with a task-out output. It is also used to create multiple channels and add them to a task. It is created separately for the channels to be collected in different units, such as current and voltage (Figure 4.29).

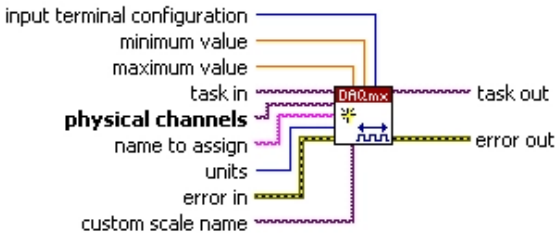


Figure 4.29 NI-DAQmx Create Channel

- *NI-DAQmx Timing:* It configures the schedule for data acquisition operations and gives options as to whether the process should be continuous or finite. Timing settings such as sampling frequency and the sample per channel are adjusted with the NI-DAQmx Timing function (Figure 4.30).

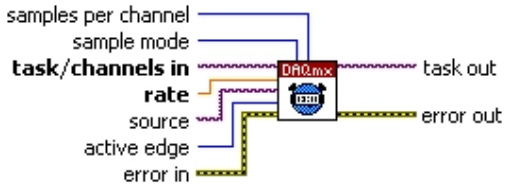


Figure 4.30 NI-DAQmx Timing

- *NI-DAQmx Start Task:* It makes a task run explicitly. In the run state, the task performs the specified work or production. After the NI-DAQmx Start Task function starts the task, the NI-DAQmx Read function becomes active and starts the reading process (Figure 4.31).



Figure 4.31 NI-DAQmx Start Task

In Turbine: Part-A, shown in Figure 4.32, the part from the selection of the channels to the start of the task is explained in detail below.

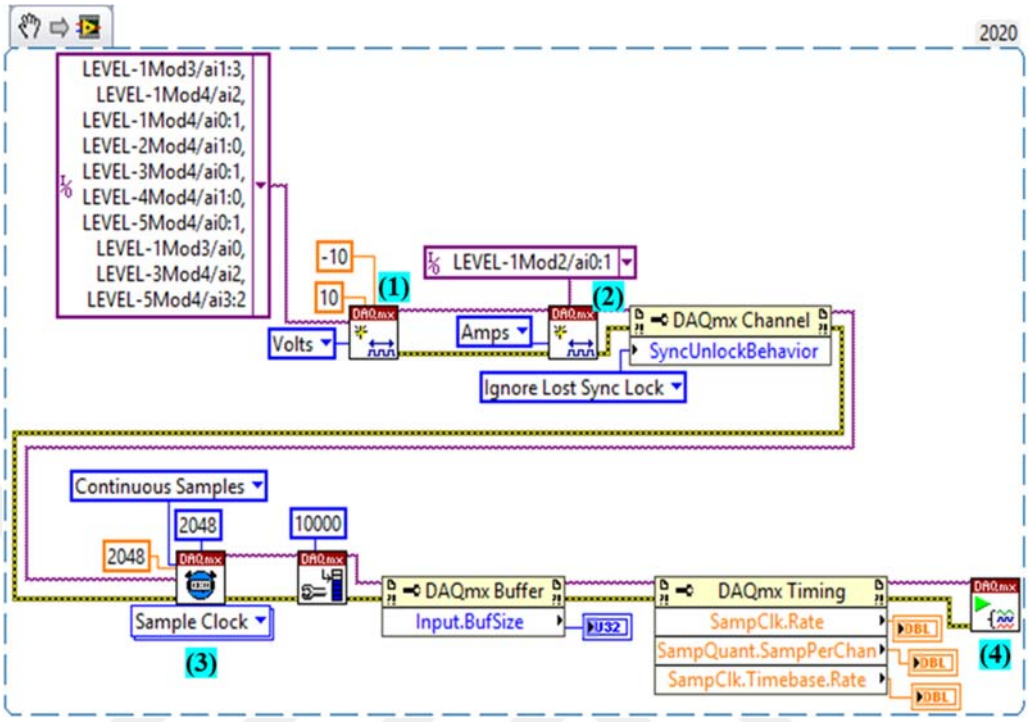


Figure 4.32 Turbine: Part-A; Starting a task by selecting channels with NI-DAQmx functions

Part-A (1-2): Channel is created with the DAQmx-Create Channel function using the LabVIEW DAQmx-Data Acquisition palette. All channels can be selected with physical channels and then create constant on this function. As a unit, the selection is made according to the sensors' input and output types. There are two different outputs in the project, voltage, and current. The channels are selected separately for the data to be collected in these two units. In addition, the minimum and maximum voltage, and current values that the sensors can read are assigned as ±5V and ±20mA, respectively, by the characteristics of the sensors.

Part-A (3): Sampling frequency and sample per channel are configured with the DAQmx-Timing function after selecting the channels. In such projects, continuous data acquisition is required to avoid data loss. The Continuous Samples option in this function packs the collected data cyclically and makes it ready for reading. The sampling frequency determined in this project is 2048 Hz/sec. The sample per channel refers to the buffer size in which the collected data is written, and 2048 is chosen to be compatible with the sampling frequency.

Part-A (4): The channels to receive data and their timing features are determined. However, the system still needs to start acquiring data. After these settings, the task is made operational with the DAQmx-Start function, and data collection starts from the determined channels.

4.2.5.2.2 Turbine: Part-B. After starting the task to collect the data, it includes the stages of reading, filtering, calibration, detrending of the collected data, and making it ready for transfer with the double buffer mechanism. Some essential functions used in the coding in Turbine: Part-B are described in the order below.

- *NI-DAQmx Read:* It reads samples from the specified task. The function reads different samples according to the collection method (analogue, digital, or counter), the number of channels, the number of samples, and the data type to be selected (Figure 4.33).

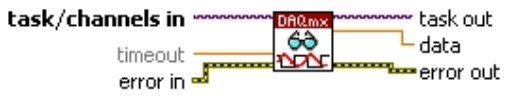


Figure 4.33 NI-DAQmx Read

- *Digital FIR Filter:* It filters signals of single or multiple waveform types. It allows specifying the FIR filter properties for the signals to be filtered (Figure 4.34).

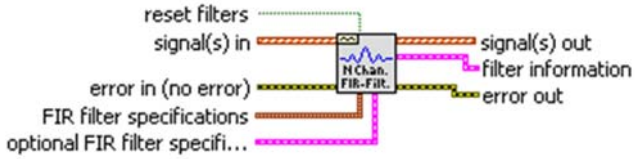


Figure 4.34 Digital FIR Filter

- *Detrend:* It is a function that removes the trend component from a univariate or multivariate time series. This function estimates and refines the trend by curve fitting methods (Figure 4.35).

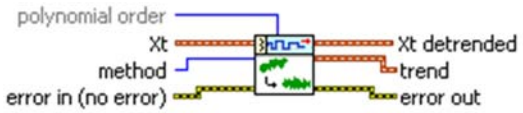


Figure 4.35 Detrend function

- *Decimate 1D Array:* It divides the elements of an array into the output arrays, putting elements into the outputs sequentially (Figure 4.36).



Figure 4.36 Decimate 1D Array function

In Turbine: Part-B, shown in Figure 4.37, the part from the selection of the channels to the start of the task is explained in detail below.

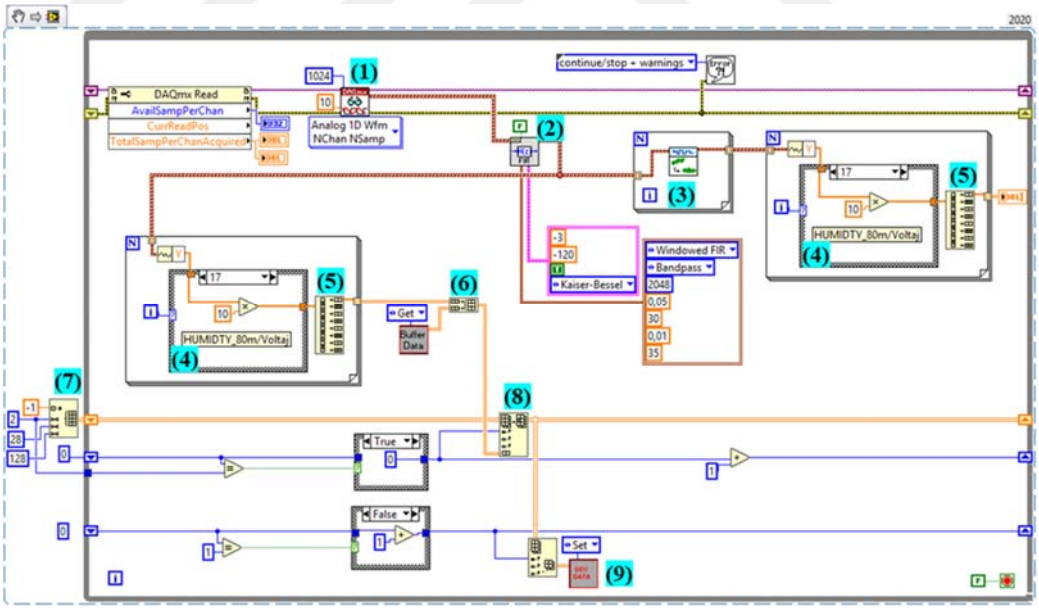


Figure 4.37 Turbine: Part-B; Reading with NI-DAQmx functions and processing collected data

Part-B (1): DAQmx-Read function starts to read the data flowing in the while loop. The loop time is set to 500 ms. Thus, the data collected at 2048 Hz per second is configured to read 1024 samples in 500 ms with the DAQmx-Read function.

Part-B (2): The Digital FIR Filter function modifies the frequency content of the read waveform data. The properties of the filter formed with brown (FIR filter specifications) and pink (optional FIR filter specifications) cables as filter inputs are shown in Figure 4.38. The time history graph and power spectral density (PSD) of the 10-minute raw and filtered data set are shown in Figure 4.39 and Figure 4.40, respectively.

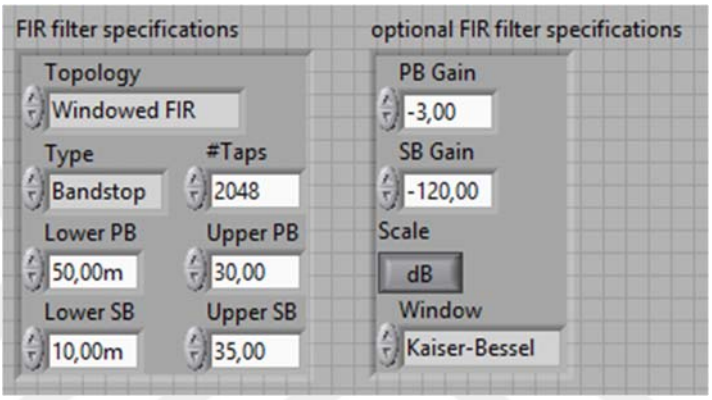


Figure 4.38 Digital FIR Filter features

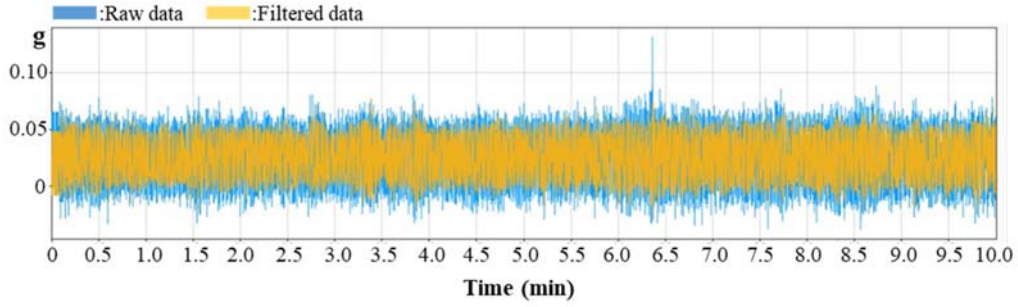


Figure 4.39 Time-acceleration plot of raw and filtered data

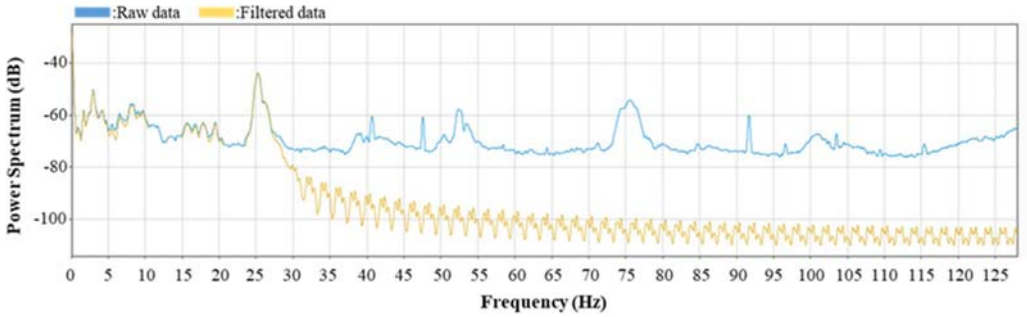


Figure 4.40 PSD graph of raw and filtered data

The primary purpose of filtering is to prevent aliasing effects before decimation. The decrease in dB level after 30 Hz frequency in the PSD graph shows that the filter is working.

Part-B (3): Detrend function removes the effects of a trend from a data set. The linear detrend method is used in this function. Raw and filtered data are shown in Figure 4.41.

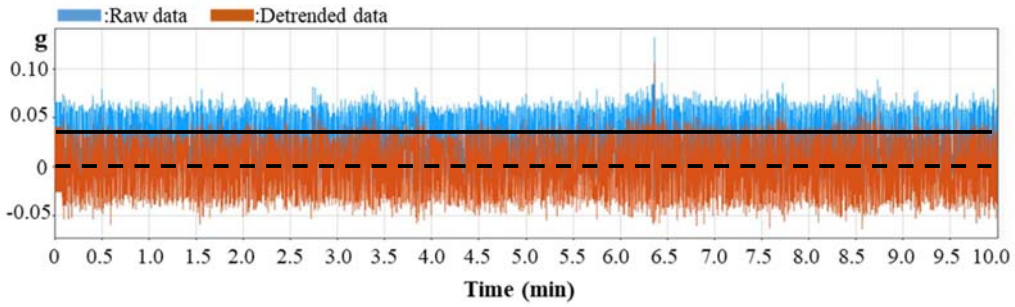


Figure 4.41 Time-acceleration plot of raw and detrended data

The raw data average is around 0.03g (solid line in Figure 4.41). After detrending process mean value is around 0 g (dashed line). Thus, the Direct Current (DC) components in the output signals are removed, and the average values of the signals in the time history domain are pulled to zero with the detrend function.

DC components appear at high energy levels in the frequency domain, making it challenging to identify low-frequency modes. In the Power Spectral Density (PSD) graph (Figure 4.42), the signal's energy around 0 Hz before the detrending process is significantly reduced after the detrending process so that the first mode frequency of the turbine becomes prominent.

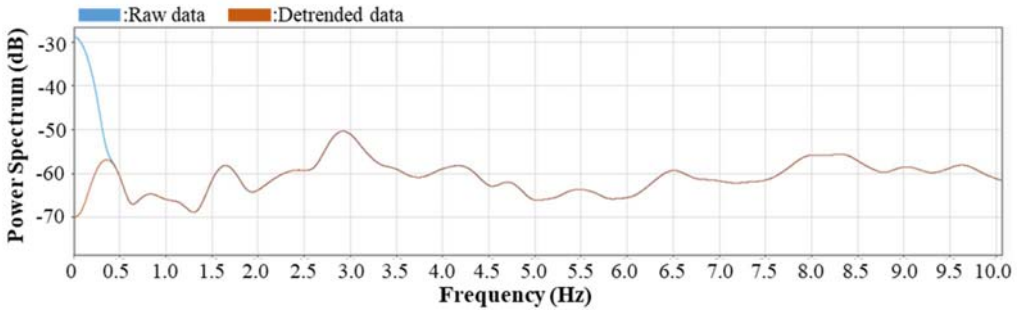


Figure 4.42 PSD graph of detrended data

Part-B (4): Measurements are made with outputs such as voltage and current from each sensor placed in the tower. In order to convert these outputs to units such as acceleration and temperature, each sensor data is calibrated with the calibration coefficients at this stage.

Part-B (5): NI DAQ modules collect data with a minimum sampling frequency of 1613 Hz. However, lower sampling rates are required for this system, which worked for a long time, to be sufficient in terms of storage and transfer of data faster. For this reason, the data collected with a sampling frequency of 2048 Hz is reduced to 256 Hz with the Decimate 1D Array function, reducing the packet sizes and thus increasing the transfer rates.

Part-B (6): Nineteen sensor data acquired from the tower, seven channels transferred from SCADA to the turbine, and the artificial sine wave created are combined in a single array with the data collected from 28 channels with the Build Array function.

A double buffer mechanism is established to avoid any loss during the combined data filing and transfer. Accordingly, each cycle's data collected from 28 channels are written into two indexes. For example, the data collected in the first loop is written in the first index, and the data collected in the second loop is written in the second index. While the data is written to the second directory, the data in the first directory is put into storage and transfer processes. Thus, while writing data to the first index array, the data in the second index array is processed simultaneously.

Part-B (7): Two empty arrays with 28 channels are created.

Part-B (8): The data acquired in each iteration is written to these arrays sequentially.

Part-B (9): The array to be filed and transferred is separated and sent to the relevant loops.

4.2.5.2.3 Turbine: Part-C. The stages of transferring the SCADA data from the switchyard to the turbine with TCP protocol and transmitting it to the Part-B loop to be combined with the sensor data are explained in Part C. Some essential functions used in the coding in Part C are described below.

- *TCP Open Connection:* It starts the TCP network connection with the corresponding port and IP address (Figure 4.43).

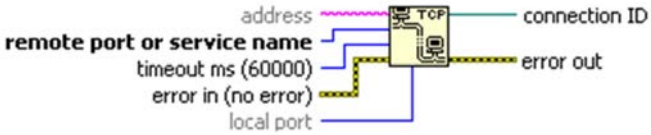


Figure 4.43 TCP Open Connection

- *STM Read Message:* It receives any data from a remote host. This function also reads and unpacks the metadata arrays (Figure 4.44).

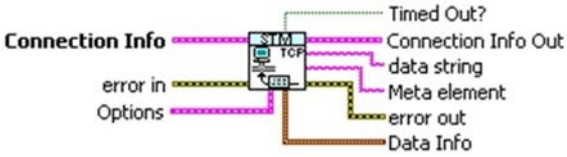


Figure 4.44 STM Read Message

- *STM Read Meta Data:* It is used to retrieve metadata information from a remote computer. This function also reads and opens the metadata array that can be passed to the read and write functions (Figure 4.45).

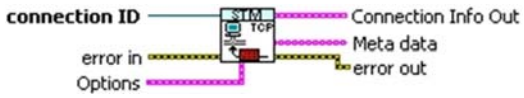


Figure 4.45 STM Read Meta Data

Turbine: Part-C includes transferring SCADA data from the switchyard to the turbine via TCP protocol and transmitting it to the Turbine: Part-B loop to be combined with the sensor data (Figure 4.46). This part is explained in detail below.

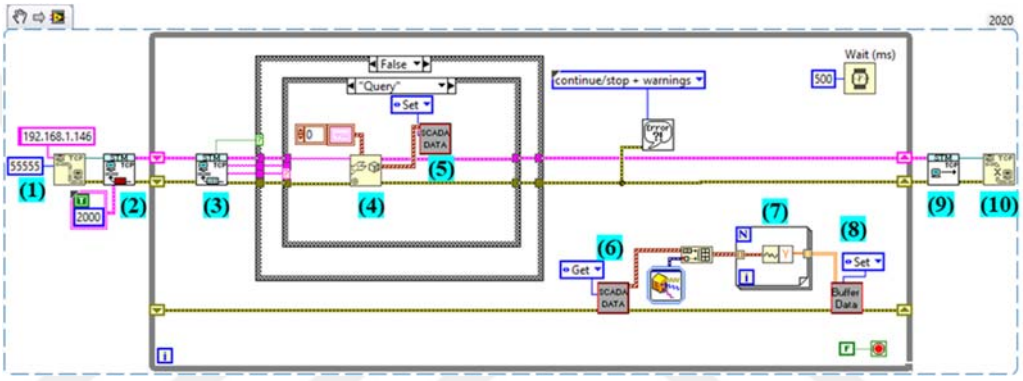


Figure 4.46 Turbine: Part-C; Processing of SCADA data transferred from the switchyard to the turbine

Part-C (1): TCP connection is established between two points by assigning the listener port number and IP number of the point with the TCP Open Connection function.

Part-C (2): The STM Read Meta Data function reads the metadata array of the data sent from the switchyard and makes it ready for reading.

Part-C (3): The STM Read Message function processes the metadata in the relevant case structure according to their names. For example, the data from the switchyard is sent with the metadata name "Query" in the turbine. The timeout period of this function is connected to the case structure with a light green cable. As seen in the figure, if this function is not timeout (False), as long as the server in the switchyard responds to the data request, the incoming data enters the "Query" case structure.

Part-C (4): The data read in String format is converted to Waveform format with the String to Flatten function.

Part-C (5): SCADA data read in Waveform format can be used within the loop or between the loops with the SCADA DATA function. SCADA data read from this function is resampled at a frequency of 256 Hz to ensure that it is at the same frequency as the sensor data.

Part-C (6): The SCADA DATA function is brought to the "Get" state and combined with SCADA data with a frequency of 256 Hz (red cable) and an artificial sine wave with a sampling frequency of 256 Hz (blue cable). The artificial sine wave is used to test whether there is distortion and loss in signals during the inter-loops transfer or data transfer to the campus.

Part-C (7): SCADA and sine data in waveform format are converted to the same data format (double float) as the sensor data.

Part-C (8): The Scada data, ready to be processed and transferred, is transmitted to the Part-A loop with the Buffer Data function. The data is combined with the sensor data in Part-A (6).

Part-C (9-10): The connection reference is taken with the STM Get Connection and TCP Close functions, and the TCP connection is safely closed.

4.2.5.2.4 Turbine: Part-D. The stages of filing and saving the collected sensor and SCADA data in .tdms format are explained in Turbine: Part-D. Some essential functions used in the coding in Part-D are explained in the order below.

- *Get Date/Time String:* It converts the computer's numeric time and date value to the date and time sequence in text format (Figure 4.47).

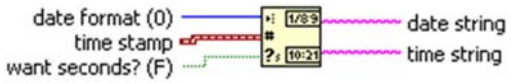


Figure 4.47 Get Date/Time String

- *Build Path:* It allows specifying the address where the files will be saved on the computer (Figure 4.48).

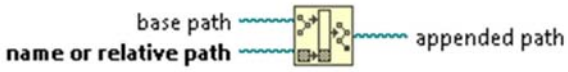


Figure 4.48 Build Path

- *TDMS Open:* It opens a .tdms file from which data will be read or written (Figure 4.49).

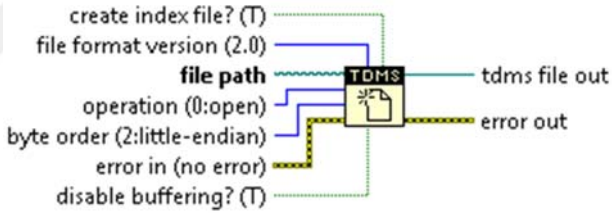


Figure 4.49 TDMS Open

- *TDMS Write:* It writes data to the specified .tdms file. It also creates a name for each channel and writes it in separate columns (Figure 4.50).

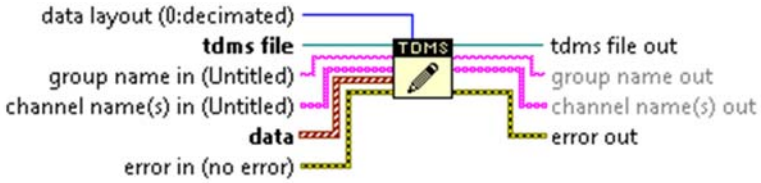


Figure 4.50 TDMS Write

- *TDMS Close*: It closes the .tdms file opened with the TDMS Open function (Figure 4.51).

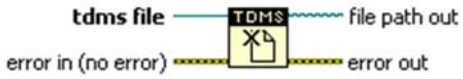


Figure 4.51 TDMS Close

- *Strip Path:* The previously created path is reused to save files (Figure 4.52).

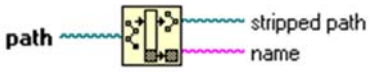


Figure 4.52 Strip Path function

Turbine: Part-D (1, 2, 3, 4, 5, 6, 7, and 8) includes filing and saving the collected sensor and SCADA data in .tdms format (Figure 4.53). This part is explained in detail below.

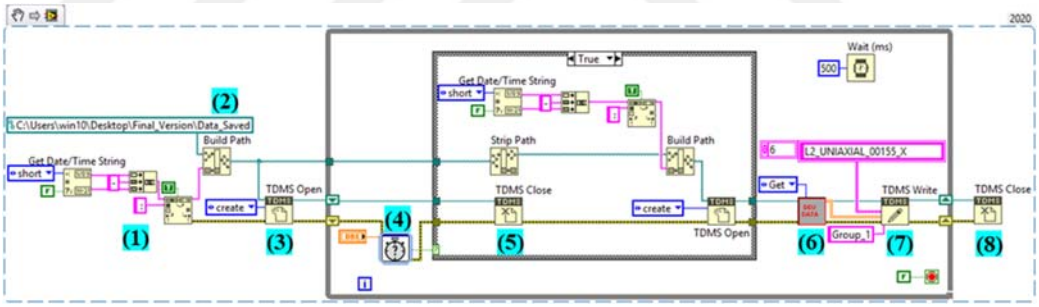


Figure 4.53 Turbine: Part-D; filing and saving sensor and SCADA data in .tdms format

Part-D (1): The date and time of the computer are converted to a text format before creating the file for naming the files with the Get Date/Time String function. Each opened file is named "date-time".

Part-D (2): The path where the files are saved on the computer is entered with the Build Path function. The turquoise cable defines this address, and the pink cable defines the name of the created file.

Part-D (3): The .tdms format is used in the filing process. The .tdms file is opened with the path and name specified with the TDMS Open function.

Part-D (4): The period during which each file remains open and saves data is determined with the File Elapse Time function. In this project, each file saves 600 seconds data packets.

Part-D (5): The .tdms file is closed with the TDMS Close function when the 600 seconds period determined by the File Elapse Time function is expired (True). Immediately after, a new file is opened by repeating the processes specified in Part-D (1,2,3). If this time has not expired (False), data is continued to be written to the open file for 10 minutes as specified in Part-D (6).

Part-D (6-7): All data to be saved in the file is transferred from Turbine: Part-B (9) to the loop by setting the DEU DATA function in the "Get" state. The yellow cable from the DEU DATA function is connected to the TDMS Write function and written to the .tdms file. The names given for each channel are assigned with the pink cable connected to the TDMS Write function.

Part-D (8): The last .tdms file opened with the TDMS Close function is closed if the code is stopped.

4.2.5.2.5 Turbine: Part-E. The transfer of sensor and SCADA data acquired in the industrial computer in the turbine to the campus is explained in Turbine: Part-E. Creating server and receiver loops with Network Stream function via TCP infrastructure is simple. Therefore, LabVIEW Network Stream functions are used to continuously transfer the data from the turbine to the campus without waiting and losing. Some essential functions used in the coding in Turbine: Part-E are explained in the order below.

- *Create Network Stream Writer Endpoint / Create Network Stream Reader Endpoint:* It creates a network connection between the server and the reader, from which data is sent and read (Figure 4.54).

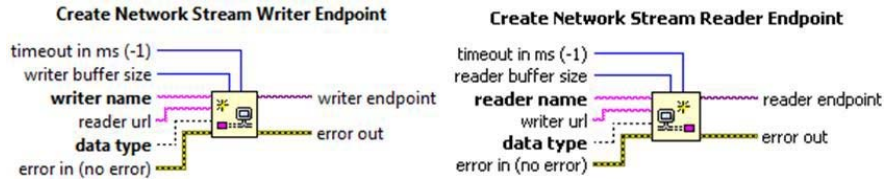


Figure 4.54 Create Network Stream Writer Endpoint / Create Network Stream Reader Endpoint

- *Read Multiple Elements to Stream:* It reads an array of items waiting in a network stream (Figure 4.55).

- *Write Multiple Elements to Stream:* It writes a series of items to a network stream and requests the reader to read this data (Figure 4.55).

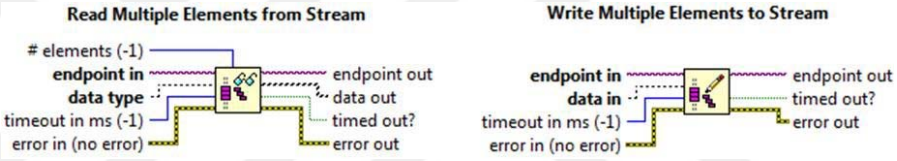


Figure 4.55 Read Multiple Elements to Stream / Write Multiple Elements to Stream

- *Flush Stream:* It ensures the reader receives all data before stopping the flow on the side that writes the data. Thus, before the endpoints are destroyed, the writing and reading operations of the data in the stream are completed (Figure 4.56).

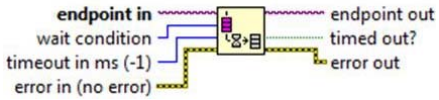


Figure 4.56 Flush Stream

- *Destroy Stream Endpoint:* It stops communication from both endpoints (Figure 4.57) when data flow between endpoints is not required.

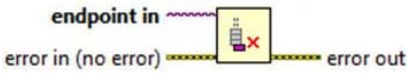


Figure 4.57 Destroy Stream Endpoint

Turbine: Part-E (1, 2, 3, 4, and 5) includes transferring the sensor and SCADA data collected in the turbine to the campus (Figure 4.58). This part is explained in detail below.

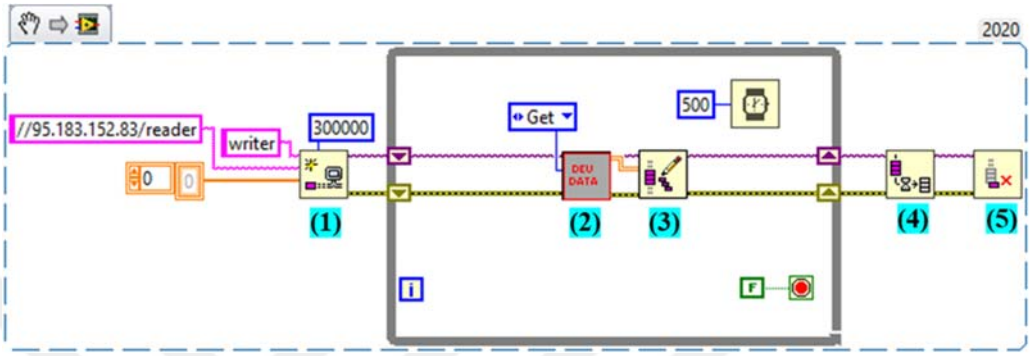


Figure 4.58 Turbine: Part-E; transferring the sensor and SCADA data collected in the turbine to the campus

Part-E (1): The Create Network Stream Writer Endpoint function assigns the sender's name that sends the data. The "writer" connected with the pink cable here is defined as the sender's name. In addition, the IP number and name of the receiver that will read the data are assigned. The IP number of the workstation on the campus is 95.183.152.83, and its name is assigned as "reader". The orange cable connecting to the function defines the data format, the index in a two-dimensional "double float".

Part-E (2-3): The DEU DATA function is set to the "Get" state, and all the data transmitted to the campus is transferred from the Turbine: Part-B (9) to the transfer loop. The yellow cable from the DEU DATA function is connected to the Write Multiple Elements to Stream function and transferred.

Part-E (4-5): The connection reference is taken with the Flush Stream and Destroy Stream Endpoint functions, and the TCP connection is safely closed.

4.2.5.3 Codes Developed to Run on Campus

The previous steps explain all the coding required for the instant and synchronous transfer of all sensor and SCADA data collected in the turbine to the campus

environment. At this stage, the steps of reading and packaging the data sent with Network Stream functions to be transferred to the campus and sending a warning mail to the specified e-mail addresses in case of any interruption are explained.

4.2.5.3.1 Campus: Part-A. The stages of reading, packaging, and filing the SCADA and sensor data transferred to the campus are explained. Data is sent from the turbine and read with Network Stream functions. Some essential functions used in the coding in Campus: Part-A are explained in the order below.

Empty Array: It checks whether the array with the data is empty (Figure 4.59).



Figure 4.59 Empty Array

Obtain Queue: It creates a queue according to the specified data type (Figure 4.60).

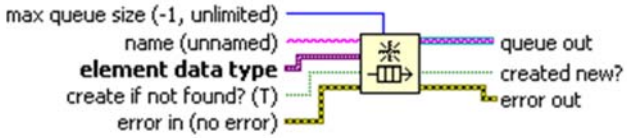


Figure 4.60 Obtain Queue

Enqueue Element: It allows the data to enter the queue (Figure 4.61).

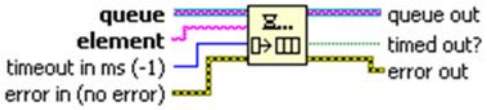


Figure 4.61 Enqueue Element

Release Queue: It ensures the queue is closed after receiving the data from the queue (Figure 4.62).

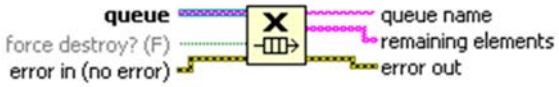


Figure 4.62 Release Queue

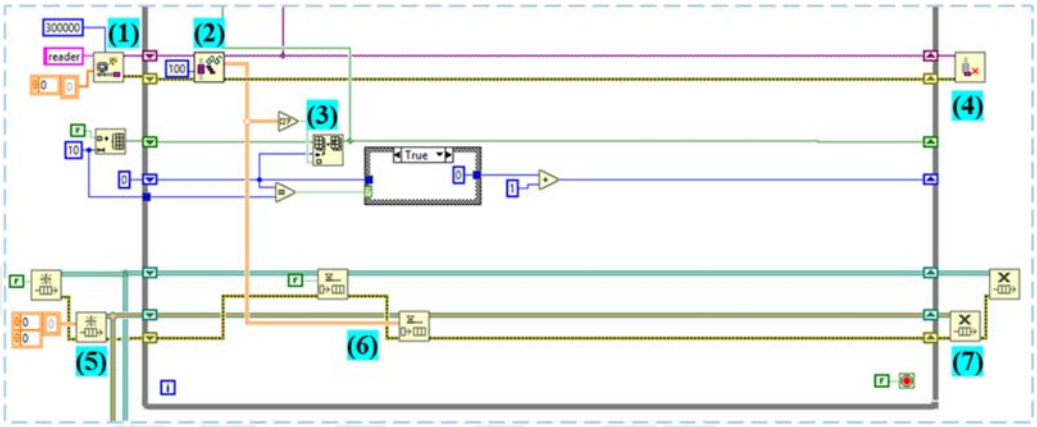


Figure 4.63 Campus: Part-A; Reading SCADA and sensor data sent from the turbine to the campus

Campus: Part-A (1, 2, 3, 4, 5, 6, and 7), which includes reading and preparing the SCADA and sensor data sent from the turbine to the campus (Figure 4.63), is explained in detail below.

Part-A (1): The Create Network Stream Reader Endpoint function assigns the receiver's name that reads the data. The reader connected with the pink cable here is defined as the receiver's name. The orange cable connecting to the function defines the data format, the index in a two-dimensional double float.

Part-A (2): The data is read and made ready for packaging and filing with the Read Multiple Elements to Stream function. The yellow cable coming out of this function transmits SCADA and sensor data transferred from the turbine to the campus.

Part-A (3): The connection reference is taken with the Destroy Stream Endpoint function, and the connection established between the two points is safely closed.

Part-A (4): It is checked with the Empty Array function whether the array in which the read data is written is empty after the reading process starts. If this array is empty,

an e-mail is sent to the relevant e-mail addresses to check the data flow, as described in the Campus: Part-B section.

The filing of the read data is carried out in a different loop. LabVIEW Queue functions prevent any data loss during the transfer of this data to the filing loop.

Part-A (5): The Obtain Queue function creates a queue according to the type of array where the data to be queued is written. The collected data is of two-dimensional double float type, and this is defined by the yellow cable connected to the function. Queued data is sent to the loop to be filed. The filing procedures are the same as for the Turbine: Part-D part. SCADA and sensor data are written to .tdms files in 600-seconds packages and saved on the campus storage device.

Part-A (6): The Enqueue Element function ensures that the data transferred from the turbine to the campus join the queue created for filing.

Part-A (7): The Release Queue function closes the queue created after the program is stopped.

4.2.5.3.2 Campus: Part-B. If the data flow from the turbine to the campus breaks, the Network Stream functions will notify the relevant people by e-mail in Campus: Part-B. Thus, the continuous flow of data to the campus is controlled. Sending warning e-mails is done with Simple Mail Transfer Protocol (SMTP). Some essential functions used at this stage are explained below.

Network Stream Endpoint: It obtains information about the ongoing data flow (Figure 4.64).

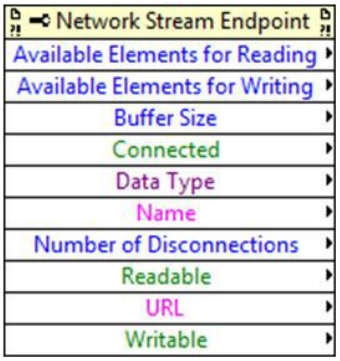


Figure 4.64 Network Stream Endpoint function

Open Handle: It creates a new SMTP client using the specified SMTP server (Figure 4.65).

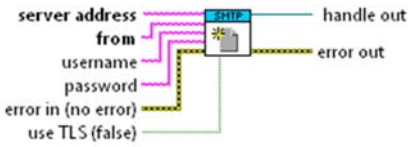


Figure 4.65 Open Handle

Set Recipients: It sets the list of recipients to e-mail (Figure 4.66).

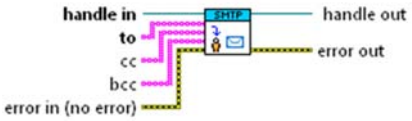


Figure 4.66 Set Recipients

Set Message: It sets the e-mail subject and the message to be sent (Figure 4.67).

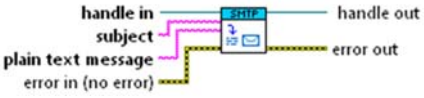


Figure 4.67 Set Message

Send: It sends the prepared mail to the e-mail addresses in the recipient list (Figure 4.68).

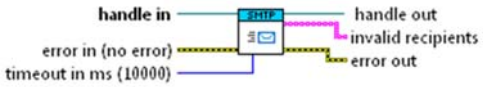


Figure 4.68 Send

Close Handle: It closes the connection to the SMTP server created by Open Handle (Figure 4.69).



Figure 4.69 Close Handle

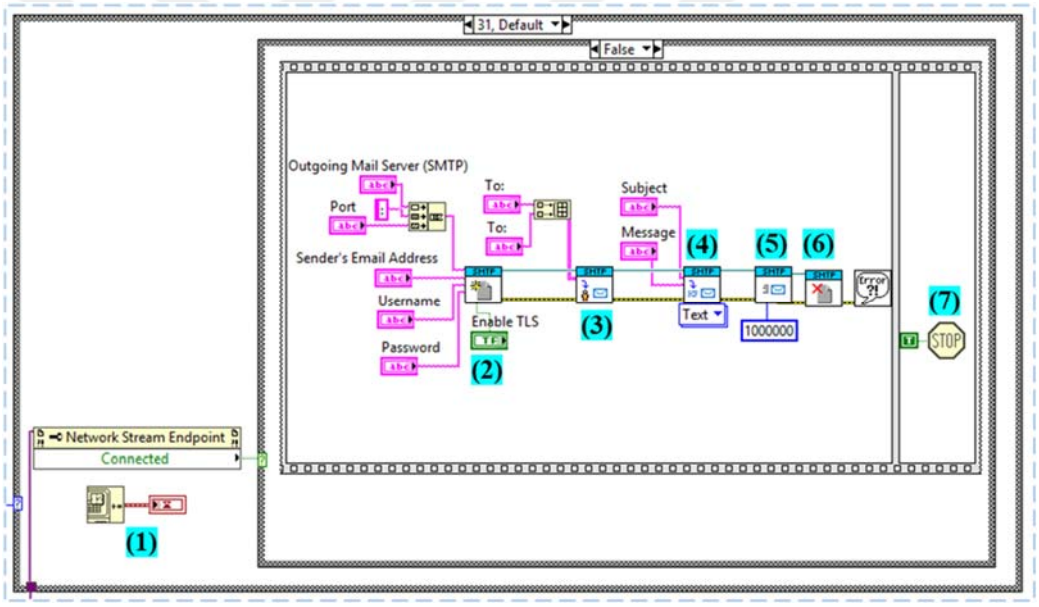


Figure 4.70 Campus: Part-B; Notification by e-mail in case the data flow to the campus breaks

Campus: Part-B (1, 2, 3, 4, 5, 6, 7), which includes sending a message via e-mail in case the data flow between the campus and the turbine stops (Figure 4.70), is explained in detail below.

Part-B (1): It is checked whether the array where the data transferred to the campus is written is empty in Campus: Part-A (4) If this array is empty, it is queried whether there is a network connection between the turbine and the campus with the Network Stream Endpoint function.

If the connection is broken, if it is Connected (False), a warning message is sent to the specified e-mail addresses.

Part-B (2): It is specified which SMTP server and port to send an e-mail with the Open Handle function. The "Google Mail" server is used for mailing. Gmail SMTP server: smtp.gmail.com and port: 587 are assigned. Then, the sender's e-mail address and password are assigned via the same function. Warning e-mails are sent via the created "deysi@gmail.com" account.

Part-B (3): The Set Recipients function defines the Addresses to send e-mails.

Part-B (4): The subject and content of the message are determined with the Set Message function.

Part-B (5): The e-mail created with the Send function is forwarded to the recipients.

Part-B (6): The connection with the SMTP server is closed with the Close Handle function.

Part-B (7): The code is stopped by the STOP function after sending the e-mail,

4.2.5.4 Execution of Codes and Data Flow Chart in Switchyard, Turbine, and Campus

The coding studies carried out in the switchyard, turbine, and campus are explained in the previous sections with all their details. The data flow throughout the system is programmed as the transfer of SCADA data from the switchyard to the turbine, combining the SCADA and sensor data acquired in the turbine and transferring it to the campus.

It should be observed that SCADA data flows to the NI OPC Server and that there is data flow from the sensors in the turbine before these codes are run. Then, the

switchyard-turbine and turbine-campus communication should be tested by pinging between these computers with a command prompt.

After all the controls are satisfied, the codes are run in the following order (Figure 4.71):

1) The code in the switchyard is run and waits for approval to send SCADA data to the turbine.
2) Approval is awaited from the turbine to receive SCADA and sensor data by running the code on campus.
3) SCADA data transfer from the switchyard, data acquisition in the turbine, and the transfer of this data to the campus are started by running the code in the turbine.

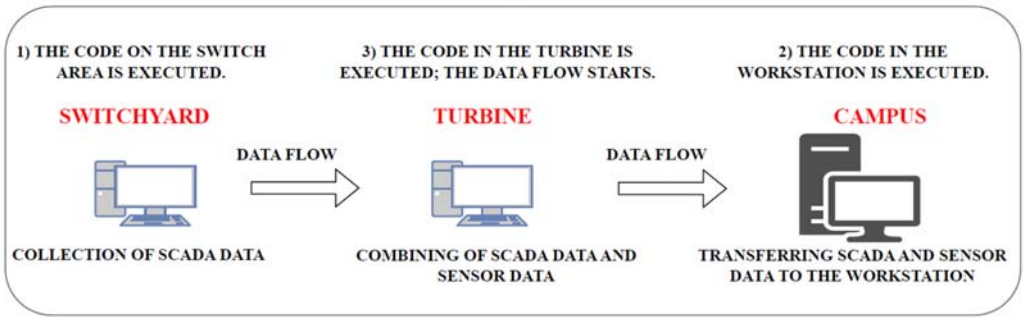


Figure 4.71 Order of Execution of Codes and Data Flow Diagram

These codes work autonomously without any intervention. If there is a break in the data flow, a notification is sent by the code running on the campus via e-mail. These breaks in data flow are usually caused by weak network connections. Long-term (2-3 days) power outages on campus can also cause data flow to stop. Unless there are such reasons, it is tested that the codes in the three stations work synchronously and continuously to ensure data transfer. In long-term tests, the error codes taken from the codes are resolved individually, ensuring the program's stability and real-time operation.

CHAPTER 5
AUTONOMOUS SYSTEM IDENTIFICATION

The estimation of modal parameters from the recorded data needs considerable amount user intervention. This leads to a great loss of time when it is necessary to process a large number of datasets. In the scope of the thesis work, to determine the effect of operational and environmental conditions on dynamic characteristics of the wind turbines, it is necessary to estimate modal parameters by processing many datasets recorded under different conditions. For this reason, all the system identification processes need to be fully automated. This process consists of mainly four parts:

1. Simultaneously recording acceleration, operational and environmental data
2. Preprocessing of the acceleration data (decimation, filtering and detrending)
3. System identification using an operational modal analysis method
4. Correlating modal parameters with operational and environmental conditions.

The first two steps are explained in detail in Chapter Four. This chapter focuses on the last two steps of the process.

5.1 Operational Modal Analysis using p-LSCF Method

In a stabilization diagram mathematical (spurious/virtual) poles can be appeared as well as the physical modes. To separate mathematical modes and detect physical modes correctly damping estimates can be used. Damping values of the virtual modes usually estimates negative or physically meaningless. Another distinguish feature is the location of the poles. Physical modes appear at almost the same frequency values for different orders on the stabilization diagram (line order) while mathematical modes are located random points. To develop a fully automated system identification process, choosing a method that generates a very clean stabilization diagram (minimum number of mathematical modes) is essential.

p-LSCF method is chosen for system identification since it estimates negative damping values for mathematical modes and constructs a clearer stabilization diagram than other parametric methods.

The MATLAB Toolbox for Experimental and Operational Modal Analysis (MACEC) provides modal parameter estimation with p-LSCF method (Peeters & De Roeck 1999; Reynders & De Roeck 2008; Reynders, Pintelon, & De Roeck 2008; Reynders, Degrauwe, De Roeck, Magalhães, & Caetano, 2010; Reynders 2012; Reynders, Maes, Lombaert, & De Roeck, 2016; Reynders 2021). The MACEC has a graphical user interface but requires user intervention at every stage of the analysis. In batch mode, there are only code lines, and these lines can be run continuously once they are adapted to a specific problem.

5.1.1 Preparation of Data

Synchronously recorded 600 seconds long data (acceleration, temperature, and relative humidity data from different point of the turbine and other operational and environmental data form SCADA system) is stored up after preprocessing (filtering, decimating, and detrending) by LabVIEW. This file is imported to MATLAB and each acceleration channel is assigned to the relevant point on the created turbine model. In operational modal analysis, only the relative positions of the data recording points to each other are the geometric information required for the estimation of the modal parameters and the dimensions of the structure like radius, thickness, and section shape do not matter. Wind turbine measurement points and the MACEC model of the turbine are presented in Figure 5.1.

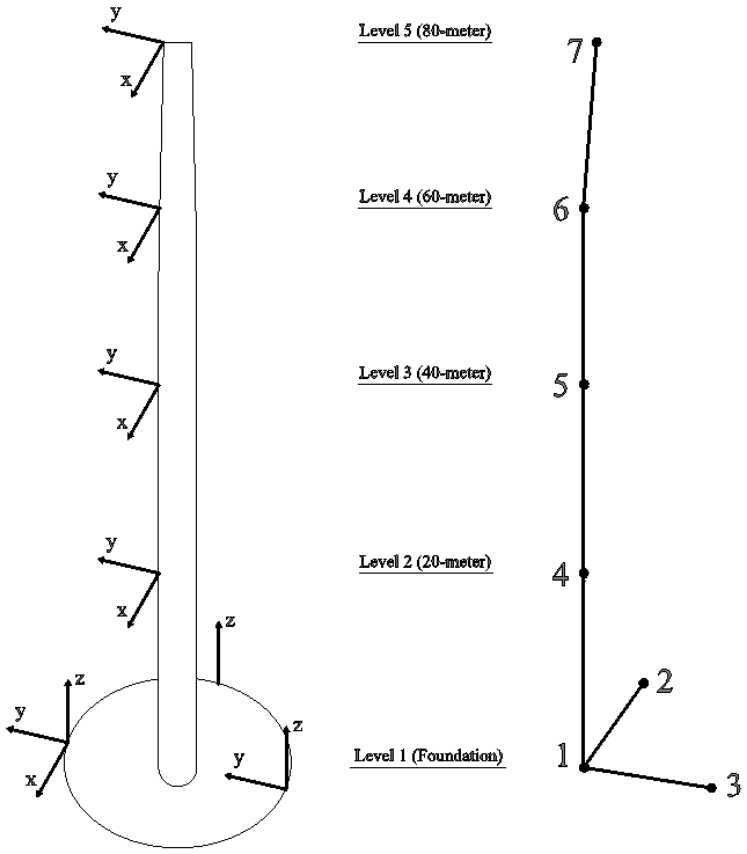


Figure 5.1 Wind turbine acceleration measurement points and the MACEC model of the turbine

5.1.2 Stabilization Diagram

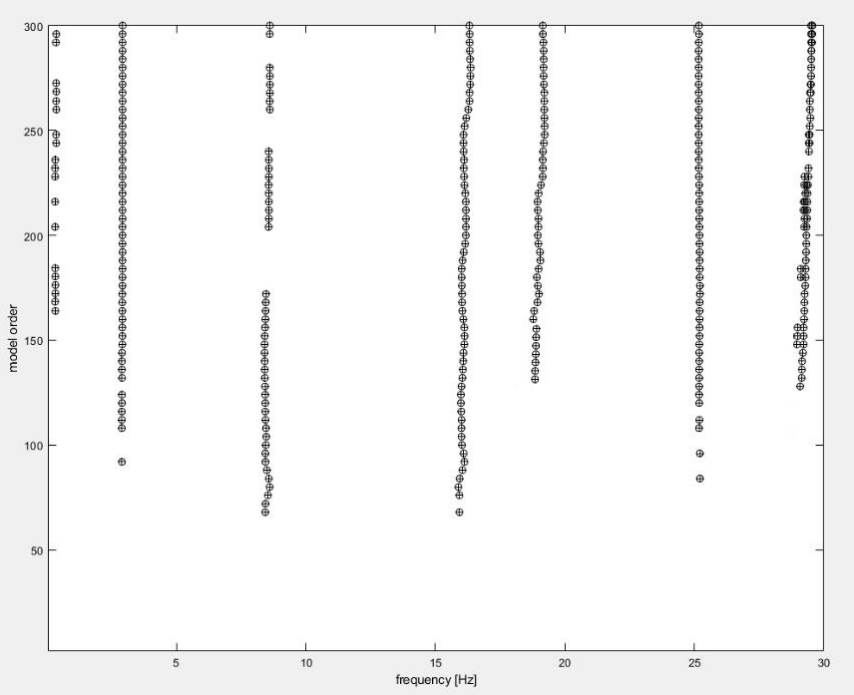
In OMA, the stabilization diagram is a useful tool to distinguish physical and non-physical (mathematical/spurious/virtual) modes. Physical modes tend to line up at nearly the same frequency values while mathematical ones jump around. Using an OMA method produces clear stabilization diagram is essential for developing an autonomous system identification process. Because stabilization diagram with many non-physical poles makes it difficult to determine the physical system modes in an autonomous mode picking process.

After assigning acceleration channels to the relevant point in MACEC model, stabilization diagram is constructed using p-LSCF method and Data-Driven Stochastic Subspace Identification (SSI-DATA) which is another parametric method (Peeters &

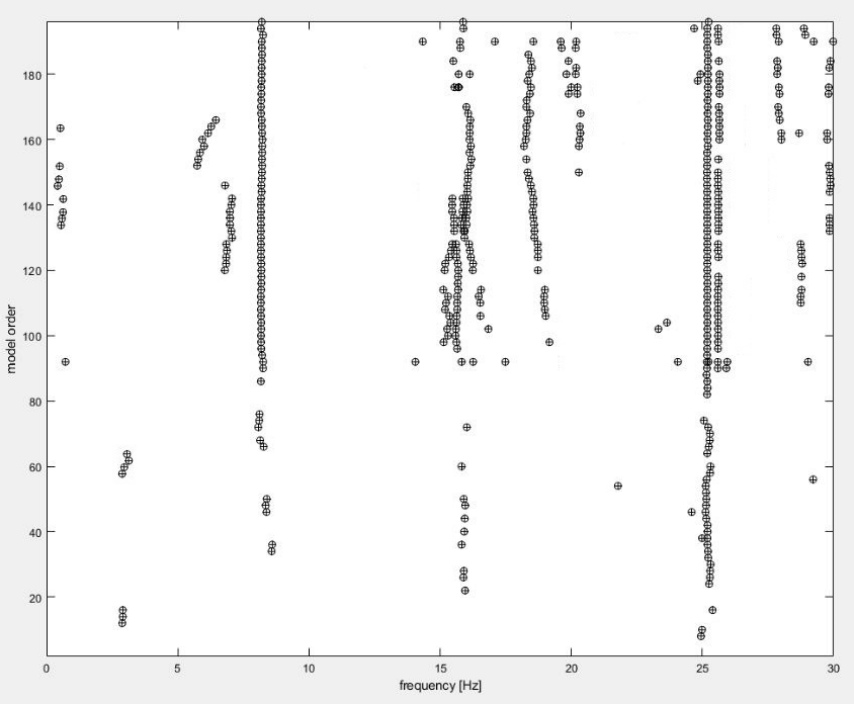
De Roeck, 2001). To eliminate most of non-physical modes and obtain clearer stabilization diagram some stabilization criteria are applied for both methods:

- df= 10% frequency stabilization criterium
- dxi= 25% damping ratio stabilization criterium
- dm= 10% mode shape stabilization criterium
- dampco= 10% damping ratio upper bound
- damplco= 0% damping ratio lover bound
- trnormco= 50 if, for a certain model order, the modes are ordered in descending modal transfer norm, only the first trnormco modes are stable
- dmtn= 50% modal transfer norm stabilization criterium
- maxfrstd= 5 upper bound on the standard deviation of the frequency
- maxdmpstd= 5 upper bound on the standard deviation of the damping ratio
- maxmodstd= 5 upper bound on the standard deviation on any real or imaginary component of the mode shape
- mpclb= 0.5 lower bound on the modal phase collinearity
- mpub= 90º upper bound on the mean phase
- mpdub= 90º upper bound on the mean phase deviation

Two stabilization charts are presented in Figure 5.2 for comparison.



(a)



(b)

Figure 5.2 Stabilization diagrams constructed using (a) p-LSCF method, and (b) SSI-DATA method

As can be seen from Figure 5.2, the p-LSCF method constructed a very clear stabilization diagram shows seven structural modes lined up on certain frequencies: 0.35 Hz, 3.00 Hz, 8.30 Hz, 16.00 Hz, 18.30 Hz, 25.00 Hz, and 29.00 Hz. Stabilization diagram obtained by using SSI-DATA method has many mathematical modes. This makes it difficult to select physical modes even with expert user intervention. In that case, distinguishing physical modes from non-physical ones with an autonomous process cannot be reliable. Note that, since the data recorded from an operational wind turbine includes the effects of complex components like rotary mechanical parts, it is not possible to obtain clean stabilization diagrams with every OMA method.

5.1.3 Autonomous Mode Picking

After the stabilization diagram is created, the physical modes must be selected among the stable points in this diagram. All points lined up on a column (on the same frequency) contain almost the same modal parameter information (frequency, damping, and mode shape). Among this group of points, the most reliable results can be found at the point with the lowest order. Based on this information, one can easily select the physical modes from stabilization diagram like Figure 5.2a.

To determine the effect of operational and environmental conditions on dynamic characteristics of the wind turbine, more than ten thousand data will be processed. In the stabilization diagrams obtained from the data recorded under different conditions, the modes are expected to be lined up on slightly different frequencies. In addition, a few mathematical modes may appear in some stabilization diagrams. A procedure has been developed for correct selection of physical modes in a stabilization diagram. In this procedure, all stable modes determined according to the criteria mentioned in Chapter 5.1.2 are checked. If three stable modes are lined up in consecutive orders within a small tolerance at a certain frequency value, the mode with the lowest order number is selected as the physical mode of the system. Other points on the same column are not evaluated in the physical mode selection. The autonomous mode picking procedure is presented as a flowchart in Figure 5.3.

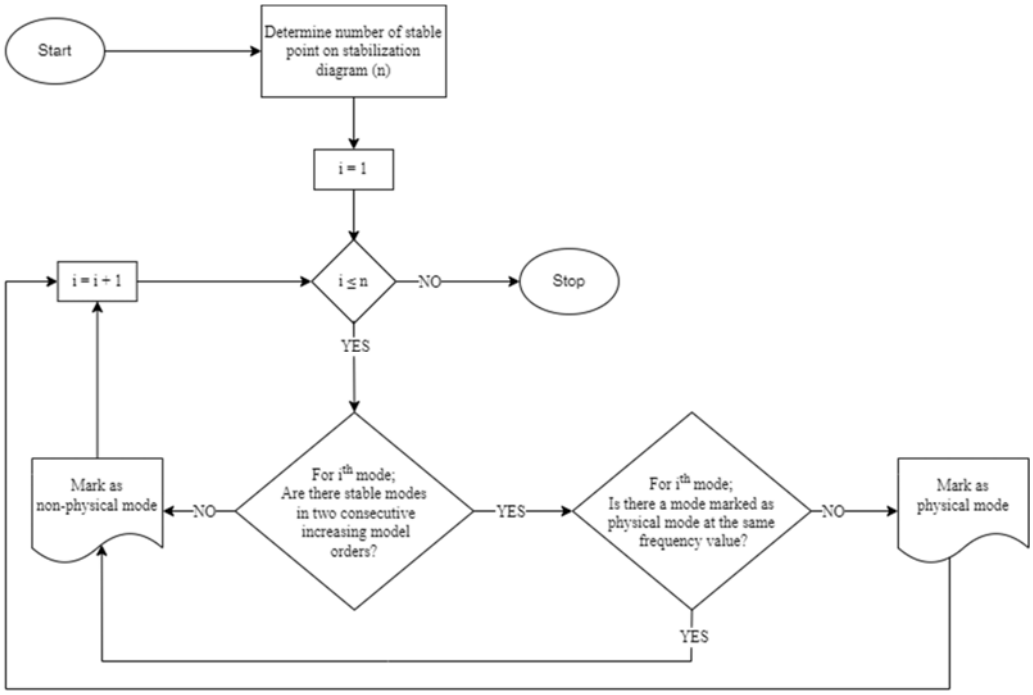


Figure 5.3 Procedure for autonomous mode picking

Selected physical modes using the autonomous mode picking procedure in stabilization diagram shown in Figure 5.2a are presented in Figure 5.4 and Table 5.1.

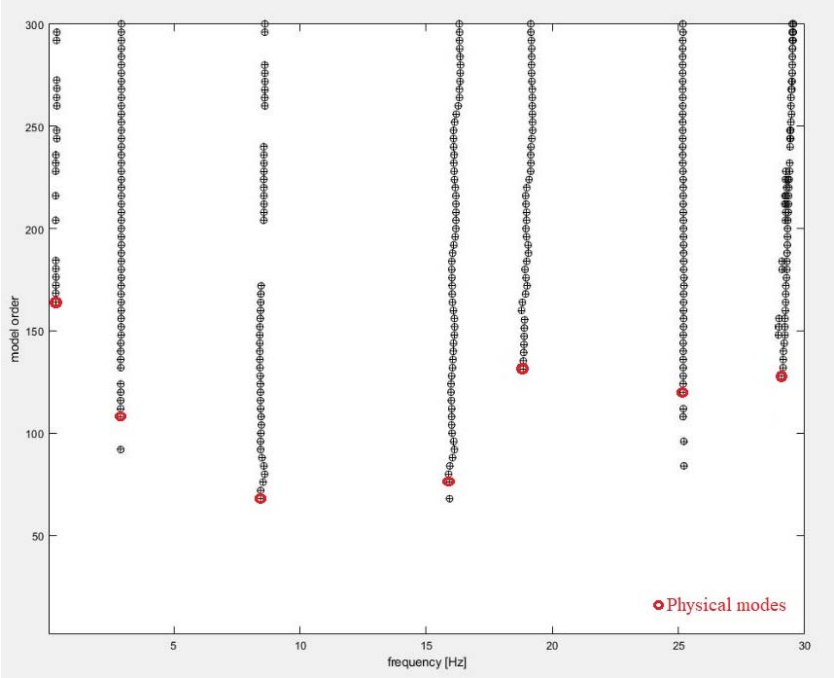


Figure 5.4 Selected physical modes using autonomous mode picking procedure

Table 5.1 Selected physical modes using autonomous mode picking procedure

Frequency (Hz)	0.355	3.031	8.597	15.909	18.884	25.279	28.987
Damping (%)	2.4	0.8	3.6	2.3	2.5	1.5	1.1
Order	164	108	68	76	132	120	128

5.2 Fully Automated Data Acquisition and System Identification Process

In order to determine the effect of operational and environmental conditions on dynamic characteristics of an operating wind turbine, a vast number of data must be acquired and processed. For this purpose, an Autonomous and Continuous System Identification (ACSI) system has been developed, from data acquisition to estimation of modal parameters, which does not require any user intervention. Steps of this automated system are summarized below:

1. 14 channels acceleration, 3 channels temperature and 2 channels humidity data are simultaneously acquired by the sensors of the distributed data acquisition system specially designed for the subject wind turbine.

2. Acceleration data is prepared for system identification using preprocessing methods: Filtering, decimating, and detrending.

3. Environmental (e.g., temperature, wind speed, relative humidity, and wind direction) and operational data (e.g., rotor speed, nacelle direction, pitch angle, and actual power) flowing in turbine's SCADA system are acquired simultaneously with the acceleration data.

4. Environmental and operational data are transferred from the switchyard to the wind turbine by P2P antennas. Internet access is also shared to the data acquisition system deployed on the turbine by this remote connection.

5. All acquired data is saved in 600 seconds long files continuously. The data files are transferred to the campus environment and stored in NAS devices for further analyses.

6. The directory where the data files are stored is constantly checked. A new file transferred from the turbine every 600 seconds is read for processing.

7. The acceleration data is processed by using the p-LSCF method and stabilization diagram is constructed according to the predefined stabilization criteria.

8. Physical vibration modes are selected from the stabilization diagram and modal parameters (e.g., mode frequencies, damping ratios and mode shapes) are estimated.

9. Operational and environmental conditions are calculated by averaging 600 seconds long data.

10. The estimated modal parameters are matched with operational and environmental conditions and saved as a row in the results file with the date and time stamp.

11. Modal parameters estimated from each 600 seconds long data file compared with the reference (benchmark) state. Considering the effect of operational and environmental conditions on modal parameters, if there is a difference more than the threshold value, a report stating that there may be a damage on the wind turbine is automatically prepared and sent to the relevant people by e-mail.

These steps are performed autonomously every 600 seconds. From 7th July 2022 to 7th February 2023 a total of 13277 data files were recorded and processed. Modal parameters are estimated in both MWD and SWD directions for statistical analyses.

Note that some data on the aforementioned dates could not be recorded, as the troubleshooting continues during the process of data acquisition by the system.

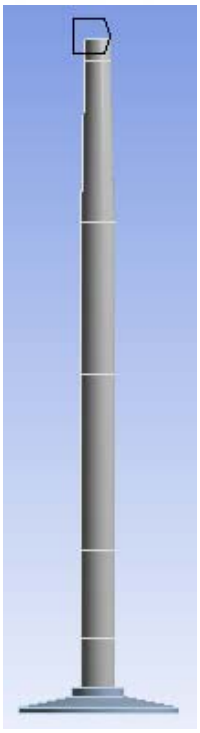
Although step 11 is not within the scope of the thesis, considerable progress has been made in integrating this step into the system. After the regression analyzes are completed, the ACSI system will evolve into a structural health monitoring system.

This fully automated system will continue to acquire and process data from the wind turbine for a long time. The valuable data recorded by this system will enable other academic studies to be carried out in the future besides thesis work.

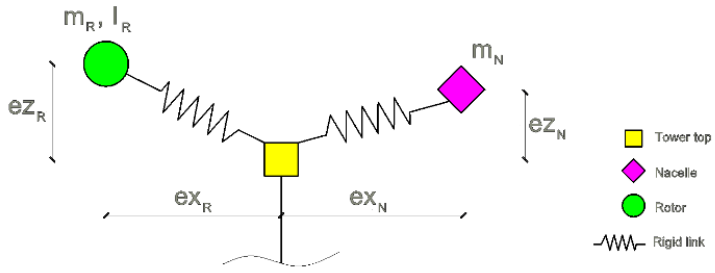
CHAPTER 6
MODEL UPDATING OF THE WIND TURBINE

6.1 Finite Element Model of the Wind Turbine

The wind turbine is introduced in Chapter 4.1, consists of four main components: reinforced concrete foundation, steel tower, rotor, and nacelle. According to a study conducted in 2021 (Ali, Risi, & Sextos, 2021), it is important to take into account the eccentricities of the rotor and nacelle with reference to the tower top center point and the rotational moment of inertia of the rotor while creating the numerical model for wind turbines, for the correct determination of the dynamic properties of the turbine. Considering the results of the study and avoiding computationally expensive analyses; Foundation and tower are modelled with finite elements (Figure 6.1(a)), while the rotor and nacelle with a simplified approach (Figure 6.1(b)). The finite element model of the wind turbine created in ANSYS (2019) environment.



(a)



(b)

Figure 6.1 (a) Finite element model for the reinforced concrete foundation and steel tower (b) a simplified model for the rotor and nacelle

Rotor and nacelle are defined as lumped masses with their eccentricities (ez_R, ex_R, ez_N, and ex_N respectively) and bounded to the tower top with infinite rigid links. The rotor blade's moment of inertia is also defined in the model as I_R.

Meshing is the essential part while creating a finite element model. Results obtained using analytical models with insufficient mesh quality are unreliable. Finite elements with six surfaces and twenty-four degrees-of-freedom are used in the model of the wind turbine. Relatively smaller mesh sizes are used in the model of the tower, whose thickness is much smaller than the foundation and the analysis results are more sensitive. Since the tower and foundation are circular, radial meshing technique is used. Therefore, continuity of meshes is ensured from all parts of the model, especially at the foundation-tower interface.

As it is known, the smaller the mesh size, the more accurate results are obtained, while the computational burden increases. The optimum mesh size should be determined for each problem. To determine optimum mesh sizes, a single load is applied parallel to the ground from the turbine tower top and top displacement values are obtained for different finite element sizes. A total of 10 linear analyses are performed. Figure 6.2's X axis represents how many equal parts (slices) the tower and foundation are divided radially while Y axis shows the normalized top displacement.

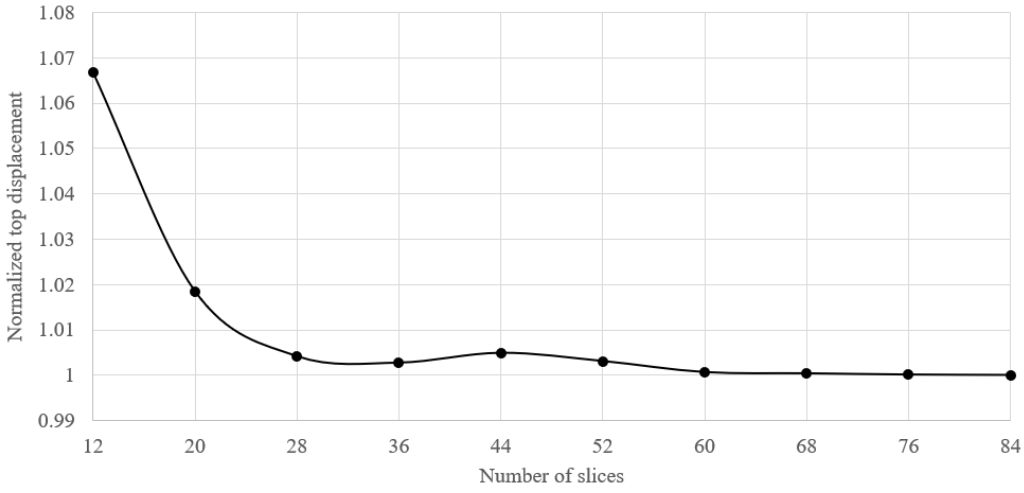


Figure 6.2 Mesh convergence

As seen in Figure 6.2, increasing the mesh number after a point does not significantly change the result. Therefore, it was decided to divide the tower and the foundation into 60 equal parts radially. Figure 6.3 presents meshing along the wind turbine.

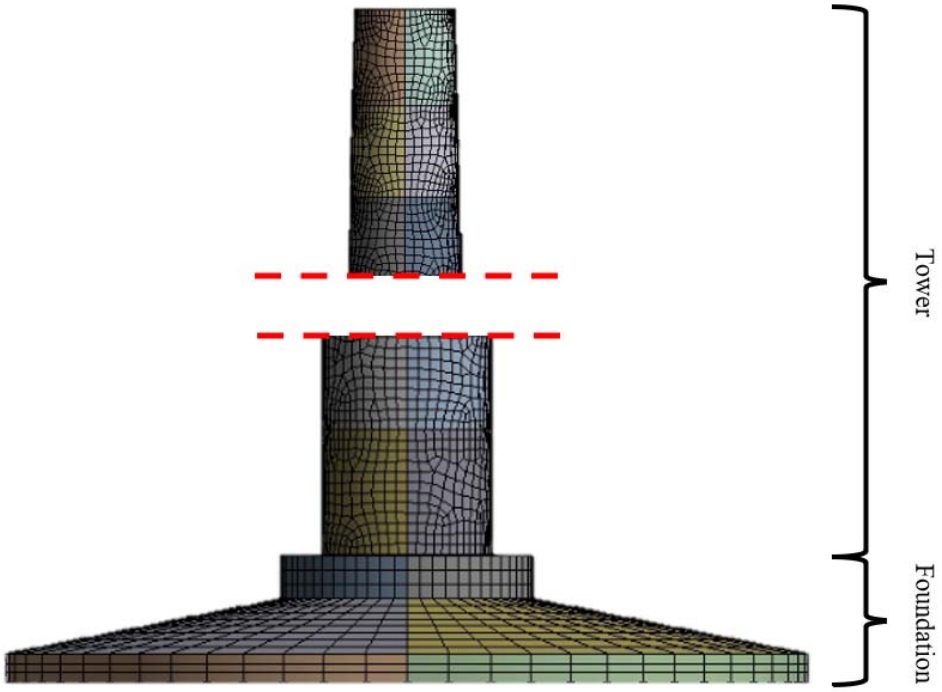


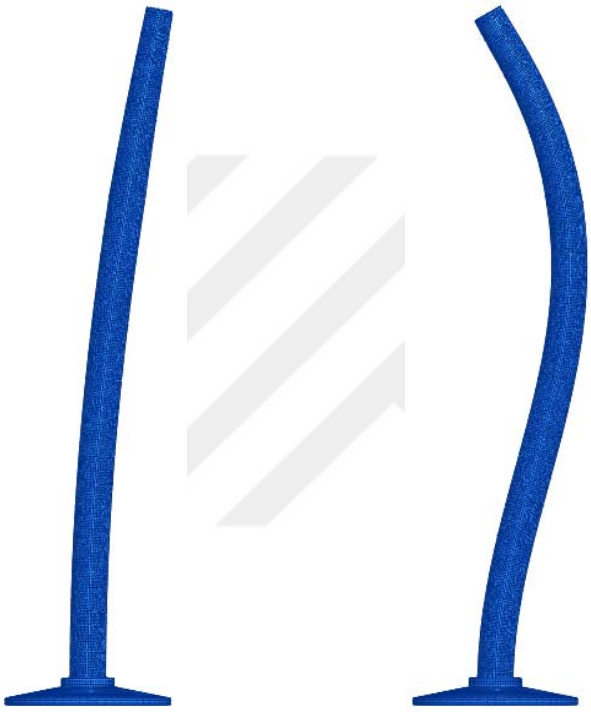
Figure 6.3 Finite element meshing of the wind turbine

6.2 Analytical Modal Analysis

After the turbine modeling is completed in ANSYS environment, analytical modal analysis is performed, and the first 10 modes of the wind turbine are obtained. The first 4 modes obtained are the structural modes in two perpendicular directions (fore-aft and side-side), while the remaining 6 modes correspond to the local buckling modes. The natural mode frequencies of the structural modes are presented in Table 6.1, and the mode shapes are presented in Figure 6.4. Since the foundation and tower are circular, they have a symmetrical geometry for each direction. However, since the rotor and nacelle are located in one direction (fore-aft), the only symmetry axis of wind turbine is the fore-aft direction.

Table 6.1 Mode frequencies.

Frequency (Hz)	Direction	Description
0.355	Fore-aft	1st structural
0.355	Side-side	1st structural
3.031	Fore-aft	2nd structural
3.064	Side-side	2nd structural



(a) (b)

Figure 6.4 (a) First (fundamental), and (b) second structural mode shapes

6.3 Pairing Analytical and Experimental Modes

In order to update the numerical model of the wind turbine, the 600-second-long acceleration data set recorded by data acquisition system introduced in Chapter 4 under the environmental and operational conditions presented in Table 6.2. Acceleration data is processed using the system identification software (please see Chapter 5) and the modal parameters of the turbine are estimated.

Table 6.2 Environmental and operational conditions while recording data for FEM updating

Wind Speed	10 m/s
Wind Direction	11°
Temperature	26°C
Relative Humidity	32%
Rotor Speed	15.5 RPM
Nacelle Direction	11° (*)
Pitch Angle	0°
Actual Power	1645 kW

(*) One of the acceleration recording directions

In real structure since the rotor-nacelle direction changes according to the wind direction for energy production efficiency. By definition, fore-aft and side-side directions of the wind turbine are change with the wind direction. In addition, accelerometers are place and record only fixed two directions (Figure 4.6). In order to pair the experimental and analytical modes correctly, data is collected when the fore-aft and side-side directions of the turbine and the sensor's recording directions matched. Otherwise, one can only pair the analytical modes with the projection of experimental modes to analytical axes. It would lead to find inaccurate finite element updating results.

Experimentally identified first two structural modes in fore-aft direction are paired with the analytical counterparts. The Modal Assurance Criterion (MAC) values showing the spatial compatibility of the paired mode shapes (Figure 6.5) and frequencies presented in Table 6.3.

Table 6.3 Paired mode frequencies and MAC values

	1st mode	*2nd mode*
Experimentally identified mode frequency	0.356 Hz	2.985 Hz
Analytically calculated mode frequency	0.355 Hz	3.031 Hz
Frequency difference	-0.30%	1.56%
MAC value	98.9%	94.6%



Figure 6.5 Paired (a) 1st (fundamental) mode, and (b) 2nd mode shapes

6.4 Construction of Objective Function and Design Variables

As can be seen in Figure 6.5 and Table 6.3, the results obtained from the analytical model of the turbine are consistent with the results estimated from the experimental data. However, there are also differences due to numerical model assumptions and non-structural elements in the turbine. It is very important to minimize these differences as much as possible and to create a more realistic analytical model, and then to obtain more realistic results in detailed analyses using this analytical model.

For this purpose, the objective function needs to be created first. Paired modes' frequency and MAC value residuals are selected to minimize. Since mode frequencies are more trustable responses, higher weighting coefficients are used when creating the objective function (Table 6.4).

Table 6.4 Response residuals of objective function

Response No	Response Name	Weighting Coefficient
1	1st mod frequency residual	5.0
2	2nd mod frequency residual	5.0
3	1st mod MAC value residual	1.0
4	2nd mod MAC value residual	1.0

Although the presence of non-structural elements and errors made during the production/manufacturing phase affect the rigidity and mass of the structure, it is very difficult to consider these situations in the analytical model. Therefore, elasticity modulus and mass density are frequently chosen as the parameters to be updated (design variables) while performing FEM updating.

The turbine tower consists of four segments, each approximately 20 meters high. In the analytical model, the finite elements corresponding to each segment are grouped and the elasticity modulus of each segment is chosen as a separate update parameter. In addition to these, the mass of the rotor and nacelle are also chosen as design parameters. The subject wind turbine is erected 2009 (14 years before). So, considering the possibility of reduced stiffness due to mini-cracks and material fatigue, the change of the elasticity modulus representing the stiffness is chosen in a wider range compared to the mass (Table 6.5).

Table 6.5 Parameters to be updated (design variables)

Parameter No	Parameter Name	Weighting Coefficient	Lower Bond	Upper Bond
1	0-20 m. elasticity modulus	1.0	-25%	25%
2	20-40 m. elasticity modulus	1.0	-25%	25%
3	40-60 m. elasticity modulus	1.0	-25%	25%
4	60-78 m. elasticity modulus	1.0	-25%	25%
5	Rotor mass	1.0	-10%	10%
6	Nacelle mass	1.0	-10%	10%

6.5 Sensitivity Analysis

In order to determine the response residuals are affected based on changes in design variables, the sensitivity matrix is calculated and presented Figure 6.6. In this graphic two horizontal axes are the responses (Table 6.4) and the parameters (Table 6.5) while the vertical axis represents sensitivity. Sensitivity matrix is also presented in table format to show all values in it (Table 6.6).

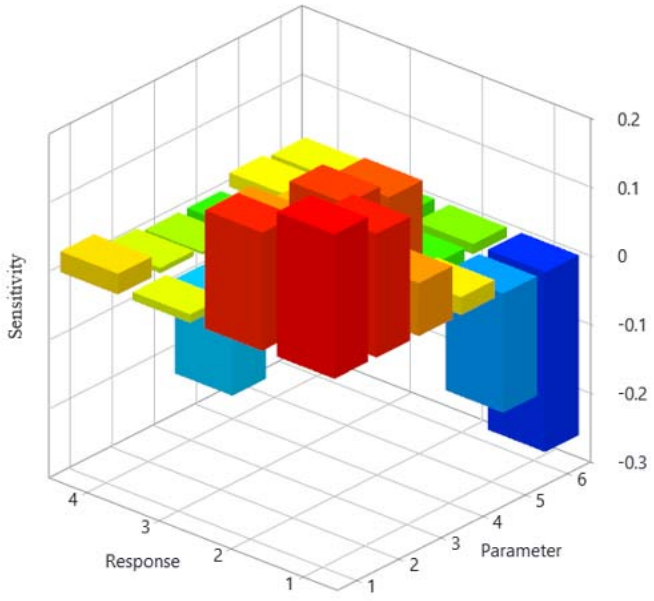


Figure 6.6 The sensitivity matrix

Table 6.6 The sensitivity matrix

Parameter / Response	1	2	3	4	5	6
1	0.210	0.180	0.077	0.026	-0.173	-0.262
2	0.172	0.037	0.152	0.130	-0.034	-0.015
3	-0.012	-0.137	0.079	0.045	0.001	-0.032
4	0.030	0.008	-0.004	-0.037	0.020	0.016

As can be seen from the sensitivity matrix, as the elasticity modules of each segment of tower increase, the structural mode frequencies increase, while the increase in rotor and masses decreases the mode frequencies. While the change in rotor and nacelle mass is highly effective on the 1st mode frequency (high sensitivity values), the 2nd mode frequency is less affected by the mass changes (low sensitivity values). The sensitivity of the MAC values to the update parameters generally remains at low levels, it can take negative and positive values with the effect of decreasing and increasing, respectively.

6.6 Model Updating

To obtain a more realistic analytic model of the wind turbine, model updating process with sensitivity-based method is performed in FEMtools (2017) software. The mode frequencies are defined as priority target responses (by assigning larger weighting values) while MAC values are secondary targets. The model update is completed as a result of two iterations. The parameters obtained after the model updating are presented in Table 6.7 in comparison with the initial values. Modes from analytical modal analysis with updated parameters are presented in comparison with the experimentally identified counterparts (Table 6.8).

Table 6.7 Initial and update parameter values

	Initial Value	Updated Value	Difference
0-20 m. elasticity modulus	200.000 MPa	202.049 MPa	1.02%
20-40 m. elasticity modulus	200.000 MPa	196.954 MPa	-1.52%
40-60 m. elasticity modulus	200.000 MPa	193.241 MPa	-3.38%
60-78 m. elasticity modulus	200.000 MPa	182.770 MPa	-8.62%
Rotor mass	55.0 ton	55.37 ton	0.67%
Nacelle mass	91.0 ton	87.76 ton	-3.56%

Table 6.8 Experimental and analytical mode pairs

	1st mode	2nd mode
Experimental Frequency (Hz)	0.356	2.985
Analytical Frequency (Hz)	0.356	2.985
(Before update)	(0.355)	(3.031)
Frequency Difference (Hz)	-0.01%	0.01%
(Before update)	(-0.30%)	(1.56%)
MAC value	99.2%	95.8%
(Before update)	(98.9%)	(94.6%)

As a result of sensitivity-based FEM updating, the structural frequencies of the first two modes are equalized to the mode frequencies of the real structure. The mode shapes, on the other hand, are a little closer to the experimentally estimated mode shapes. The model update has been stopped in the second iteration, as the parameter changes required for more convergence of the MAC values caused the analytical mode frequencies to move away from the experimental frequencies. It has been evaluated that the currently reached MAC values are sufficiently close to the mode shapes of the first two structural modes.

After the update, the modulus of elasticity of the first 20-meter segment of the turbine tower increased by 1%, while the elasticity modules of the second, third and fourth 20-meter segments of the tower decreased by 1.5%, 3.4%, and 8.6%, respectively. Rotor and nacelle masses of 55 tons and 91 tons, respectively, have been updated to 55.37 tons and 87.76 tons.

6.7 Multi-Hazard Analysis with Updated Model

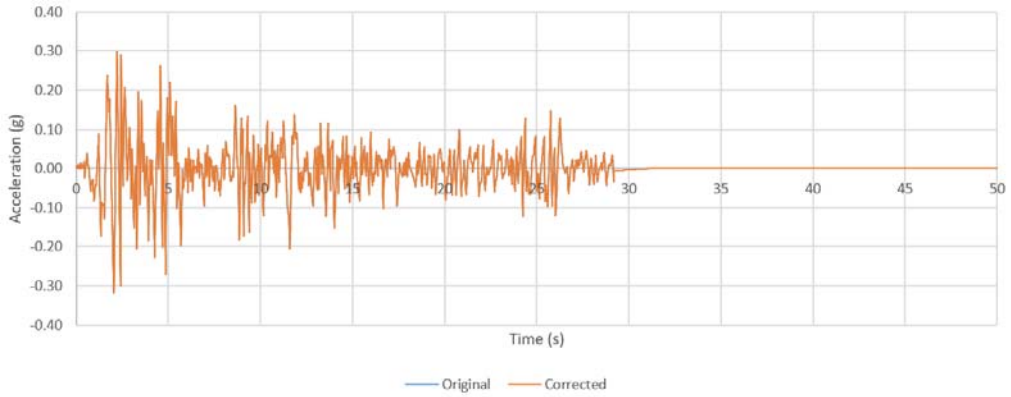
For wind turbines, the wind hazard is as important as the earthquake hazard. Therefore, multi-hazard approaches that combine wind and earthquake effects simultaneously should be used in analyzes to determine the structural behavior of wind turbines. In the following sections; a selected earthquake record is prepared for analysis, wind loads are calculated for the wind turbine tower and blades, and the results of the analyses performed in the time doming under the effect of wind and earthquake are interpreted.

6.7.1 Earthquake Record

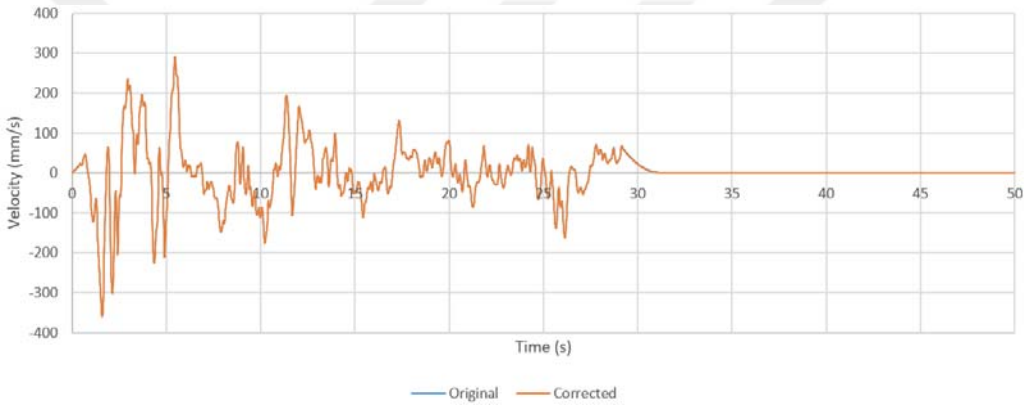
Acceleration record of the Imperial Valley earthquake (1940) is selected to analyze the structure. Some information about the earthquake is presented in Table 6.9. This record is 32 seconds long and extended up to 50 seconds by adding "zero" acceleration values to the end of the record in order to observe the free vibration behavior of the structure. When the original recording is reviewed, the acceleration value is zero at the 32^{nd} second, while the velocity and displacement values are 1.099 mm/sec and 3.115 mm, respectively. Therefore, baseline correction is made by preserving the frequency content on the record. With the help of this process, the acceleration, velocity, and displacement values in the 32^{nd} second are reduced to zero. In Figure 6.7, the records before and after the baseline correction process are presented.

Table 6.9 Imperial Valley earthquake (1940) features

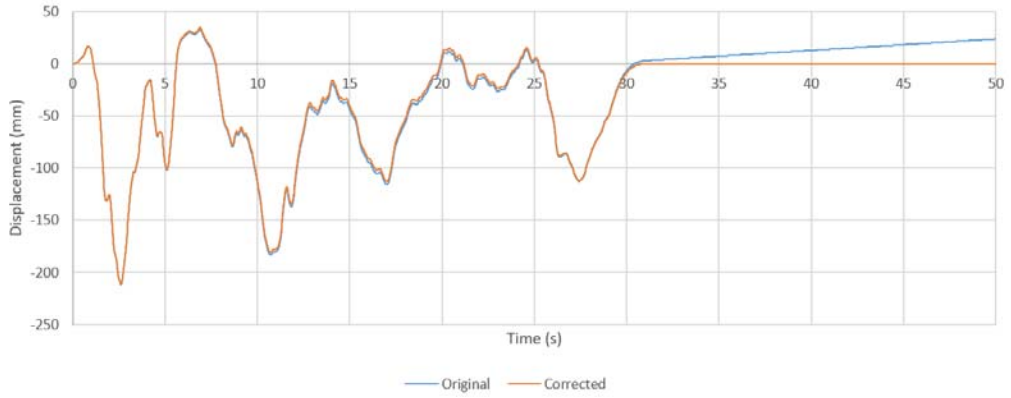
Magnitude	6.95 Mw
Significant duration ($DS_{5\text{-}95}$)	24.2 s
Arias intensity (I_A)	1.6 m/s
Mechanism	Strike slip
Joyner-Boore distance (R_{jb})	6.09 km
Shear wave velocity (Vs_{30})	213.44 m/s



(a)



(b)



(c)

Figure 6.7 Original and corrected data of Imperial Valley Earthquake. a) acceleration, b) velocity, and c) displacement.

6.7.2 Wind Loads

The wind loads acting on the turbine blades at certain wind speeds can be calculated using the Blade Element Momentum (BEM) Method (Dixon & Hall, 2013). This method originates from the combination of the momentum theory and the blade element theory. The BEM algorithm is used to determine the performance of a given rotor geometry under some known operating conditions and structural design of the wind turbines. In this method lift and drag forces created by the wind impinging on the rotor blade in motion can be calculated Figure 6.8.

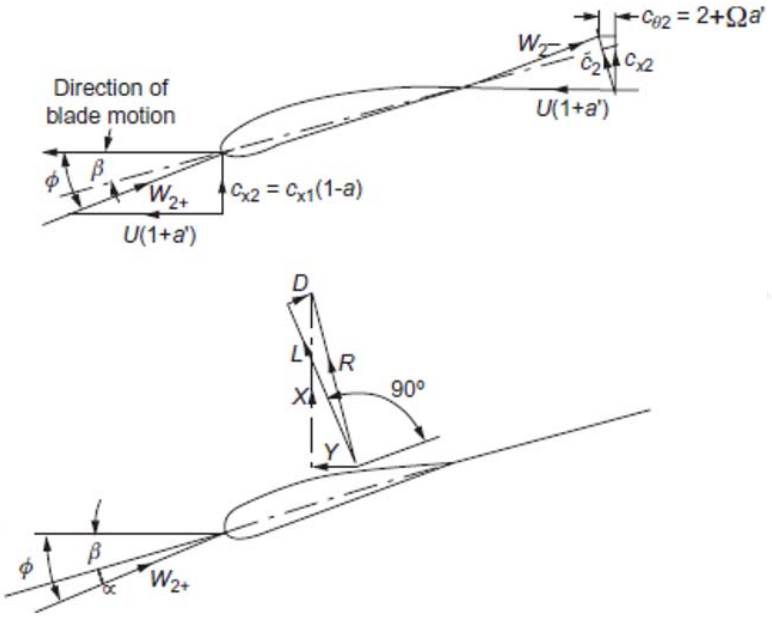


Figure 6.8 Lift and drag forces acting on moving rotor blade (Dixon & Hall, 2013)

where L is lift force, D is drag force, β is pitch angle, ϕ is attack angle, c_{x1} and c_{x2} are upstream and disc wind velocities respectively, *a* and *a'* axial and tangential induction factors respectively, Y and X force per unit blade length in the direction of motion and perpendicular to direction motion respectively. Wind turbine blade section properties vary along blade length. Blades of subject turbine are divided into 8 parts to calculate wind loads separately (Table 6.10).

According to BEM method, wind loads vary according to the wind speed, pitch angle of the blades and rotor rotation speed. At the subject wind turbine, there is a control system that regulates the pitch angles of the blades and rotor speed according to the wind speed in order to generate maximum energy and ensure turbine safety. Wind farm operating company provides a 12-month data file containing the wind speed, rotor rotation speed and pitch angles of the 3 rotor blades. This data file is examined in detail and the necessary parameters are determined precisely for each wind speed. As can be seen in Table 4.1, the cut-in wind speed of the subject wind turbine is 3 m/s while the cut-out wind speed is 25 m/s. Seven wind speeds is selected to calculate wind loads within this range: 3 m/s, 7 m/s, 11 m/s, 15 m/s, 19 m/s, 23 m/s and 25 m/s. In the light of this information, the wind forces acting on the rotor and rotor presented in Table 6.11

Table 6.10 Wind turbine blades properties

Part	Chord (m)	Length (m)	Distance from root (m)	Twist (^{o})	Twist (rad)
1	2.574	5.0	2.5	6.2	0.108210
2	2.934	5.0	7.5	8.8	0.153588
3	3.161	1.0	10.5	10.15	0.177150
4	2.785	9.0	15.5	6.8	0.118682
5	2.030	10.0	25.0	2.2	0.038397
6	1.403	10.0	35.0	0.35	0.006108
7	0.850	3.0	41.5	0.2	0.003490
8	0.289	0.8	43.4	3.2	0.055850

Table 6.11 Parameters corresponding to the selected wind speeds and wind loads acting on the rotor

Wind Speed (m/s)	Rotor Speed (RPM)	Pitch Angle (°)	Rotor Wind Load (kN)
3	9.6	0.0	25.8
7	12.5	0.0	38.7
12	16.0	0.0	110.8
15	16.0	12.3	98.3
19	16.0	18.7	82.2
23	16.0	24.2	60.2
25	16.0	28.0	15.2

As the pitch angle increases, the effective wind surface of the blades decreases. For this reason, despite the increase in wind speed, the total wind force on the rotor decreases after 15 m/s wind speed.

The selected wind speeds are at the turbine hub height of 80 m. However, for the calculation of the wind forces that will occur on the turbine tower, the wind profile along the tower height for each selected wind speed is created with the help of the following equation (Equation 6.1).

$$v_2 = v_1 \frac{\ln\left(\frac{h_2}{z_0}\right)}{\ln\left(\frac{h_1}{z_0}\right)} \tag{6.1}$$

where; v_1 is reference wind speed, h_1 is reference height, v_2 is wind speed at any height, h_2 corresponding height, z_0 roughness length. The roughness length is taking into account as 0.03 m, which corresponds to the land with natural hills away from construction Table 6.12. The wind profile calculated for 15 m/s wind speed at hub height is shown in Figure 6.9.

Table 6.12 Roughness lengths

Roughness length, z_0 (m)	Land cover types
0.0002	Water surfaces: seas and Lakes
0.0024	Open terrain with smooth surface, e.g., concrete, airport runways, mown grass etc.
0.03	Open agricultural land without fences and hedges; maybe some far apart buildings and very gentle hills
0.055	Agricultural land with a few buildings and 8 m high hedges separated by more than 1 km
0.1	Agricultural land with a few buildings and 8 m high hedges separated by approx. 500 m
0.2	Agricultural land with many trees, bushes and plants, or 8 m high hedges separated by approx. 250 m
0.4	Towns, villages, agricultural land with many or high hedges, forests, and very rough and uneven terrain
0.6	Large towns with high buildings
1.6	Large cities with high buildings and skyscrapers

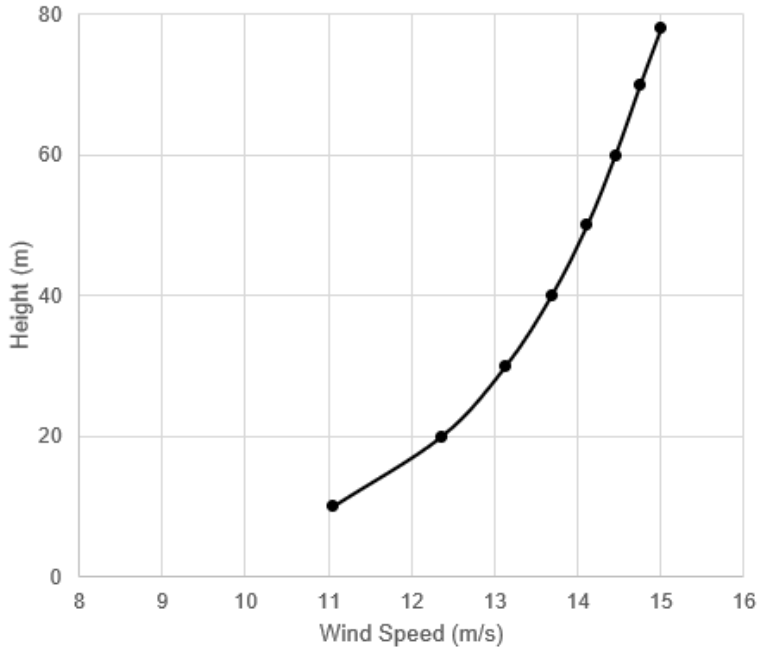


Figure 6.9 Wind profile for 15 m/s wind speed

In terms of modelling ease, the turbine tower is divided into three sections: 0-20 meter, 20-40 meter and 40-78 meter. Wind loads of these sections are calculated considering the average wind speed Figure 6.10.

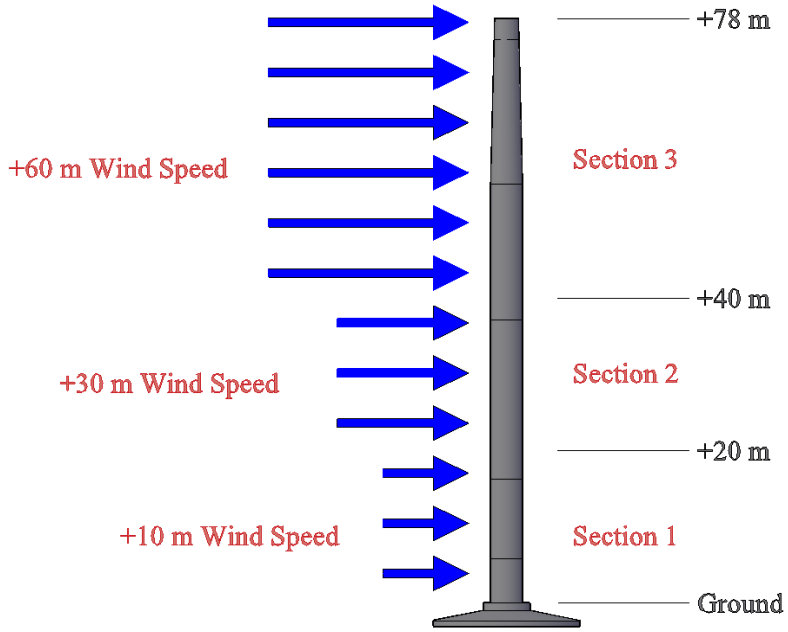


Figure 6.10 Defining wind load on analytical model

The wind force acting on circular cross-section structures such as a wind turbine tower consists of the sum of the pressure force perpendicular to the surface and the friction force parallel to the surface (Figure 6.11). The equation 6.2 presented below is used to calculate the total thrust, which is the sum of these pressure and friction forces.

$$F_D = 0.5\rho C_D U_r^2 A_r \tag{6.2}$$

where F_D is total thrust force, ρ is air density, C_D thrust coefficient of surface, U_r is wind speed and A_r is area exposed to the wind.

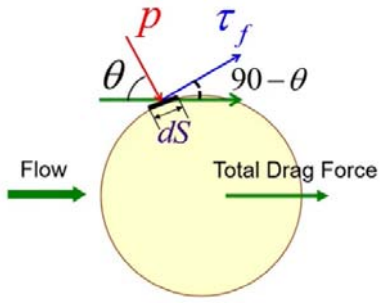


Figure 6.11 Wind loads acting on circular cross-section structures

C_D coefficients in wind load calculations are read from the chart in Figure 6.12 depending on the surface shape and Reynolds number.

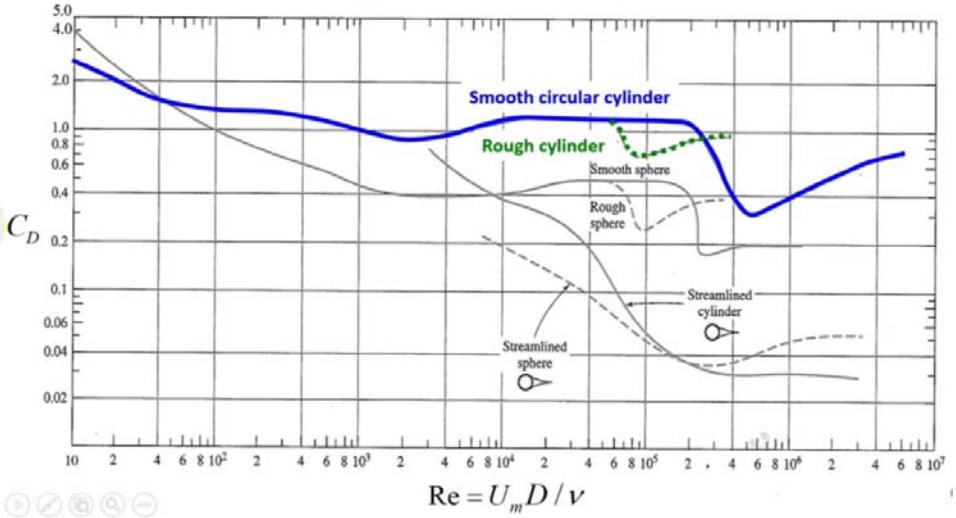


Figure 6.12 Thrust coefficient of surface (C_D)

Wind loads acting on turbine tower is presented in Table 6.13. After calculating the wind loads acting on the rotor and the tower separately, the wind loads acting on the entire turbine for the selected wind speeds are shown in Table 6.14.

Table 6.13 Wind loads acting on turbine tower

Hub Wind Speed (m/s)	Section	Wind Speed (m/s)	Air Density (kg/m^3)	Kinematic Viscosity (m^2/s)	Reynolds Number	Thrust Coefficient	Area (m^2)	Wind Load (kN)
3	3	2.89	1.2754	1.48E-05	7.8E+05	0.32	135.1	0.23
	2	2.63			7.1E+05	0.31	79.9	0.11
	1	2.21			6.0E+05	0.29	80.3	0.07
7	3	6.74			1.8E+06	0.48	135.1	1.88
	2	6.13			1.6E+06	0.45	79.9	0.86
	1	5.15			1.4E+06	0.42	80.3	0.57
12	3	11.56			3.2E+06	0.56	135.1	6.45
	2	10.51			2.9E+06	0.54	79.9	3.04
	1	8.84			2.4E+06	0.51	80.3	2.04
15	3	14.45			3.9E+06	0.62	135.1	11.15
	2	13.13			3.5E+06	0.59	79.9	5.19
	1	11.05			3.0E+06	0.57	80.3	3.56
19	3	18.31			5.0E+06	0.65	135.1	18.78
	2	16.64			4.5E+06	0.63	79.9	8.90
	1	13.99			3.8E+06	0.61	80.3	6.11
23	3	22.16			6.0E+06	0.70	135.1	29.62
	2	20.14			5.5E+06	0.67	79.9	13.86
	1	16.94			4.6E+06	0.64	80.3	9.41
25	3	24.09			6.5E+06	0.72	135.1	36.00
	2	21.89			5.9E+06	0.69	79.9	16.86
	1	18.41			5.0E+06	0.66	80.3	11.46

Table 6.14 Wind loads acting on wind turbine

Wind Speed (m/s)	Rotor Wind Load (kN)	Tower Wind Load (kN)	Total (kN)
3	25.8 (98%)	0.4 (2%)	26.2
7	38.7 (92%)	3.3 (8%)	42.0
12	110.8 (91%)	11.5 (9%)	122.3
15	98.3 (83%)	19.9 (17%)	118.2
19	82.2 (71%)	33.8 (29%)	116.0
23	60.2 (53%)	52.9 (47%)	113.1
25	15.2 (19%)	64.3 (81%)	79.5

At low wind speeds, almost all of the wind loads acting on the wind turbine are the loads acting on the rotor. As the wind speed increases, the loads acting on the tower become more and more important. It should be noted that the distance of the wind loads on the rotor to the tower base is greater than those of tower.

6.7.3 Multi-Hazard Analysis Results

When the climate regime is examined, it can be understood that the average annual wind speed of the region where the turbine is located is approximately 7 m/s. So, multi-hazard analyses with the Imperial Valley Earthquake (1940) record (Figure 6.7) and wind loads for 7 m/s and 12 m/s (maximum wind load on turbine) wind speed (Table 6.11 and 6.13) are performed. In order to see the wind effect clearly, another analysis is performed with only earthquake hazard. These analyses are carried out with the updated FE model considering the material and geometrical nonlinearity. Tower top displacement and maximum stress (at any point) on the tower history are presented in Figure 6.13 and Figure 6.14 respectively.

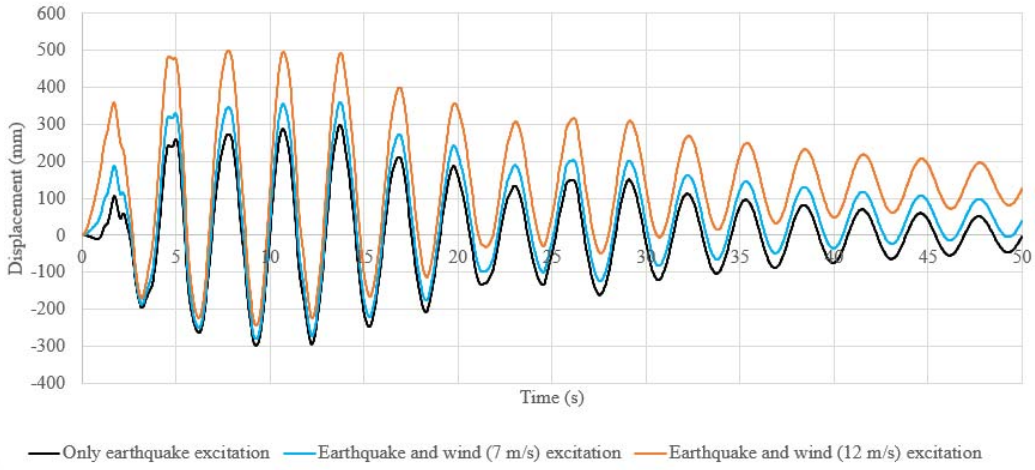


Figure 6.13 Tower top displacement histories

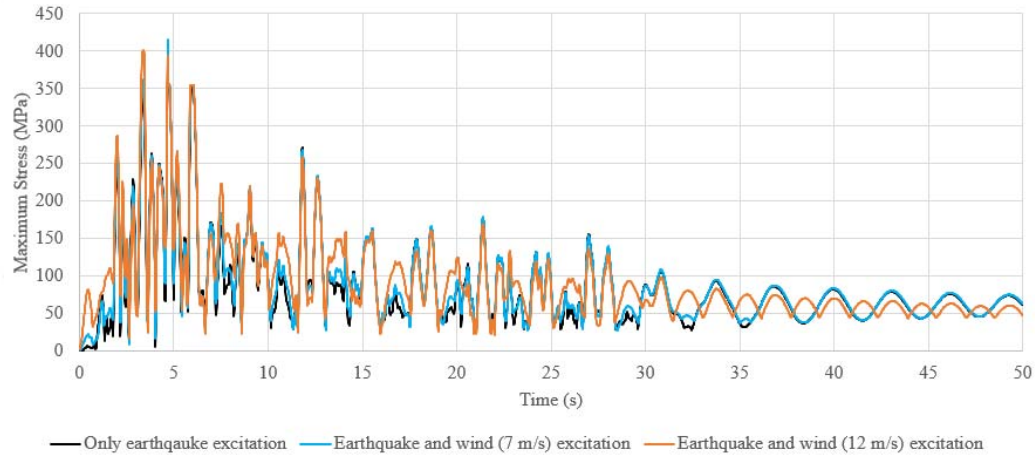


Figure 6.14 Maximum stress (at any point) on the tower histories

It can be seen from Figure 6.12; the wind effect shifted the oscillation of the turbine in the direction of the wind and increased the amplitudes of the oscillation. However, when focusing on the free vibration part (32-50s), it can be concluded that vibration period of the turbine remains the same as 3.1 seconds in the cases of with wind and without wind. In addition, the wind loads slightly increased the maximum stress on the wind turbine tower. Generally maximum stress values obtained in the case with 7 m/s wind speed. In free vibration part stresses in the 12 m/s case are lower than other two cases. In all cases, the yield stress of the material, 455 MPa, is exceeded for a small area around 5th second.

CHAPTER 7
THE EFFECT OF OPERATIONAL AND ENVIRONMENTAL CONDITIONS ON WIND TURBINE DYNAMIC CHARACTERISTICS

7.1 Introduction

In order to determine the effect of operational and environmental conditions on wind turbine characteristics, 600 seconds long 13277 data files were recorded from 7th July 2022 to 7th February 2023 and processed by the ACSI system presented in Chapter 5. These data files were acquired over a period of 7 months under various operational and environmental conditions. Figure 7.1 shows the wind speed histogram of the dataset.

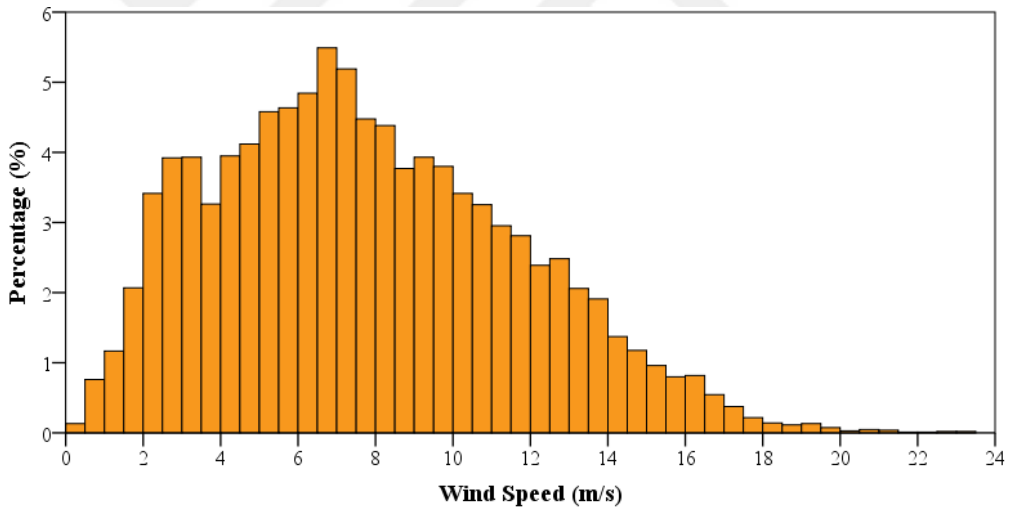


Figure 7.1 Wind speed histogram

The wind generally blew at speeds between 1 m/s and 15 m/s. The average wind speed of the dataset is 7.2 m/s and the maximum value 23.2 m/s which is lower than cut-out wind speed (Table 4.1). So, during the data recording period, there was no emergency shutdown due to excessive wind speed. The distribution of temperature is presented in Figure 7.2. Since the temperature values acquired by the own sensors of the data acquisition system at 0, 40 and 80 meters in the tower are in parallel with the

outside temperature recorded by the SCADA system, only outside temperature values are presented.

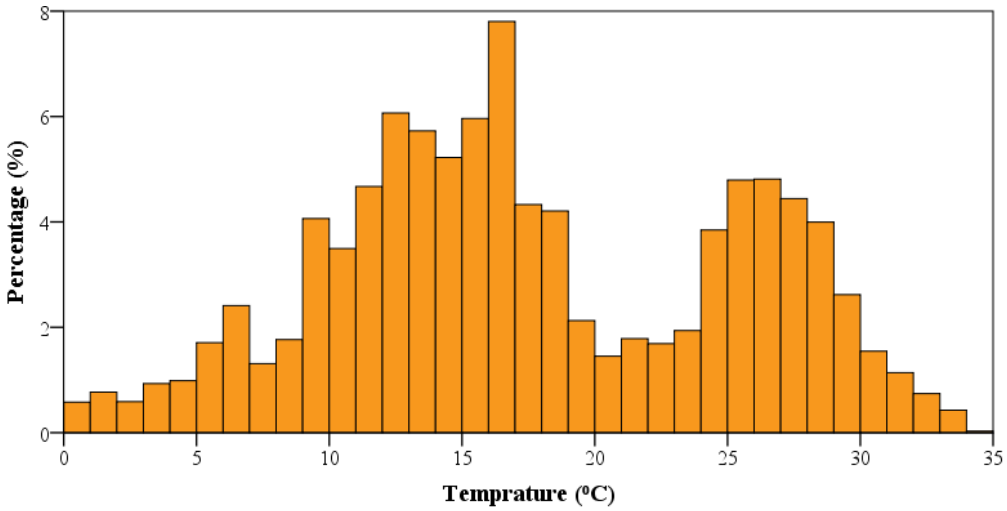


Figure 7.2 Temperature histogram

In 7 months period, the acceleration data were recorded under the temperature range of 0°C to 35°C. Temperature values are concentrated between 9-19°C and 24-30°C values. Figure 7.3 shows the humidity histogram. As the relative humidity values recorded at 0 and 80 meters inside the tower are similar as expected, only the relative humidity values at the 80 meters level are shown.

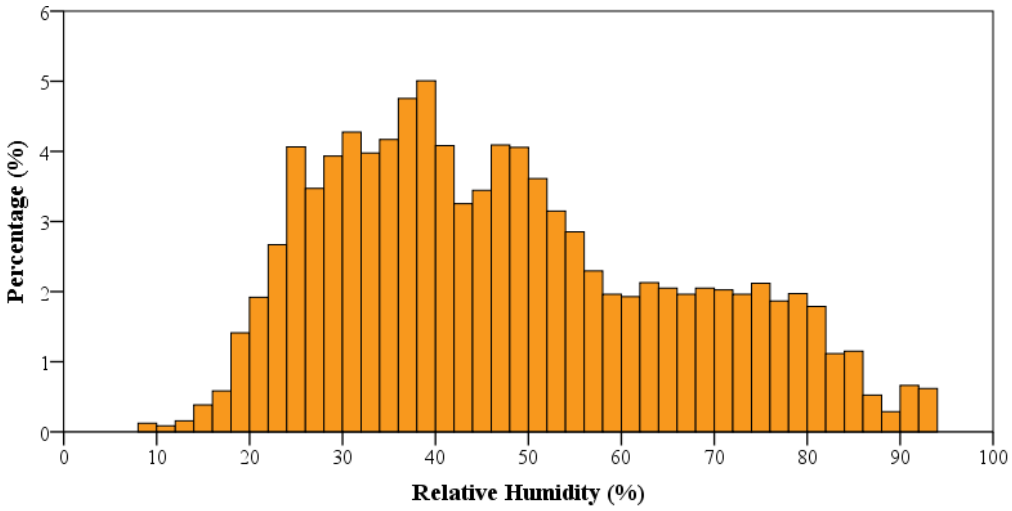


Figure 7.3 Relative humidity histogram

Due to the climate of the region, the records were generally recorded in a humid environment. Relative humidity values are concentrated between 18-82%. The distribution of wind direction and nacelle direction are presented in Figure 7.4 and Figure 7.5 respectively.

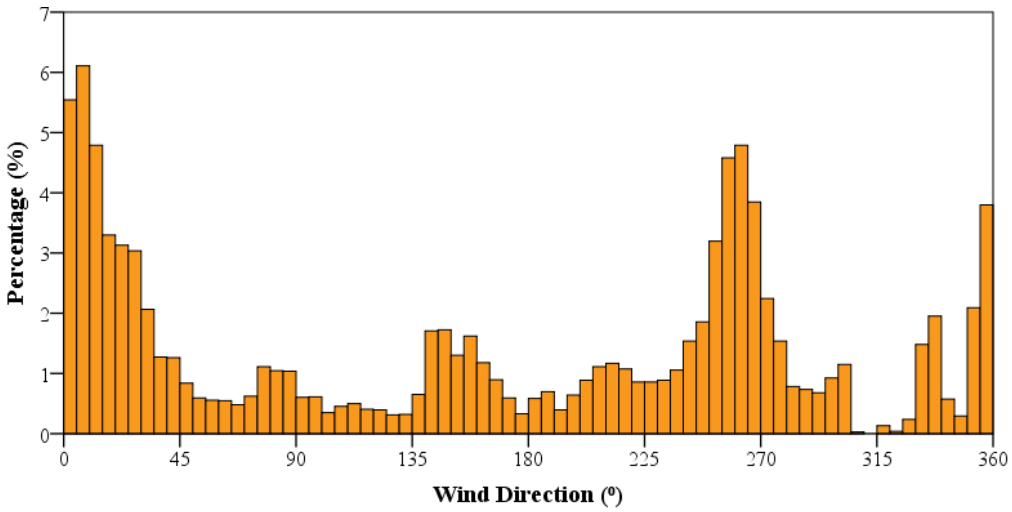


Figure 7.4 Wind direction histogram

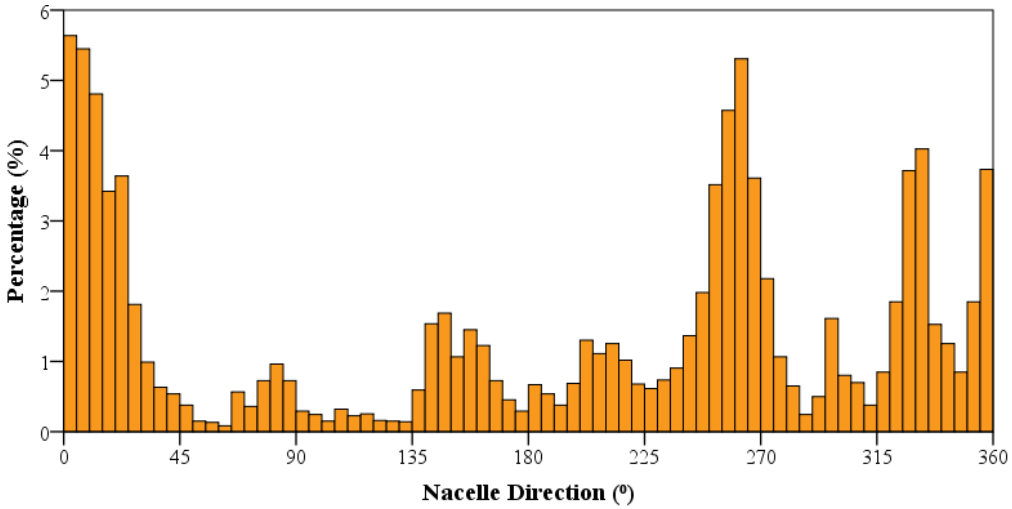


Figure 7.5 Nacelle direction histogram

In Figure 7.4 and 7.5, 0° represent the exact north direction and the values increase clock-wise. As expected, the percentage of data recorded in the Main Wind Direction (MWD) (detailed information is presented in Chapter 4) is higher than in other directions. In order to produce energy, the nacelle is rotated in the direction of the wind

by the wind turbine's control system. So, wind direction and the nacelle direction generally at the same orientation. Yet, some differences are observed in the two graphs above, as the wind direction must remain constant for a while for the nacelle to rotate. The distribution of the rotor speed values is presented in Figure 7.6.

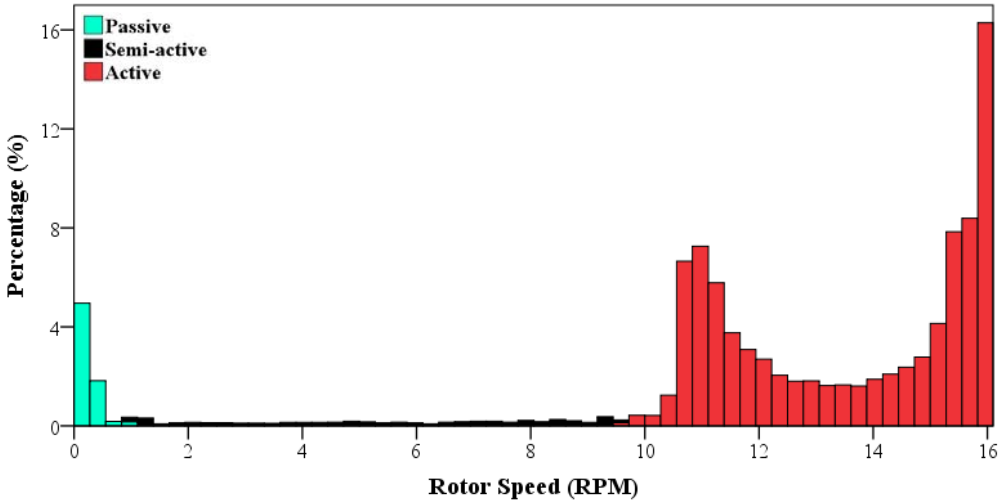


Figure 7.6 Rotor speed histogram

The cut-in wind speed of the wind turbine is 3 m/s (Table 4.1). In the 0 to 3 m/s wind speed range, the turbine does not produce any energy. It is called passive condition in the scope of the thesis. In passive condition, the rotor brakes are engaged, and the rotor speed is 0 RPM. Yet sometimes the brakes are not engaged, and the turbine blades rotate softly (0 to 1 RPM). After the wind blows faster than 3 m/s for a while, the turbine starts to produce energy (active condition). The subject wind turbine operates between 9.6 to 16 RPM (Table 4.1). The cases where the turbine condition changes from active to passive or passive to active states are called semi-active cases. Note that all the data stored as 600 seconds long datafiles and the operational and environmental condition values are presented by averaging 600 seconds of data. In semi-active cases rotor speed appears in the range of 1 to 9.6 RPM. In summary, all cases are divided into 3 groups according to rotor speed:

- Passive: 0 to 1 RPM
- Semi-active: 1 to 9.6 RPM
- Active: 9.6 to 16 RPM.

The rated wind speed of the turbine is 12 m/s. In the 3-12 m/s wind speed range, rotor speed increases as wind speed increases. After the rated wind speed, rotor speed should remain constant as 16 RPM (maximum energy production). To ensure that, pitch angle of the rotor blades is increased by the turbine control system. At a pitch angle of 0°, the wind hits the entire blade chord. As the pitch angle increases, the effective wind surface of the blades decreases. In passive cases, pitch angle is set to 0°, 70-72°, and 85-90° randomly (Figure 7.7).

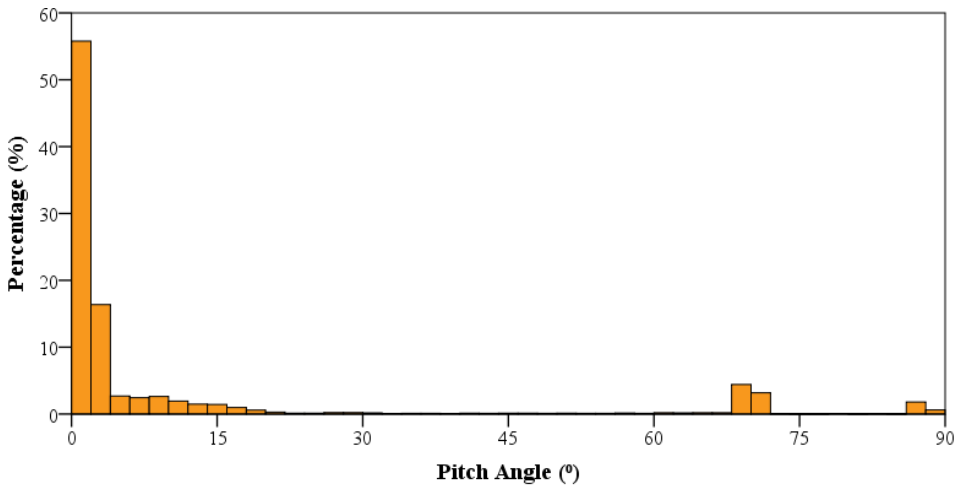


Figure 7.7 Pitch angle histogram

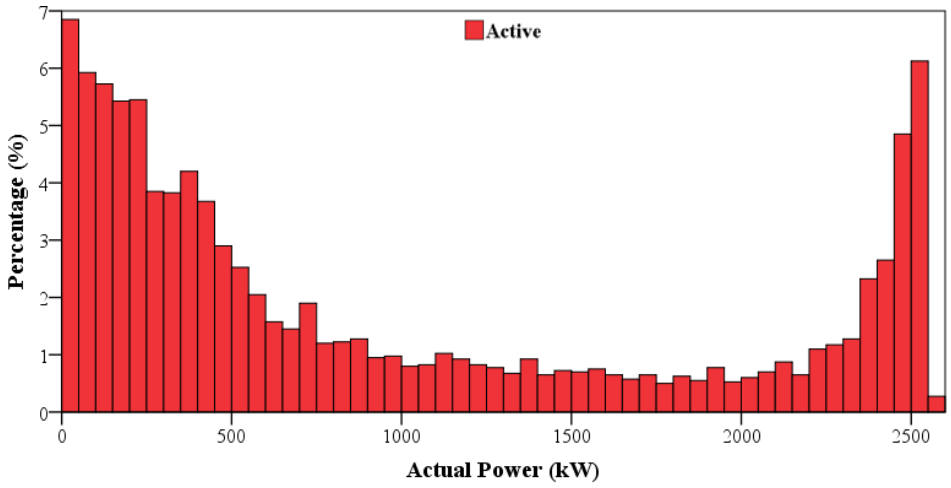


Figure 7.8 Actual power histogram

The distribution of actual power generated by turbine is presented in Figure 7.8 for Active cases. Although the rated power is stated as 2.5 MW in the turbine's datasheet, actual power can reach 2560 kW.

7.2 Relationship Between Operational and Environmental Conditions

In the scope of the thesis eight operational and environmental variables are recorded to investigate their effect on the wind turbine on the dynamic characteristic. To correctly interpret these effects, the relationship between operational and environmental conditions should be known first. The relationship between wind speed-rotor speed, wind speed-actual power, wind speed-pitch angle, rotor speed-pitch angle, and rotor speed-actual power are presented in Figure 7.9- Figure 7.13 respectively.

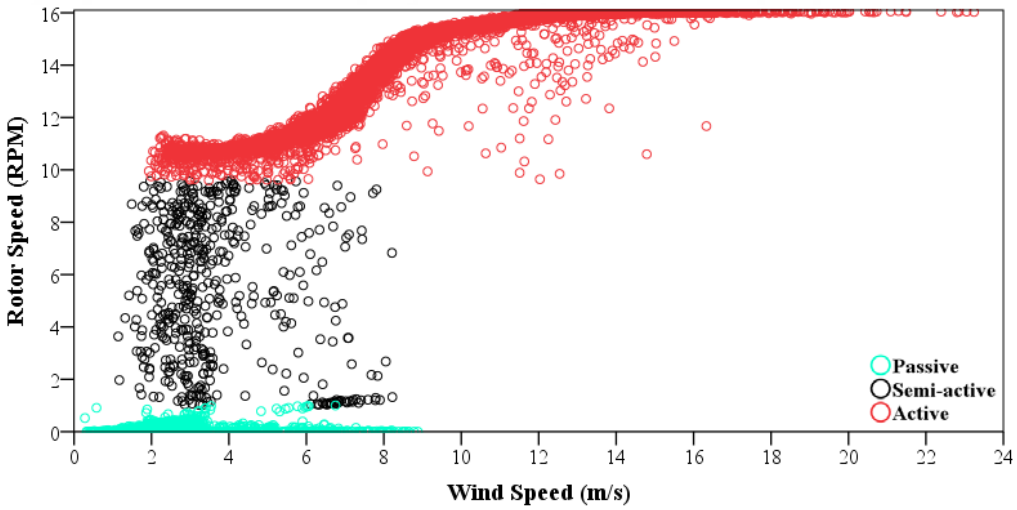


Figure 7.9 The relationship between wind speed and rotor speed

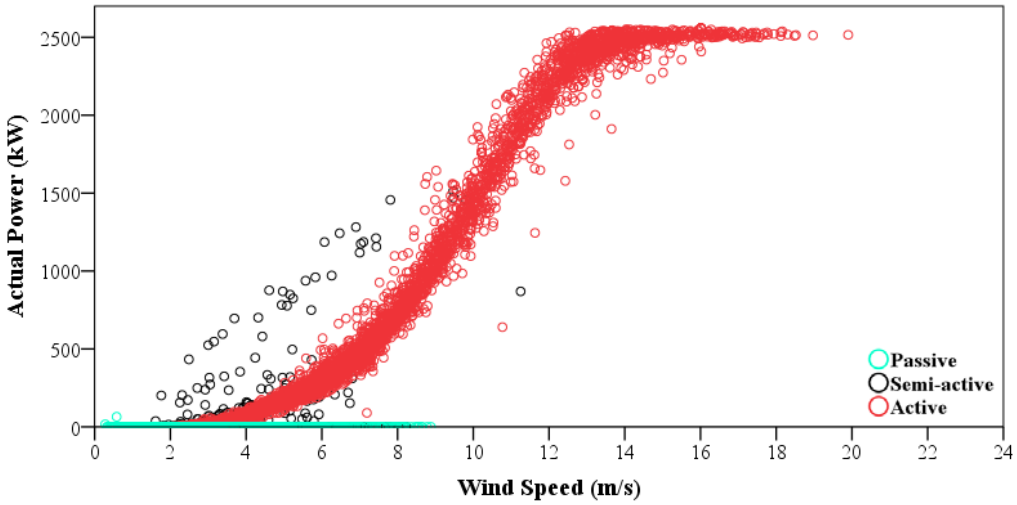


Figure 7.10 The relationship between wind speed and actual power

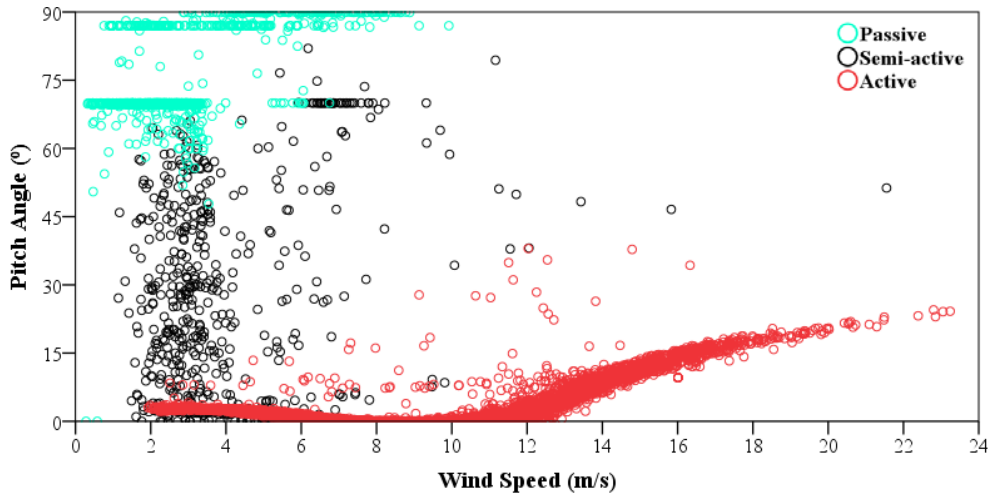


Figure 7.11 The relationship between wind speed and pitch angle

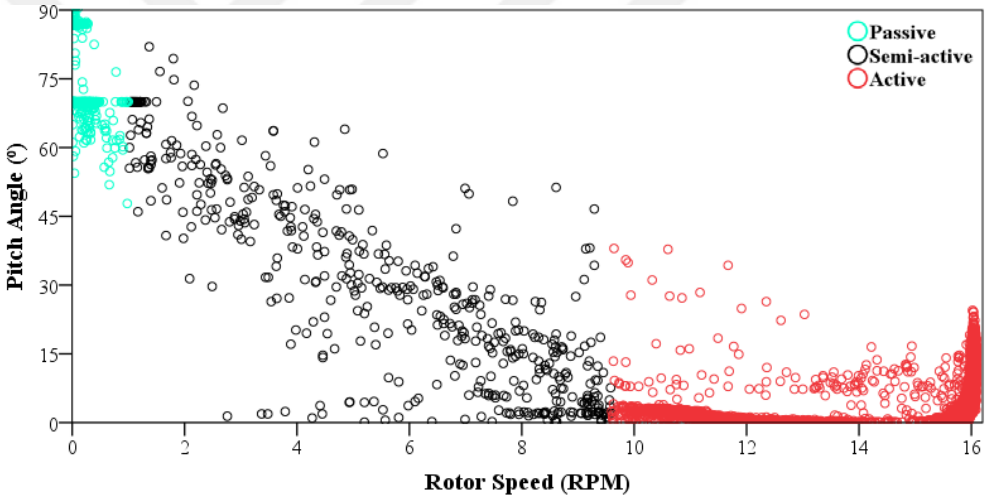


Figure 7.12 The relationship between rotor speed and pitch angle

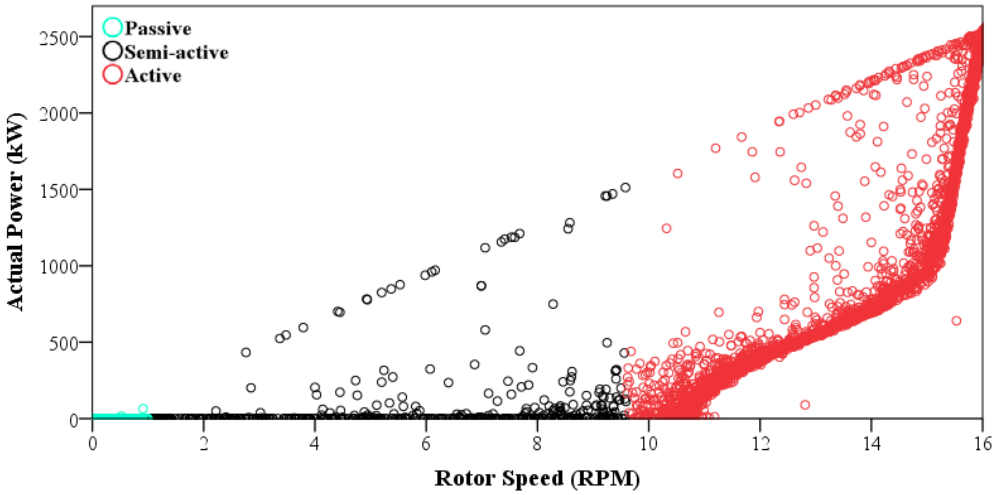


Figure 7.13 The relationship between rotor speed and actual power

It can be seen that from Table 4.1, the cut-in, rated, and cut-out speed of the wind turbine are 3 m/s, 12 m/s, and 25 m/s respectively. The operating principle of the wind turbine can be explained in 4 regions according to wind speed:

- *0-3 m/s wind speed range:* Turbine does not operate and produce power. So, the rotor speed is 0 RPM, and the actual power is 0 kW. The pitch angle of the blades does not matter and can be at different values.

- *3-12 m/s wind speed range:* The rotor speed and the actual power accordingly increase with the increase in wind speed. Pitch angle remains constant at 0 and the wind hits the blade chord upright.

- *12-25 m/s wind speed range:* Rotor speed is 16 RPM (rated rotor speed) in this region. With the increase in the wind speed, the pitch angle increases so that the rotor speed remains constant. The wind turbine produces 2.5 MW of actual power.

- *25 m/s wind speed and more:* Wind turbine is stopped by the turbine control system in order to prevent structural damage under excessive wind effects. Pitch angle is set as 90º to minimize wind loads on the rotor.

Note that, to change the active/passive condition of the turbine, the wind speed must be above/below a cut-in wind speed for a while. Some exceptional points in the graphics were formed due to the intervention of the control system of the turbine or due to maintenance.

Figure 7.14 shows the relationship between temperature and relative humidity.

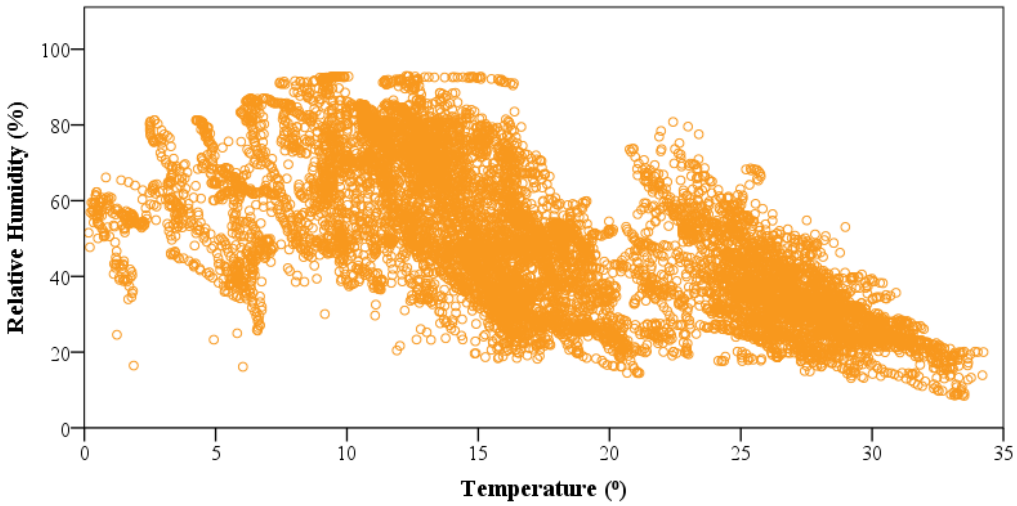


Figure 7.14 The relationship between temperature and relative humidity

Low humidity values are recorded at high temperatures and the scattering of humidity values is high at temperatures below 25 ºC.

Figure 7.15 shows correlation of the wind and nacelle directions.

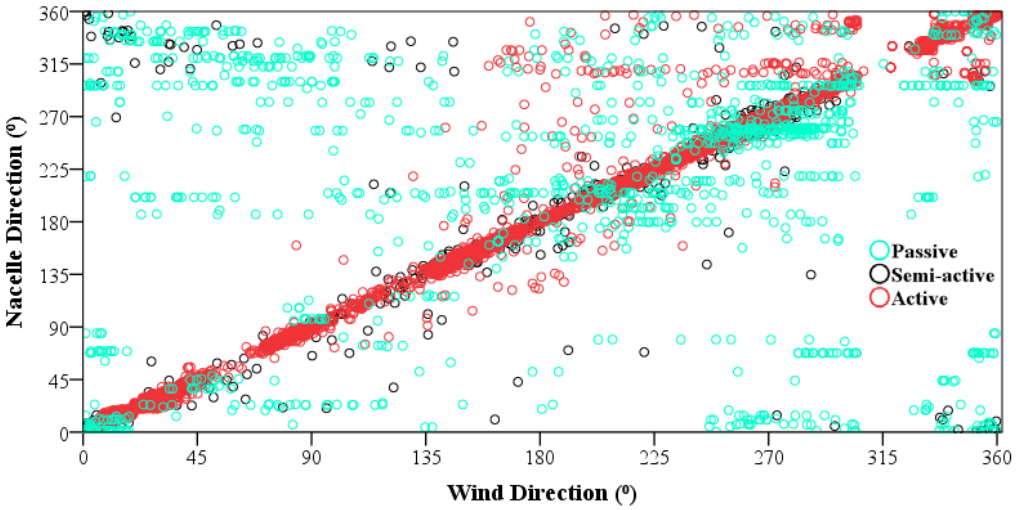


Figure 7.15 The relationship between wind direction and nacelle direction

For energy production efficiency, nacelle is rotated to the wind direction by control system of the turbine. So, there is a linear correlation between wind direction and the nacelle direction when the turbine is active. Since the wind must blow in a certain direction for a while to rotate the nacelle, this relationship is sometimes the wind and

nacelle direction were recorded at different angles. In passive and semi-active cases, the nacelle is randomly positioned.

7.3 The Effect of Operational and Environmental Conditions on Mode Frequency

Vibration mode frequencies are the most reliable modal parameters. Yet, wind turbine's mode frequencies can be influenced by operational and environmental conditions. In this section, the relationship between the estimated first four mode's frequencies and operational/environmental factors is examined. Figure 7.16 – Figure 7.23 show the effect of operational and environmental conditions on mode frequency estimated around 0.35 Hz. In graphs where a trend can be observed, a straight line representing this trend is placed.

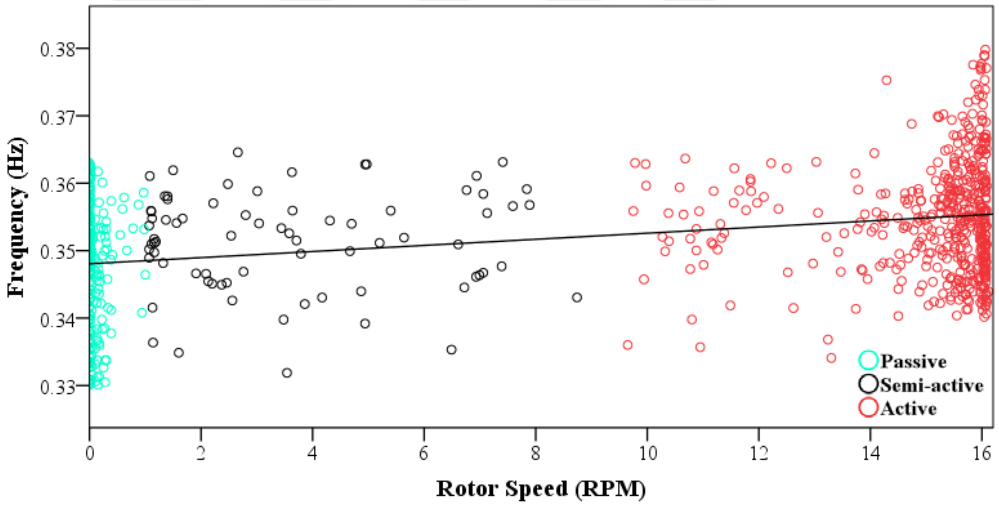


Figure 7.16 Rotor speed vs frequency (estimated around 0.35 Hz)

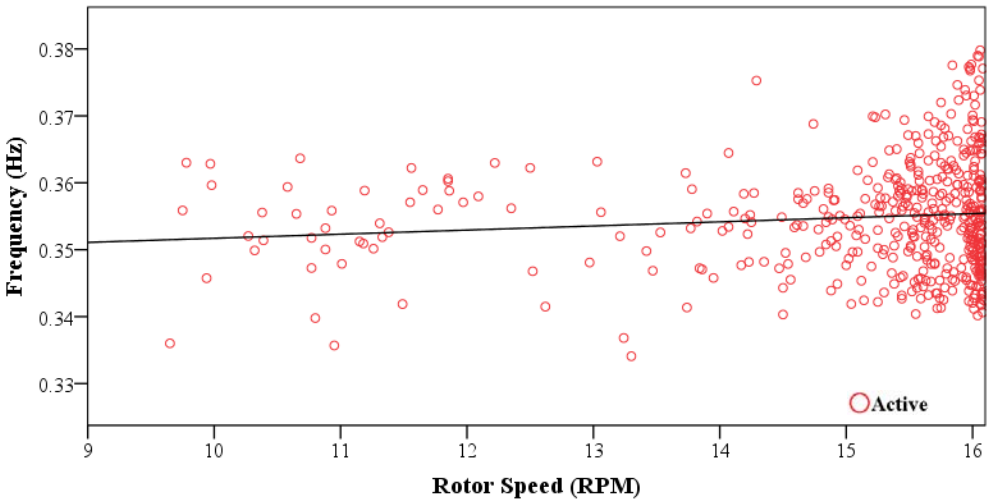


Figure 7.17 Rotor speed vs frequency (estimated around 0.35 Hz) for only active cases only

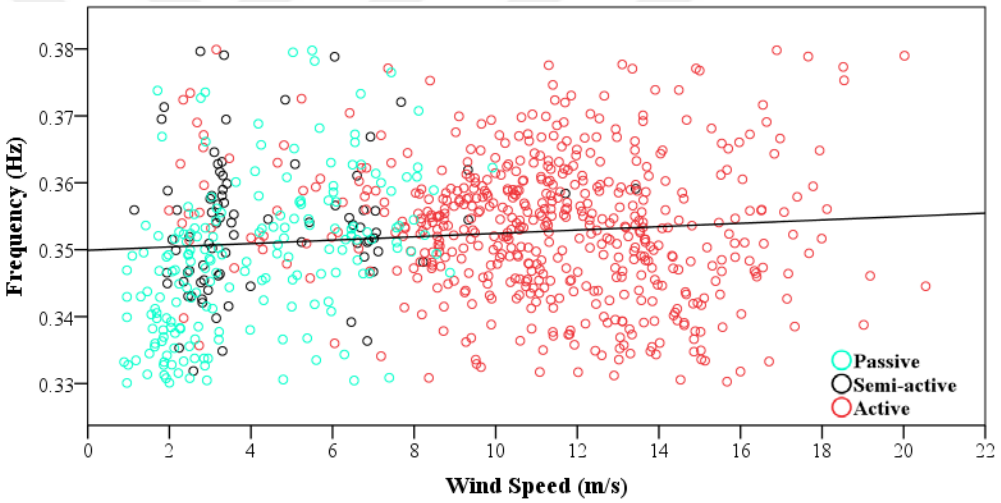


Figure 7.18 Wind speed vs frequency (estimated around 0.35 Hz)

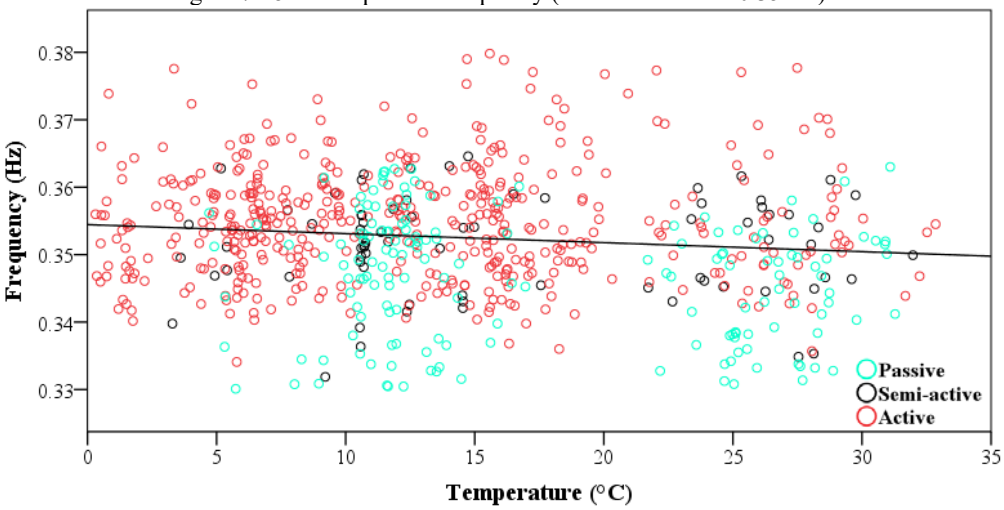


Figure 7.19 Temperature vs frequency (estimated around 0.35 Hz)

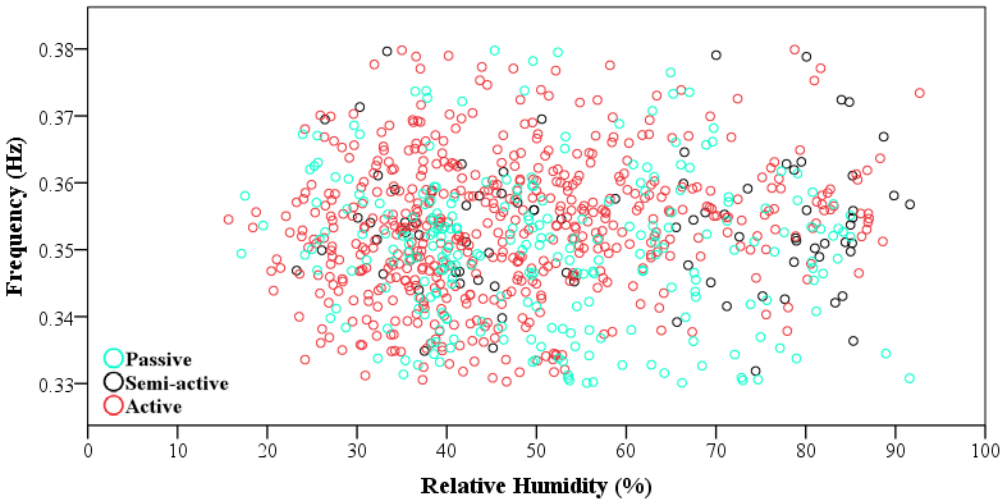


Figure 7.20 Relative humidity vs frequency (estimated around 0.35 Hz)

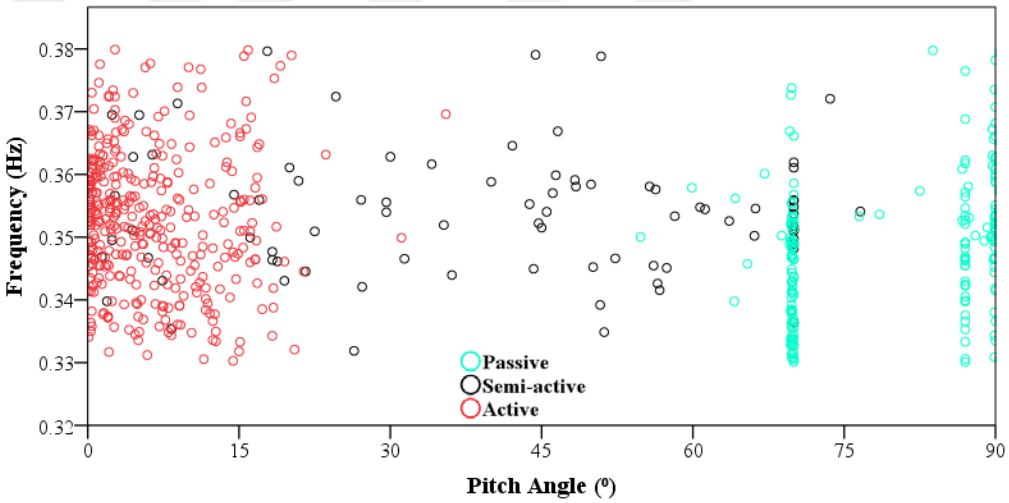


Figure 7.21 Pitch angle vs frequency (estimated around 0.35 Hz)

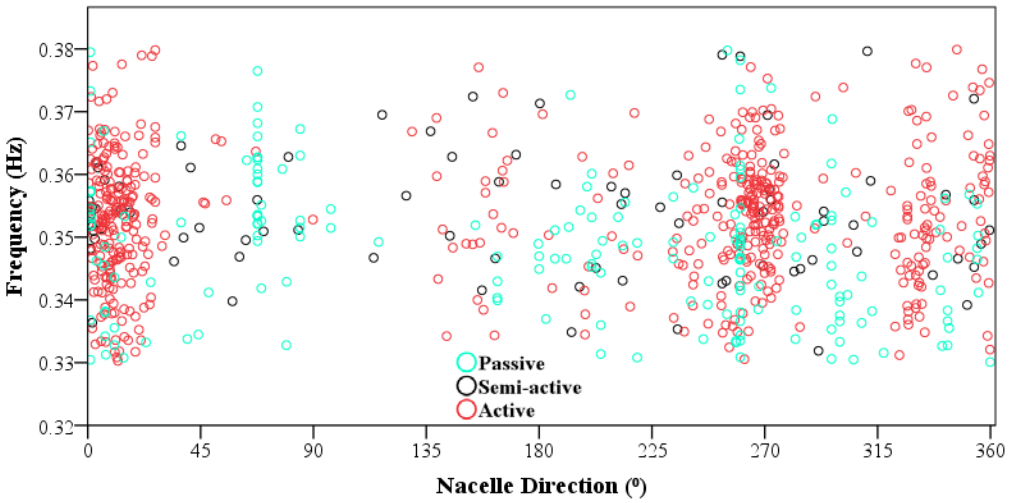


Figure 7.22 Nacelle direction vs frequency (estimated around 0.35 Hz)

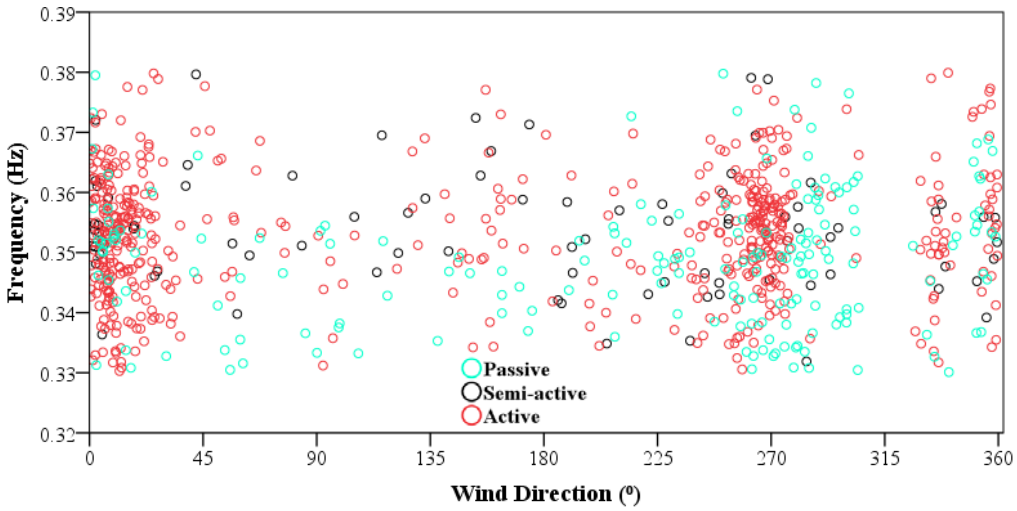


Figure 7.23 Wind direction vs frequency (estimated around 0.35 Hz)

It can be seen from figures, estimated frequency around 0.35 Hz is not affected by relative humidity, pitch angle, nacelle direction, and wind direction. It is observed that the frequency values increase with the increase in rotor speed or wind speed for all cases. Yet, it should not be forgotten that in 3-12 m/s wind speed range (cut-in and rated wind speed) there is a positive correlation between wind speed and rotor speed. It is seen that the frequencies estimated around 0.35 Hz decrease with the increase in ambient temperature.

Figure 7.24 – Figure 7.31 show the effect of operational and environmental conditions on mode frequency estimated around 3.00 Hz. In graphs where a trend can be observed, a straight line representing this trend is placed.

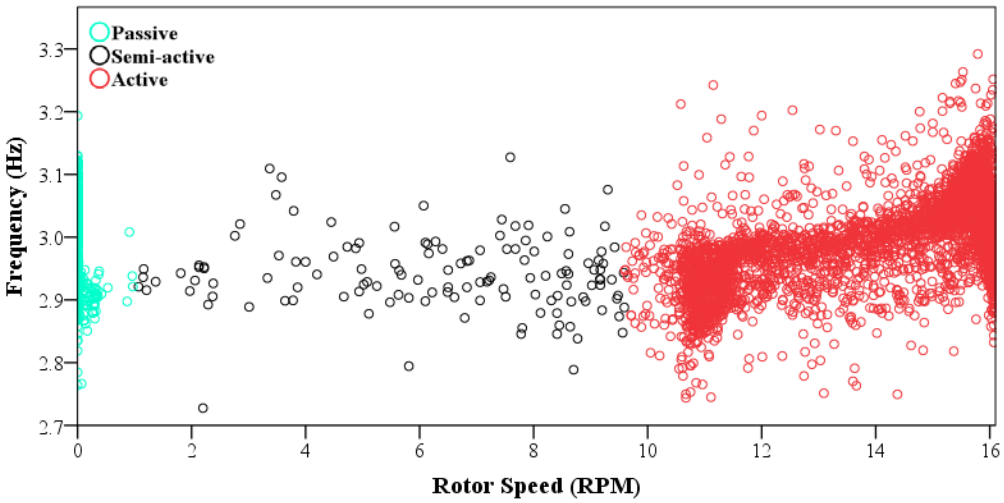


Figure 7.24 Rotor speed vs frequency (estimated around 3.00 Hz)

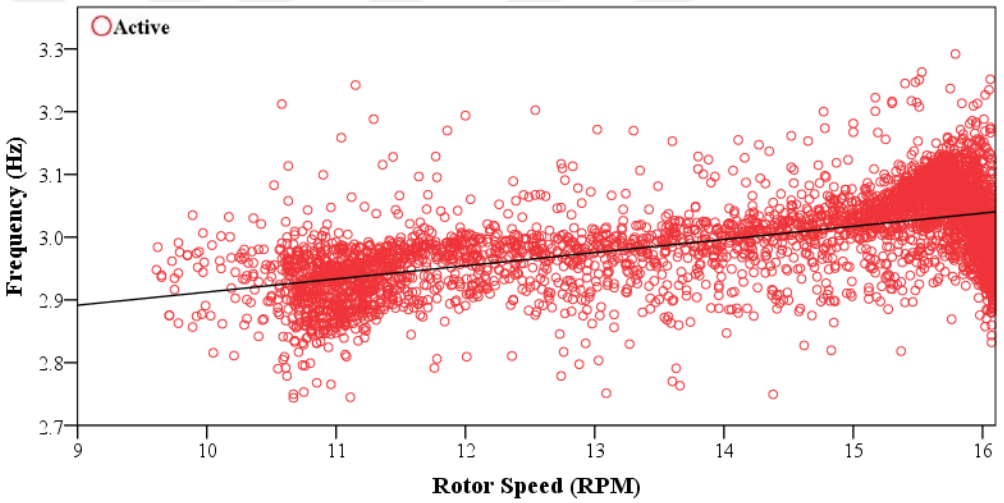


Figure 7.25 Rotor speed vs frequency (estimated around 3.00 Hz) for active cases only

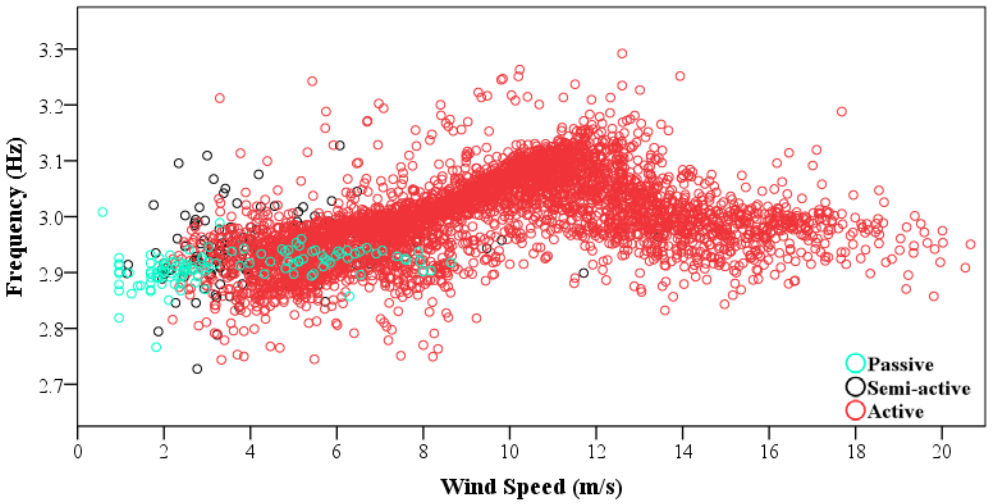


Figure 7.26 Wind speed vs frequency (estimated around 3.00 Hz)

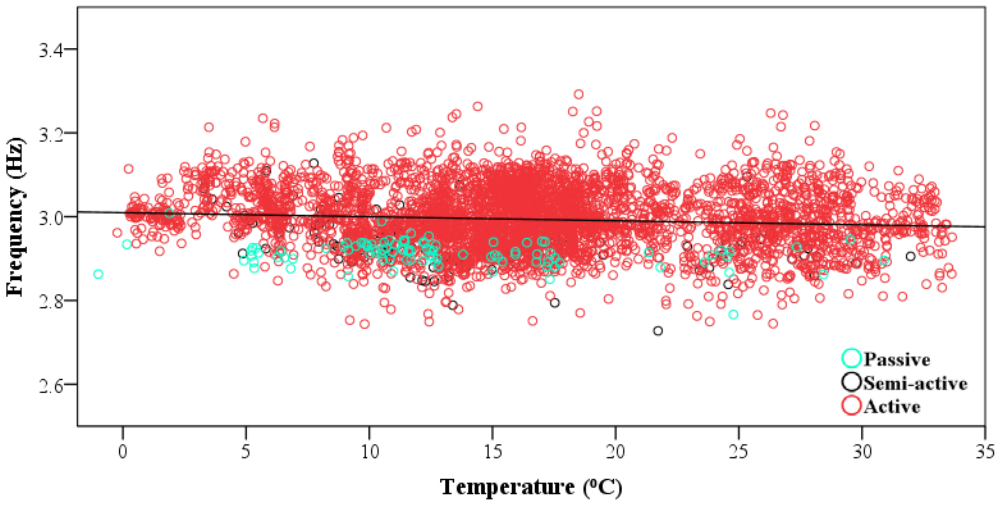


Figure 7.27 Temperature vs frequency (estimated around 3.00 Hz)

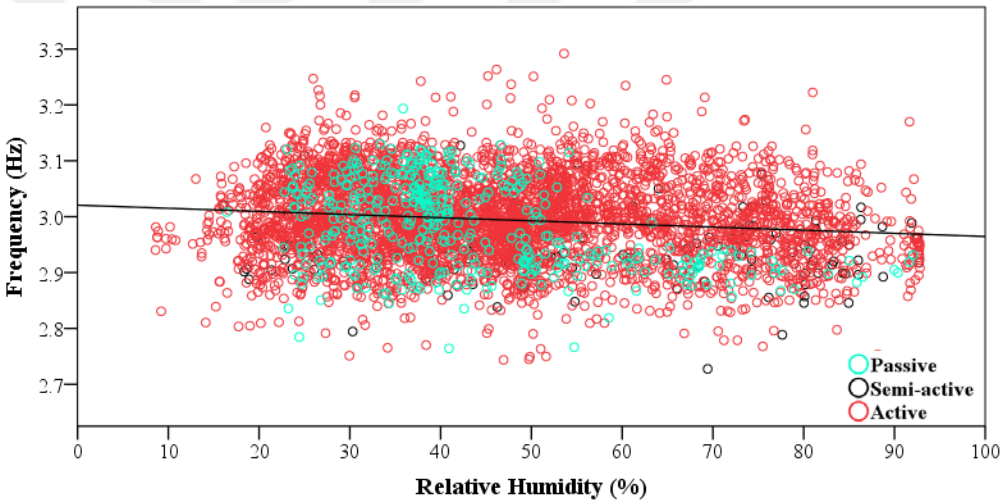


Figure 7.28 Relative humidity vs frequency (estimated around 3.00 Hz)

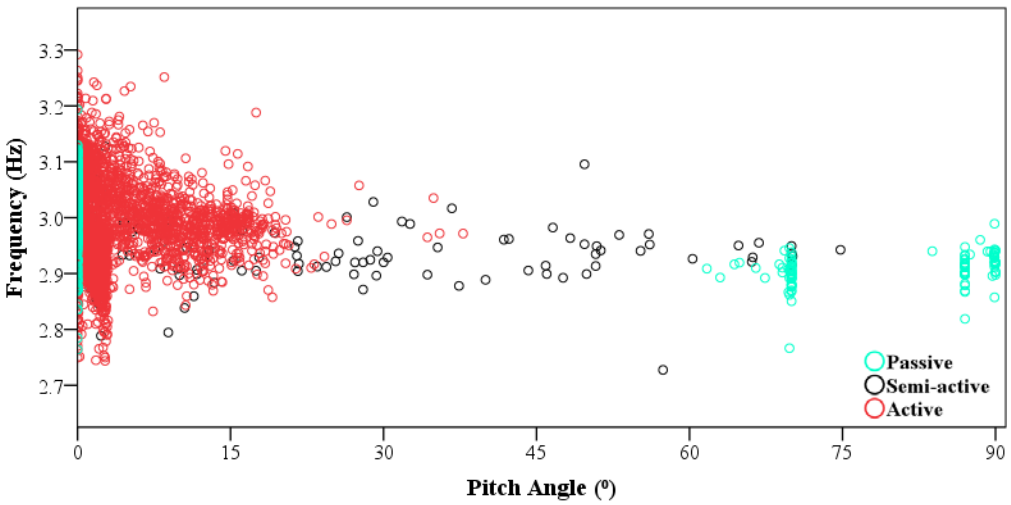


Figure 7.29 Pitch angle vs frequency (estimated around 3.00 Hz)

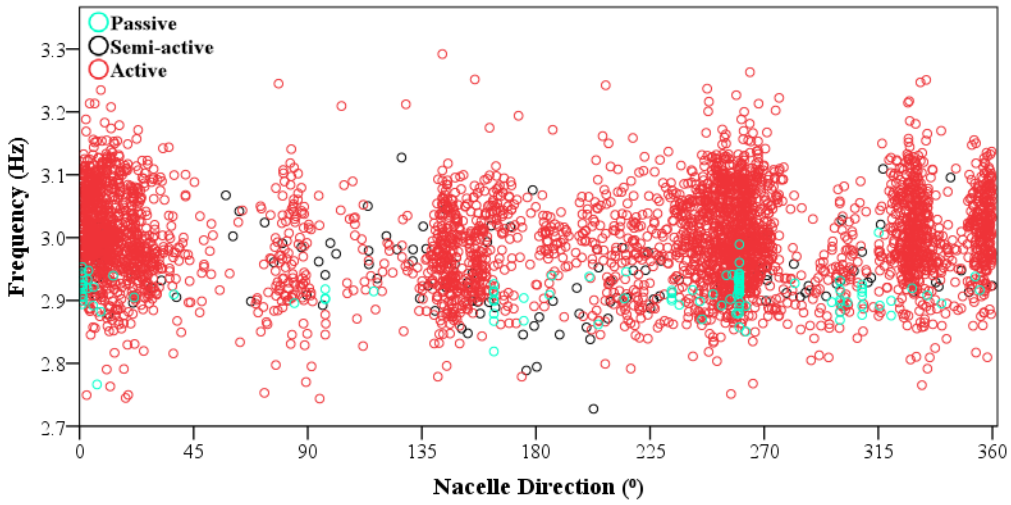


Figure 7.30 Nacelle direction vs frequency (estimated around 3.00 Hz)

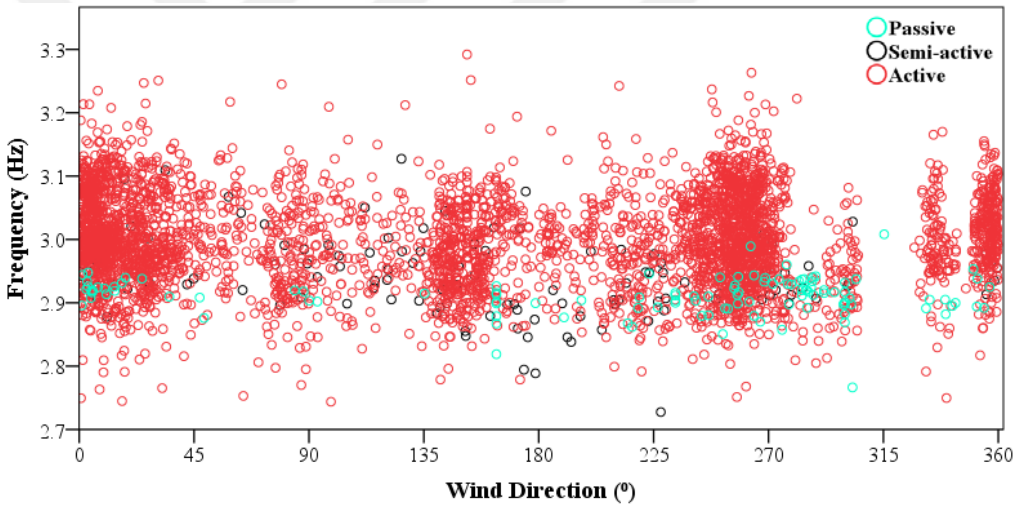


Figure 7.31 Wind direction vs frequency (estimated around 3.00 Hz)

For active cases, the estimated frequencies around 3.00 Hz increase as the rotor speed increases while frequency estimations are immune to change in rotor speed for passive and semi-active cases. From Figure 7.26, there is a positive correlation between wind speed and frequency estimates up to the rated wind speed of the turbine (12 m/s). Yet, a decrease in frequencies is observed after rated wind speed. It is seen that from Figure 7.11, the pitch angle of the blades is increased by the turbine control system to keep the rotor speed at a constant 16 RPM after the rated wind speed. With the increase in the pitch angle, wind loads acting on the rotor get considerably lower (Table 6.11). The decrease in the thrust force on the wind turbine caused the frequency estimates to decrease (Figure 7.26 and Figure 7.29). It can be concluded that mode

frequency slightly increases as the turbine oscillates in a shifted manner under high wind loads (Figure 6.12). Frequency scattering considerably decreases after 5º pitch angle. The standard deviation of frequencies are 0.077 and 0.050 for 0º-5º and 5º-30º pitch angle range respectively. Figure 7.27 and Figure 7.28 show that frequencies estimated around 3.00 Hz decrease with increasing ambient temperature and humidity. There is no correlation between frequencies around 3.00 Hz and wind/nacelle direction.

Figure 7.32 – Figure 7.39 the effect of show operational and environmental conditions on mode frequency estimated around 8.29 Hz.

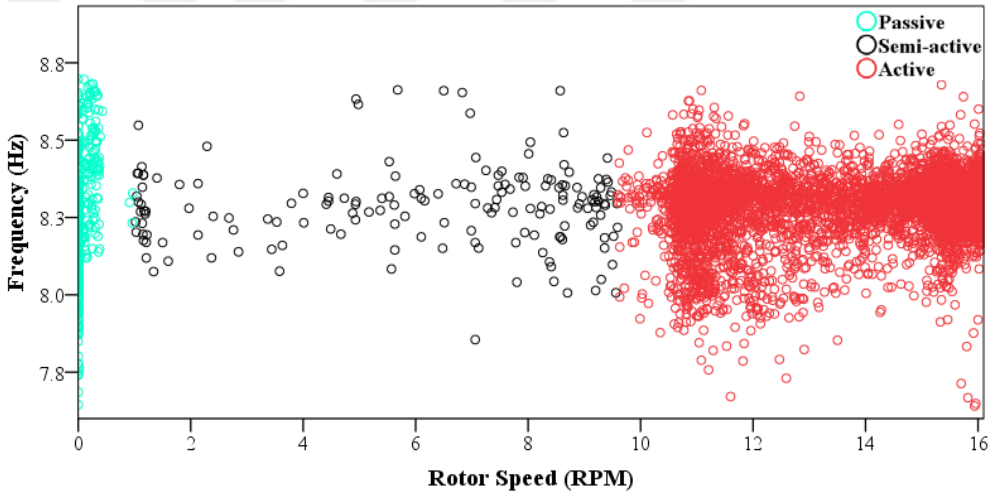


Figure 7.32 Rotor speed vs frequency (estimated around 8.29 Hz)

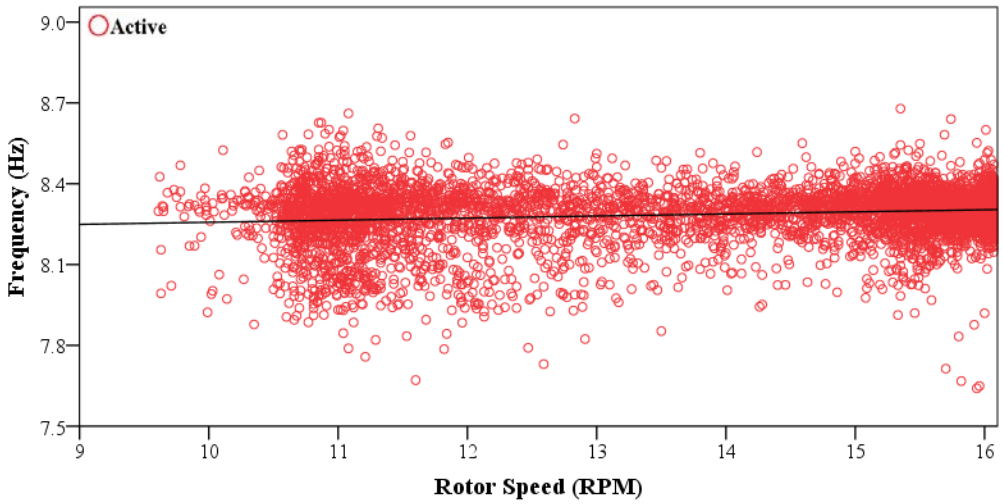


Figure 7.33 Rotor speed vs frequency (estimated around 8.29 Hz) for active cases only

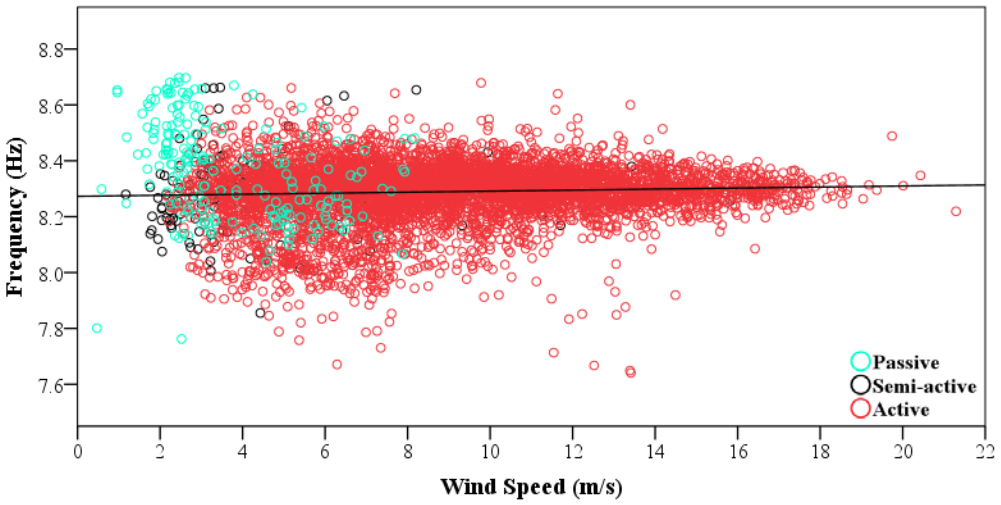


Figure 7.34 Wind speed vs frequency (estimated around 8.29 Hz)

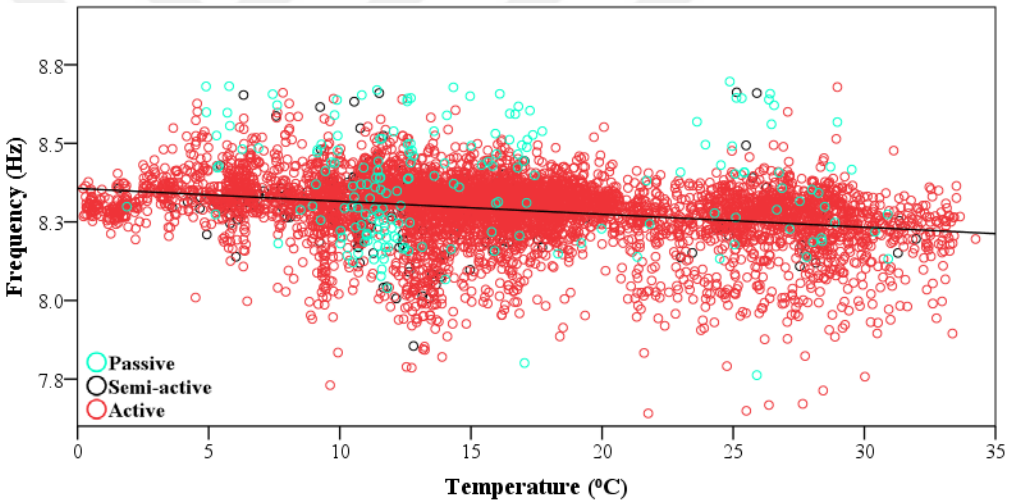


Figure 7.35 Temperature vs frequency (estimated around 8.29 Hz)

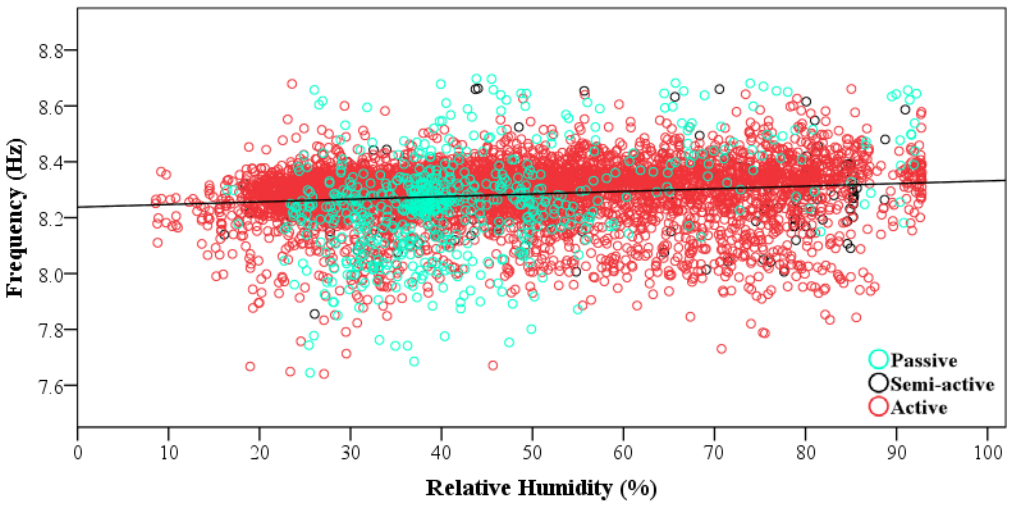


Figure 7.36 Relative humidity vs frequency (estimated around 8.29 Hz)

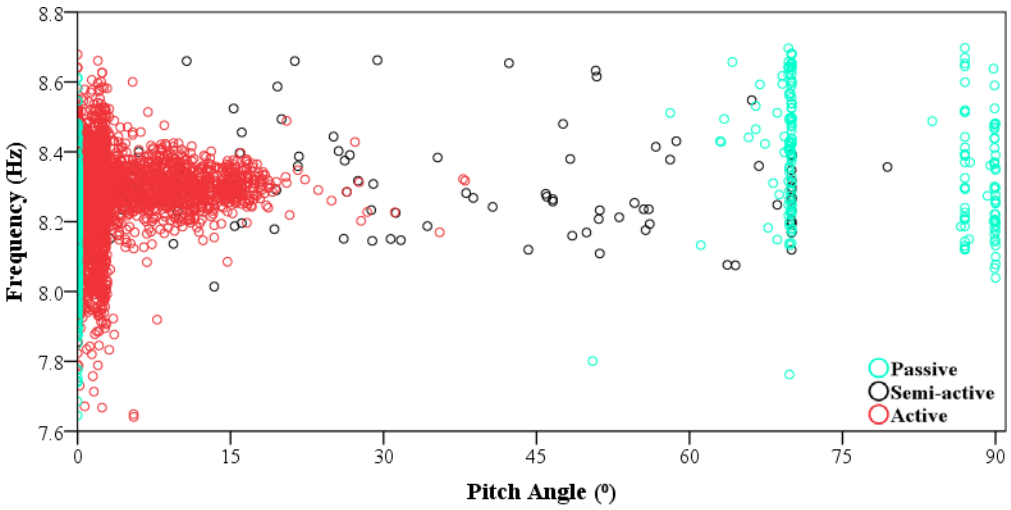


Figure 7.37 Pitch angle vs frequency (estimated around 8.29 Hz)

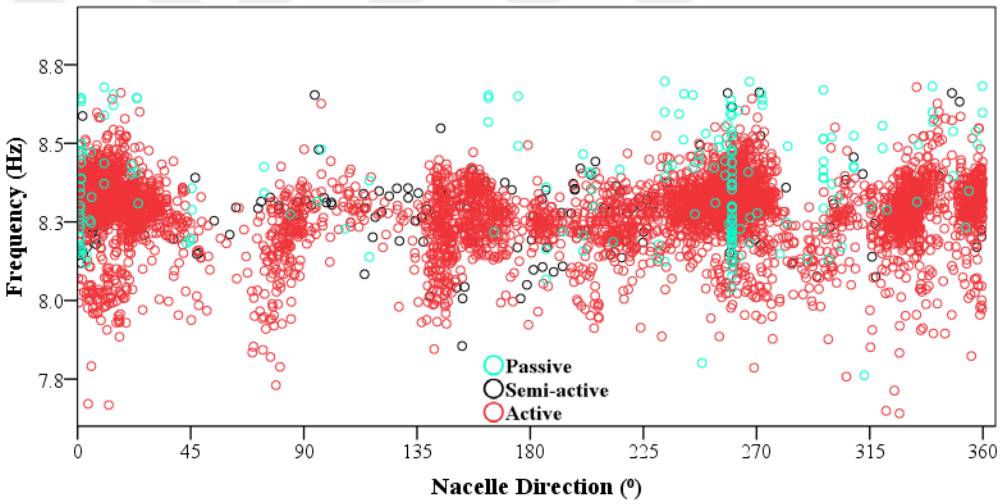


Figure 7.38 Nacelle direction vs frequency (estimated around 8.29 Hz)

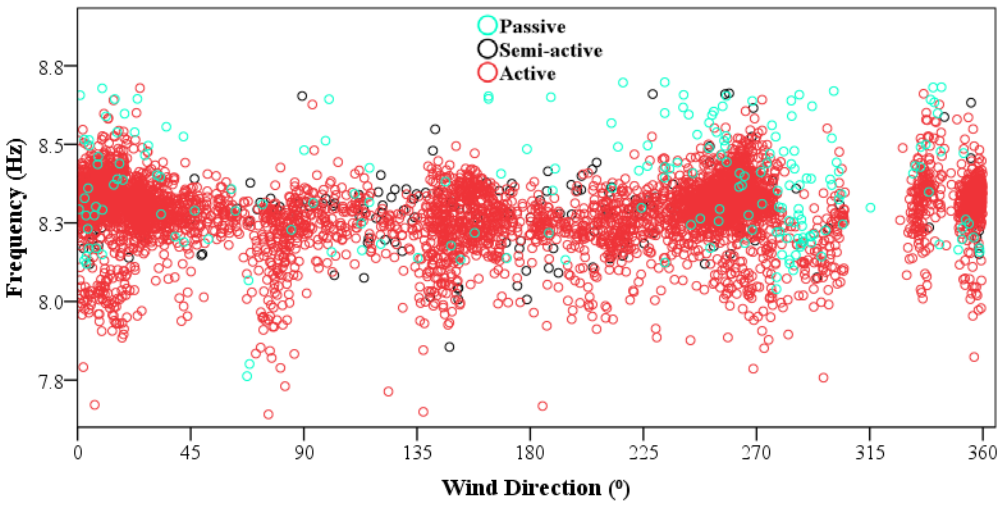


Figure 7.39 Wind direction vs frequency (estimated around 8.29 Hz)

In addition, there is no relationship between rotor speed and frequency estimated around 8.29 Hz, the variance of the estimated frequency values is high for passive and semi-active cases. For active cases, there is a positive correlation between the frequency estimated around 8.29 Hz and rotor speed, which is relatively low compared to the previous two modes. As the wind speed increases, an increasing trend is observed in the frequency values and there is a decrease in scattering of the frequency estimates. Standard deviation of the frequency values are 0.126 and 0.042 for 2-4 m/s and 16-18 m/s wind speed. Like the previous two modes, negative correlation is observed between temperatures and frequency estimates. By contrast with the previous mode frequencies estimated around 8.29 Hz increase with the decrease in relative humidity. The scattering of the frequency values estimated in the pitch angle range of 5º-30º (standard deviation = 0.066) is significantly lower than those in the range of 0-5 (standard deviation = 0.111) degrees. There is no correlation between frequency estimates and wind/nacelle direction.

Figure 7.40 – Figure 7.47 show the effect of operational and environmental conditions on mode frequency estimated around 16.00 Hz.

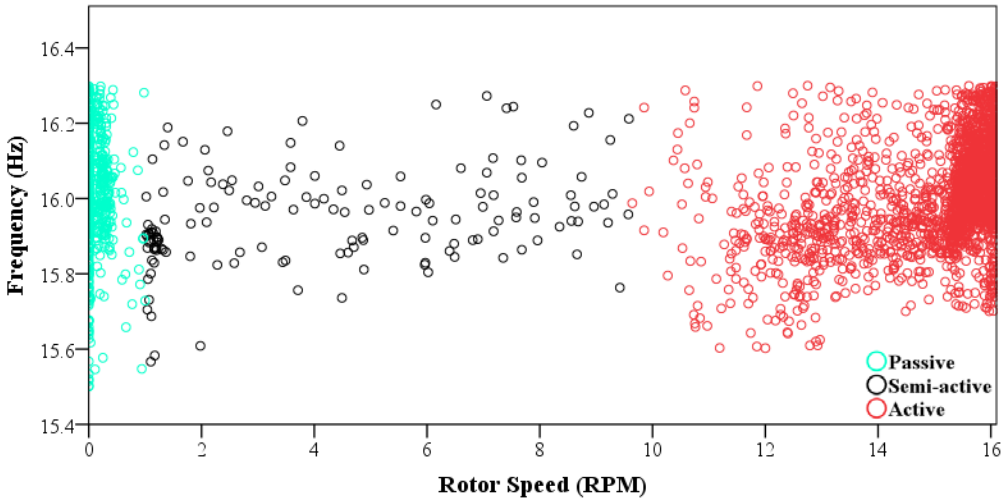


Figure 7.40 Rotor speed vs frequency (estimated around 16.00 Hz)

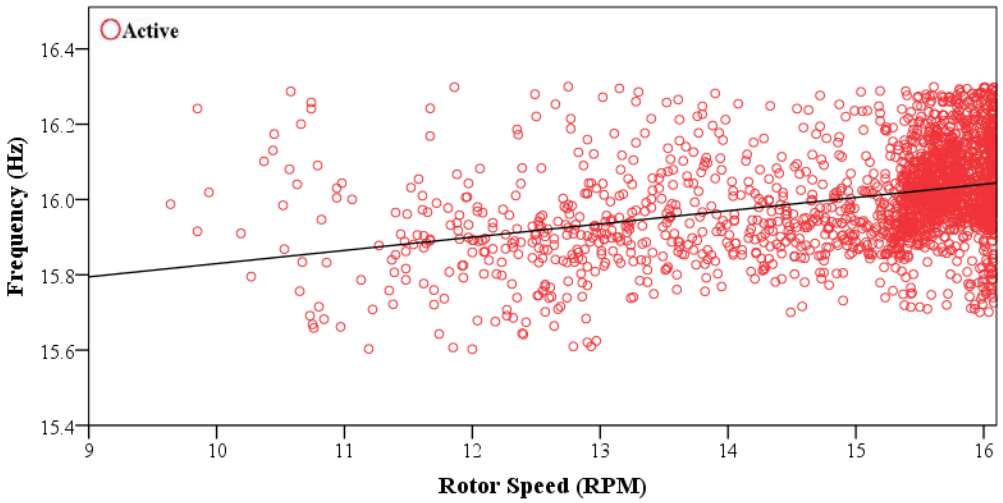


Figure 7.41 Rotor speed vs frequency (estimated around 16.00 Hz) for active cases only

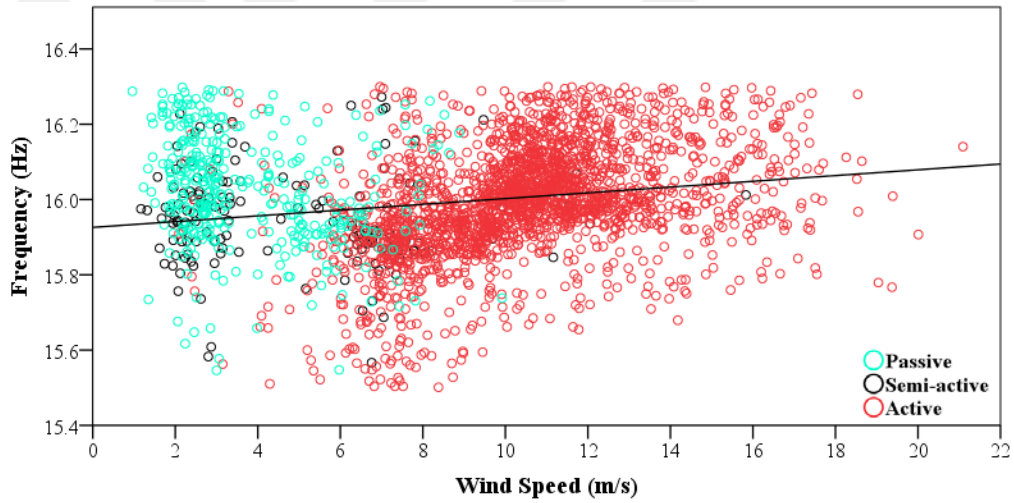


Figure 7.42 Wind speed vs frequency (estimated around 16.00 Hz)

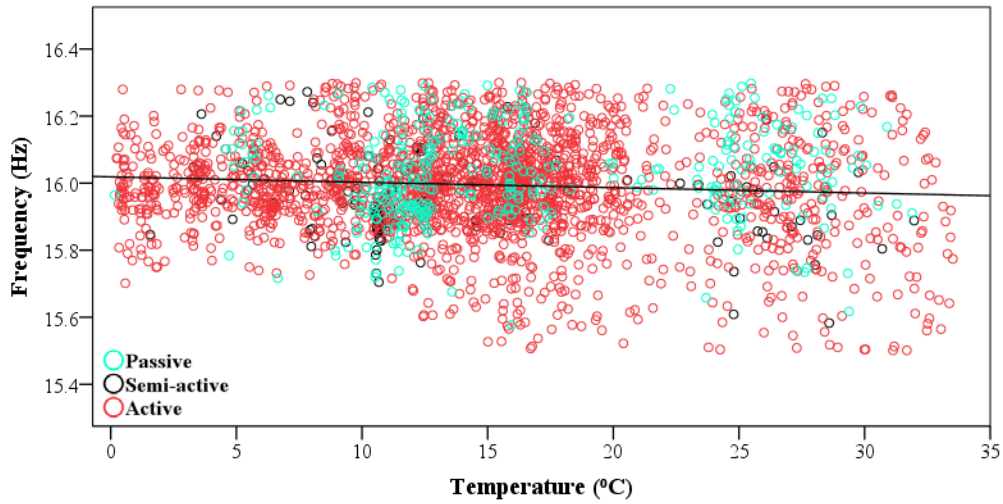


Figure 7.43 Temperature vs frequency (estimated around 16.00 Hz)

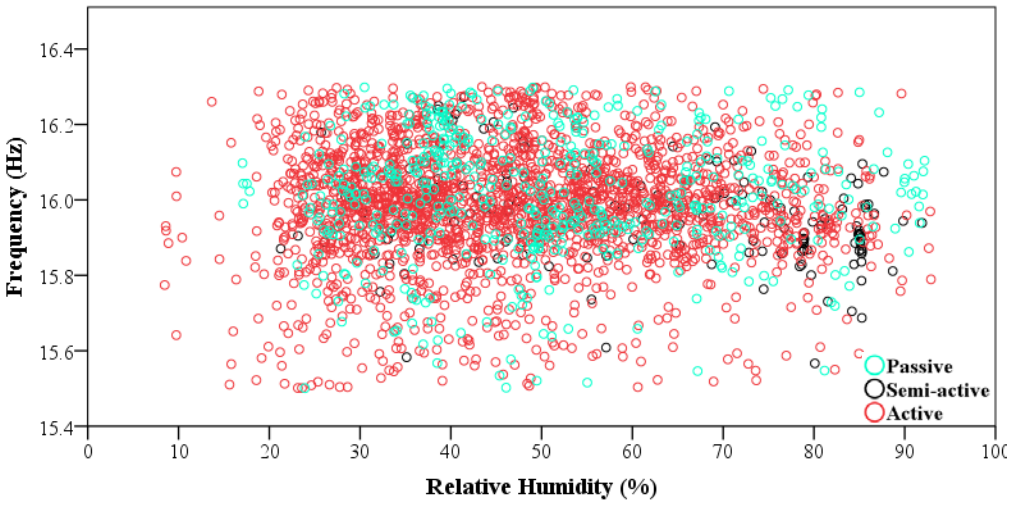


Figure 7.44 Relative humidity vs frequency (estimated around 16.00 Hz)

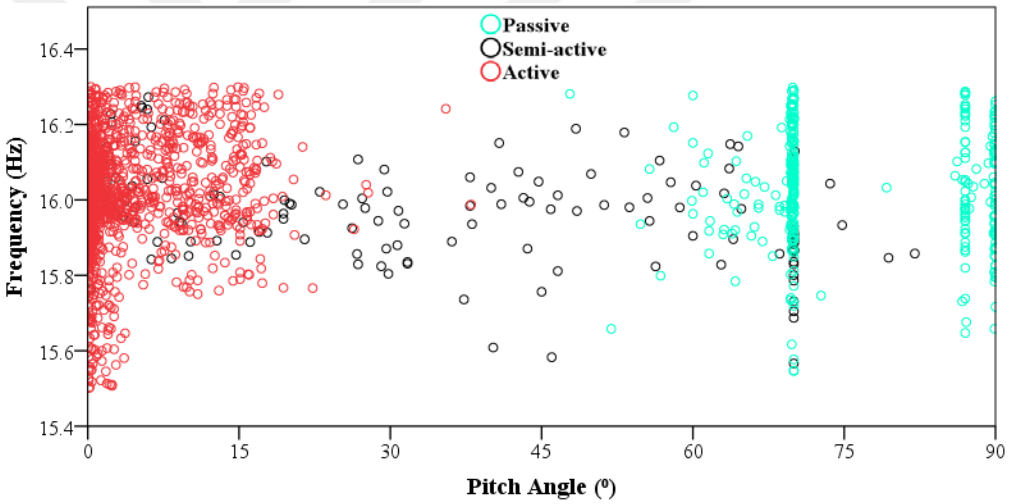


Figure 7.45 Pitch angle vs frequency (estimated around 16.00 Hz)

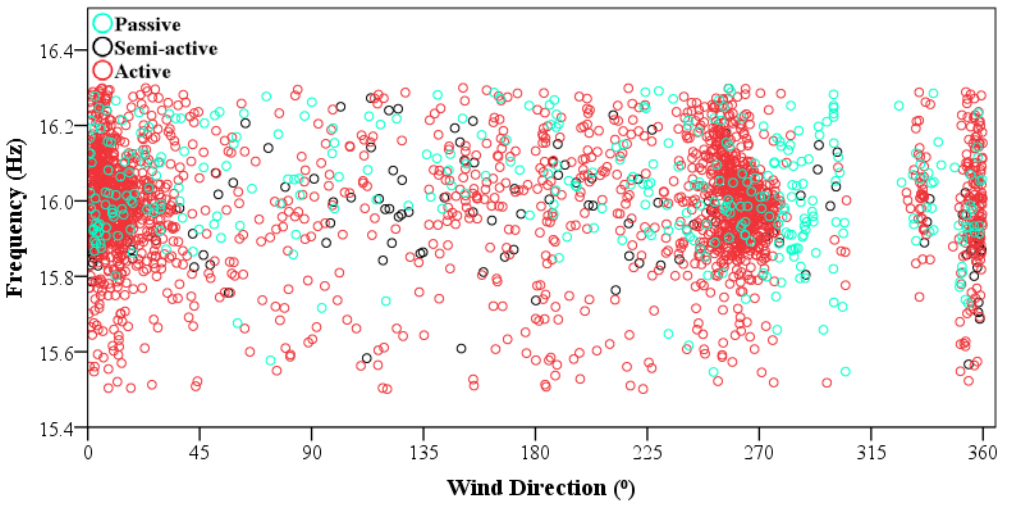


Figure 7.46 Wind direction vs frequency (estimated around 16.00 Hz)

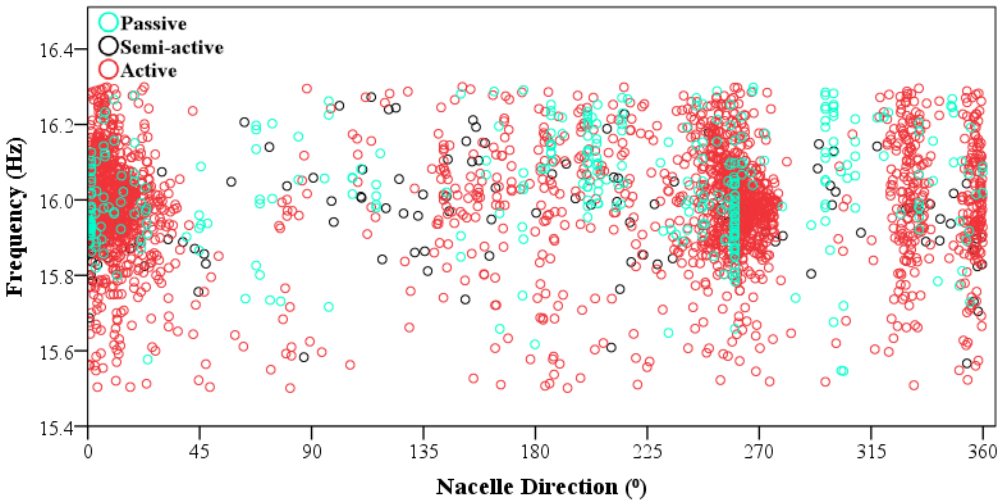


Figure 7.47 Nacelle direction vs frequency (estimated around 16.00 Hz)

For passive and semi-active cases no correlation between rotor speed and frequencies estimated around 16.00 Hz is observed while frequency estimation increases with increasing rotor speed for active cases. With the increase in wind speed, estimated frequencies are in rise trend. After the rated wind speed of the turbine, a slight decrease in frequency is observed due to lower wind thrust load on the wind turbine. Negative correlation is observed between frequency and ambient temperature. Like the previous two modes, the standard deviation of the frequency values estimated above 5º pitch angle (0.089) is significantly lower than others (0.149) for active cases. No obvious relationship is observed frequency estimations around 16.00 Hz and relative humidity, wind direction, and nacelle direction.

7.4 The Effect of Operational and Environmental Conditions on Mode Damping

In the literature vibration mode's damping ratios are generally affected by rotor speed due to aerodynamic damping caused by the interaction of turbine blades as they pass near the tower. In this section, the relationship between the estimated first four mode's damping ratios and operational/environmental factors is examined. Figure 7.48 – Figure 7.56 show the effect of operational and environmental conditions on mode damping ratios estimated around 0.36 Hz frequency. In graphs where a trend can be observed, a straight line representing this trend is placed.

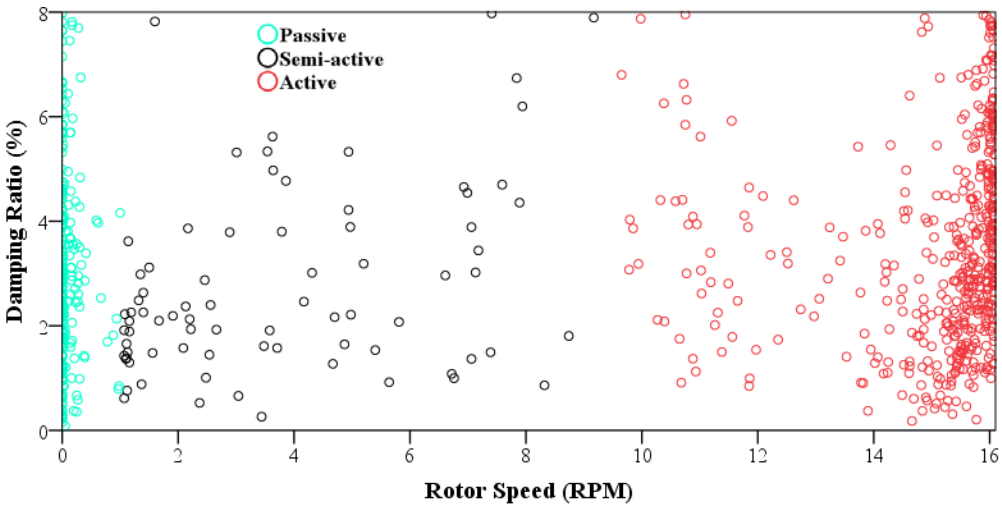


Figure 7.48 Rotor speed vs damping ratio (around 0.35 Hz frequency)

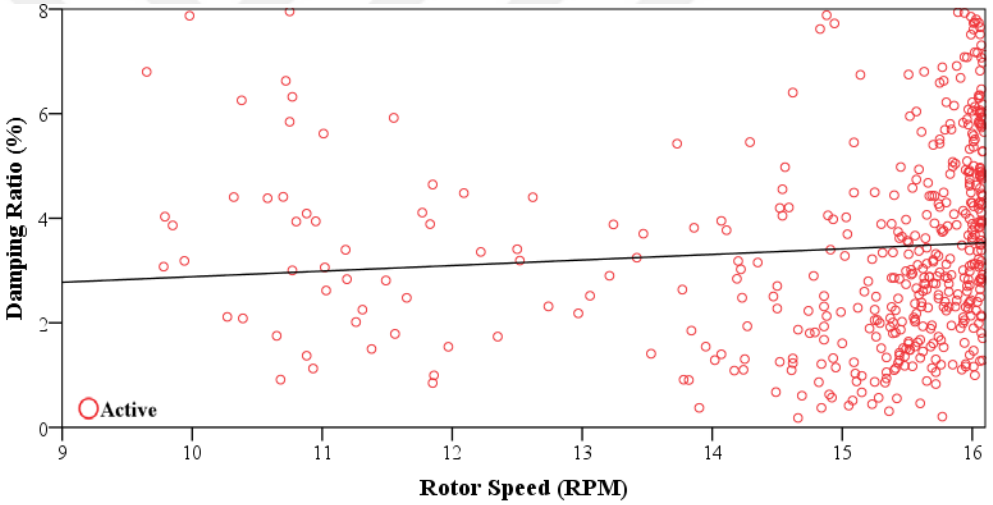


Figure 7.49 Rotor speed vs damping ratio (around 0.35 Hz frequency) for active cases only

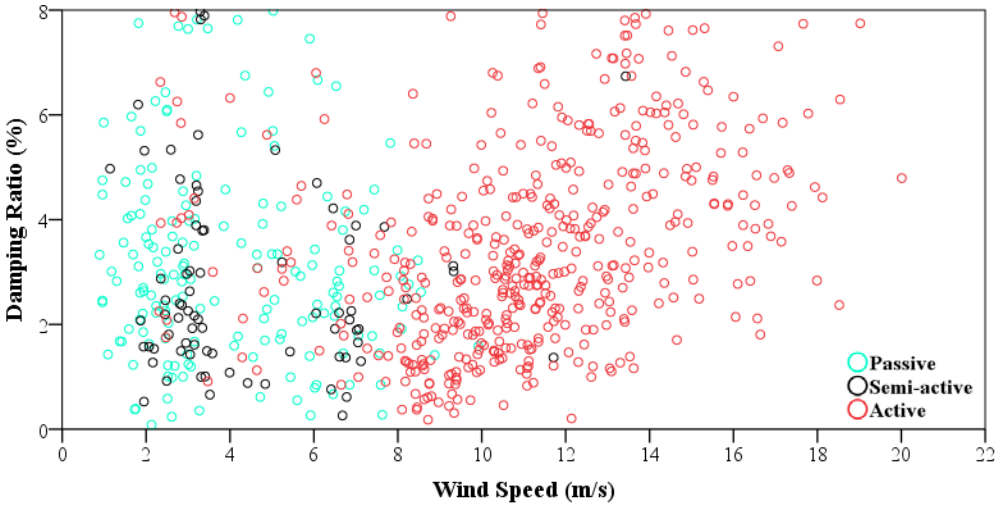


Figure 7.50 Wind speed vs damping ratio (around 0.35 Hz frequency)

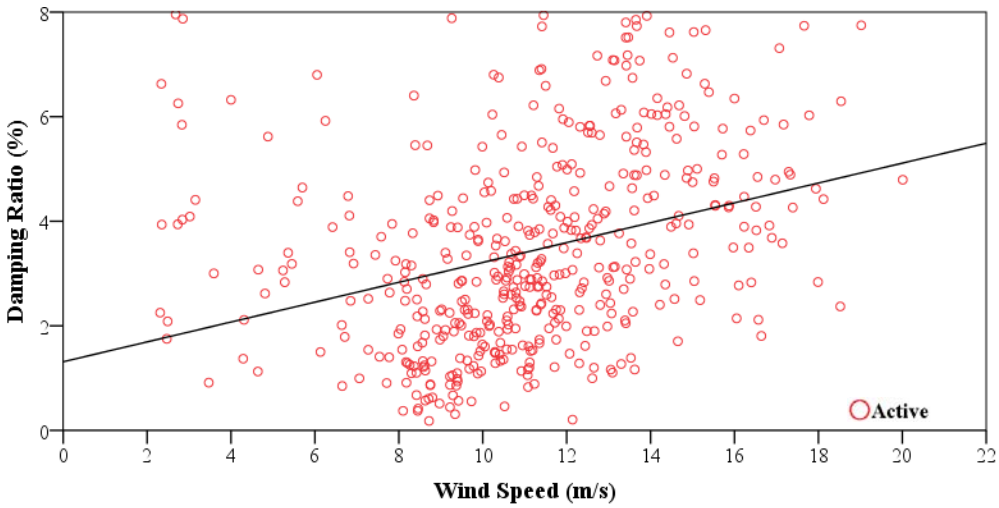


Figure 7.51 Wind speed vs damping ratio (around 0.35 Hz frequency) for active cases

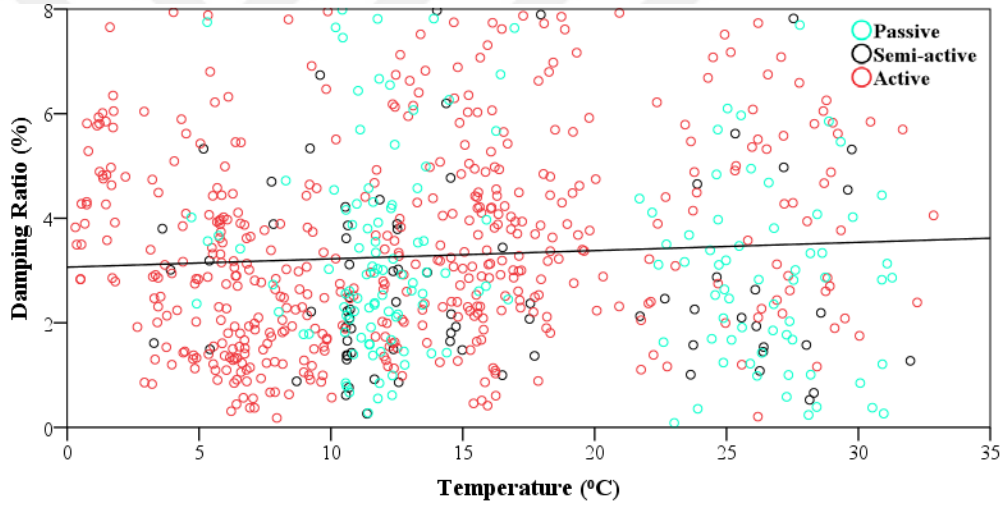


Figure 7.52 Temperature vs damping ratio (around 0.35 Hz frequency)

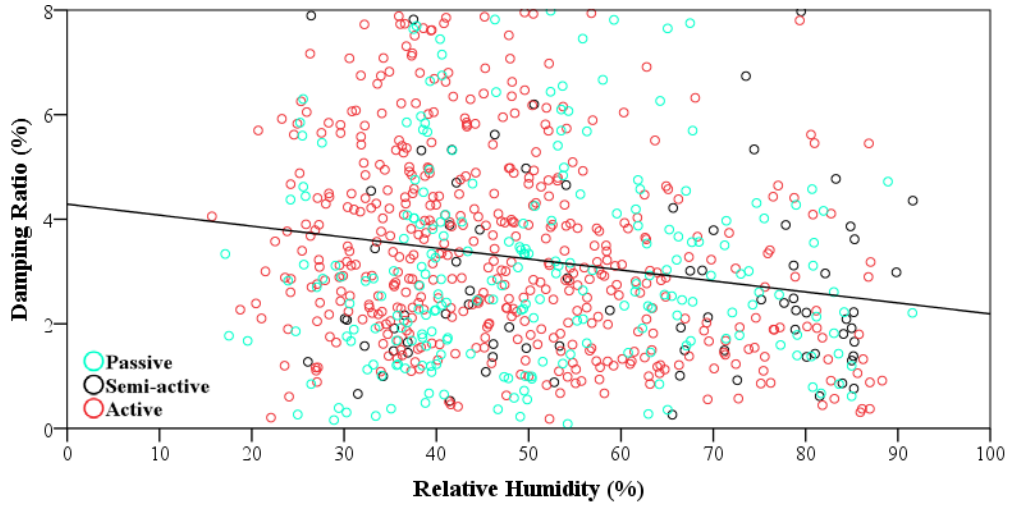


Figure 7.53 Relative humidity vs damping ratio (around 0.35 Hz frequency)

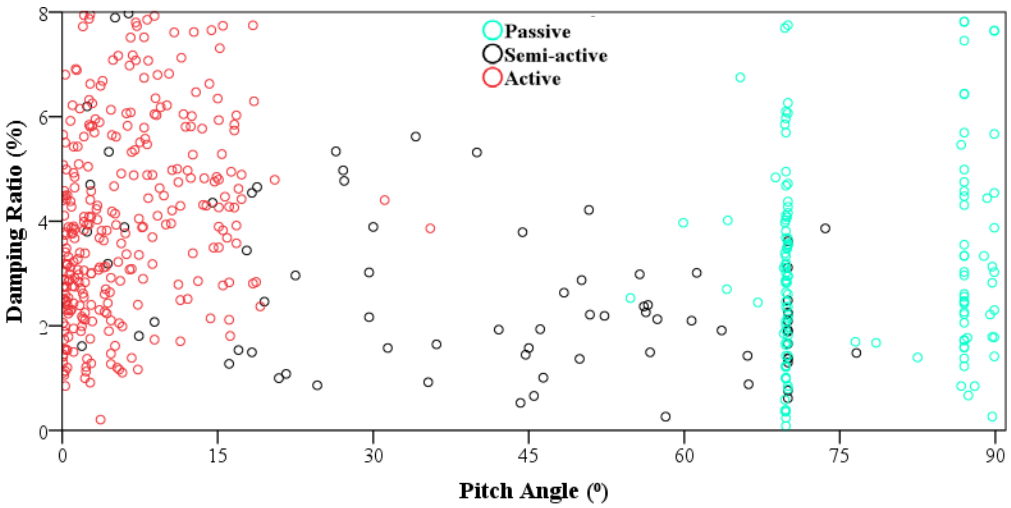


Figure 7.54 Pitch angle vs damping ratio (around 0.35 Hz frequency)

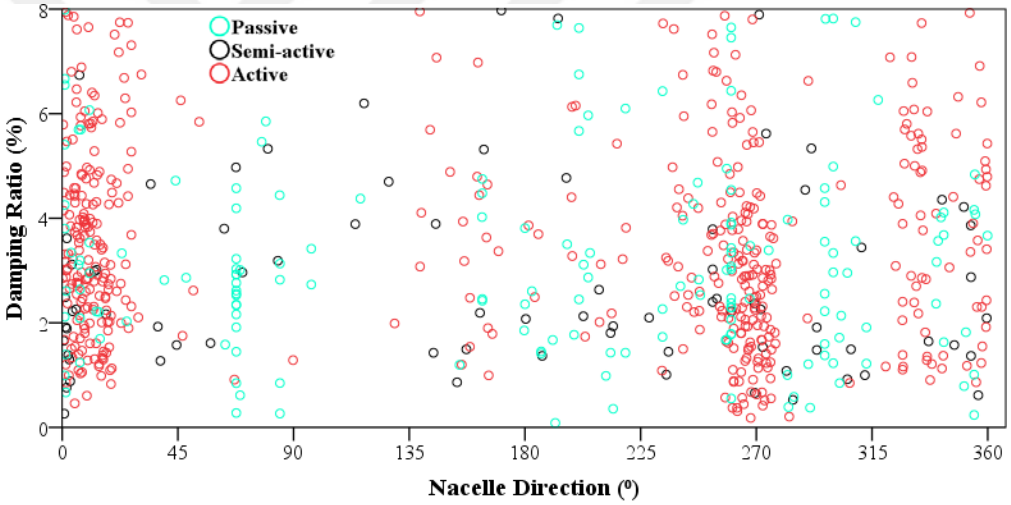


Figure 7.55 Nacelle direction vs damping ratio (around 0.35 Hz frequency)

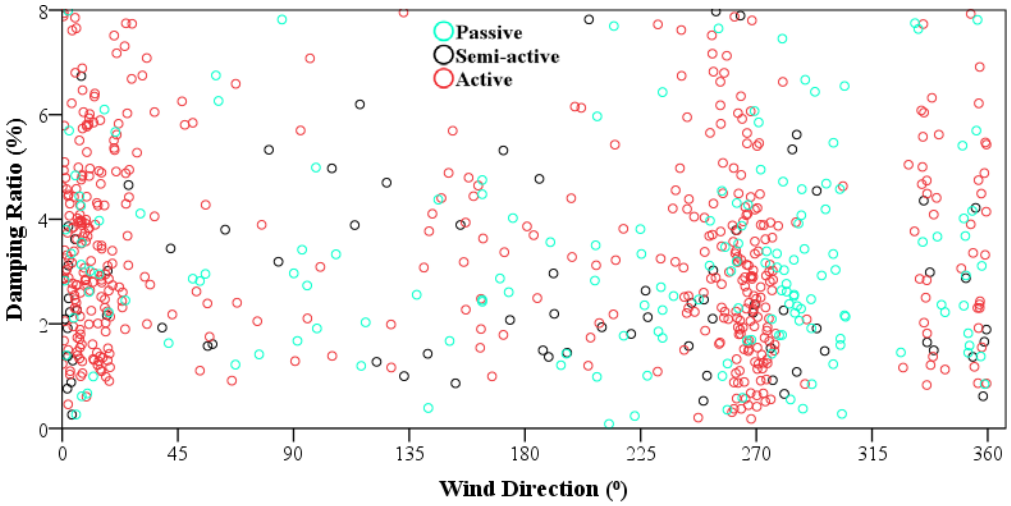


Figure 7.56 Wind direction vs damping ratio (around 0.35 Hz frequency)

The average value of the damping ratios estimated around 0.35 Hz frequency is 2.97% for passive and semi-active cases, and 3.42% for active cases. Damping ratio increases with increasing rotor speed and wind speed for active cases. There is a slight positive correlation between damping ratio and temperature while the estimated damping ratios tend to decrease with the increase in the ambient humidity. The change in the pitch angle, nacelle direction, and wind direction does not affect the damping ratio estimates around 0.35 Hz frequency.

Figure 7.57 – Figure 7.64 show the effect of operational and environmental conditions on mode damping ratios estimated around 3.00 Hz frequency. In graphs where a trend can be observed, a straight line representing this trend is placed.

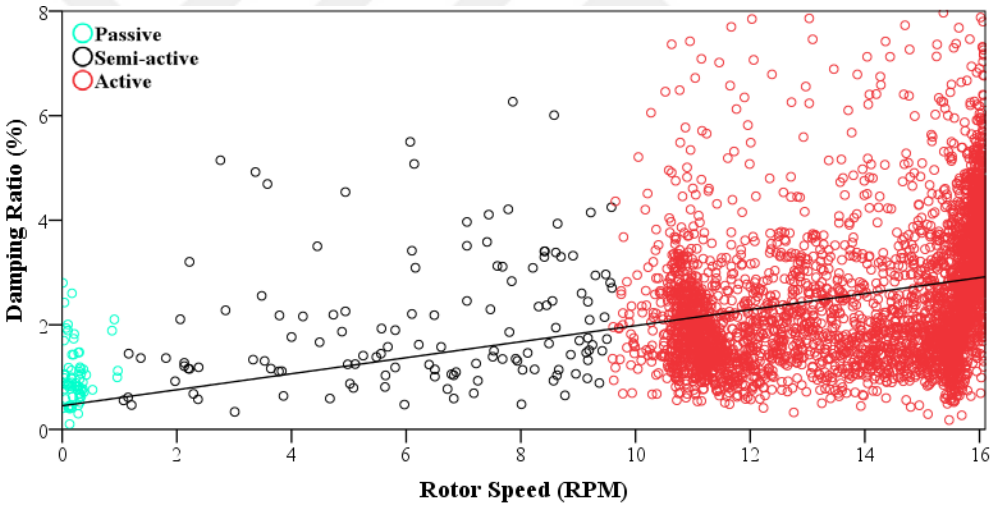


Figure 7.57 Rotor speed vs damping ratio (around 3.00 Hz frequency)

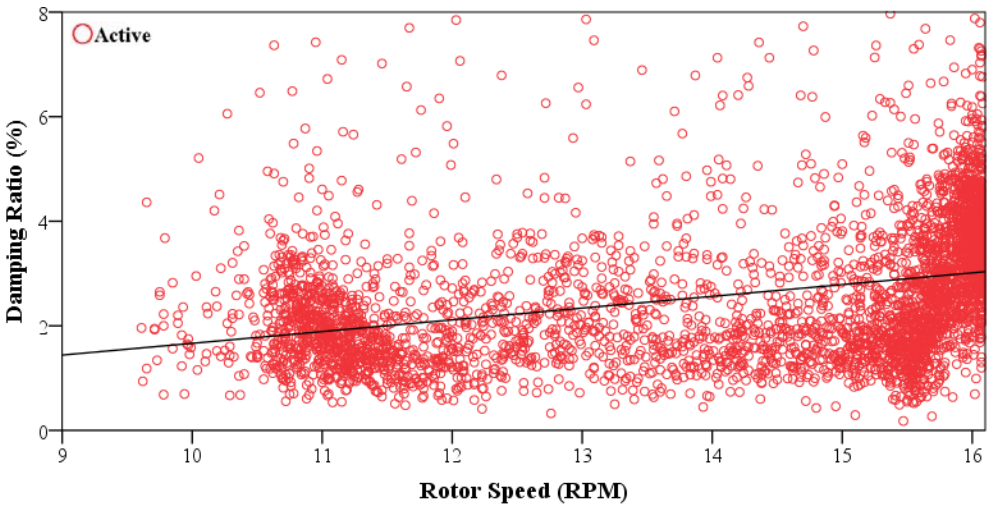


Figure 7.58 Rotor speed vs damping ratio (around 3.00 Hz frequency) for active cases only

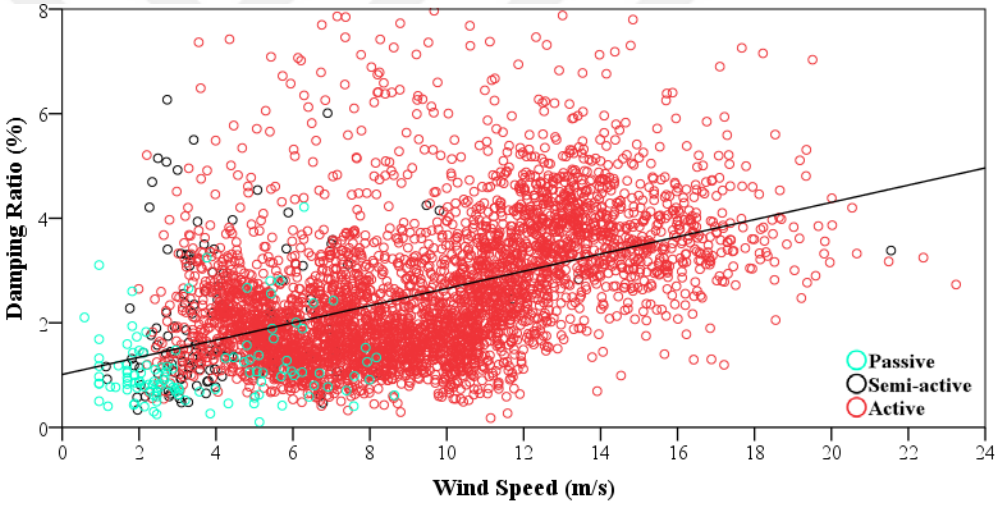


Figure 7.59 Wind speed vs damping ratio (around 3.00 Hz frequency)

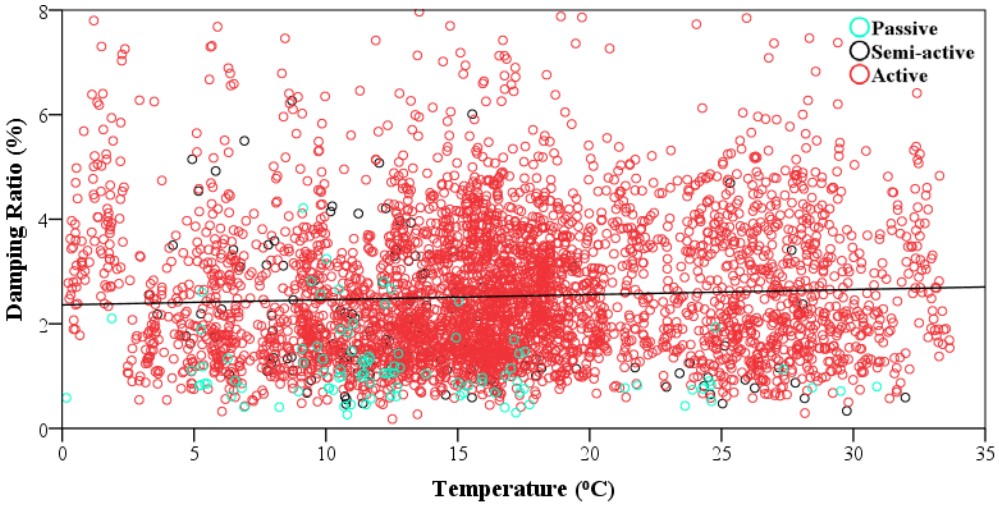


Figure 7.60 Temperature vs damping ratio (around 3.00 Hz frequency)

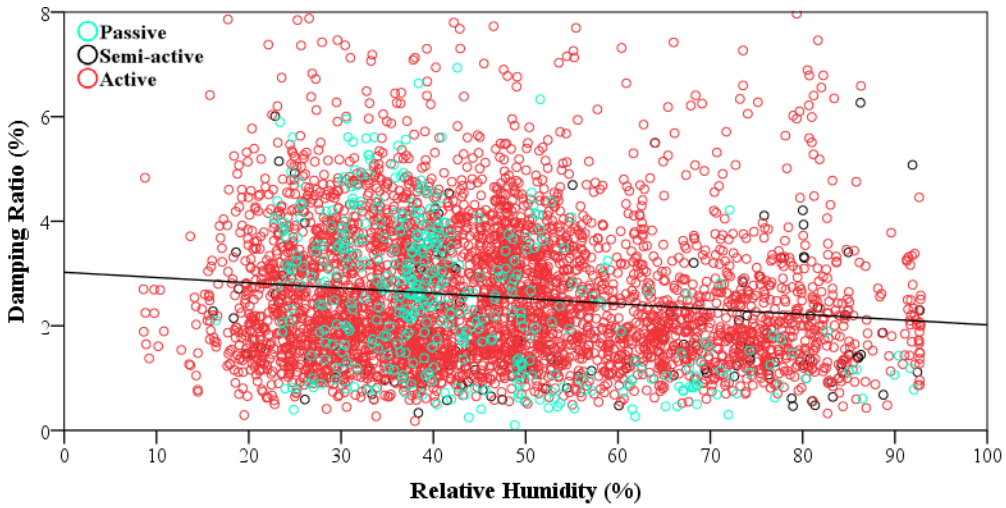


Figure 7.61 Relative humidity vs damping ratio (around 3.00 Hz frequency)

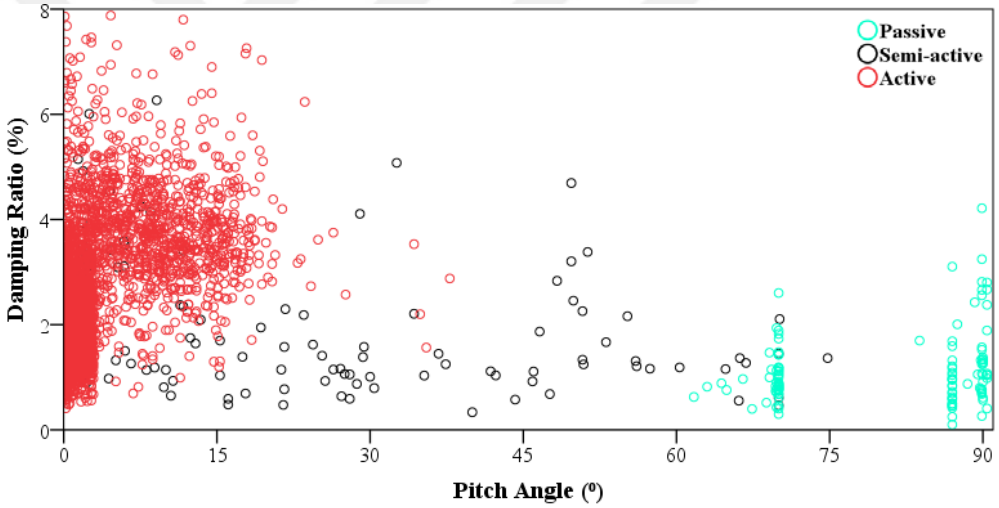


Figure 7.62 Pitch angle vs damping ratio (around 3.00 Hz frequency)

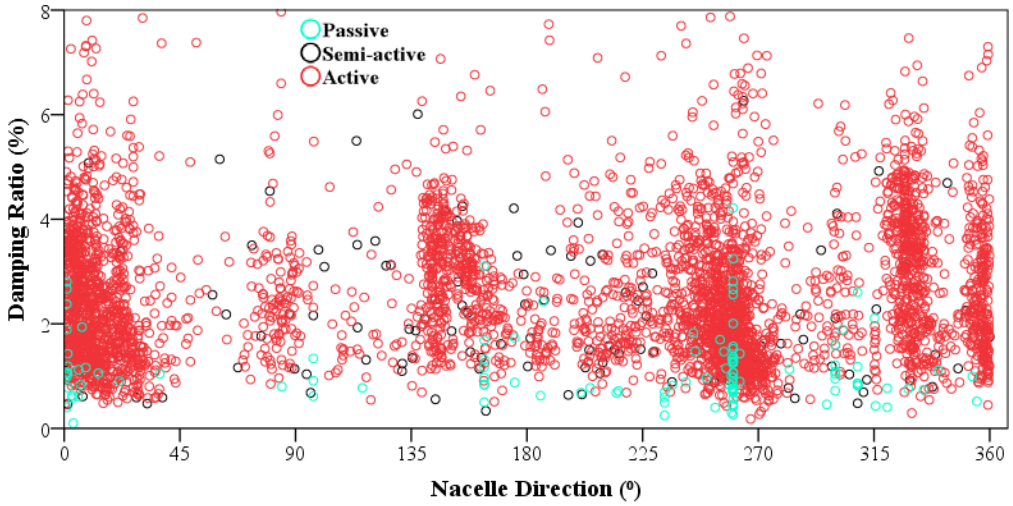


Figure 7.63 Nacelle direction vs damping ratio (around 3.00 Hz frequency)

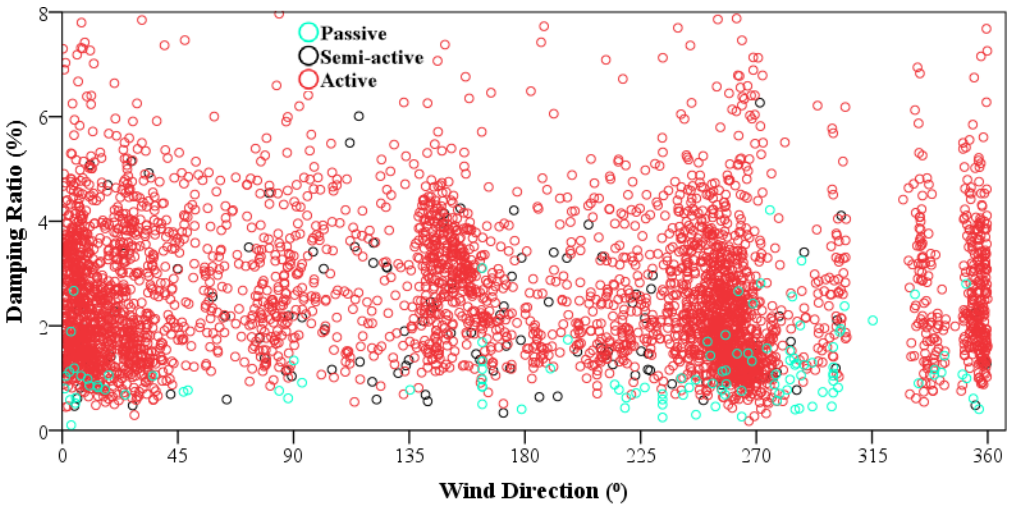


Figure 7.64 Wind direction vs damping ratio (around 3.00 Hz frequency)

Damping ratio estimates around 3.00 Hz frequency increase as rotor speed increases for all cases. Standard deviation of the high rotor speed damping values (1.28) is higher than other's (1.11) since after rated wind speed damping ratios get higher while rotor speed remains 16 RPM. The average of the damping ratios is 1.02%, 2.09%, and 2.57% for passive, semi-active and active cases respectively. From Figure 7.59 there is a positive correlation between damping ratios and wind speed. At rated wind speed (12 m/s) a jump in damping ratios is observed from about 2.00% to around 3.70%. Like the previous mode, damping ratio correlated positively with the temperatures and negatively with the ambient humidity. For active cases, the scattering of the damping ratio estimates suddenly dropped at 3º pitch angle (standard deviation dropped from 1.20 to 1.04). At pitch angle values higher than 60º, the reason for estimating low damping ratios is that the turbine is in passive condition (rotor speed lower than 2 RPM). There is no relationship between damping ratio and nacelle/wind direction.

Figure 7.65 – Figure 7.72 show the effect of operational and environmental conditions on mode damping ratios estimated around 8.29 Hz frequency. In graphs where a trend can be observed, a straight line representing this trend is placed.

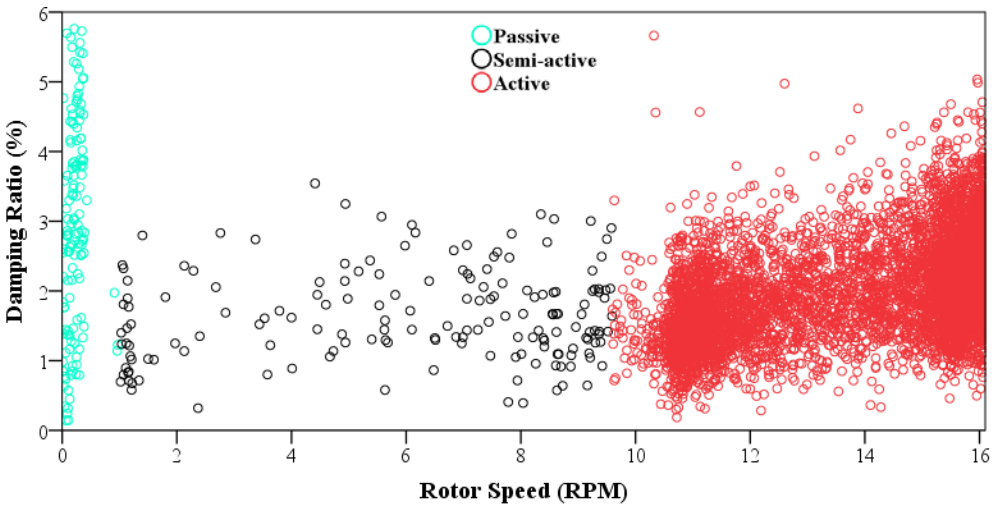


Figure 7.65 Rotor speed vs damping ratio (around 8.29 Hz frequency)

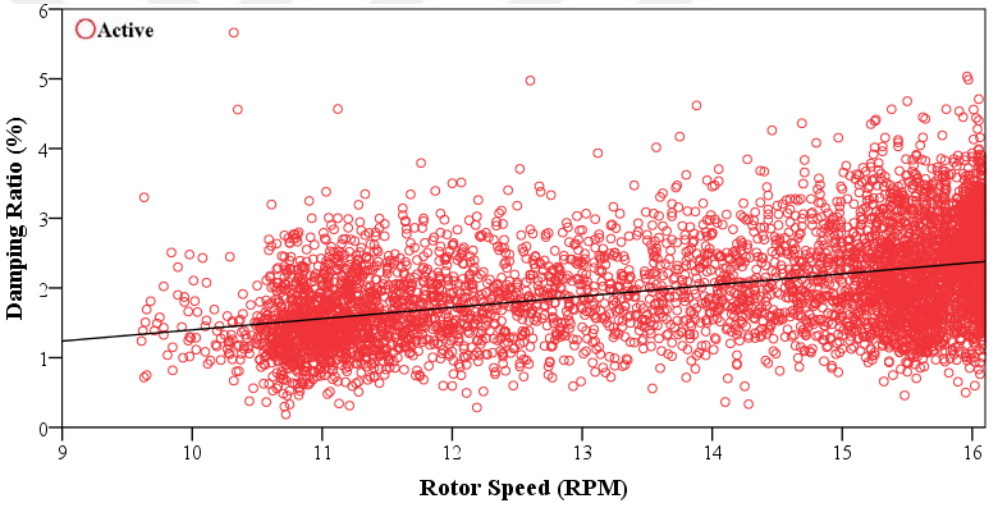


Figure 7.66 Rotor speed vs damping ratio (around 8.29 Hz frequency) for active cases only

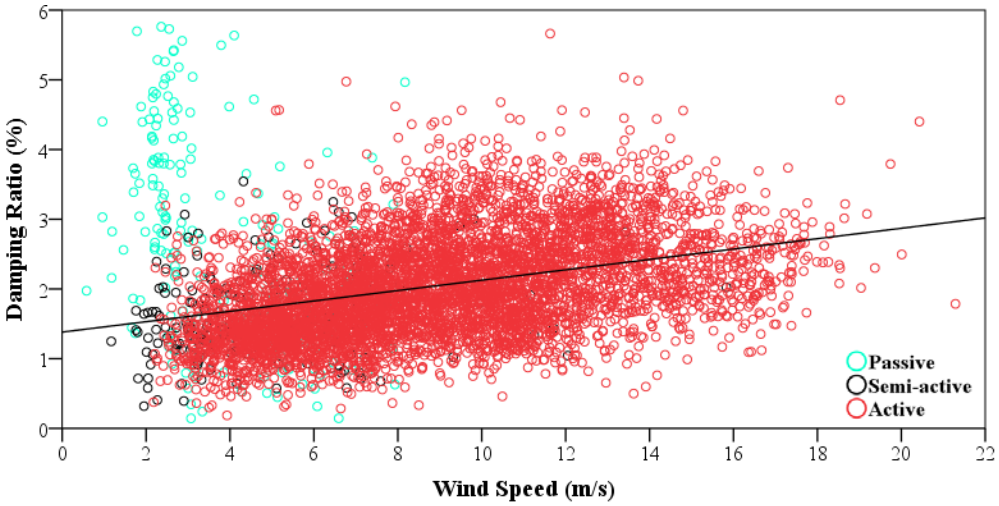


Figure 7.67 Wind speed vs damping ratio (around 8.29 Hz frequency)

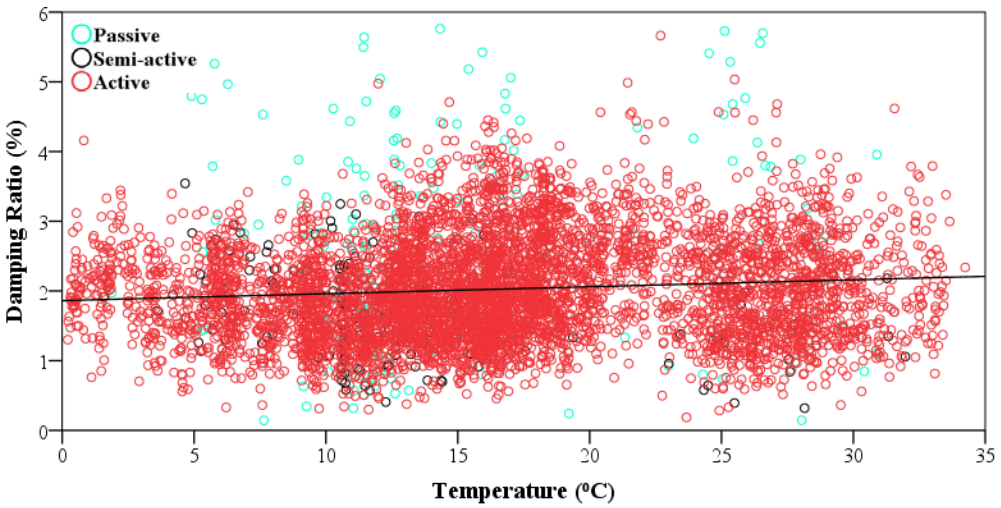


Figure 7.68 Temperature vs damping ratio (around 8.29 Hz frequency)

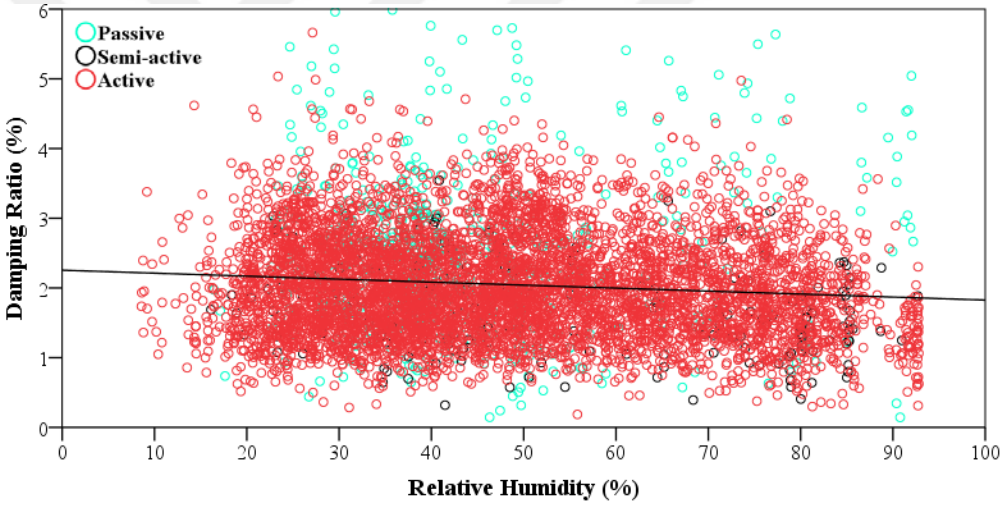


Figure 7.69 Relative humidity vs damping ratio (around 8.29 Hz frequency)

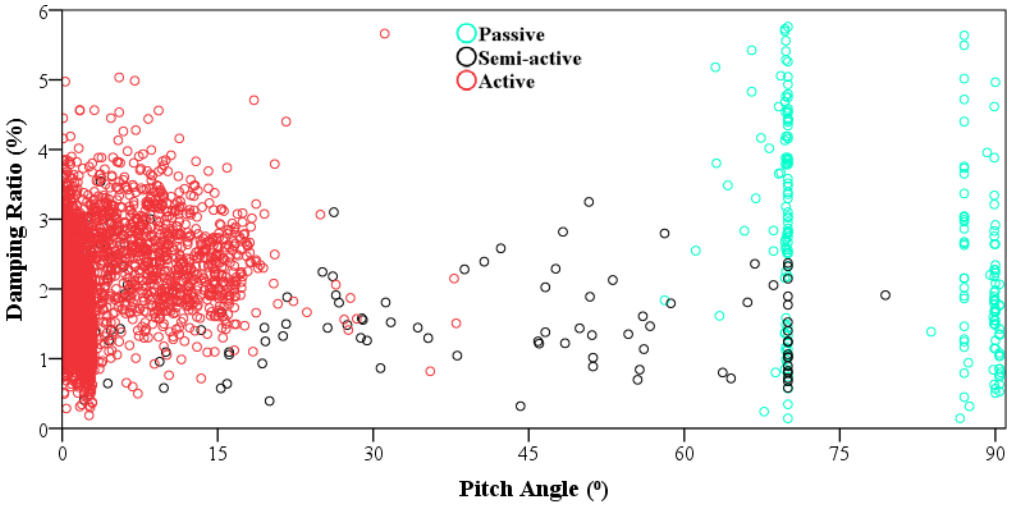


Figure 7.70 Pitch angle vs damping ratio (around 8.29 Hz frequency)

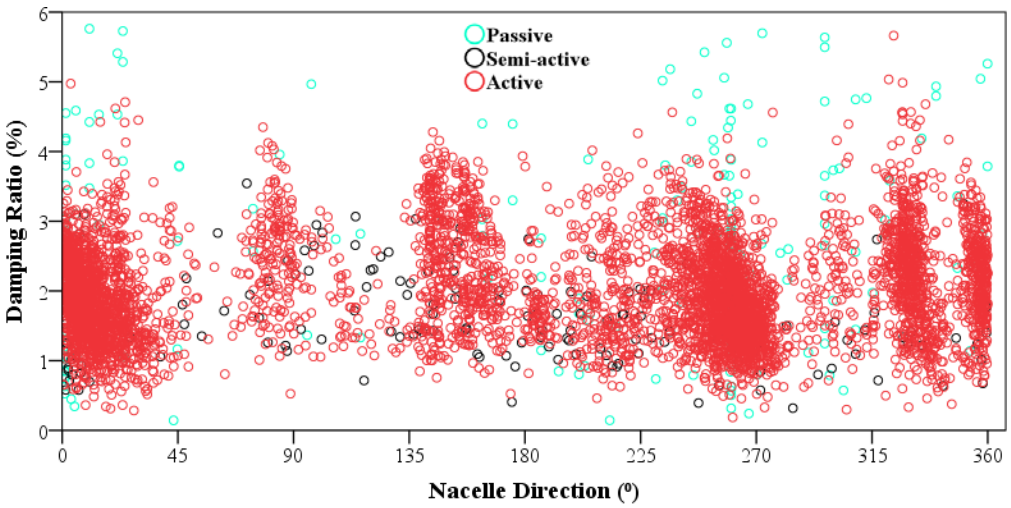


Figure 7.71 Nacelle direction vs damping ratio (around 8.29 Hz frequency)

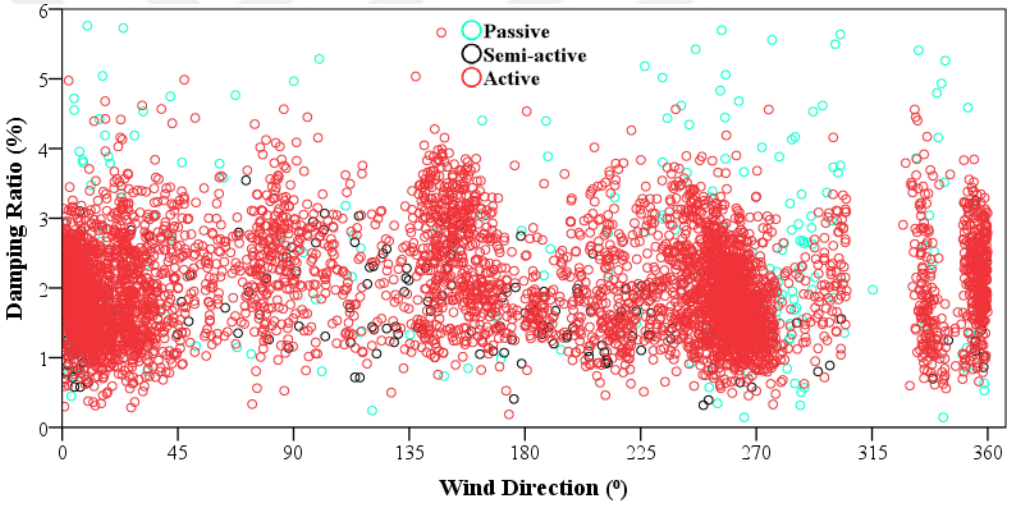


Figure 7.72 Wind direction vs damping ratio (around 8.29 Hz frequency)

Unlike the previous two modes, maximum damping ratio estimated around 8.29 Hz frequency is 6% and the average value is 2.03%. Mean values are 2.64%, 1.71%, and 2.01% for passive, semi-active, and active cases respectively. For passive cases scattering of the damping ratios is higher than semi-active and active cases. The standard deviations of the damping ratios are 1.52, 0.66, and 0.72 for passive, semi-active, and active cases respectively. For active cases, estimated damping ratios increase with increasing rotor speed and wind speed. There is a slight positive correlation between damping ratio and temperature and negative correlation between damping ratio and ambient humidity. For active cases scattering of damping ratios suddenly drops after 3º pitch angle (standard deviation dropped from 0.69 to 0.59) and

damping ratios decrease as the pitch angle increases. No relationship could be detected between wind direction and damping ratio.

Figure 7.73 – Figure 7.82 show the effect of operational and environmental conditions on mode damping ratios estimated around 16.00 Hz frequency. In graphs where a trend can be observed, a straight line representing this trend is placed.

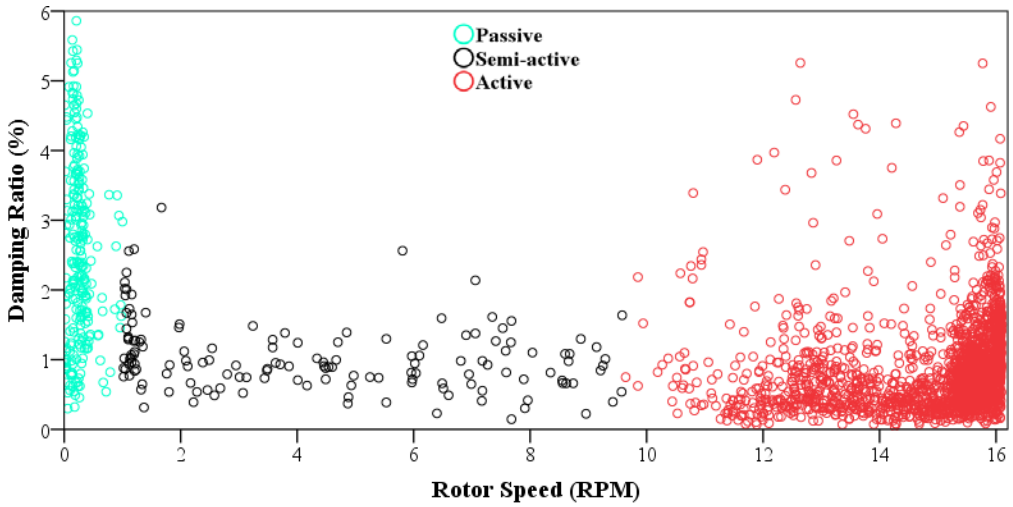


Figure 7.73 Rotor speed vs damping ratio (around 16.00 Hz frequency)

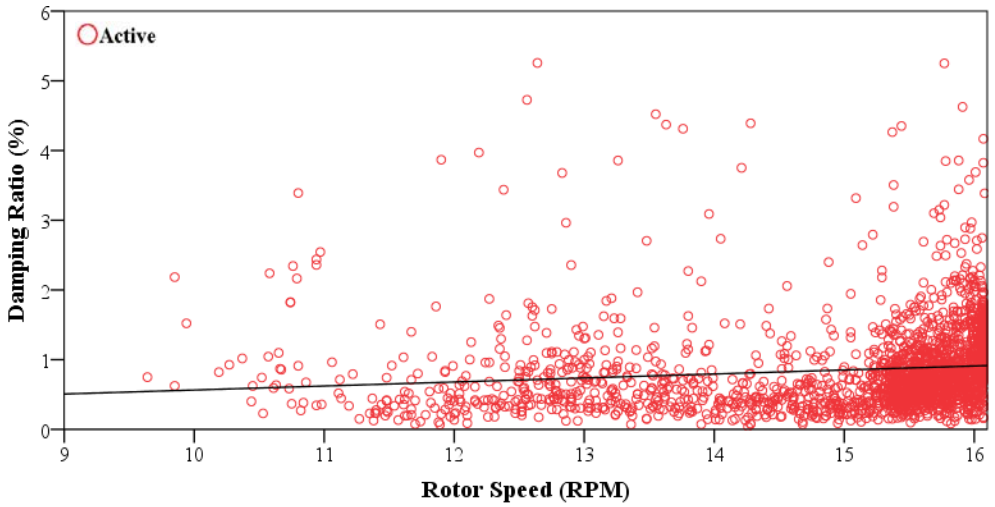


Figure 7.74 Rotor speed vs damping ratio (around 16.00 Hz frequency) for active cases only

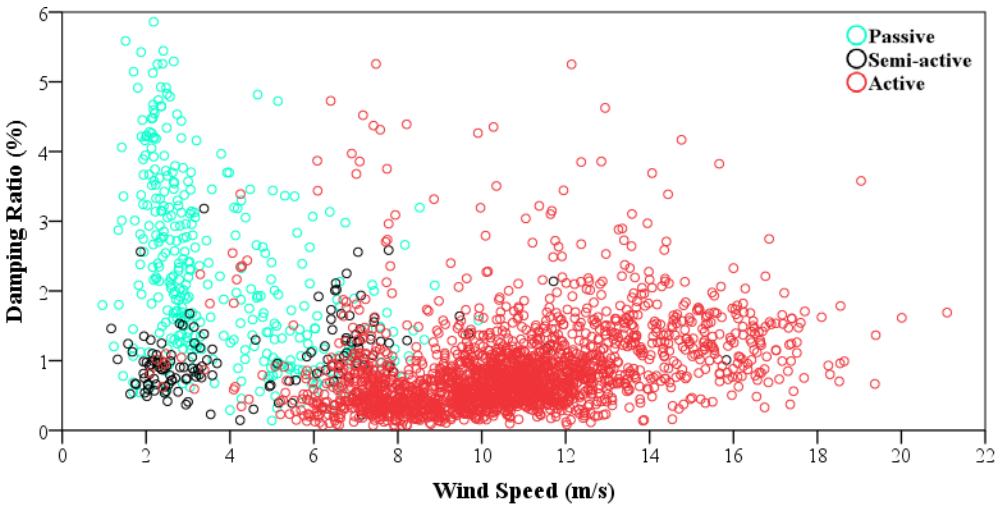


Figure 7.75 Wind speed vs damping ratio (around 16.00 Hz frequency)

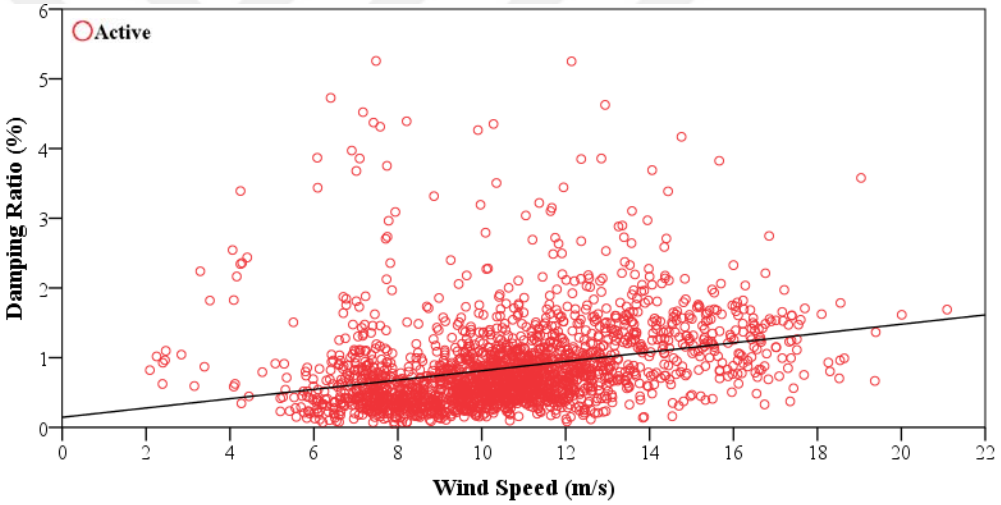


Figure 7.76 Wind speed vs damping ratio (around 16.00 Hz frequency) for active cases only

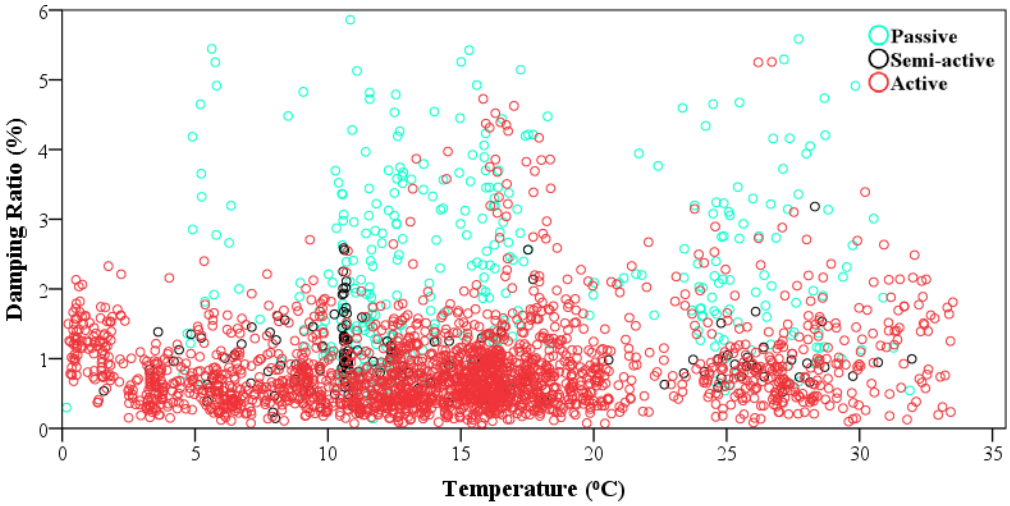


Figure 7.77 Temperature vs damping ratio (around 16.00 Hz frequency)

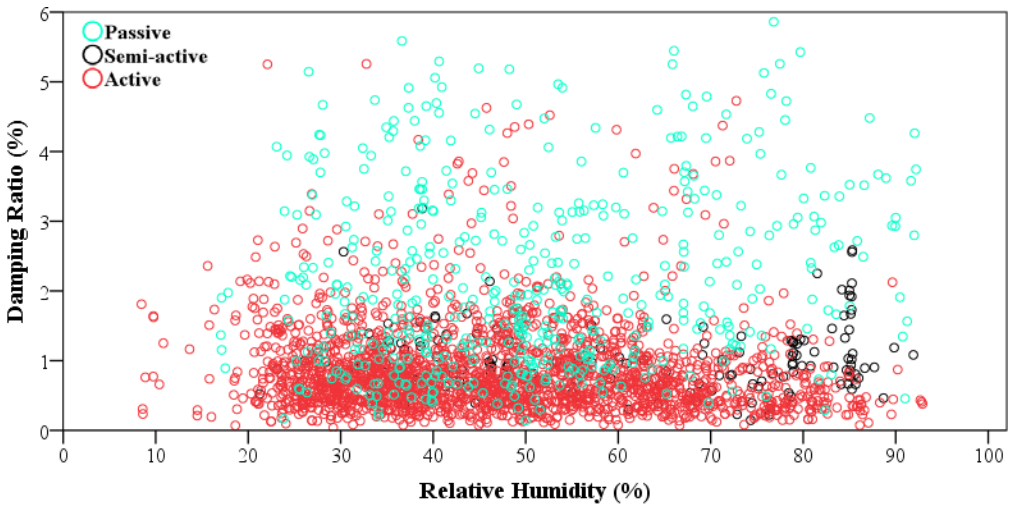


Figure 7.78 Relative humidity vs damping ratio (around 16.00 Hz frequency)

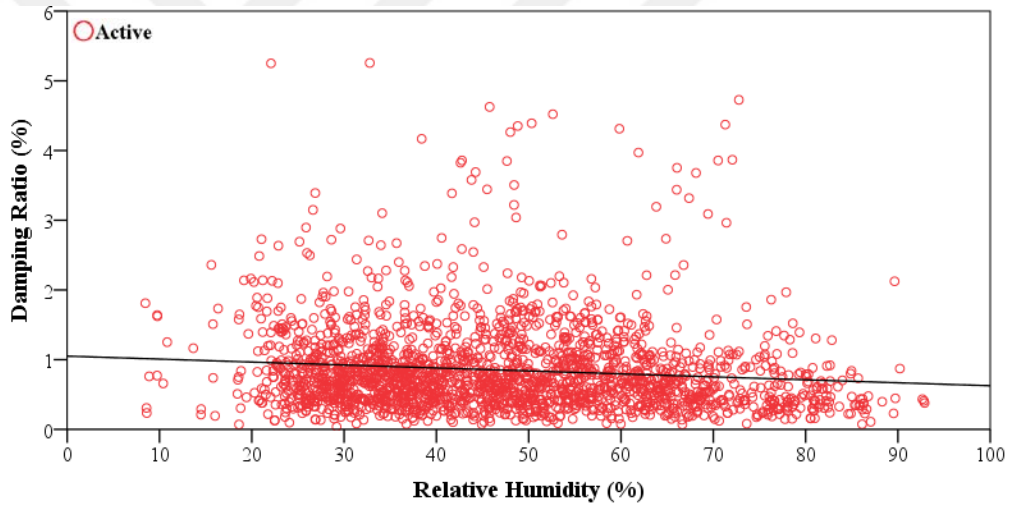


Figure 7.79 Relative humidity vs damping ratio (around 16.00 Hz frequency) for active cases only

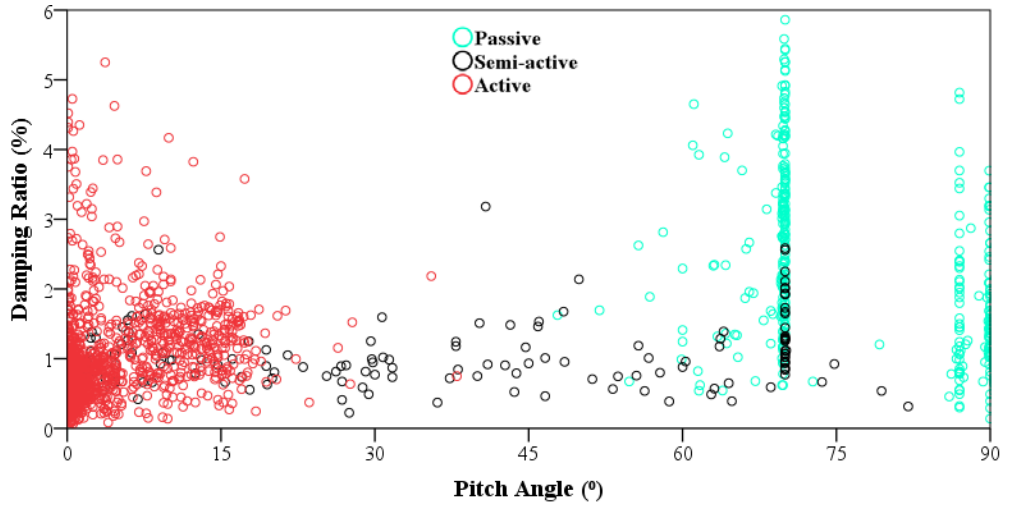


Figure 7.80 Pitch angle vs damping ratio (around 16.00 Hz frequency)

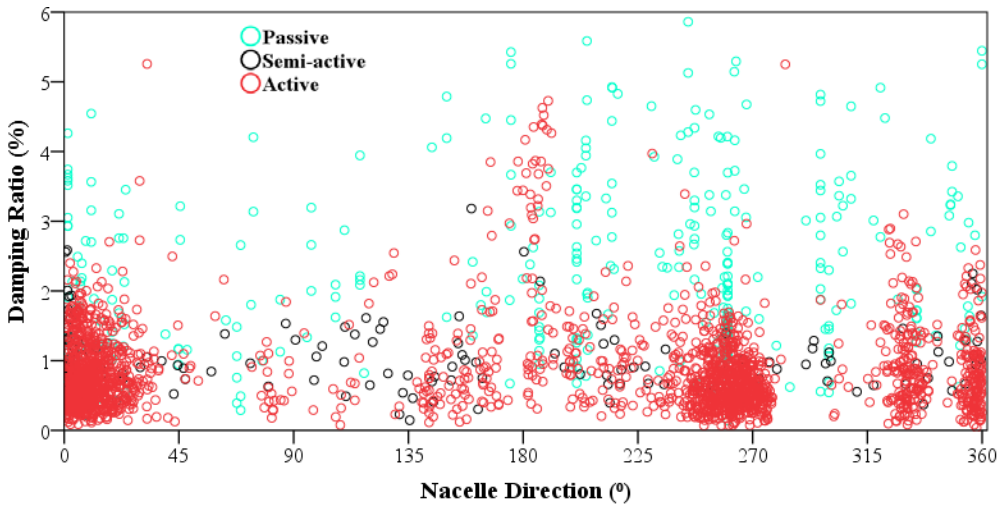


Figure 7.81 Nacelle direction vs damping ratio (around 16.00 Hz frequency)

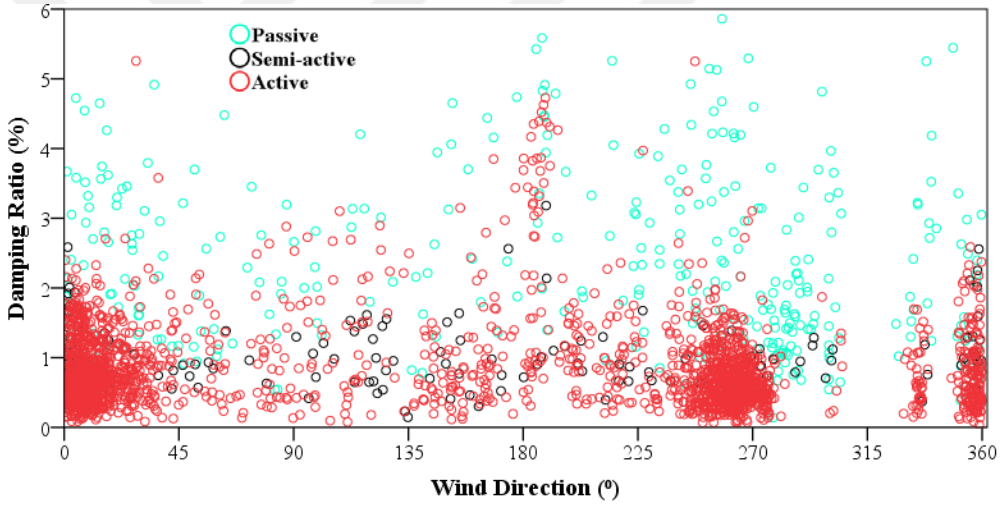


Figure 7.82 Wind direction vs damping ratio (around 16.00 Hz frequency)

Like the previous mode, maximum damping ratio estimated around 16.00 Hz frequency is 6% and the average value is 1.03%. Mean values are 2.34%, 0.91%, and 0.85% for passive, semi-active, and active cases respectively. For passive cases scattering of the damping ratios is higher than semi-active and active cases. The standard deviations of the damping ratios are 1.31, 0.39, and 0.62 for passive, semi-active, and active cases respectively. In the 9.6 – 15 RPM rotor speed range, damping ratio estimates stay constant around 0.5%. After 15 RPM damping ratios started to increase. For semi-active and active cases, a positive correlation between damping ratio and wind speed can be seen from graphs. The average damping ratio values are estimated around 1.5% and 0.6% for 0 – 2 ºC and 2 - 35 ºC temperature range

respectively. For active cases damping ratio estimates decrease with increasing ambient humidity. Scattering of damping ratios drops after 5º pitch angle (standard deviation dropped from 0.57 to 0.49) and damping ratios increase as the pitch angle increases for active cases. There is no relationship between damping ratio and nacelle/wind direction.

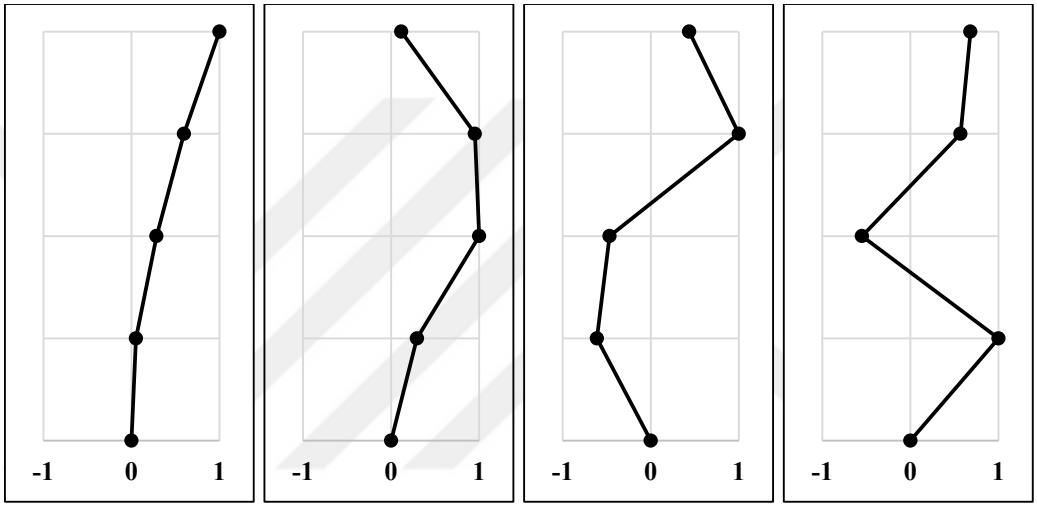
7.5 The Effect of Operational and Environmental Conditions on Mode Shape

In order to determine the effect of operational and environmental conditions on the vibration mode shapes, the following procedure is applied:

- All identified modes are normalized by dividing the amplitude at each level by the maximum amplitude of the mode shape.
- The level with the maximum amplitude is chosen as the reference level.
- The occurrence percentages of the reference level at each level are determined (Table 7.1).
- The principal mode shape is determined by averaging amplitudes of each level of the estimated modes with highest occurrence percentages (Figure 7.83).
- The Modal Assurance Criterion (MAC) values between the principal mode shape and each mode shape are calculated.
- Correlations between MAC values and the operational and environmental conditions are presented.

Table 7.1 Occurrence percentages of reference level

	Level-2	Level-3	Level-4	Level-5
0.35 Hz	0%	0%	1%	99%
3.00 Hz	0%	63%	37%	0%
8.29 Hz	5%	0%	95%	0%
16.00 Hz	38%	24%	19%	19%



(a) (b) (c) (d)

Figure 7.83 The principal mode shape estimated around (a) 0.35 Hz frequency, (b) 3.00 Hz frequency, (c) 8.29 Hz frequency, and (d) 16.00 Hz frequency

Figure 7.84 – Figure 7.90 show the correlation between MAC values and operational/environmental conditions for estimated modes around 0.35 Hz frequency. For this mode, the occurrence percentage is over 99% when the maximum amplitudes of the mode shapes are at Level-5.

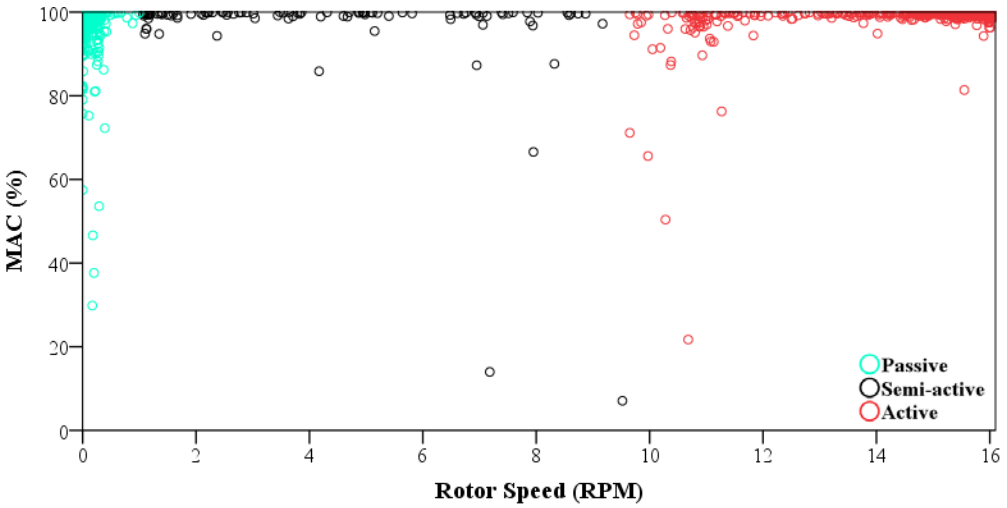


Figure 7.84 Rotor speed vs MAC value (around 0.35 Hz frequency)

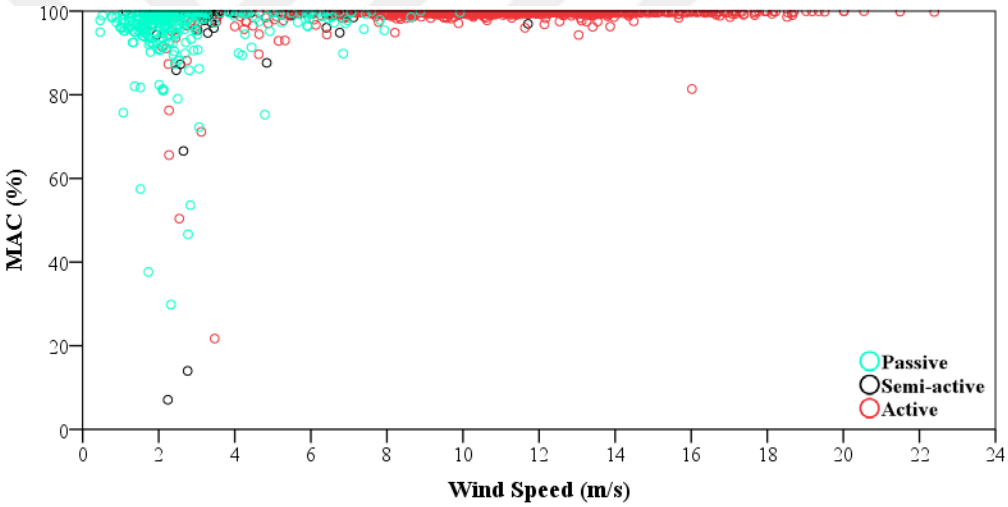


Figure 7.85 Rotor speed vs MAC value (around 0.35 Hz frequency)

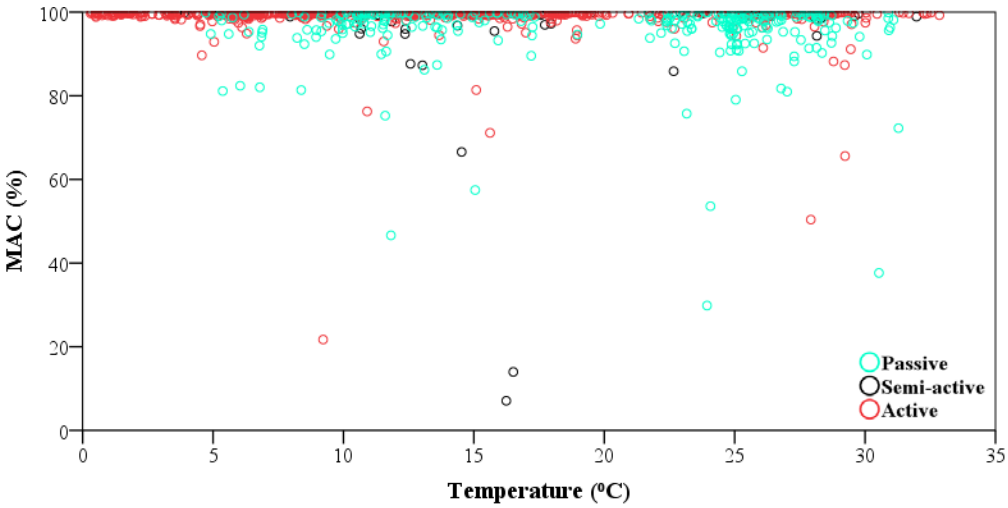


Figure 7.86 Temperature vs MAC value (around 0.35 Hz frequency)

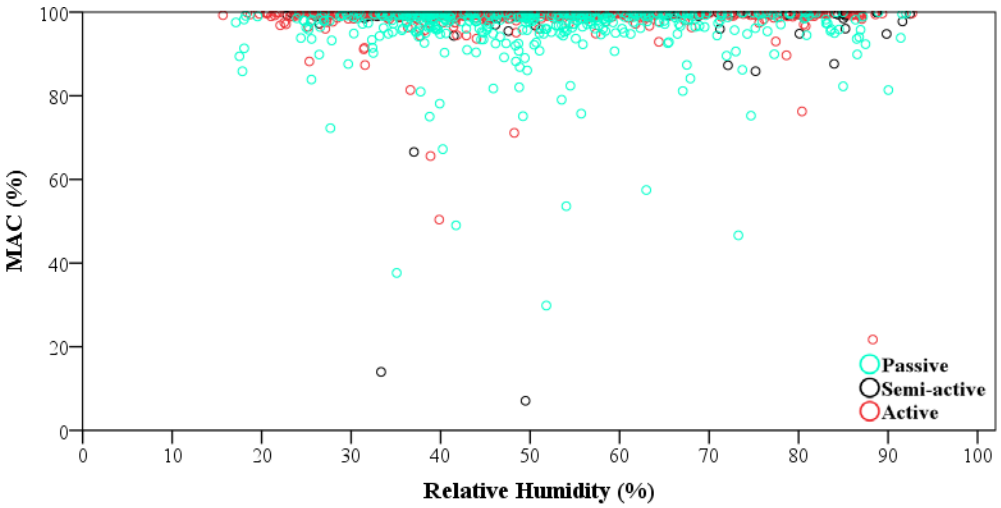


Figure 7.87 Relative humidity vs MAC value (around 0.35 Hz frequency)

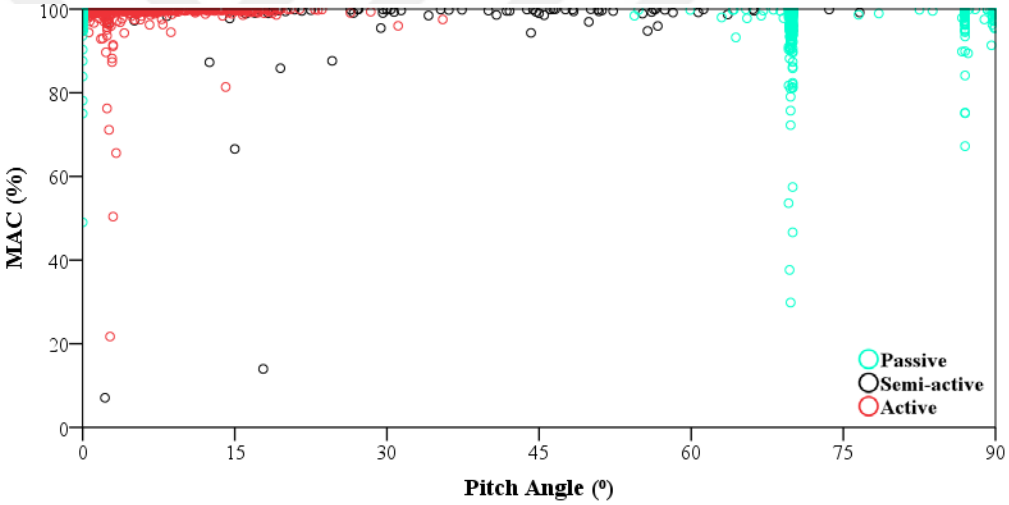


Figure 7.88 Pitch angle vs MAC value (around 0.35 Hz frequency)

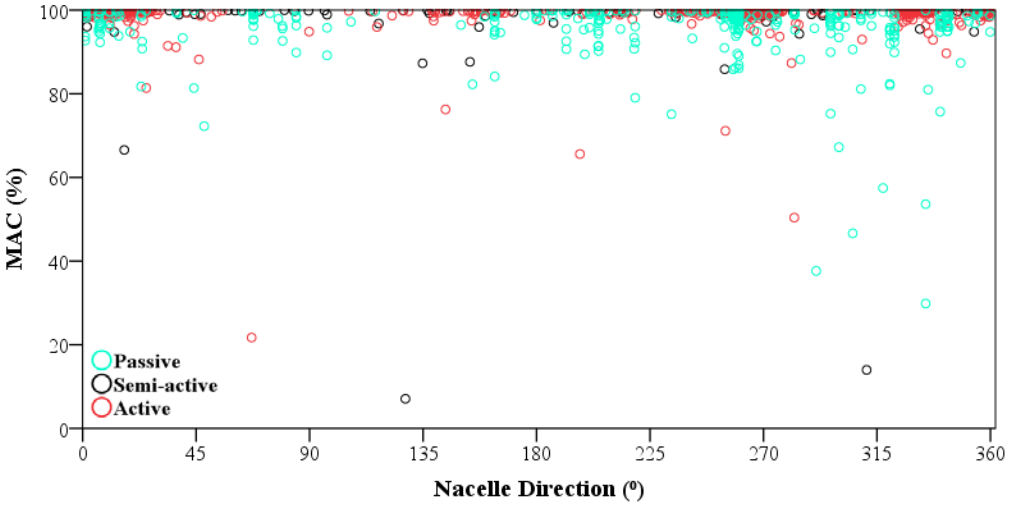


Figure 7.89 Nacelle direction vs MAC value (around 0.35 Hz frequency)

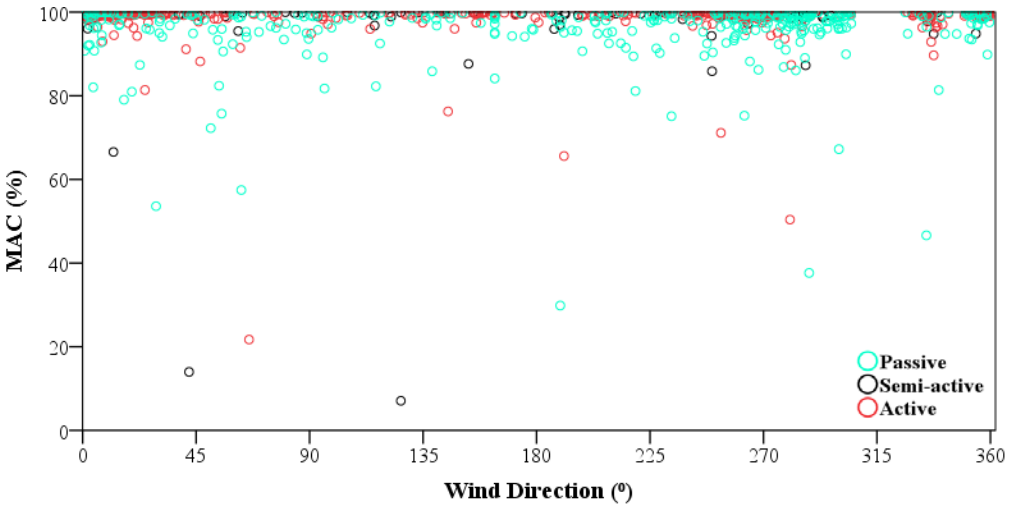


Figure 7.90 Wind direction vs MAC value (around 0.35 Hz frequency)

The estimated mode shapes around 0.35 Hz are generally parallel to each other. In 1 – 4 m/s wind speed range, mode shapes differ from the principal mode shape. In addition, at 11 and 16 RPM rotor speeds slight decreases are observed in MAC values. The decrease at 16 RPM rotor speed disappears with the increase of wind speed and therefore the pitch angle. It is observed that MAC values decrease around 30º, 260º, and 330º nacelle directions. Temperature, relative humidity, and wind direction have no clear influence on the mode shape.

Figure 7.91 – Figure 7.97 show the correlation between MAC values and operational/environmental conditions for estimated modes around 3.00 Hz frequency.

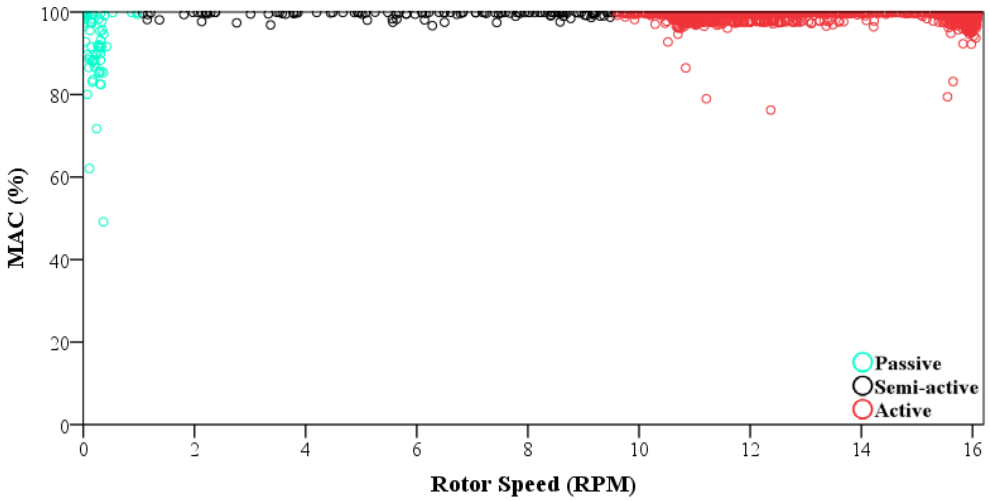


Figure 7.91 Rotor speed vs MAC value (around 3.00 Hz frequency)

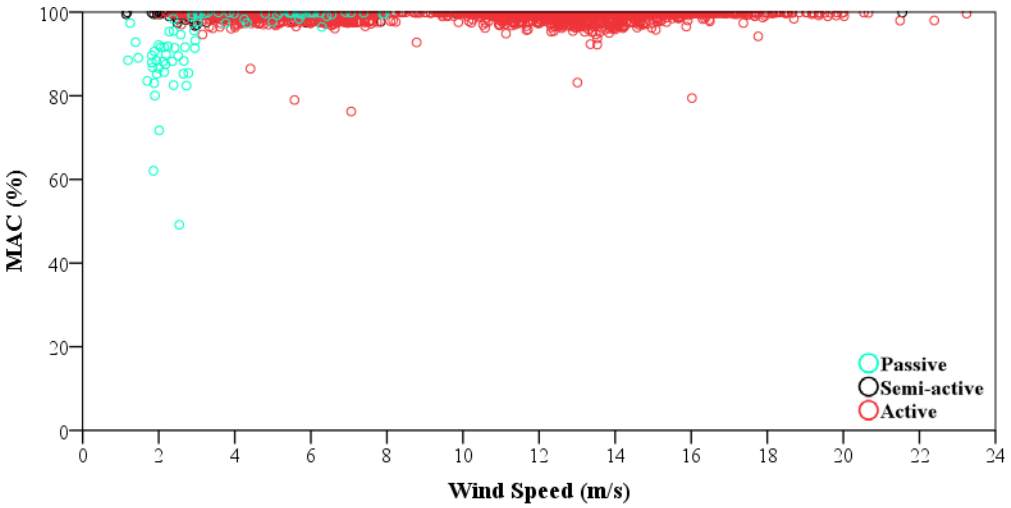


Figure 7.92 Wind speed vs MAC value (around 3.00 Hz frequency)

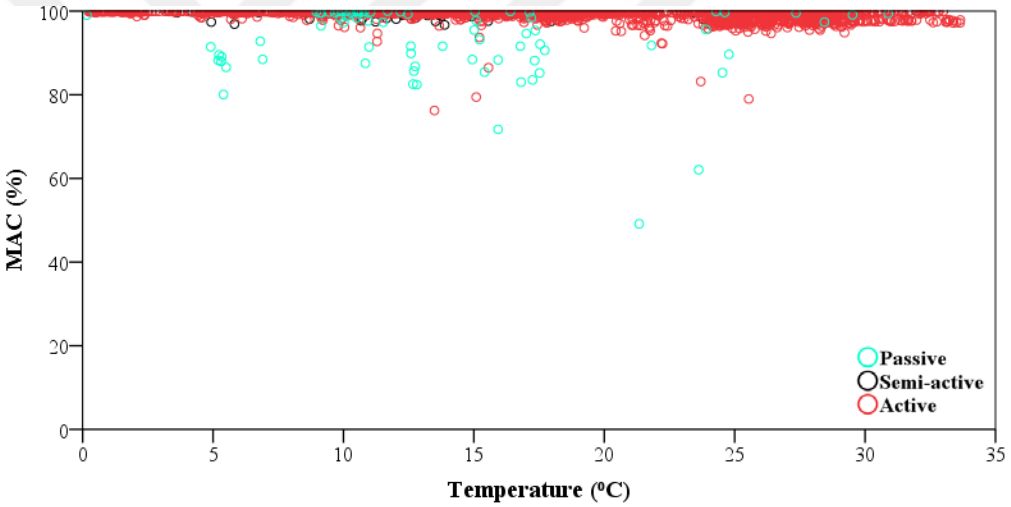


Figure 7.93 Temperature vs MAC value (around 3.00 Hz frequency)

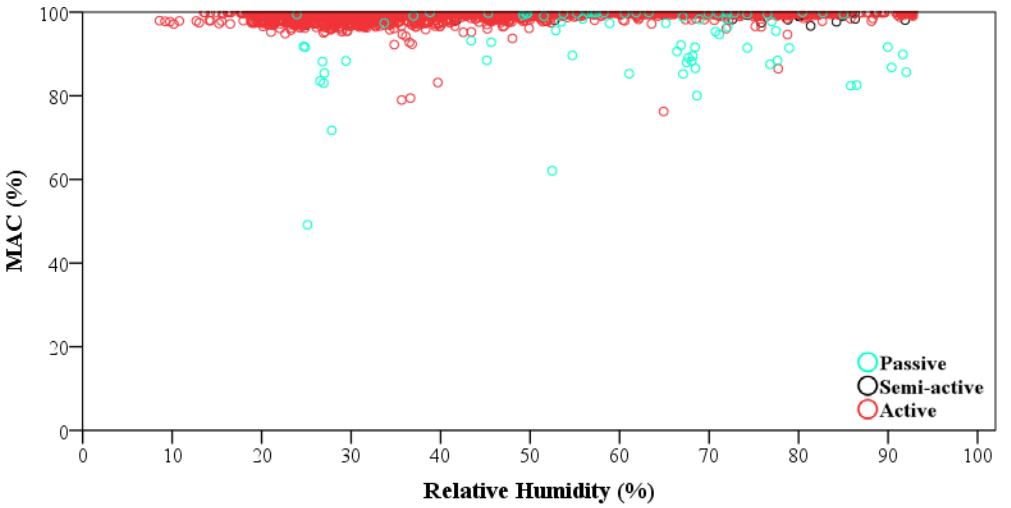


Figure 7.94 Relative humidity vs MAC value (around 3.00 Hz frequency)

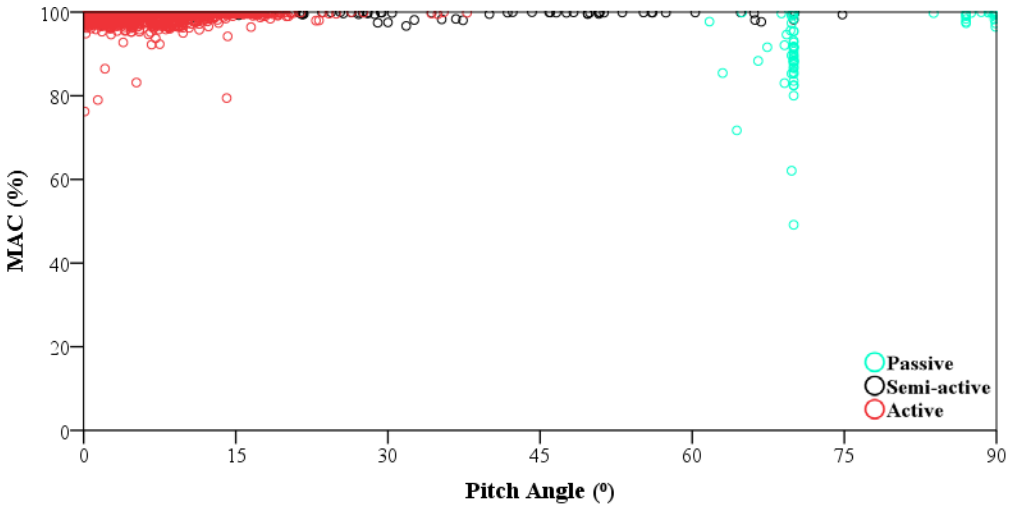


Figure 7.95 Pitch angle vs MAC value (around 3.00 Hz frequency)

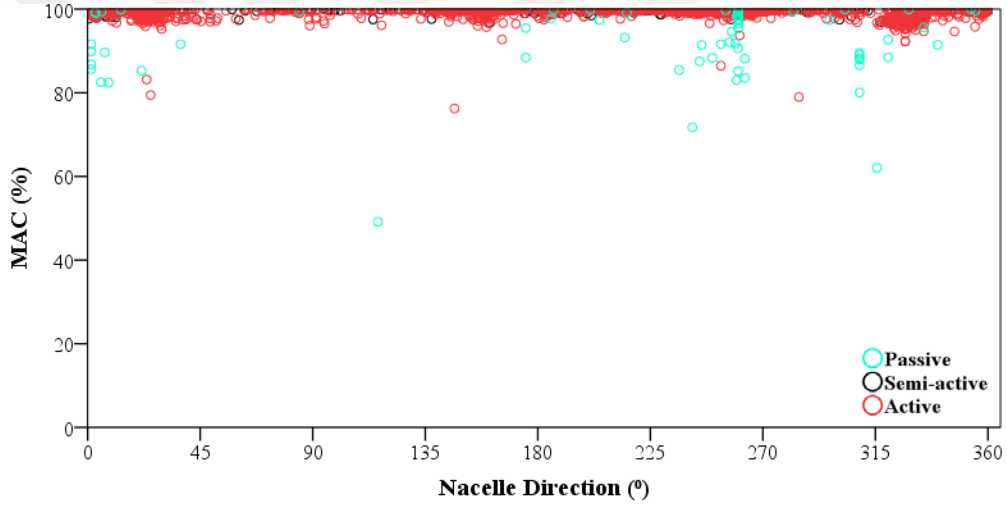


Figure 7.96 Nacelle direction vs MAC value (around 3.00 Hz frequency)

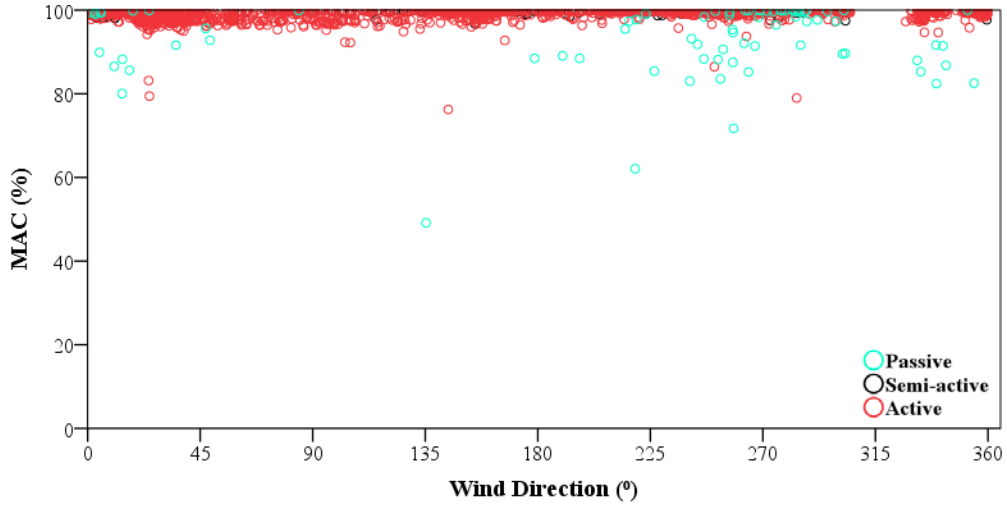


Figure 7.97 Wind direction vs MAC value (around 3.00 Hz frequency)

The majority of the MAC values of mode shapes estimated around 3.00 Hz are above 95%. Mode shapes of the passive state of the turbine in the 1-3 m/s wind speed range are estimated differently from the principal mode shape. Like the previous mode, MAC values decrease slightly at 11 and 16 RPM rotor speed. The decrease at 16 RPM rotor speed disappears after 15º pitch angle. It is observed that MAC values decrease around 30º, 150º, 260º, and 330º nacelle directions. There is no relation between MAC values and temperature, relative humidity, and wind direction.

Figure 7.98 – Figure 7.104 show the correlation between MAC values and operational/environmental conditions for estimated modes around 8.29 Hz frequency.

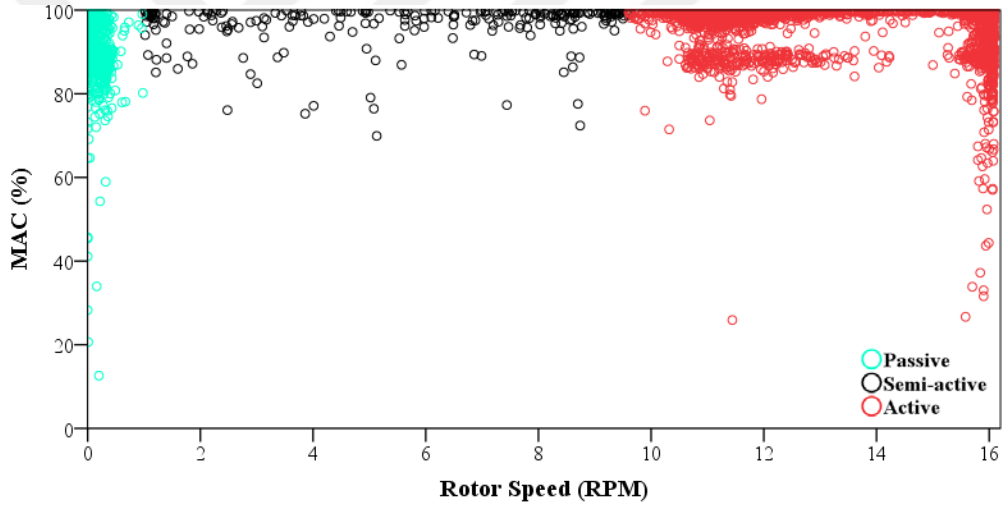


Figure 7.98 Rotor speed vs MAC value (around 8.29 Hz frequency)

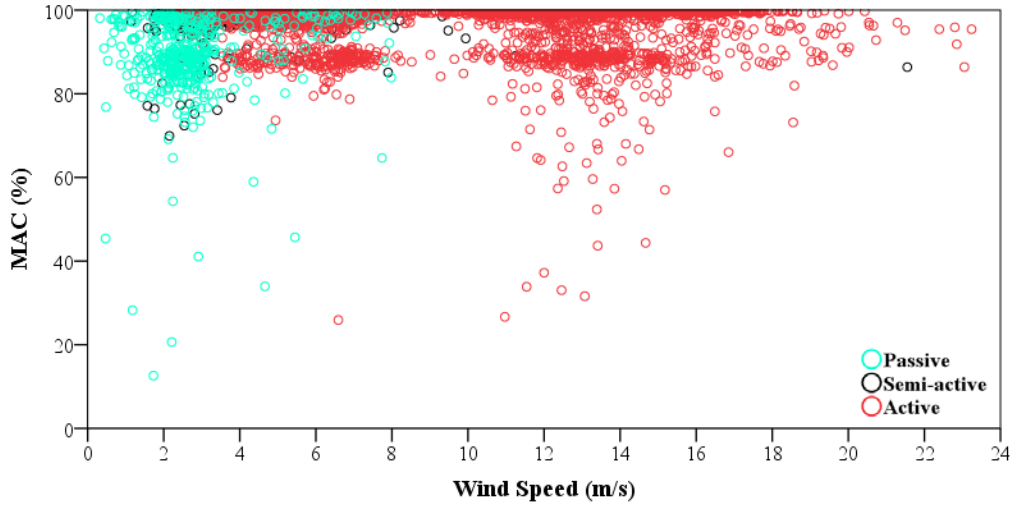


Figure 7.99 Wind speed vs MAC value (around 8.29 Hz frequency)

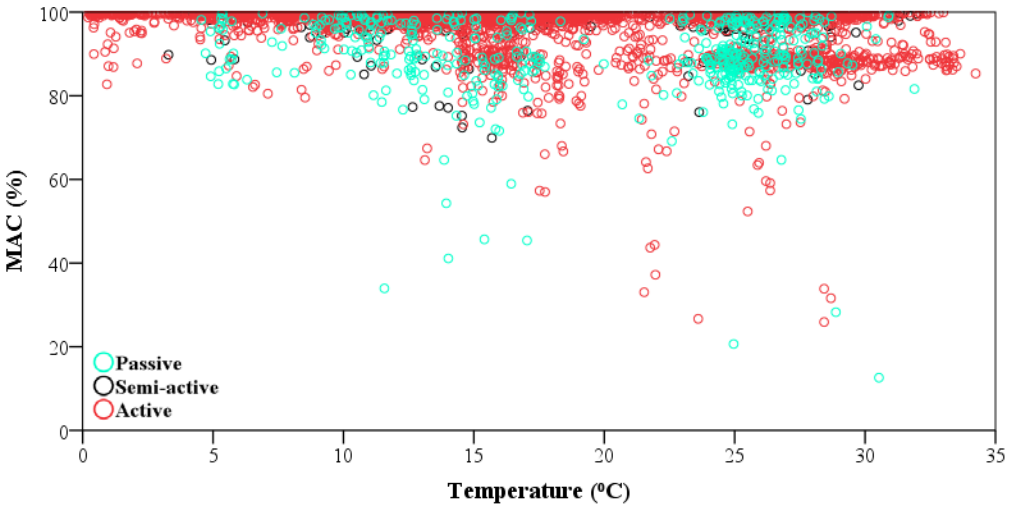


Figure 7.100 Temperature vs MAC value (around 8.29 Hz frequency)

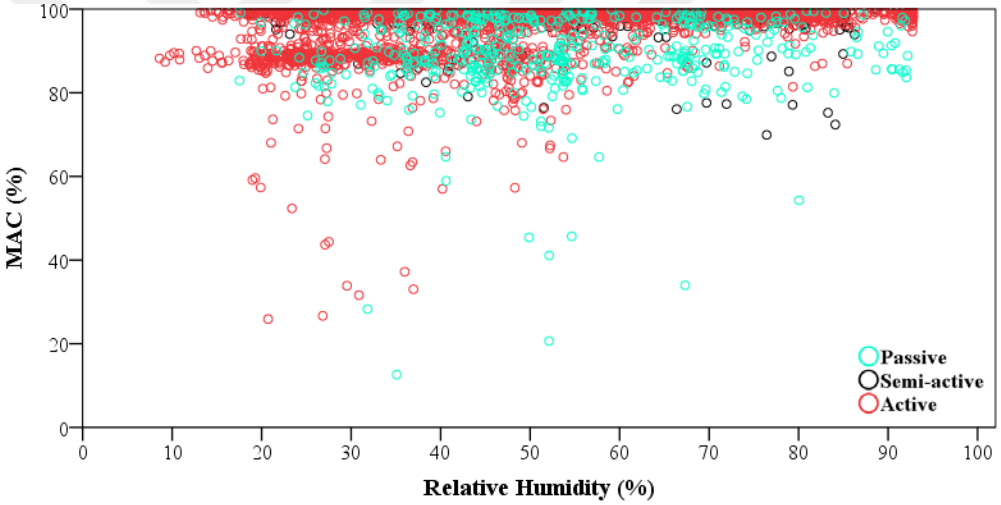


Figure 7.101 Relative humidity vs MAC value (around 8.29 Hz frequency)

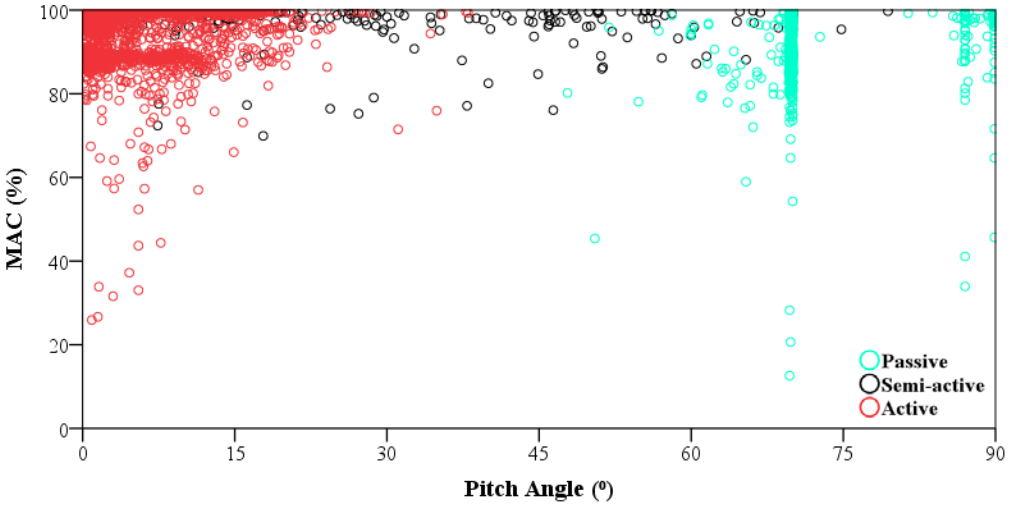


Figure 7.102 Pitch angle vs MAC value (around 8.29 Hz frequency)

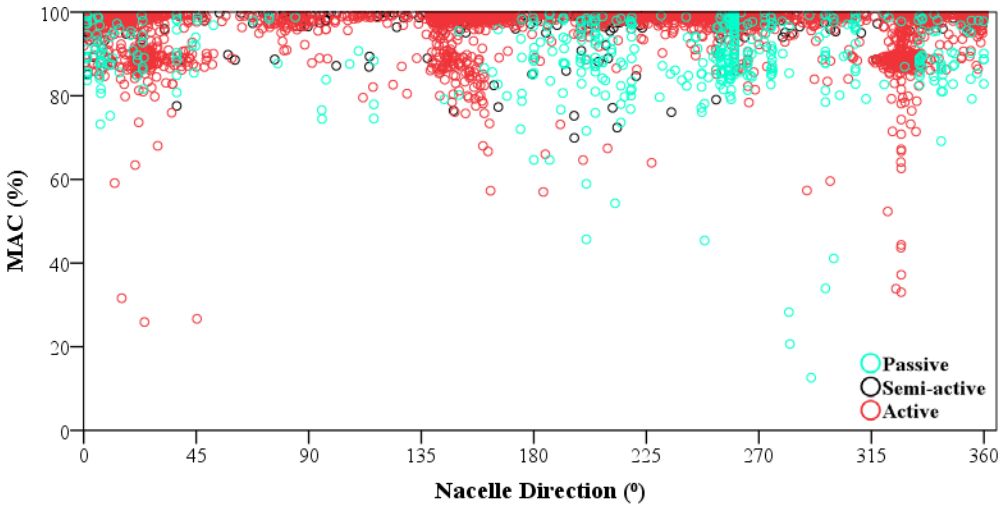


Figure 7.103 Nacelle direction vs MAC value (around 8.29 Hz frequency)

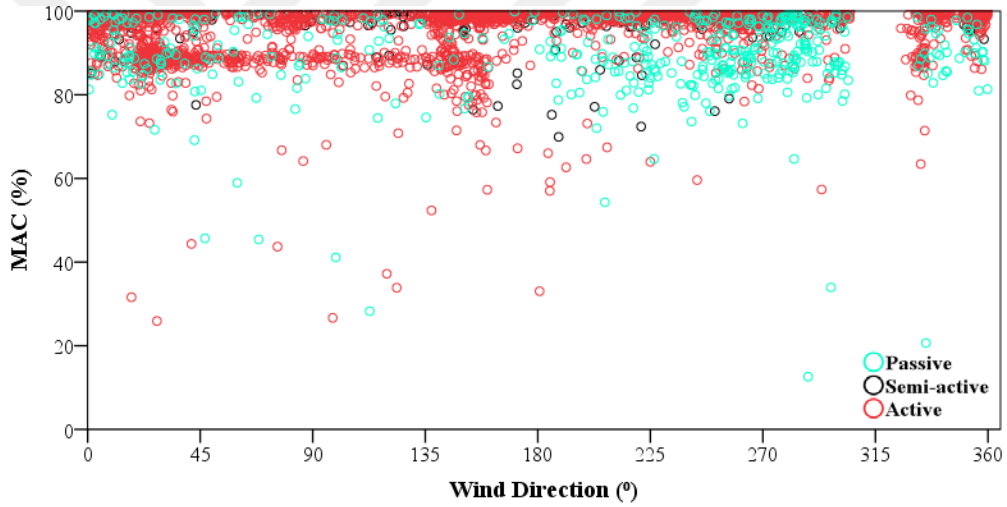


Figure 7.104 Wind direction vs MAC value (around 8.29 Hz frequency)

The majority of the MAC values of mode shapes estimated around 8.29 Hz are above 80%. Mode shapes estimated in passive cases differ according to principal mode shape at different levels. MAC values are lined up in a second row around 90% in 1 – 8 m/s and 10 – 16 m/s wind speed ranges. These wind speed ranges correspond to the rotor speed ranges of 11-13 RPM and 15-16 RPM for active cases respectively. MAC values between principal mode shape and mode shape estimated around rated wind speed (12 m/s) can take low values also. As the pitch angle rises above 15º, the scattering of the MAC values decreases, and the mode shapes are obtained closer to the principal mode shape. It is observed that MAC values decrease around 30º, 150º,

260º, 290º, and 330º nacelle directions. Temperature, relative humidity, and wind direction have no clear influence on the mode shape.

Figure 7.105 – Figure 7.111 show the correlation between MAC values and operational/environmental conditions for estimated modes around 16.00 Hz frequency.

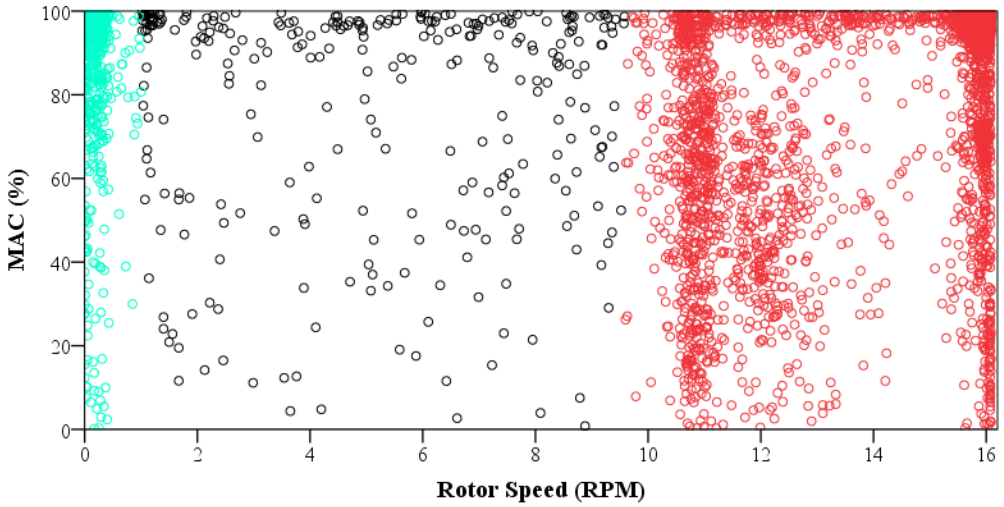


Figure 7.105 Rotor speed vs MAC value (around 16.00 Hz frequency)

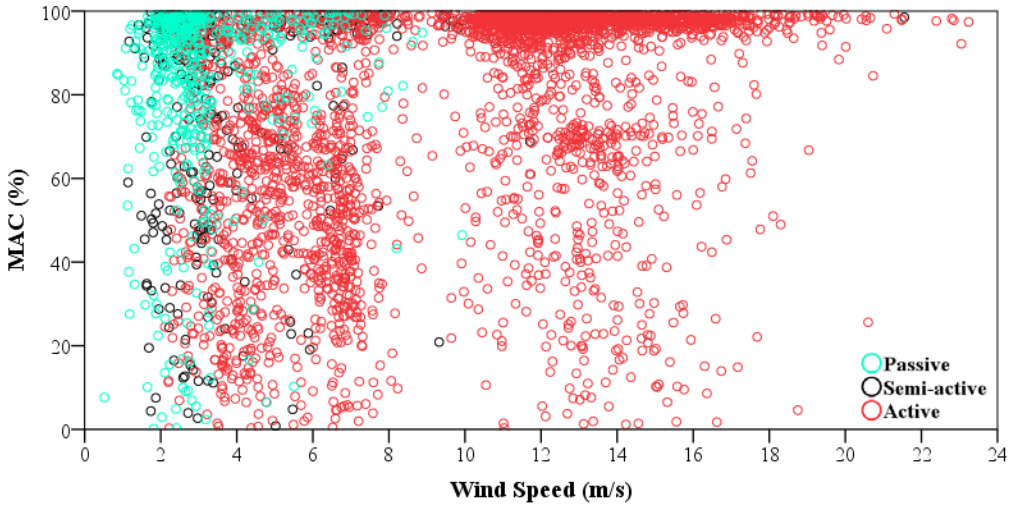


Figure 7.106 Wind speed vs MAC value (around 16.00 Hz frequency)

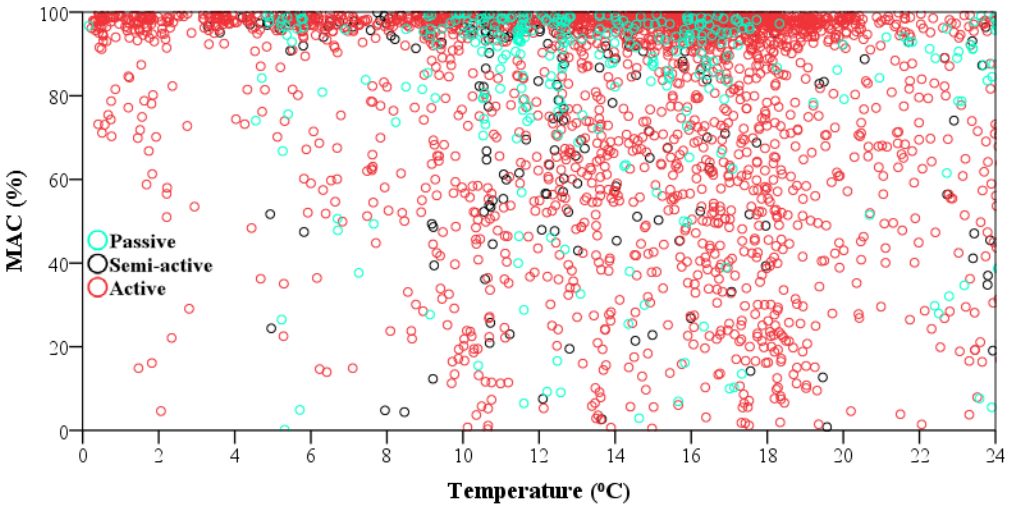


Figure 7.107 Temperature vs MAC value (around 16.00 Hz frequency)

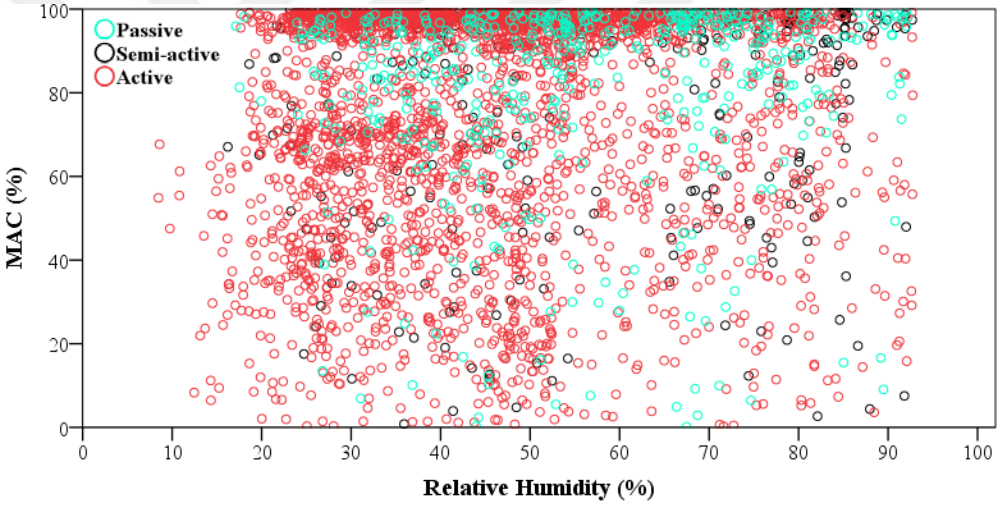


Figure 7.108 Relative humidity vs MAC value (around 16.00 Hz frequency)

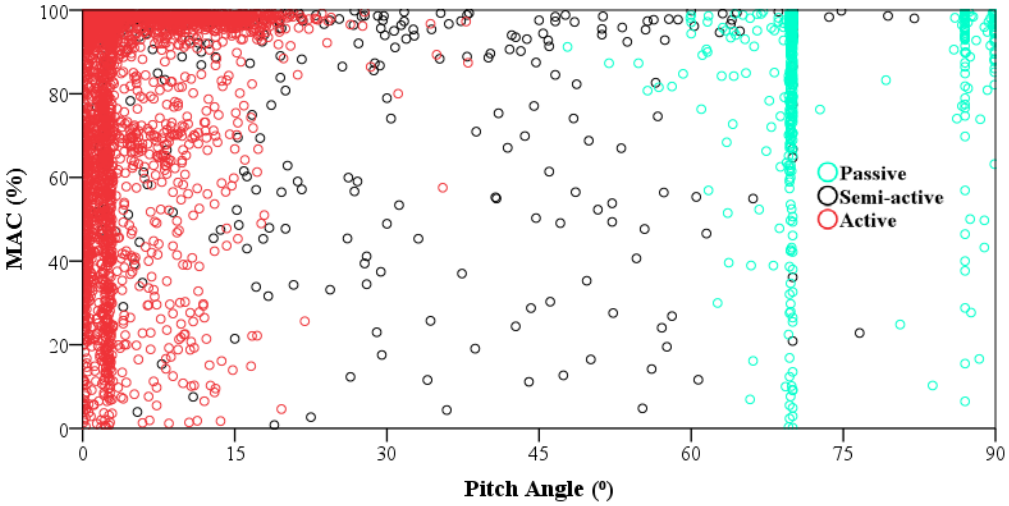


Figure 7.109 Pitch angle vs MAC value (around 16.00 Hz frequency)

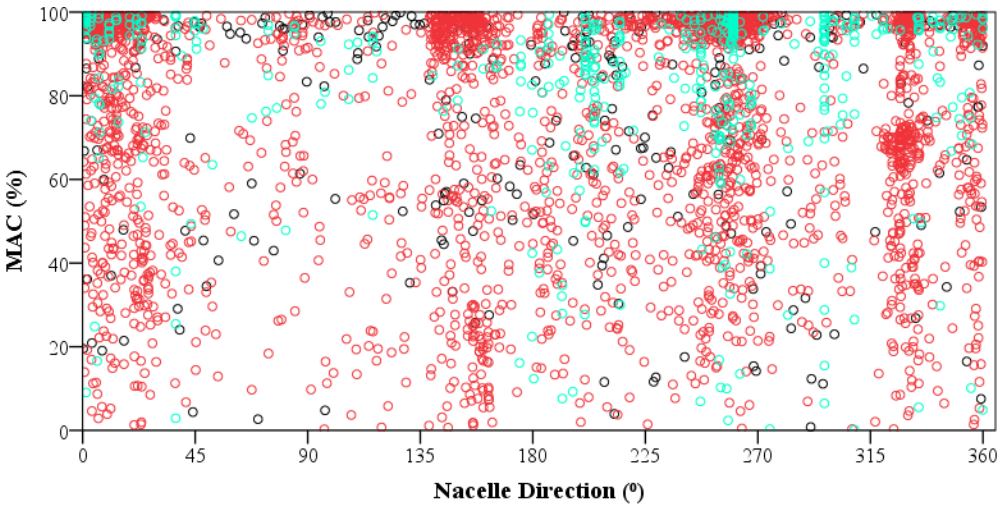


Figure 7.110 Nacelle direction vs MAC value (around 16.00 Hz frequency)

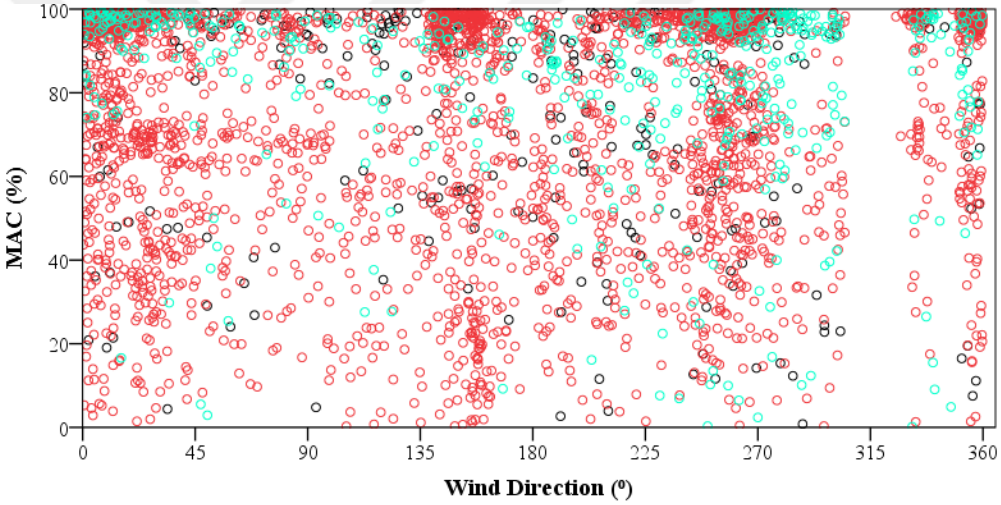


Figure 7.111 Wind direction vs MAC value (around 16.00 Hz frequency)

In 1 – 8 m/s and 10 – 16 m/s wind speed ranges, MAC values are obtained at any value between 0% and 100%. These wind speed ranges correspond to the rotor speed ranges of 11-13 RPM and 15-16 RPM for active cases respectively. After 3º pitch angle, scattering of the MAC values decrease considerably for active cases. It is observed that MAC values decrease around 30º, 150º, 260º, 330º, and 360º nacelle directions. Temperature, relative humidity, and wind direction have no clear influence on the mode shape.

CHAPTER 8
CONCLUSIONS AND FUTURE WORKS

8.1 Conclusions

The research work presented in this thesis mainly concerned with four subjects: (1) Designing a distributed data acquisition system for the subject in-service wind turbine, (2) developing a novel Autonomous and Continuous System Identification (ACSI) system, (3) sensitivity-based model updating of the wind turbine, and (4) determining the effect of operational and environmental conditions on the frequency, damping and mode shape of the wind turbine. Each of these subjects are summarized in the following.

First, a horizontal axis wind turbine with 2.5 MW capacity in Urla/Izmir is selected for the research and necessary permissions have been granted from the operating company. The wind profile of the region is identified by analyzing the four-year wind data recorded by the SCADA system. Main and secondary wind directions of the region are determined. Eleven uniaxial accelerometers, one triaxial accelerometer, three thermocouples and two relative humidity sensors are placed at the five levels of the wind turbine. The accelerometers are placed in the main and secondary wind directions. Current and voltage input modules and chassis are put at each level to digitize and synchronize the data recorded by sensors. A physical connection is provided with the turbine SCADA system to get operational and environmental data. P2P antenna set is used for the data and internet sharing between the turbine and the switchyard. Troubleshooting of all data acquisition system is done and continuous data acquisition is initialized.

A series of software is developed for fully automated data acquisition and system identification. The code run in the switchyard is in charge of instantaneously importing the operational and environmental data flowing in the SCADA system into the LabVIEW environment and transferring to the industrial computer in the turbine. Code developed for the turbine provide synchronized data acquisition from sensors,

calibration, filtering, decimating, and detrending the acceleration data, synchronizing the data sent from the switchyard with the acquired data, filing and transferring all data to the university campus. The third and last software created in the LabVIEW environment runs on the workstation in the campus. It manages getting data from the turbine and storing it to the Network Attached Storage (NAS). In case of any interruption in the data flow, it informs the relevant people via e-mail. All acquired data is saved in 600 seconds long files continuously and it can be easily changed if needed. The rest of the operations are executed by the MATLAB code developed in the campus environment. The directory where the data files are stored is constantly checked. A new file transferred from the turbine every 600 seconds is read for system identification processes. The acceleration data is processed by using the p-LSCF method and stabilization diagram is constructed according to the predefined stabilization criteria. Physical vibration modes are selected from the stabilization diagram and modal parameters (e.g., mode frequencies, damping ratios and mode shapes) are estimated. Operational and environmental conditions are calculated by averaging 600 seconds long data. The estimated modal parameters are matched with operational and environmental conditions and saved as a row in the results file with the date and time stamp. Modal parameters estimated from each 600 seconds long data file compared with the reference (benchmark) state. Considering the effect of operational and environmental conditions on modal parameters, if there is a difference more than the threshold value, a report stating that there may be a damage on the wind turbine is automatically prepared and sent to the relevant people by e-mail. Although, last part of the system is not in the scope of the thesis, considerable progress has been made in integrating this part into the system. All these operations are performed every 600 seconds without any user intervention. Autonomous and Continuous System Identification (ACSI) system continues to record and process data for further research.

An analytical model of the wind turbine is created in ANSYS environment. Foundation and tower are modelled with the finite element while a simplified approach is used for rotor and nacelle. An analytical modal analysis is performed. The first two modes identified experimentally by the ACSI system, and their analytical counterparts are matched. The frequency differences were -0.30% and 1.56% for first and second

mode respectively. The MAC values were 98.9% and 94.6% for first and second mode respectively before updating. The objective function is constructed using the aforementioned responses and elasticity modulus of different parts of the tower, rotor mass and nacelle mass are selected as parameters to be updated. Sensitivity analysis, which determines the sensitivity of the responses to unit changes in the parameters, is performed and the model updating is completed using the sensitivity matrix. As a result of sensitivity-based FEM updating, the structural frequencies of the first two modes are equalized to the mode frequencies of the real structure. The mode shapes, on the other hand, are a little closer to the experimentally estimated mode shapes. After calibrating the finite element model of the wind turbine, a series of transient analysis is needed to be performed to understand the effect of wind speed on the wind turbine dynamics. For the calculation of wind loads acting on the rotor a MATLAB code is developed using the Blade Element Momentum (BEM) theory. The wind loads that occur on the rotor blades at different wind speeds are calculated by considering the rotor speed and pitch angle changes. The wind speed profiles are determined, and wind loads acting on the turbine tower are calculated. Multi-hazard transient analyses are performed with the Imperial Valley Earthquake (1940) and two different wind speed levels (7 m/s and 12 m/s). In order to see the wind effect clearly, another analysis is performed with only earthquake hazard. It can be seen that the wind effect shifted the oscillation of the turbine in the direction of the wind and increased the amplitudes of the oscillation.

In order to determine the effect of operational and environmental conditions on wind turbine dynamic characteristics, 600 seconds long 13277 data files were recorded and processed by the ACSI system. Firstly, histograms of the eight operational and environmental conditions in which the data were collected are presented. To correctly interpret operational and environmental effects on modal parameters of the wind turbine, the relationship between operational and environmental conditions are presented and the operating principle of the wind turbine is explained in detail. The effect of operational and environmental conditions on mode frequencies of the first four modes are shown. Major findings can be summarized as follows:

- The standard deviation of the estimated frequency values for passive cases is higher than for active cases. This can be explained by the increased wind speed and the consequent rotation of the rotor, increase the excitation level of the structure and ensuring more reliable modal parameter estimates.

- For active cases, frequency estimates are increasing with the increasing of the rotor speed. The gyroscopic effect, which is formed by the rotation of the rotor blades and increases its effect with the increase of the rotation speed, limits the vibration amplitudes of the turbine.

- It is observed that wind speed and the mode frequencies are positively correlated. Note that in 3-12 m/s wind speed (cut-in and rated wind speed) range, rotor speed increases as the wind speed increases. Although the rotor speed remains constant, frequencies keep climbing after 12 m/s wind speed for identified modes around 0.35 Hz and 8.29 Hz.

- For modes around 3.00 Hz and 16.00 Hz different behavior is observed than others. After rated wind speed frequency estimates are getting lower. Because the pitch angle of the blades is increased by the turbine control system to keep the rotor speed at a constant 16 RPM after the rated wind speed. This leads to decrease wind loads on the rotor considerably. So, it can be concluded that wind loads affect the frequencies of these two modes.

- For the last three modes, the scattering of the frequency estimates is reduced with the increasing wind speed.

- Frequency estimates for all modes decrease with increasing ambient temperature. The wind turbine, which is a steel structure, becomes more flexible due to dilation.

- With the increase in relative humidity frequencies are increase for mode around 8.29 Hz and decrease for mode around 3.00 Hz. For modes around

0.35 Hz. and 16.00 Hz, no clear relationship is observed between relative humidity and frequency.

- The scattering of the frequency estimates considerably decreases after 5º pitch angle for the last three modes.

- There is no clear correlation between frequency estimates and wind/nacelle directions.

The effect of operational and environmental conditions on damping ratios of the first four modes can be summarized as follows:

- Damping ratios are estimated up to 8% for the first two vibration modes and %6 for the last two vibration modes.

- The standard deviation of the estimated damping ratios for passive cases is higher than for active cases, expect the mode identified around 3.00 Hz frequency. This can be explained by the increased wind speed and the consequent rotation of the rotor, increase the excitation level of the structure and ensuring more reliable modal parameter estimates.

- Damping ratio estimates increase as rotor speed increases. The aerodynamic damping caused by the interaction of turbine blades as they pass near the tower contributes to the total damping of the turbine.

- There is a clear positive correlation between wind speed and damping ratios. This relationship continues after the rated wind speed of 12 m/s, where the rotor speed remains constant. In addition, a jump in damping ratios is observed from about 2.00% to around 3.70% at rated wind speed for modes estimated around 3.00 Hz frequency.

- In the first three modes, the increase in ambient temperature slightly affects the damping ratio estimates. For the fourth mode, although there is a decrease in damping ratios around 2 ºC, no general trend between temperature and damping ratio is observed.

- In general, the damping ratios tend to decrease with the increase in the ambient humidity.

- Like the frequency estimates, scattering of the damping ratio estimates decrease with increasing pitch angle of the rotor blades.

- There is no clear correlation between damping ratio estimates and wind/nacelle directions.

The effect of operational and environmental conditions on mode shape of the first four modes can be summarized as follows:

- The majority of the MAC values of mode shapes estimated around 0.35 Hz, 3.00 Hz, and 8.29 Hz are above 95%, 95%, and 80% respectively. MAC values of mode shapes estimated around 16.00 Hz are obtained at any value between 0% and 100%.

- For the first three modes, around 11 RPM and 16 RPM rotor speed slight decreases are observed in MAC values. The decrease at 16 RPM rotor speed disappears with the increase of wind speed and therefore the pitch angle.

- For the first two modes, mode shapes are estimated differently from the principal mode shape in 1-4 m/s wind speed. In the mode identified around 8.29 Hz frequency, mode shapes differ according to principal mode shape at different levels for passive cases and MAC values are lined up in a second row around 90% in 1 – 8 m/s and 10 – 16 m/s wind speed ranges for active cases.

- In 1 – 8 m/s and 10 – 16 m/s wind speed ranges, MAC values are obtained at any value between 0% and 100% for the mode identified around 16.00 Hz.

- In general, standard deviation of the MAC values decreases with increasing the pitch angle of the blades. Decrease in scattering of the MAC values is observed as jumps at 10º, 15º, 15º, and 3º pitch angle for the first, second, third and the fourth vibration modes respectively.

- The nacelle direction affects the mode shape of the wind turbine. Relatively low MAC values are calculated especially around 30º, 150º, 260º, and 330º nacelle directions.

- Temperature, relative humidity, and wind direction have no clear influence on the mode shapes.

Note that the results are based on the assumption that accelerometers are not affected by changes in operational and environmental conditions.

8.2 Recommendations for Future Research

Based on the presented research, the following research recommendations are offered for future studies:

- Acceleration data recording longer than one year, extending to several years, can provide more information about the effect of environmental factors as it will be recorded under wider ranges of environmental conditions.

- A more detailed data acquisition and system identification system can be developed with sensors to be placed on the rotor blades together with the wind turbine tower.

- The ACSI system can be evolved into a comprehensive structural health monitoring system that takes into account the effect of environmental and operational conditions.

- It can be investigated how different turbines respond to changes in environmental and operational conditions, by processing the data recorded from data acquisition systems to be installed on wind turbines of different sizes and types with the ACSI system developed within the scope of the thesis.

- With the help of the data to be recorded and processed with the ACSI system during possible earthquakes, the multi-hazard (earthquake and wind) behaviors of wind turbines can be better interpreted. Since the ACSI system will continue to operate after this thesis study, it allows the mentioned study to be carried out.

- By installing the ACSI system in different engineering structures, the factors affecting the dynamic characteristics of these structures can be determined.

- A constantly updated modal parameter prediction model can be developed by processing continuously obtained modal parameter estimations and environmental operational factors with artificial neural networks.

- More reliable results can be obtained by combining the vibration-based system identification provided by the ACSI system with different system identification methods (e.g., acoustic emission and image processing methods).

- More accurate assessments can be done with integration of the ACSI system with the digital twin of the wind turbine which is a digital representation of the physical structure.

REFERENCES

Acoustical Society of America. (2001). American National Standard Vibration of Buildings - Guidelines for the Measurement of Vibrations and Evaluation of Their Effects on Buildings (ANSI S2.47). https://webstore.ansi.org/standards/asa/ansis2471990r1997

Alkayem, N. F., Cao, M., Zhang, Y., Bayat, M., & Su, Z. (2018). Structural damage detection using finite element model updating with evolutionary algorithms: a survey. *Neural Computing and Applications*, *30*(2), 389-411. https://doi.org/10.1007/s00521-017-3284-1

Ali, A., De Risi, R., & Sextos, A. (2021). Seismic assessment of wind turbines: How crucial is rotor-nacelle-assembly numerical modeling?. *Soil Dynamics and Earthquake Engineering*, *141*, 106483. https://doi.org/10.1016/j.soildyn.2020.106483

Allemang, R. J. (2003). The modal assurance criterion–twenty years of use and abuse. *Sound and vibration*, *37*(8), 14-23.

Alotto, P., Gaggero, M., Molinari, G., & Nervi, M. (1997). A" design of experiment" and statistical approach to enhance the" generalised response surface" method in the optimisation of multiminima problems. *IEEE Transactions on Magnetics*, *33*(2), 1896-1899. https://doi.org/10.1109/20.582657

Alves, M. M., Pirmez, L., Rossetto, S., Delicato, F. C., de Farias, C. M., Pires, P. F. et al. (2017). Damage prediction for wind turbines using wireless sensor and actuator networks. *Journal of Network and Computer Applications*, *80*, 123-140. https://doi.org/10.1016/j.jnca.2016.12.027

ANSYS (2019) R3 Issued by ANSYS, Inc., Southpointe 2600 ANSYS Drive Canonsburg, PA 15317, USA.

Avendaño-Valencia, L. D., & Fassois, S. D. (2017). Damage/fault diagnosis in an operating wind turbine under uncertainty via a vibration response Gaussian mixture random coefficient model based framework. *Mechanical Systems and Signal Processing*, *91*, 326-353. https://doi.org/10.1016/j.ymssp.2016.11.028

Beck, J. L., & Katafygiotis, L. S. (1998). Updating models and their uncertainties. I: Bayesian statistical framework. *Journal of Engineering Mechanics-Proceedings of the ASCE*, *124*(4), 455-462. https://doi.org/10.1061/(asce)0733-9399(1998)124:4(455)

Brincker, R., & Ventura, C. (2015). Introduction to operational modal analysis. Chichester: John Wiley & Sons.

Brincker, R., Zhang, L., & Andersen, P. (2001). Modal identification of output-only systems using frequency domain decomposition. *Smart materials and structures*, *10*(3), 441. https://doi.org/10.1088/0964-1726/10/3/303

Butterfield, C. P., Scott, G., & Musial, W. (1992). Comparison of wind tunnel airfoil performance data with wind turbine blade data. https://doi.org/10.1115/1.2929989

Carvalho, J., Datta, B. N., Gupta, A., & Lagadapati, M. (2007). A direct method for model updating with incomplete measured data and without spurious modes. *Mechanical Systems and Signal Processing*, *21*(7), 2715-2731. https://doi.org/10.1016/j.ymssp.2007.03.001

Chen, B., Zhang, Z., Hua, X., Basu, B., & Nielsen, S. R. (2017). Identification of aerodynamic damping in wind turbines using time-frequency analysis. *Mechanical Systems and Signal Processing*, *91*, 198-214. https://doi.org/10.1016/j.ymssp.2017.01.010

Chen, C., Duffour, P., & Fromme, P. (2020). Modelling wind turbine tower-rotor interaction through an aerodynamic damping matrix. *Journal of Sound and Vibration*, *489*, 115667. https://doi.org/10.1016/j.jsv.2020.115667

Chopra, A. K. (2012). *Dynamics of structures: theory and applications to earthquake engineering (4th ed.)*. Prentice Hall.

Cong, S., Hu, S. L. J., & Li, H. J. (2022). Using incomplete complex modes for model updating of monopiled offshore wind turbines. *Renewable Energy*, *181*, 522-534. https://doi.org/10.1016/j.renene.2021.09.022

Conn, A. R., Gould, N. I., & Toint, P. L. (2000). *Trust region methods*. Society for Industrial and Applied Mathematics.

Dixon, S. L., & Hall, C. (2013). *Fluid mechanics and thermodynamics of turbomachinery*. Butterworth-Heinemann.

Disaster and Emergency Management Authority [AFAD]. (2023, February 1). *Turkey Seismic Hazard Map.* http://tdth.afad.gov.tr/TDTH

Dost Enerji (2023, February 1). *Kores Kocadağ Wind Power Plant*. https://www.dostenerji.com/en/plants/kores-kocadag-wpp/

Durmazgezer, E., Yucel, U., & Ozcelik, O. (2019). Damage identification of a reinforced concrete frame at increasing damage levels by sensitivity-based finite element model updating. *Bulletin of Earthquake Engineering*, *17*(11), 6041-6060. https://doi.org/10.1007/s10518-019-00690-5

El-Kafafy, M., Guillaume, P., & Peeters, B. (2013). Modal parameter estimation by combining stochastic and deterministic frequency-domain approaches. *Mechanical Systems and Signal Processing*, *35*(1-2), 52-68. https://doi.org/10.1016/j.ymssp.2012.08.025

Emre, Ö., Özalp, S., Doğan, A., Özaksoy, V., Yıldırım, C., Göktaş, F. (2005). İzmir yakın çevresinin diri fayları ve deprem potansiyelleri (In Turkish), Mineral Research and Exploration General Directorate report.

Fang, S. E., Perera, R., & De Roeck, G. (2008). Damage identification of a reinforced concrete frame by finite element model updating using damage parameterization. *Journal of Sound and Vibration*, *313*(3-5), 544-559. https://doi.org/10.1016/j.jsv.2007.11.057

Felber, A. J. (1993). *Development of a hybrid bridge evaluation system* [Doctoral dissertation]. University of British Columbia.

FEMtools (2017) Ver.4.0.0.1830 Dynamic Design Solutions. Ambachtenlaan 14/5, B-3001, Leuven, Belgium.

Friswell M.I. & Mottershead, J.E. (1995). *Finite element model updating in structural dynamics.* Kluwer Academic Publishers.

Fontecha, R., Henneke, B., Kemper, F., & Feldmann, M. (2017). Aerodynamic properties of wind turbine towers based on wind tunnel experiments. *Procedia engineering*, *199*, 3121-3126. https://doi.org/10.1016/j.proeng.2017.09.557

García, D., & Tcherniak, D. (2019). An experimental study on the data-driven structural health monitoring of large wind turbine blades using a single accelerometer and actuator. *Mechanical Systems and Signal Processing*, *127*, 102-119. https://doi.org/10.1016/j.ymssp.2019.02.062

Guillaume, P., Verboven, P., Vanlanduit, S., Van Der Auweraer, H., & Peeters, B. (2003, February 3-6). *A poly-reference implementation of the least-squares complex frequency-domain estimator.* In Proceedings of IMAC (Vol. 21, pp. 183-192). Kissimmee, FL: A Conference & Exposition on Structural Dynamics, Society for Experimental Mechanics.

Häckell, M. W., & Rolfes, R. (2013). Monitoring a 5 MW offshore wind energy converter—Condition parameters and triangulation based extraction of modal parameters. *Mechanical Systems and Signal Processing*, *40*(1), 322-343. https://doi.org/10.1016/j.ymssp.2013.04.004

Heylen, W., Lammens, S., & Sas, P. (1998). *Modal analysis theory and testing*. Katholieke Universiteit Leuven.

Hines, E. M., Baxter, C. D., Ciochetto, D., Song, M., Sparrevik, P., Meland, H. J et al. (2023). Structural instrumentation and monitoring of the Block Island Offshore Wind Farm. *Renewable Energy*. https://doi.org/10.1016/j.renene.2022.11.115

Hofmeister, B., Bruns, M., & Rolfes, R. (2019). Finite element model updating using deterministic optimisation: A global pattern search approach. *Engineering Structures*, *195*, 373-381. https://doi.org/10.1016/j.engstruct.2019.05.047

Holland, J. (1975). *Adaptation in natural and artificial systems*. University of Michigan Press.

Hu, W. H., Thöns, S., Rohrmann, R. G., Said, S., & Rücker, W. (2015). Vibration-based structural health monitoring of a wind turbine system. Part I: Resonance phenomenon. *Engineering Structures*, *89*, 260-272. http://dx.doi.org/10.1016/j.engstruct.2014.12.034

Hu, W. H., Thöns, S., Rohrmann, R. G., Said, S., & Rücker, W. (2015). Vibration-based structural health monitoring of a wind turbine system Part II: Environmental/operational effects on dynamic properties. *Engineering Structures*, *89*, 273-290. http://dx.doi.org/10.1016/j.engstruct.2014.12.035

International Energy Agency [IEA]. (2023, February 1). *Key World Energy Statistics 2021.* https://www.iea.org/reports/key-world-energy-statistics-2021

James III, G. H., Carne, T. G., & Lauffer, J. P. (1993). *The natural excitation technique (NExT) for modal parameter extraction from operating wind turbines* (No. SAND-92-1666). Sandia National Labs., Albuquerque, NM (United States).

Kilic, G., & Unluturk, M. S. (2015). Testing of wind turbine towers using wireless sensor network and accelerometer. *Renewable Energy*, *75*, 318-325. https://doi.org/10.1016/j.renene.2014.10.010

Katafygiotis, L. S., & Beck, J. L. (1998). Updating models and their uncertainties. II: Model identifiability. *Journal of Engineering Mechanics*, *124*(4), 463-467. https://doi.org/10.1061/(asce)0733-9399(1998)124:4(463)

Khazaee, M., Derian, P., & Mouraud, A. (2022). A comprehensive study on Structural Health Monitoring (SHM) of wind turbine blades by instrumenting tower using machine learning methods. *Renewable Energy*, *199*, 1568-1579. https://doi.org/10.1016/j.renene.2022.09.032

Kim, H. C., Kim, M. H., & Choe, D. E. (2019). Structural health monitoring of towers and blades for floating offshore wind turbines using operational modal analysis and modal properties with numerical-sensor signals. *Ocean Engineering*, *188*, 106226. https://doi.org/10.1016/j.oceaneng.2019.106226

Kirkpatrick, S., Gelatt Jr, C. D., & Vecchi, M. P. (1983). Optimization by simulated annealing. *science*, *220*(4598), 671-680. https://doi.org/10.1126/science.220.4598.671

LabVIEW (2020) *Professional development system by National Instruments.* Texas, USA.

Maia, N.M.M. & Silva, J.M.M. (1997). *Theoretical and Experimental Modal Analysis.* Research Studies Press.

Marwala, T. (2010). *Finite element model updating using computational intelligence techniques: applications to structural dynamics.* London: Springer.

MATLAB (2019). *The MathWorks Inc.* Massachusetts, USA.

Meng, J., Dai, K., Zhao, Z., Mao, Z., Camara, A., Zhang, S., & Mei, Z. (2020). Study on the aerodynamic damping for the seismic analysis of wind turbines in operation. *Renewable Energy*, *159*, 1224-1242. https://doi.org/10.1016/j.renene.2020.05.181

Moaveni, B., Stavridis, A., Lombaert, G., Conte, J. P., & Shing, P. B. (2013). Finite-element model updating for assessment of progressive damage in a 3-story infilled RC frame. *Journal of Structural Engineering*, *139*(10), 1665-1674. https://doi.org/10.1061/(ASCE)ST.1943-541X.0000586

Mottershead, J. E., & Friswell, M. I. (1993). Model updating in structural dynamics: a survey. *Journal of sound and vibration*, *167*(2), 347-375. http://dx.doi.org/10.1006/jsvi.1993.1340

National Instruments (2023, February 1). *LabVIEW Documentation*. https://www.ni.com/docs/en-US/bundle/labview/page/lvhelp/labview_help.html

Neu, E., Janser, F., Khatibi, A. A., & Orifici, A. C. (2017). Fully automated operational modal analysis using multi-stage clustering. *Mechanical Systems and Signal Processing*, *84*, 308-323. https://doi.org/10.1016/j.ymssp.2016.07.031

Nocedal, J., & Wright, S. J. (1999). *Numerical optimization*. Springer New York.

Ozturkoglu O., Altunevlek, D., Olgun, G., & Ozcelik, O. (2018, September 17-18). *Model Updating and Damage Detection of a 3D Printed Model Frame.* PIET-18: International Conference on Innovation in “Engineering and Thecnology”, Paris, France.

Pacheco-Chérrez, J., & Probst, O. (2022). Vibration-based damage detection in a wind turbine blade through operational modal analysis under wind excitation. *Materials Today: Proceedings*, *56*, 291-297. https://doi.org/10.1016/j.matpr.2022.01.159

Pahner, U. (1998). *A general design tool for the numerical optimisation of electromagnetic energy transducers.* [Doctoral dissertation]. Katholieke Universiteit Leuven.

Peeters, B., & De Roeck, G. (1999). Reference-based stochastic subspace identification for output-only modal analysis. *Mechanical systems and signal processing*, *13*(6), 855-878. https://doi.org/10.1006/mssp.1999.1249

Peeters, B., Van der Auweraer, H., Guillaume, P., & Leuridan, J. (2004). The PolyMAX frequency-domain method: a new standard for modal parameter estimation?. *Shock and Vibration*, *11*(3-4), 395-409. https://doi.org/10.1155/2004/523692

Pereira, S., Pacheco, J., Pimenta, F., Moutinho, C., Cunha, Á., & Magalhães, F. (2023). Contributions for enhanced tracking of (onshore) wind turbines modal parameters. *Engineering Structures*, *274*, 115120. https://doi.org/10.1016/j.engstruct.2022.115120

Pintelon R. & Schoukens, J. (2001). *System Identification: A Frequency Domain Approach*. IEEE Press and John Wiley & Sons.

Pintelon, R., Guillaume, P., Rolain, Y., Schoukens, J., & Van Hamme, H. (1994). Parametric identification of transfer functions in the frequency domain-a survey. *IEEE Transactions on Automatic Control, 39*(11)*,* 2245-2260. https://doi.org/10.1109/9.333769

Rainieri, C., & Fabbrocino, G. (2014). Operational modal analysis of civil engineering structures. *Springer, New York*, *142*, 143. https://doi.org/10.1007/978-1-4939-0767-0

Republic of Türkiye Ministry of Energy and Natural Resources [MENR]. (2023, February 1). *Annual Average Wind Speed Distribution*. https://repa.enerji.gov.tr/REPA/bolgeler/TURKIYE-GENELI.pdf

Reynders, E. (2012). System identification methods for (operational) modal analysis: review and comparison. *Archives of Computational Methods in Engineering*, *19*(1), 51-124. http://dx.doi.org/10.1007/s11831-012-9069-x

Reynders, E. P. (2021). Uncertainty quantification in data-driven stochastic subspace identification. *Mechanical Systems and Signal Processing*, *151*, 107338. https://doi.org/10.1016/j.ymssp.2020.107338

Reynders, E., & De Roeck, G. (2008). Reference-based combined deterministic–stochastic subspace identification for experimental and operational modal analysis. *Mechanical Systems and Signal Processing*, *22*(3), 617-637. https://doi.org/10.1016/j.ymssp.2007.09.004

Reynders, E., Degrauwe, D., De Roeck, G., Magalhães, F., & Caetano, E. (2010). Combined experimental-operational modal testing of footbridges. *Journal of Engineering Mechanics*, *136*(6), 687-696. http://dx.doi.org/10.1061/(ASCE)EM.1943-7889.0000119

Reynders, E., Maes, K., Lombaert, G., & De Roeck, G. (2016). Uncertainty quantification in operational modal analysis with stochastic subspace identification: Validation and applications. *Mechanical Systems and Signal Processing*, *66*, 13-30. https://doi.org/10.1016/j.ymssp.2015.04.018

Shen, W. Z., Mikkelsen, R., Sørensen, J. N., & Bak, C. (2005). Tip loss corrections for wind turbine computations. *Wind Energy: An International Journal for Progress and Applications in Wind Power Conversion Technology*, *8*(4), 457-475. https://doi.org/10.1002/we.153

Suykens, J. A., Vandewalle, J., & De Moor, B. (2001). Intelligence and cooperative search by coupled local minimizers. *International Journal of Bifurcation and Chaos*, *11*(08), 2133-2144. https://doi.org/10.1142/S0218127401003371

Tcherniak, D., Chauhan, S., & Hansen, M.H. (2010, February 1-4). *Applicability Limits of Operational Modal Analysis to Operational Wind Turbines*. IMAC XXVIII: A Conference on Structural Dynamics, Jacksonville, FL, USA.

Tcherniak, D., & Allen, M.S. (2015, May 12-14). *Experimental characterization of an operating Vestas V27 wind turbine using harmonic power spectra and OMA SSI.* 6th International Operational Modal Analysis Conference, Gijon, Spain.

Teughels, A. (2003). *Inverse modelling of civil engineering structures based on operational modal data.* [Doctoral dissertation]. Katholieke Universiteit Leuven.

Teughels, A., & De Roeck, G. (2004). Structural damage identification of the highway bridge Z24 by FE model updating. *Journal of Sound and Vibration*, *278*(3), 589-610. https://doi.org/10.1016/j.jsv.2003.10.041

Teughels, A., De Roeck, G., & Suykens, J. A. (2003). Global optimization by coupled local minimizers and its application to FE model updating. *Computers & structures*, *81*(24-25), 2337-2351. https://doi.org/10.1016/S0045-7949(03)00313-4

Van Der Auweraer, H., Guillaume, P., Verboven, P., & Vanlanduit, S. (2001). Application of a fast-stabilizing frequency domain parameter estimation method. *Journal of Dynamic Systems, Measurement and Control*, *123*(4), 651-658. https://doi.org/10.1115/1.1410369

Worden, K., & Tomlinson, G. R. (2019). *Nonlinearity in structural dynamics: detection, identification and modelling*. CRC Press.

World Wind Energy Association [WWEA]. (2023, February 1). *Wind Power Capacity in the Net Zero Scenario.* https://www.iea.org/reports/wind-electricity

Xi, R., Wang, P., Du, X., Xu, K., Xu, C., & Jia, J. (2020). A semi-analytical model of aerodynamic damping for horizontal axis wind turbines and its applications. *Ocean Engineering*, *214*, 107861. https://doi.org/10.1016/j.oceaneng.2020.107861

Yang, Y. B., & Chen, Y. J. (2009). A new direct method for updating structural models based on measured modal data. *Engineering Structures*, *31*(1), 32-42. https://doi.org/10.1016/j.engstruct.2008.07.011

Yucel, U. (2020). *Finite element model updating and damage identification of reinforced concrete frames with different infills an unreinforced masonry walls*. [Doctoral dissertation]. Dokuz Eylül University.

Yucel, U., Durmazgezer, E., Ozcelik, O., & Misir, I. S. (2022). Damage Identification of a model frame-type structure and effects of offline tuning technique on the identification results. *Arabian Journal for Science and Engineering*, 1-16. https://doi.org/10.1007/s13369-022-07332-0

Zhao, X., & Lang, Z. (2019). Baseline model based structural health monitoring method under varying environment. *Renewable Energy*, *138*, 1166-1175. https://doi.org/10.1016/j.renene.2019.02.007

Zhou, L., Li, Y., Liu, F., Jiang, Z., Yu, Q., & Liu, L. (2019). Investigation of dynamic characteristics of a monopile wind turbine based on sea test. *Ocean Engineering*, *189*, 106308. https://doi.org/10.1016/j.oceaneng.2019.106308